The Cyclic Stress-Strain Behavior of a Single Crystal Nickel-Base Superalloy

Timothy P. Gabb
Lewis Research Center
Cleveland, Ohio

February 1988

NASA

TABLE OF CONTENTS

ACKNOWLEDGEMENTS

THE CYCLIC STRESS-STRAIN BEHAVIOR OF A SINGLE CRYSTAL NICKEL-BASE SUPERALLOY

Timothy P. Gabb
National Aeronautics and Space Administration
Lewis Research Center
Cleveland, Ohio 44135

SUMMARY

The utilization of single crystal nickel-base superalloys in load bearing structural applications requires the accurate prediction of monotonic and cyclic stress-strain response with proper consideration of variables such as temperature, strain rate, and temperature/deformation history. But the complexities involved in the deformation of these anisotropic alloys often precludes the application of classical continuum mechanics-based isotropic constitutive models. This behavior can often be more clearly understood and predicted through the relation of the mechanical response to the deformation mechanisms involved.

The purpose of this study was to characterize the cyclic stress-strain response and corresponding deformation structures of the single crystal nickel-base superalloy PWA 1480 under a specific set of conditions. The isothermal low cycle fatigue response and deformation structures were characterized at a representative intermediate temperature, 650 °C, and high temperature, 1050 °C. Specimens oriented near the [001], [$\bar{2}$ 5 20], [$\bar{3}$ 6 10], [011], [$\bar{2}$ 3 4], and [$\bar{1}$11] crystallographic orientations were tested at 650 °C, where significant crystallographic orientation effects were expected. Specimens oriented near the [001] and [$\bar{1}$11] crystallographic orientations were tested at 1050°C, where more moderate orientation effects were expected. This enabled the characterization of the deformation structures at each of the two temperatures and their relationship to the observed cyclic stress-strain behavior.

The initial yield strength of all specimens tested at 650 °C was controlled by the shearing of the γ' precipitates by dislocation pairs. Low cycle fatigue tests at 650 °C had cyclic hardening, which was associated with dislocation interactions in the γ matrix. The initial yield strength of specimens tested at 1050 °C was associated with dislocation bypassing of the γ' precipitates. Low cycle fatigue tests at 1050 °C had cyclic softening, associated with extensive dislocation recovery at the γ-γ' interfaces along with some γ' precipitate coarsening. Low cycle fatigue deformation at 650 °C was significantly affected by prior deformation at 1050 °C, but had little effect on subsequent low cycle fatigue deformation at 1050 °C. Low cycle fatigue deformation at 1050 °C was only slightly affected by prior deformation at 650 °C, and had major effects on subsequent low cycle fatigue deformation at 650 °C.

I. INTRODUCTION

Nickel-base superalloys are currently utilized in many engineering applications requiring good strength and ductility from room temperature to 1100 °C. Their application as gas turbine blades and vanes at the extreme upper end of this temperature range have dictated the use of directional solidification to

produce components having grains elongated in the high stress direction, or composed of a single grain (single crystal) to improve creep and thermal fatigue resistance. The monotonic and cyclic stress-strain response of these directionally solidified alloys are anisotropic with complex temperature and strain rate dependencies. This response can often be more clearly understood and predicted through the relation of the mechanical response to the deformation mechanisms involved. The purpose of this dissertation was to characterize the cyclic stress-strain response and the associated deformation structures of the single crystal nickel-base superalloy PWA 1480 at the temperatures of 650 and 1050 °C, which represent the extremes of application temperatures.

Chapter II of this report presents a literature review of the physical metallurgy, cyclic stress-strain response, and deformation structures of both polycrystalline and single crystal superalloys. The experimental procedures employed in this program are described in chapter III. The results of this work are presented in chapter IV. These results and the relationships between the mechanical response and the deformation structures are considered in the discussion of chapter V. The conclusions drawn from this study are presented in chapter VI.

II. LITERATURE REVIEW

THE PHYSICAL METALLURGY OF NICKEL-BASE SUPERALLOYS

The γ and γ' Phases

Nickel-base superalloys are utilized in many high temperature engineering applications requiring high strength and good ductility. These alloys are employed at temperatures of up to 1100 °C, which is over 90 percent of their melting points. A majority of these alloys are made up of a nickel-chromium γ-FCC matrix which is strengthened by $Ni_3(Al,Ti)$ γ' $L1_2$ structure precipitates. The physical metallurgy and strengthening mechanisms in nickel-base superalloys have been reviewed by Decker (ref. 1).

The γ phase consists of solid-solution-strengthened FCC nickel. This phase possesses good inherent ductility and is amenable to alloying without phase instability (ref. 2). It therefore usually contains solid solution additions of chromium along with cobalt, molybdenum, tungsten, vanadium, titanium, aluminum, and iron. At least 10 wt % of Cr is usually included for oxidation resistance and solid solution strengthening. In addition to chromium, aluminum, molybdenum, and tungsten also provide substantial solid solution strengthening. Titanium, cobalt, iron, and vanadium, included primarily for strengthening the γ' phase, are only weak solid solution strengtheners.

The γ' precipitate phase $Ni_3(Al,Ti)$ has an $L1_2$ intermetallic structure which can be considered ordered FCC with aluminum and titanium atoms at the corner positions and nickel atoms at the face centers. This structure is quite compatible with the γ-FCC matrix phase, with easy precipitation and lattice constant mismatch of less than 1 percent. The mechanical properties of the γ' phase have been extensively reviewed by Pope and Ezz (ref. 3). The strength of this phase increases quite substantially with increasing temperature (refs. 4 and 5) up to about 650 °C. This is attributed to the thermally activated cross slip pinning of superdislocations, as will be discussed in detail later. The

γ' phase is often highly alloyed, with cobalt, chromium, molybdenum, vanadium, and iron substituting for the nickel positions, and niobium, tantalum, vanadium, molybdenum, chromium, and iron substituting for the aluminum/titanium positions. All of these elements provide γ' solid solution strengthening to some extent.

γ' Strengthening in Superalloys

The γ' phase strengthens superalloys by introducing local elastic strains at the precipitate-matrix interfaces and by physically providing obstacles to dislocations travelling in the γ matrix. These effects are coupled, but will be treated separately for simplicity.

The sources of local interfacial strains are lattice mismatch and elastic constant mismatch. The mismatch in lattice parameters for the γ and γ' phases produces coherency strains near the interface proportional (fig. 1) to the unconstrained lattice mismatch or misfit δ:

$$\delta = 2\left(\frac{a_{\gamma'} - a_{\gamma}}{a_{\gamma'} + a_{\gamma}}\right) \tag{1}$$

The hardening due to these coherency strains of the precipitates is called coherency hardening. In an early study of a series of nickel-titanium-aluminum $\gamma-\gamma'$ alloys (ref. 6), the room temperature hardness was shown to vary directly with δ. In later work (ref. 7), the unconstrained lattice mismatch and yield strength of a series of experimental $\gamma-\gamma'$ alloys of positive and negative misfits were measured from 25 to 800 °C. Lattice mismatches became more negative with increasing temperature for all of the alloys, as the thermal expansion coefficient of the γ phase exceeded that of the γ' phase. Alloys of high misfit magnitude had higher yield strength, a strong dependence of yield strength on misfit, and deformation characterized as dislocation bypassing. Alloys of low misfit magnitude had lower yield strength, reduced misfit dependence, and dislocation shearing of the precipitates. These dislocation interactions are discussed below. Elastic strains at the $\gamma-\gamma'$ interface may also arise from differences in the elastic constants of the two phases. A remote stress applied normal to such an interface would produce different elastic strains in each phase and compatibility strains at the interface. This effect has not been systematically investigated experimentally, due to the experimental problems of measuring in situ the elastic constants of each phase accurately.

Dislocations interact with the γ' precipitates by either shearing or bypassing them. Precipitate shearing occurs for small γ' precipitate size and interparticle spacing while bypassing occurs at larger precipitate size and spacing. The critical precipitate size and spacing where the transition from shearing to bypassing occurs is dependent (ref. 8) on γ' volume fraction, temperature which influences dislocation mobility, and the sources of elastic strain previously considered. Superalloy composition and dislocation substructure also have roles in this dependence.

The γ' precipitates can be sheared by pairs of normal FCC dislocations of Burgers vectors $\mathbf{b} = 1/2\langle 110 \rangle$ or, at elevated temperatures and low strain rates, by more complex dislocations produced through dislocation reactions.

The former mechanism is usually observed in tensile and LCF loading and will first be discussed. An entire shear displacement in γ' is $\langle 110 \rangle$; this is achieved by the glide of a pair of $a/2\langle 110 \rangle$ total dislocations. Each of these two total dislocations may be dissociated into a pair of $a/6\langle 112 \rangle$ Shockley partial dislocations, separated by a superlattice stacking fault. The passage of the first total dislocation creates an antiphase boundary (APB) which impedes its motion, while the glide of the second total dislocation removes the APB. This shear process increases the shear strength by an amount proportional to the APB energy, the volume percent of γ', and the γ' size (ref. 9). For high γ' volume fraction superalloys such as MAR-M200, this increase in shear strength has been estimated (ref. 10) to be:

$$\Delta\tau = \frac{\gamma_{APB}}{(2b)} \qquad (2)$$

where γ_{APB} is the APB energy and $\mathbf{b}$ is the Burgers vector. As previously mentioned, the yield strength of γ' increases with increasing temperature up to 650 °C. When precipitate shearing is operative, this gives sustained or slightly increasing superalloy yield strength over this temperature range. This temperature dependence of yield strength has been attributed to the thermally activated cross slip of the lead dislocation of the pair onto to the cube cross slip plane (ref. 11) which has a lower APB energy than octahedral planes (ref. 5).

In creep loading at temperatures near 760 °C, primary creep at low stresses in high γ' volume fraction superalloys occurs by $\langle 112 \rangle$ slip (refs. 12 and 13) on $\{111\}$ planes. This requires the dissociation of an $a/2\langle 110 \rangle$ dislocation into an $a/3\langle 112 \rangle$ dislocation which shears the precipitate, creating an intrinsic stacking fault, and an $a/6\langle 112 \rangle$ dislocation which remains at the interface.

Dislocation bypassing of γ' precipitates occurs by Orowan looping at low to intermediate temperatures. The resulting increase in shear strength has been estimated (ref. 14) to be:

$$\Delta\tau_L = 0.2\ G\ b\ K\left(\frac{2}{\lambda}\right)\ \ln\left(\frac{d}{2\mathbf{b}}\right) \qquad (3)$$

where G is the shear modulus, K is a function of dislocation character, d is the γ' particle diameter, and λ is the interparticle spacing which varies inversely with γ' volume fraction. At high temperatures bypassing can occur by dislocation climb looping at high applied stresses, $\sigma > G\ \mathbf{b}/\lambda$, according to the Weertman equation (ref. 15):

$$\dot{\varepsilon} = 2\ \sigma^4\ \frac{^2D}{d\ G^3 kT} \qquad (4)$$

where k is Boltzmann's constant. At low stresses, $\sigma < G\ \mathbf{b}/\lambda$, dislocations climb around γ' precipitates without looping according to the Nabarro-Herring creep equation (ref. 16):

$$\dot{\varepsilon} = \frac{\sigma \mathbf{b}^3\ D}{2k\ d^2\ T} \qquad (5)$$

4

Processing of Nickel-Base Superalloys

Superalloy properties are sensitive to compositional accuracy and the presence of impurities. Therefore vacuum induction melting, vacuum arc remelting, and electroslag remelting are often employed. After melting at temperatures over 2300 °F, workable alloys are cast into ingots. Alloys which will not be worked are cast to the desired shape. In addition, powder is sometimes produced, with each powder particle in effect being a "microcasting," greatly reducing segregation.

Polycrystalline superalloys designed for intermediate temperature (400 to 760 °C) applications such as turbine disks possess fair workability (ref. 17), but superalloys designed for high temperature (760 to 1050 °C) applications such as turbines blades and vanes (e.g., PWA 1480) are usually not workable and are only heat treated after casting. The casting macrostructure in these alloys is not fully removed during most subsequent commercial heat treatments, and it can influence the resulting mechanical properties. Superalloys solidify over a large temperature range, therefore the cast structure is usually dendritic (ref. 18). Because of the FCC structure of the γ phase, the primary, secondary, and tertiary dendrite arms grow in $\langle 001 \rangle$ directions. Primary γ-γ' eutectic often forms in the interdendritic regions and at grain boundaries during casting due to the resulting composition variations and the presence of nucleation sites in these regions. This primary γ' does not easily redissolve during solution heat treatments, and usually some remains in the interdendritic regions and grain boundaries in the fully heat treated microstructure.

For high temperature applications in which creep and thermal fatigue limit life, large columnar-oriented grains or single crystal macrostructures are often preferred. In this structure the grain boundaries transverse to the stress axis are greatly reduced in number or eliminated, negating the grain boundary failure mode. This improves creep and fatigue resistance. The grains are aligned with their columnar axis very near the [001] crystal axis, producing a lower elastic modulus than equiaxed structures. This improves low cycle fatigue and thermal fatigue resistance in this direction by reducing the stress produced by an imposed strain. These castings are produced by directional solidification (ref. 19 and 20), in which solidification occurs only in the axial direction.

In heat treatment (ref. 21), nickel-base superalloys are usually first solution treated at a temperature between 1000 and 1290 °C. This forces most of the existing γ' to go back into γ solution and homogenizes the resulting γ solution in order to facilitate later uniform γ' precipitation. One or more aging treatments are then employed in order to precipitate the γ' phase. These treatments are usually performed at temperatures between 840 °C and 1100 °C for times of up to 48 hr to give γ' precipitates of the desired size and morphology. Sometimes a short aging time at high temperature (1000 to 1100 °C) for γ' nucleation is combined with a long low temperature (800 to 900 °C) aging step for slow, controlled γ' growth.

LOW CYCLE FATIGUE

Components in many engineering applications are subjected to alternating loads. These alternating loads often limit their useful life before failure. The associated stresses may be generated at constrained locations of the component, such as notches or internal points, where the surrounding material constrains and therefore controls the deformation. This is a "strain-controlled" situation. In a low cycle fatigue (LCF) test large cyclic loads are applied between fixed total strain limits to simulate "strain-controlled" conditions, to produce a relatively short (low) cyclic fatigue life of less than 10^4 cycles.

The stress and strain response in the first fatigue cycle generally resembles the hysteresis curve or loop shown schematically in figure 2. The cyclic stress and strain parameters utilized to describe this low cycle fatigue response, as indicated in figure 2, are cyclic stress range $\Delta\sigma$, total strain range $\Delta\varepsilon_t$, and cyclic inelastic strain range $\Delta\varepsilon_{in}$. In an LCF test, the total strain range defines the fixed total strain limits within which cycling occurs, and is usually constant in magnitude. Typically, total strain is employed as the controlling variable in a testing machine, such that sufficient load is applied to produce a total strain which varies periodically with time in a controlled manner. But the material response, as measured by the cyclic stress range $\Delta\sigma$ and the inelastic strain range $\Delta\varepsilon_{in}$, often changes with continued cycling though cyclic stability is often attained.

LCF stress-strain response is generally characterized in terms of (1) the cyclic stress hardening/softening response, and (2) the cyclic stress-strain curve (ref. 22). The cyclic stress hardening response concerns the transient cyclic stress range variation as a function of fatigue cycles. The cyclic stress hardening response is illustrated in figure 3, with the associated cyclic stress and strain response of the hysteresis loops. If the material becomes more resistant to the applied strains ("cyclic hardening"), $\Delta\sigma$ increases with continued cycling while $\Delta\varepsilon_{in}$ decreases. Alternatively, the material may become less resistant to the applied strains ("cyclic softening"), and $\Delta\sigma$ decreases with continued cycling while $\Delta\varepsilon_{in}$ increases.

As indicated above, the stress-strain response of a material often changes from the original monotonic response. The stress-strain response of a material subsequent to fatigue cycling is therefore important for engineering design. This response is characterized by the cyclic stress-strain curve, which deals with the eventual stable "saturated" hysteresis loop which is often attained in LCF tests after a number of cycles. The cyclic stress range is plotted versus the inelastic strain range of the stabilized loops from several LCF tests to generate a curve. This curve describes the cyclic flow behavior in a manner analogous to that of a monotonic tensile test stress-strain curve. This curve is usually modeled with an equation of the general form:

$$\frac{\Delta\sigma}{2} = A \left(\frac{\Delta\varepsilon_{in}}{2}\right)^{m'} \qquad (6)$$

6

THE CYCLIC STRESS-STRAIN BEHAVIOR OF NICKEL-BASE SUPERALLOYS
AT LOW-INTERMEDIATE TEMPERATURES

Polycrystals

Nickel-base superalloy deformation from room temperature to 800 °C is generally heterogeneous with planar slip. For polycrystalline Ni-base superalloys the cyclic stress-strain response and operative deformation mechanisms are dependent on the γ' precipitate size and spacing (refs. 23 and 24) and the test temperature. When the interparticle spacing is small enough to impede dislocation bowing according to the mechanism of Orowan, precipitate shearing is encouraged. If the γ' precipitate spacing and size is somewhat larger, Orowan looping occurs and dislocations are stored at the particle interfaces. In their heat treated forms, most modern wrought and cast nickel-base superalloys for turbine disk and blade applications have relatively small average precipitate size and interparticle spacing. This produces γ' precipitates shearing at low to intermediate temperatures in a majority of these alloys (refs. 25 to 27).

In fatigue studies of wrought Udimet 700 at room temperature (ref. 25) and 760 °C (ref. 26), LCF tests of significant inelastic strain produced γ' shearing with initial cyclic hardening, attributed to the antiphase boundary formation process of the γ' dislocation pairs and to general dislocation accumulation. This was immediately followed by cyclic softening, attributed to particle disordering through increasingly irreversible shear. Therefore no stable cyclic stress-strain state was attained. In a study of the effects of γ' size on the LCF response of Waspaloy (ref. 23), specimens with γ' precipitates smaller than a critical size were found to display γ' shearing with the above response. Specimens having a γ' size exceeding the critical size displayed dislocation bowing around the precipitates. This produced cyclic hardening to a stable equilibrium cyclic stress-strain state. For LCF tests of a given inelastic strain range, the cyclic stress amplitude increased with the γ' size. A fatigue study (ref. 27) of seven nickel-base superalloys of various γ' volume fractions and microstuctures at 650 °C showed that the cyclic stress amplitude increased with γ' volume fraction. In the microstructures, only grains oriented to produce a high shear stress were deformed. All of the alloys displayed γ' shearing in these grains, but alloys having a uniform, fine γ' distribution had planar slip, while alloys also having larger γ' precipitates had more homogeneous γ' shearing. A majority of the alloys displayed slight cyclic hardening in these tests of relatively low inelastic strains.

Single Crystals

Relatively less information is available on the cyclic stress-strain behavior of single crystal nickel-base superalloys, but the cyclic response reported in other FCC single crystal alloys can sometimes be extended to superalloys. In studies of the room temperature LCF behavior of a two phase Al-Cu single crystal alloy displaying planar slip, a significant crystallographic orientation dependence was observed (ref. 28). Specimens deforming on a single slip system display a low initial stress response with a high hardening rate and saturation stress. When resolved on the operative slip system by Schmid's Law (ref. 29):

$$\tau = \sigma \cos \phi \cos \lambda \quad \text{and} \quad \gamma = \frac{\varepsilon}{\cos \phi \cos \lambda} \tag{7}$$

these specimens had quite comparable shear stress and strain response. Specimens deforming by multiple slip had an increased initial stress response but a reduced hardening rate and saturation stress. Orowan looping of primary slip dislocations around the precipitates was dominant in single slip specimens, while precipitate particle shearing and a high density of secondary slip system dislocations were observed in multiple slip specimens. The single crystal nickel-base superalloy Rene N4 displayed similar cyclic hardening curves at 760 °C (ref. 30). Specimens displaying octahedral slip on a single system have a low initial stress response with little strain hardening for 10 to 20 fatigue cycles, followed by rapid hardening to a saturation value. Specimens near [001] deformed on several octahedral slip systems and had increased initial hardening. However the cyclic stress-strain curve at saturation was comparable for all specimens. In these tests of large inelastic strain, γ' precipitate shearing was observed both within slip bands and throughout the microstructure. In LCF tests of very low inelastic strains of another experimental single crystal nickel-base superalloy (ref. 31), dislocations were only observed in the γ phase extending between the γ' precipitates.

However single crystal nickel-base superalloys with high γ' volume fractions (>55 percent) show significant deviations from classical FCC alloy planar slip response at intermediate temperatures. Rather than the conventional FCC alloy octahedral slip (slip in ⟨101⟩ directions on {111} planes), [$\bar{1}$11]-oriented single crystals of PWA 1480 (ref. 32) and Rene N4 (ref. 30) deform by primary cube slip (slip in the [$\bar{1}$10] direction on the (001) plane) in tensile (ref. 32) and LCF (ref. 30) loading at intermediate temperatures. This has been attributed to the lower antiphase boundary energy of {001} planes compared to {111} planes (ref. 10), and the higher resolved shear stress on this slip system than the octahedral system (ref. 32) for crystals oriented near [$\bar{1}$11]. In addition, when deforming by octahedral slip these same superalloys do not obey Schmid's Law for monotonic and cyclic yield strength in tension and compression in this temperature range. Instead they display a significant orientation-dependent tension-compression anisotropy in monotonic yield strength (ref. 32), which is sustained in LCF cycling (ref. 30). The nearly identical tension-compression anisotropy in single phase γ' was attributed (refs. 33 and 34) to the orientation-dependent effect of the applied stress direction in either aiding or retarding the cross slip of dissociated dislocations by constricting or extending them, respectively. This cross slip occurs onto the cube planes; it is driven by the lower antiphase boundary energy of the cube planes and is thermally activated. As previously mentioned, its occurrence greatly impedes normal dislocation glide on the octahedral planes and accounts for the increasing yield strength of γ' from room temperature to about 760 °C. These specific dislocation glide and cross slip tendencies within the γ' precipitates were therefore used to explain the tension-compression anisotropy of PWA 1480 and Rene N4.

In single phase copper where planar slip was observed the cyclic stress-strain curve displays a broad constant stress plateau (ref. 35). This stress has been characterized (ref. 35) as the stress required to generate persistent slip bands in the undeformed microstructure. A similar stress plateau was observed in Mar-M200 single crystals at room temperature (ref. 36), with persistent slip bands of γ' shearing present. But this stress plateau is eliminated as the temperature is increased, as both Mar-M200 (refs. 36 and 37) and

8

Rene N4 (ref. 30) display a significant hardening slope in their cyclic stress-strain curves at intermediate temperatures, where deformation is no longer confined to slip bands.

THE CYCLIC STRESS-STRAIN BEHAVIOR OF NICKEL-BASE SUPERALLOYS AT HIGH TEMPERATURES

Polycrystals

Nickel-base superalloy deformation at temperatures above 870 °C is generally homogeneous with "wavy" slip. Stress range softening with continued fatigue cycling has been generally observed in polycrystalline superalloys (refs. 38 and 39). This was attributed to the enhanced dislocation cross slip and climb brought on by increased stacking fault energy and thermal activation at high temperatures (ref. 40). Unlike monotonic deformation, γ' shearing was usually precluded in cyclic deformation in this temperature range. Orowan looping was prevalent, giving dislocation storage at the γ-γ' interfaces. Fatigue cycling has produced somewhat accelerated γ' coarsening in many superalloys in this temperature regime. The accelerated coarsening has been attributed to enhanced diffusion brought on by the dislocation networks at the γ-γ' interfaces (ref. 41). This γ' coarsening is often used to explain the stress range softening with continued cycling (ref. 42), as suggested by the particle size dependence of yield strength in the Orowan equation. Typical is a fatigue study of Rene 80 at 871 and 982 °C (ref. 38). LCF produced rapid initial softening followed by gradual softening, attributed to γ' coarsening. For tests of a given inelastic strain range, cyclic stress amplitude decreased with increasing temperature and decreasing strain rate. Hexagonal networks of chiefly edge dislocations were generated at the γ-γ' interfaces.

Single Crystals

The literature contains less information on the LCF response of single crystal nickel-base superalloys at high temperatures. Directionally solidified (ref. 43) and single crystal (refs. 30 and 44) superalloys also have displayed cyclic stress softening with continued fatigue cycling in this temperature range. This was again attributed to fatigue-accelerated γ' coarsening. Rather than γ' shearing, homogeneous dislocation glide with climb around precipitates occurred (ref. 45). These deformation dislocations accumulate at the γ-γ' interfaces, where they rearrange into networks facilitating the relief of interfacial strains. The cyclic stress-strain curves observed here had a higher hardening slope than that at intermediate temperatures (refs. 30 and 44). In one study (ref. 30) of Rene N4 at 982 °C, specimens oriented near [$\bar{1}$11] had a lower cyclic stress-strain curve hardening slope (m' = 0.13) than that of specimens oriented in several other directions (m' = 0.3). The [$\bar{1}$11] specimens also had a significant tension-compression anisotropy ($\sigma_{tension}$ > $\sigma_{compression}$) which was sustained (ref. 30) in fatigue cycling. This was not present for the other specimens. This cyclic tension-compression anisotropy of [$\bar{1}$11]-oriented specimens has also been reported (ref. 46) in the LCF of PWA 1480 at 980 °C.

Misfit Dislocations

The dislocation networks observed at the $\gamma-\gamma'$ interfaces after high temperature LCF are believed to relieve the strains at the $\gamma-\gamma'$ interfaces induced by lattice mismatch and applied external loads. The dislocation characteristics and dislocation network configurations required to efficiently relieve pure dilational interfacial strains due to lattice mismatch (misfit) have been extensively investigated. But these aspects are not as well understood for more complex strain states and for the application of external loads.

Misfit dislocation network theory is based in large part on the work of Van der Merwe (ref. 47) and Frank and of Jesser and Kuhlmann-Wilsdorf (ref. 48). This work was recently reviewed by Shiflet (ref. 49). Individual dislocations most efficient at relieving misfit strains due to lattice mismatch are edge in character and have a Burgers vector in the plane of the interface, figure 1. Utilizing these rules for the $a/2\langle 110 \rangle$-type dislocations usually found in the γ phase of $\gamma-\gamma'$ superalloys, Lasalmonie, and Strudel (ref. 50) derived and experimentally verified a consistent three-dimensional description of the misfit dislocation networks surrounding the γ' precipitates. In this model, {111} interfaces would contain three sets of $a/2\langle 110 \rangle$ edge dislocations knitted in hexagonal networks (i.e. for the (111), $b_1 = 1/2[\bar{1}01]$, $b_2 = 1/2[\bar{1}10]$, and $b_3 = 1/2[0\bar{1}1]$). The {001} interfaces would contain two sets of edge dislocations (i.e. for the (001), $b_1 = 1/2[\bar{1}10]$ and $b_2 = 1/2[110]$) in a square network. This is shown schematically in figure 4. It should be noted that the nodes of the {001} square network often relax into four closely spaced threefold nodes by dislocation reactions. The identical equilibrium misfit dislocation network has been independently derived by O-lattice construction, often employed in grain boundary theory (refs. 49 and 51). The spacing p of the individual dislocations relieving the misfit strain is theoretically inversely proportional to the lattice mismatch magnitude $|\delta|$, as shown in figure 1:

$$\delta = 2 \left(\frac{a_{\gamma'} - a_{\gamma}}{a_{\gamma'} + a_{\gamma}} \right) \tag{8}$$

and

$$p = \frac{|\bar{b}|}{|\delta|} \tag{9}$$

Experimental observations of dislocation networks generated by the extended high temperature aging of $\gamma-\gamma'$ superalloys have been in reasonable agreement with these predictions. The individual dislocation spacing has usually agreed reasonably well with the above equation. However, dislocation character, the dislocation Burgers vector - interface plane relationship, and network configuration have agreed in two studies (refs. 50 and 52) and disagreed in another (ref. 53). In the latter case, the dislocations' edge components resolved in the plane of the interfaces were employed in the dislocation spacing computations.

Mechanical loading at elevated temperatures has accelerated the accumulation of dislocations at the $\gamma-\gamma'$ interfaces (refs. 38, 50, 52, and 54).

While relatively few characterizations of these dislocations have been per-
formed, more variability in dislocation characteristics seems evident. The
monotonic creep loading (ref. 52) of [001] single crystals of an experimental
superalloy at 1050 °C produced dislocations of Burgers vectors corresponding
to the operative octahedral slip systems: $b = 1/2[\bar{1}01]$, $1/2[101]$, $1/2[0\bar{1}1]$,
and $1/2[011]$. These were aligned near the $[\bar{1}10]$ and $[110]$ directions on (001)
interfaces. These Burgers vectors do not lie in this plane. Creep and LCF
loading of Rene 80 at 871 °C was reported (refs. 38 and 54) to produce hexa-
gonal networks of chiefly edge dislocations. Similar hexagonal networks were
also reported for Mar-M200 (refs. 37 and 55) and PWA 1480 (ref. 56). No gen-
eral comparisons of interfacial dislocations' Burgers vectors and interface
planes were reported in these studies. LCF loading of Rene N4 single crystals
at 982 °C produced square dislocation networks on near-{001} plane interfaces
and hexagonal dislocation networks on {110} and {111} plane interfaces
(ref. 45). The dislocations of these networks often had Burgers vectors
corresponding to octahedral slip. Therefore near-edge dislocations of
$b = 1/2[\bar{1}01]$ and $1/2[101]$ were observed on (010) interfaces, while mixed
dislocations of an octahedral slip Burgers vector were knitted to near-edge
dislocations of $b = 1/2[\bar{1}10]$ on (001) interfaces.

ANALYSIS OF THE PROBLEM

The utilization of single crystal alloys in load bearing structural appli-
cations requires the accurate prediction of monotonic and cyclic stress-strain
response with proper consideration of variables such as temperature, strain
rate, and temperature/deformation history. But the complexities involved in
the deformation of these alloys often precludes the application of classical
continuum mechanics-based constitutive models. The monotonic and cyclic plas-
tic and creep anisotropy observed here, which have variable temperature, strain
rate, and history dependencies, can be more clearly understood and predicted
through the relation of the mechanical response to the deformation mechanisms
involved. This understanding exists to some degree for some copper and single
phase γ' single crystal alloys, but is incomplete for single crystal nickel-
base superalloys. The purpose of this study was to characterize the cyclic
stress-strain response and the corresponding deformation structures of the sin-
gle crystal nickel-base superalloy PWA 1480 under a specific set of chosen con-
ditions. The isothermal low cycle fatigue response and deformation structures
was characterized at a representative intermediate temperature, 650 °C, and
high temperature, 1050 °C. Specimens oriented near the [001], [2 5 20],
[3 6 10], [011], [2 3 4], and [$\bar{1}$11] crystallographic orientations were tested
at 650 °C, where significant crystallographic orientation effects were
expected. Specimens oriented near the [001] and [$\bar{1}$11] crystallographic orien-
tations were tested at 1050 °C, where moderate orientation effects were
expected. This enabled the characterization of the deformation mechanisms at
each of the two temperatures and their relationships to the observed cyclic
stress-strain behavior.

III. EXPERIMENTAL

MATERIAL

The composition of the material master heat is listed with the nominal
composition in table 1. The material was cast into single crystal bars,

nominally 21 mm diam and 140 mm length, and single crystal slabs, nominally 160 mm long by 60 mm wide by 13 mm thick, by the withdrawal directional solidification process. All bars and slabs were radiographed to check for excessive porosity. The bars and slabs were subsequently solution treated in argon at an average temperature of 1270 °C for 4 hr, air quenched, and then aged in argon at 1080 °C for 4 hr and then at 871 °C for 32 hr. The growth axes of the bars and slabs were all within 10° of the [001] crystallographic direction.

Specimens of [001] crystallographic orientation were machined directly from the bars. Specimen blanks were spark-machined at various chosen angles in the slabs in order to obtain specimen axes oriented near the [001], [011], [$\bar{1}$11], [$\bar{3}$ 6 10], and [$\bar{2}$ 3 4] crystallographic directions. The specimens (fig. 5) were machined from the blanks by low-stress grinding. The final polishing marks on the gage section of each specimen were oriented parallel to the specimen axis. The crystallographic orientation of each specimen was determined to within ±1.5° by Laue back-reflection x-ray measurement.

The specimens' microstructure was generally characterized in both the as-heat-treated and the deformed states by optical, scanning electron, and transmission electron microscopy. The average γ' size was determined using the line intercept technique by counting the number of γ-γ' interface crossings on random lines drawn parallel to the [100] and [010] directions on [001]-oriented specimens. The γ' volume fraction was determined by phase extraction. The volume fraction of the γ-γ' eutectic pools and interdendritic porosity was measured using standard metallographic area fraction point counting. The overall alloy composition was measured using standard chemical analysis techniques while the composition of selected features was measured with a microprobe.

MECHANICAL TESTING

Specimens aligned near the [001], [$\bar{2}$ 5 20], [$\bar{3}$ 6 10], [011], [$\bar{2}$ 3 4], and [$\bar{1}$11] crystallographic orientations were selected for fatigue testing at 650 °C while those near [001] and [$\bar{1}$11] were fatigue tested at 1050 °C. Specimens of each orientation were tested at 650 and 1050 °C in low cycle fatigue (LCF) at total strain ranges selected to produce initial inelastic strain ranges of near 0.0008, 0.0017, and 0.0025 mm/mm, table 2. Several additional LCF tests were interrupted at a chosen number of cycles, unloaded, and then cooled to room temperature. Specimens of each orientation were also tensile tested at each temperature in order to determine monotonic tensile properties. To examine the effects of prior non-isothermal deformation on fatigue response, several specimens were fatigue cycled to saturation at one of the temperatures listed above, repolished, and then tested at the other temperature until failure.

The LCF and tensile tests were performed on a closed loop servohydraulic testing machine. This machine had a load cell of ±45 N resolution for load measurement and an axial extensometer of 12.7 mm gage length and ±0.00005 mm/mm resolution for strain measurement. In the LCF and tensile tests at 650 °C and the tensile tests at 1050 °C the specimens were heated with a three-zone clamshell resistance heating furnace in which the temperature was controlled to ±1.5 °C. The temperature gradient along the specimen's 12.7 mm gage length was less than ±5 °C. In the LCF tests at 1050 °C the specimens were heated with a 5 kW radio frequency induction unit. The temperature was controlled here with

a closed-loop proportioning controller utilizing a spring-loaded flattened thermocouple held tightly against the specimen gage section for temperature measurement. This temperature was calibrated and independently monitored with another thermocouple spot-welded to the specimen gage section and with a non-contacting optical pyrometer. The temperature was controlled here to ±4 °C, and the temperature gradient along the specimen gage length was less than ±7 °C. In all tests load and strain were continuously recorded on a strip chart recorder. The load signal was also independently monitored on a digital multimeter. Fatigue hysteresis loops were periodically recorded on an X-Y recorder.

The cyclic stress-strain response in these strain-controlled LCF tests can be affected by inaccuracies in strain measurement. These inaccuracies may be related to the insecure attachment of the extensometer or variations and insta-bilities of the specimen's temperature during the test. In order to establish the absence of extensometer probe slippage which would affect the stress-strain response, several tests were reproduced under different conditions. These tests were performed: (1) with the same test machine on specimens of various orientations having deep surface scratches to prevent any possible probe slip; and (2) with an entirely different test machine employing diametral extensome-try and direct resistance heating on hourglass-shaped [001] specimens. In order to establish the absence of specimen temperature variations or instabili-ties in tests at 1050 °C, several LCF tests of the [001] and [$\bar{1}$11] specimens were reproduced under different conditions here also. In these tests the spec-imen temperature was controlled by a closed-loop proportioning controller employing a noncontacting infrared pyrometer for temperature measurement. The pyrometer measured the specimen's temperature at a heavily-etched location of constant emissivity in the gage section. The temperature was calibrated and independently monitored with a thermocouple spot-welded to the specimen gage section.

In the LCF tests total strain was employed as the controlling variable ("total strain control"). Sufficient load was applied as commanded by the closed loop algorithm of the testing machine control system to produce the required strain. A function generator was employed to produce a varying dc voltage signal as a function of time. This signal was utilized as the required strain voltage in the control system of the servohydraulic testing machine. The total strain control signal was varied periodically with time in a con-trolled manner within total strain limits held constant in most of the tests as shown in figure 3. Several additional LCF tests were performed at a constant inelastic strain range by continuously adjusting the total strain range as required. At 650 °C where specimens often yielded by discontinuous "jerky" flow, a 0.1 Hertz sinusoidal waveform was employed as the strain control sig-nal. This waveform produces slower strain rates near the strain limits where the discontinuous yielding occurred, allowing better system control. Previous work (ref. 56) has shown that the mechanical response of this alloy is not highly strain rate dependent in this temperature regime. At 1050 °C, the mechanical properties of superalloys are known to be more dependent on strain rate. Therefore a sawtooth waveform of constant strain rate was employed. The strain rate of 0.002 sec^{-1} was comparable to the average strain rate of the 650 °C LCF tests. The LCF tests were sometimes interrupted before failure for subsequent testing at another temperature. These tests were interrupted by slowly reducing the total strain amplitude to zero.

Because the extensometer was only capable of measuring strain up to 0.20 mm/mm, the tensile tests were performed in "stroke control," in that the actuator displacement as measured by an LVDT was employed as the control variable. The function generator was utilized to produce a ramp wave giving a constant actuator displacement rate of 8 mm/sec. This produced a strain rate of 0.001 to 0.003 sec^{-1} in the specimen.

ELECTRON MICROSCOPY

Several [001] and [$\bar{1}$11] LCF specimens were sectioned longitudinally and transversely to enable scanning electron microscope examination of the microstructure before and after LCF testing. These specimens were prepared using standard metallographic techniques and then etched with a solution composed of 33 percent nitric acid - 33 percent acetic acid - 33 percent H_2O - 1 percent hydrofluoric acid. These specimens were examined with a Cambridge 200 scanning electron microscope.

Foil blanks for transmission electron microscopy (TEM) were sliced with a low speed saw to obtain foils oriented either normal to the centerline axis or parallel to the operative slip planes of specimens deformed at 650 °C where planar slip was observed. Foil blanks were only sliced normal to the centerline axis and parallel to the (011) plane of specimens deformed at 1050 °C where homogeneous slip was observed. Disks of 3 mm diameter were then spark machined from the blanks. The disks were carefully marked in order to record the orientation of the load axis. Therefore no indexing assumptions were required in the later TEM analysis of these foils. The disks were mechanically polished to 0.1 mm thickness on 600 grit sand paper. The disks were then electrochemically thinned with a twin-jet thinner using a solution of 10 percent perchloric acid, 45 percent acetic acid, 45 percent butylcellusolve at 0 °C. The foils were examined with a Phillips EM400T transmission electron microscope operated at 120 kV. At least four foils from every specimen selected for TEM analysis were generally surveyed; two of these foils were analyzed in detail. Foils were also prepared from an undeformed specimen in order to verify that the preparation procedures did not produce significant deformation in the observed microstructure.

ANALYTICAL TECHNIQUES

Slip System Determination

The operative slip systems of deformed specimens of a given crystallographic orientation were determined and redundantly verified by several techniques. Slip traces, when observable on the specimen surface, were analyzed to determine the corresponding slip planes by standard slip trace analysis. In monotonic deformation of single crystals, the crystallographic orientation of the specimen loading axis rotates towards the slip direction. Therefore the crystallographic orientations of the deformed gage sections and of the undeformed ends of the tensile specimens were determined to indicate rotations of the tensile axis and the corresponding slip directions. The TEM foils were also analyzed as described below to determine the dislocations' Burgers vectors (which indicates the slip direction) and their slip planes.

14

Dislocation Analysis

In the TEM analysis of the deformation structure of a given specimen, one or more regions of a foil was first extensively analyzed with redundant extensive tilting experiments to determine and accurately characterize dislocations' Burgers vectors, line directions, planes, and collective arrangements. Brief tilting experiments utilizing a series of three or four micrographs were then designed and performed over numerous regions of several foils, in order to determine the statistical significance of the previous determinations. These brief experiments also indicated the relative statistical frequency of observations for comparisons between different specimens.

The dislocations' Burgers vectors were determined by $\mathbf{g} \cdot \mathbf{b}$ image analysis (ref. 57). Micrographs of four different reflections were employed in this analysis (only three reflections are required) in order to allow a redundant test of every determination. $+\mathbf{g}/-\mathbf{g}$ imaging experiments (ref. 58) were performed when necessary to determine the relative sign of the dislocations' Burgers vectors. Dislocation line directions were determined by standard stereographical line trace analysis (ref. 59). The dislocations' planes were determined by large angle tilting experiments in which dislocations of appreciable curvature were tilted to where their projections were straight lines as illustrated in figure 6. The dislocations' planes were sometimes also determined by measuring the line directions of several different segments of a curved dislocation. The cross product of these directions is the normal of the dislocation's plane. The slip planes of near-edge dislocations were also sometimes estimated as the cross product of the Burgers vector and the line direction. However, this computation required the assumption that no dislocation climb had occurred and was therefore not usually relied upon.

IV. <u>RESULTS</u>

METALLURGICAL CHARACTERIZATION OF THE TEST MATERIAL

The actual composition of the test material, determined by standard chemical analysis, is listed in table 2 along with the nominal PWA 1480 composition in weight percent. The material was directionally solidified by the withdrawal process into single crystal slabs nominally 60 mm wide by 160 mm long by 13 mm thick, and single crystal bars nominally 140 mm long by 21 mm diameter. The slabs and bars both had their long dimension nominally parallel to the [001] crystal growth direction.

The slabs and bars had comparable macrostructures. The primary dendrite arm spacing of the slabs was 640 μm with a standard deviation of 130 μm (640±130 μm), figure 7, while that of the bars was 726±226 μm, figure 8. The secondary dendrite arm spacing was somewhat difficult to discern in the fully heat treated specimens, but in both the slabs and bars it ranged from 200 to 400 μm.

The microstructures of the slabs and bars were also quite comparable. The various features of the microstructure are shown in figure 9. As in most directionally solidified superalloys, a significant amount of casting microporosity was present in the test material, principally in the interdendritic regions, figure 7. In the slabs and bars, this porosity had a volume fraction

of 0.30±0.09 percent. These micropores were of widely varying size, at times
as large as 50 μm, but were typically 5 to 10 μm in diameter. The material
also contained γ-γ' eutectic pools. These eutectic pools had a volume frac-
tion of 2.3±0.3 percent in the bars and 2.9±1 percent in the slabs. The pools
were present throughout the microstructure, including near dendrite cores,
figure 10(a). But the eutectic pools were more numerous in the interdendritic
regions, figure 10(b), with a local volume fraction of over 4 percent measured
at one point in a slab. The eutectic pools were mostly constituted of the γ'
phase. The measurement of the composition of neighboring large and small
eutectic pools with a microprobe showed that the chromium level of the pools
was significantly reduced, while the tantalum level was increased from that
of the normal γ-γ' microstructure, figure 11. This is consistent with the
high tantalum level in this alloy and the slow diffusivity of this element in
nickel. As shown in figures 10 and 11, the eutectic pools were irregularly
shaped and varied in size from 10 to 100 μm in diameter.

The slabs had a γ' volume fraction of 65.7±1.6 percent, while the bars
had a γ' volume fraction of 65.6±3.4 percent. The γ' precipitates usually
had a cuboidal morphology, figure 12. In both the slabs and bars these precip-
itates were 0.55±0.18 μm in width over 1000 measurements. In the interden-
dritic regions near the eutectic pools, the precipitates were sometimes larger
in diameter (0.8 to 1.0 μm) and irregularly shaped, figure 9. But as shown in
the extreme left of figure 11, the average composition here was still compara-
ble to that of the normal γ-γ' microstructure, unlike that of the eutectic
pools on the right.

LOW CYCLE FATIGUE AT 650 °C

Mechanical Response

Operative slip systems at 650 °C. - Tensile tests were performed to aid
in the determination of the active slip systems. The 650 °C tensile test
results are given in table 3. The axial stress-strain curves of these tests
are depicted in figure 13. The crystallographic rotations of these tensile
specimens are depicted in figure 14. A single crystal rotates towards the
operative slip direction in a tensile test (ref. 29). These rotations indi-
cated that the [$\bar{3}$ 6 10], [$\bar{2}$ 5 20], and [011] specimens had [$\bar{1}$01] slip, while
the [$\bar{1}$11] and [$\bar{2}$ 3 4] specimens had [$\bar{1}$10] slip. The [001] specimen exhibited
negligible rotation, indicating slip in multiple octahedral slip directions:
[$\bar{1}$01], [101], [0$\bar{1}$1], and [011]. The planes of the observed slip offsets on the
specimens' surfaces were identified on both the tensile and LCF specimens, as
shown in figure 15. The [$\bar{3}$ 6 10], [$\bar{2}$ 5 20], and [011] specimens had distinct
slip traces on the (111) plane, while the [$\bar{2}$ 3 4] and [$\bar{1}$11] specimens had dif-
fuse traces on the (001). The [001] specimens infrequently displayed slip
traces on the ($\bar{1}$11), ($1\bar{1}$1), or ($11\bar{1}$) planes, again indicating slip on several
octahedral slip systems. The operative slip systems at 650 °C (fig. 16) were
therefore primary octahedral slip (on the (111) plane in the [$\bar{1}$01] direction)
for the [$\bar{3}$ 6 10], [$\bar{2}$ 5 20], and [011] specimens and primary cube slip (on the
(001) plane in the [$\bar{1}$10] direction) for the [$\bar{2}$ 3 4] and [$\bar{1}$11] specimens. The
[001] specimens had several operative slip systems, deforming on several {111}
planes in several ⟨101⟩ directions. These results were later reverified in
the TEM characterizations of the tensile and LCF specimens.

The monotonic and cyclic stress-strain response at 650 °C varied directly with the operative slip systems; these results will therefore be presented accordingly.

Initial yield strength. - The initial axial yield strengths at an inelastic strain of 0.0005 mm/mm in tension and compression are listed in table 4. This data was obtained from the tensile tests and from the first half cycles of the LCF tests.

The yield strengths of the octahedral slip specimens was modeled using Schmid's Law (ref. 29) in which the yield stress resolved on the operative slip system is assumed to be a constant, the critical resolved shear stress τ_{crss}:

$$\tau_{crss} = \sigma_y \cos \phi \cos \lambda \qquad (10)$$

The factor $\cos \phi \cos \lambda$, where ϕ is the angle between the slip plane normal and the load direction, and λ is the angle between the slip direction and load direction, is known as the Schmid factor, S. The best fit of the data with least squares analysis (appendix, table A1) produced the equation:

$$\frac{1}{\sigma_y} = 0.002641 \cos \phi \cos \lambda = 0.002641 \ S \ MPa^{-1} \qquad (11)$$

This indicated τ_{crss} was $1/0.002641 = 379$ MPa for octahedral slip. But a systematic variation from this equation's predictions of yield strengths in tension and compression is evident for the octahedral slip specimens: [001], [2 5 20], [3 6 10], and [011]. The yield strengths of these specimens were therefore also modeled with the equation (refs. 29 and 61) derived to allow for the tension-compression anisotropy of single phase γ' and γ'-strengthened superalloys:

$$\frac{1}{\sigma_y} = b_1 S_1 + b_2 S_2 + \delta \ b_3 S_3 \qquad (12)$$

where S_1 is the Schmid factor on the (111) plane in the [$\bar{1}$01] direction, S_2 is the Schmid factor on the (010) plane in the [$\bar{1}$01] direction, S_3 is the Schmid factor on the (111) plane in the [1$\bar{2}$1] direction, and δ is +1 in tension and -1 in compression. In this model, $1/(b_1S_1)$ is proportional to the resolved shear stress driving a gliding dislocation on the (111) plane, $1/(b_2S_2)$ is proportional to the resolved shear stress driving the dislocation to cross slip onto the (010) cube cross slip plane, and $1/(b_3S_3)$ is proportional to the resolved shear stress constricting or extending a dissociated gliding dislocation on the (111) plane. The resulting equation determined by multiple linear regression (appendix, table A2) was:

$$\frac{1}{\sigma_y} = 0.002642 \ S_1 - \delta \ 0.000227 \ S_3 \ MPa^{-1} \qquad (13)$$

These values are comparable to those obtained from this equation in other studies of Rene N4 and PWA 1480 (refs. 60 and 32, respectively). The constant b_2 was statistically insignificant and therefore dropped just as in the other studies.

Schmid's Law worked well for specimens deforming by primary cube, [$\bar{2}$ 3 4], and [$\bar{1}$11], producing (appendix, table A3) the equation:

17

$$\frac{1}{\sigma_y} = 0.00282 \cos \phi \cos \lambda = 0.00282 \, S \, MPa^{-1} \tag{14}$$

Here, S is the Schmid factor on the (001) plane in the [$\bar{1}$10] direction. This indicated τ_{crss} was $1/0.00282 = 355$ MPa on this slip system.

LCF cyclic hardening response. - The LCF test results at 650 °C are tabulated in table 5. The cyclic stress and inelastic strain response of these tests are given in figures 17 to 34, while typical hysteresis loops at cycle 1 and half of cyclic life are depicted in figures 35 to 40. In these figures, the responses of the LCF tests with $\Delta\varepsilon_{in \, 1} \sim 0.001$, 0.0017, and 0.0025 mm/mm are indicated by open, half-filled, and filled symbols, respectively.

Primary octahedral slip: Outside of the differences in the initial tension and compression yield strengths discussed above, the LCF cyclic stress, mean stress, and inelastic strain hardening responses of all specimens deforming by primary octahedral slip, [$\bar{2}$ 5 20], [$\bar{3}$ 6 10], and [011], were quite comparable, (figs. 17 to 25 and 35 to 37). Fatigue cycling initially produced moderate "jerky" flow (ref. 30) with only slight strain hardening for 10 to 20 fatigue cycles, similar to the stage I hardening at the beginning of the tensile tests. The jerky flow then abated as significant hardening occurred, as in the stage II response of the tensile tests. The hardening continued until a saturation stress and inelastic strain were attained, stage III. The number of fatigue cycles before the onset of stage II behavior generally varied inversely with initial inelastic strain range.

This cyclic stress hardening response resembled that of the monotonic tensile tests in general behavior, suggesting similar strain hardening mechanisms. The cyclic hardening response was therefore expressed as cyclic shear stress as a function of cumulative inelastic shear strain (ref. 61) to enable comparison with the monotonic response. The inelastic strain range was modeled (appendix, tables A4 to A8) with the recorded data as a function of fatigue cycles with the polynomial:

$$\Delta\gamma_{in} = A + BN + CN^2 + DN^3 + EN^4 + F\ln N \tag{15}$$

for each test. The cumulative inelastic shear strain, which is just the sum of the inelastic shear strain incurred in each fatigue cycle, was then modeled (appendix, tables A4 to A8) with this result by:

$$\gamma_c = \Sigma_i 2(\Delta\gamma_{in})_i \tag{16}$$

using a polynomial of the same form. The comparative monotonic resolved shear stress-inelastic shear strain curves in the monotonic tensile tests were computed from the formulations of Schmid and Boas (ref. 29) which take into account crystal rotation:

$$\tau = \sigma \cos \lambda_1 \cos \chi_1 \tag{17}$$

$$\gamma_c = \left(\frac{1}{\sin \chi_o}\right)\left((1 + \varepsilon_{in})^2 - \sin^2 \lambda_o^{0.5} - \cos \lambda_o\right) \tag{18}$$

18

Here χ_O and χ_1 are the initial and instantaneous angles between the glide plane and specimen axis, and λ_O and λ_1 are the initial and instantaneous angles between the glide direction and the specimen axis. These angles are related to inelastic strain by:

$$1 + \varepsilon_{in} = \frac{\sin \lambda_O}{\sin \lambda_1} = \frac{\sin \chi_O}{\sin \lambda_1} \tag{19}$$

The resulting $\tau - \gamma_c$ curves of typical LCF and tensile tests are depicted for the $[\bar{2}\ 5\ 20]$, $[\bar{3}\ 6\ 10]$, and $[011]$ specimens in figures 41 to 43. The tensile and LCF strain hardening curves all displayed a comparable stage I easy glide region of very little strain hardening which extended out to a cumulative strain value of about 0.071. This maximum easy glide strain (γ_g) marked the cessation of jerky flow and the onset of more rapid stable strain hardening. The γ_g values, listed for each LCF test of significant inelastic strain in table 6, were taken at the maximum change in slope of the $\tau-\gamma_c$ curves. γ_g was relatively insensitive to initial inelastic strain range and was comparable for all primary octahedral slip specimens. The subsequent stage II hardening was lower in the LCF tests than in the tensile tests.

Multiple octahedral slip: The cyclic hardening response of the [001] specimens , which deformed on several octahedral slip systems, was distinctly different from that of primary octahedral slip. Fatigue cycling produced rapid cyclic strain hardening (figs. 26 to 28 and 38) to a saturation after 10 to 20 cycles. This differed from the continual severe strain hardening observed in the monotonic tests. The continual severe strain hardening of the [001] tensile test greatly exceeds that of the LCF tests with no evident similarities. The [001] and $[\bar{2}\ 5\ 20]$ LCF hardening curves were also dissimilar, indicating that slip on several octahedral systems promotes more immediate strain hardening. Slip was operative on more than one octahedral slip system in both the tensile and LCF tests of the [001] specimens. Initial yielding can reasonably be assumed to occur on the most highly stressed slip system; the values listed in table 2 were computed in this manner. But the relative proportion of subsequent slip occurring on each operative slip system can not be easily determined. Additionally, interactions between multiple operative slip systems quite often occurs. These slip interactions, which would take place in addition to the slip occurring on each active slip system, are not easily modeled. Therefore, strain could not be resolved onto the operative slip systems.

Primary cube slip: The LCF hardening response of the $[\bar{2}\ 3\ 4]$ and $[\bar{1}11]$ specimens deforming by primary cube slip was quite comparable. LCF cycling produced temporary slight "jerky" flow accompanied by immediate gradual strain hardening (figs. 29 to 34, 39, and 40). In the tensile tests of these specimens, stage I easy glide response characterized by jerky flow with negligible strain hardening extended out to an inelastic shear strain of about 0.01. It should be noted that this cumulative shear strain value corresponds to only one or two fatigue cycles. The corresponding $\tau-\gamma_c$ curves of the LCF and tensile tests therefore appear significantly different, figures 44 and 45. The cyclic strain hardening in the LCF tests continued for nearly a third of the fatigue life.

Cyclic tension-compression anisotropy. - The tension-compression anisotropy observed in the initial yield strengths of specimens deforming by octahedral slip persisted throughout the LCF tests. The cyclic stress hardening in

these specimens was generally of comparable magnitude in tension and compression. The ratio of mean stress normalized by the stress range as a function of fatigue cycles is depicted for LCF tests of large inelastic strains for these specimens in figure 46. This ratio remained fairly constant in the LCF tests.

The cyclic hardening in tension and compression has differed significantly in studies of single phase γ' (ref. 34) single crystals subjected to LCF tests of constant inelastic strain range. Several PWA 1480 specimens were therefore tested in this fashion at $\Delta\varepsilon_{in} = 0.001$ mm/mm. The results of these tests are listed in table 7, while the cyclic stress response in these tests are given in figures 47 to 50. The specimens deforming by octahedral slip hardened more in their high strength direction, just as observed in single phase γ'. The [001] specimens had a higher initial yield strength in tension and cyclically hardened more in tension. The [$\bar{3}$ 6 10] and [011] specimens had higher initial yield strengths in compression, and cyclically hardened more in that direction. These latter specimens, which deformed on the primary octahedral slip system, displayed "jerky" flow far longer in these LCF tests than in the conventional tests. The specimens deforming by primary cube slip, [$\bar{2}$ 3 4] and [$\bar{1}$11], both cyclically hardened more in compression.

Cyclic stress-strain curves. - The cyclic stress amplitude-inelastic strain amplitude response at half of cyclic life for the LCF tests at 650 °C is shown in figure 51. The [$\bar{3}$ 6 10], [$\bar{2}$ 5 20], and [011] specimens, deforming by primary octahedral slip, had comparable response, with the stress amplitude nearly independent of inelastic strain amplitude over the range of tests. Resolving the cyclic stress and strain of these specimens on the operative system collapsed the data somewhat (fig. 52). The [$\bar{2}$ 3 4] and [$\bar{1}$11] specimens which deformed by primary cube slip had higher stress responses, figure 53. The response of these specimens was modeled (appendix, tables A9 to A14) with the standard equation of the form:

$$\frac{\Delta\tau}{2} = K'\left(\frac{\Delta\gamma_{in}}{2}\right)^{m'} \text{ MPa} \tag{20}$$

where m' is the cyclic strain hardening coefficient and K' is the cyclic strength constant. These constants are listed in table 7. The cyclic strain hardening coefficients of the primary octahedral slip specimens ranged from 0.021 to 0.091. The primary cube slip specimens, [$\bar{2}$ 3 4] and [$\bar{1}$11], had significantly higher cyclic strain hardening coefficients, 0.116 and 0.071. The [001] specimen response, figure 54, in which several octahedral slip systems were operative, was modeled (appendix, table A15) with the standard cyclic stress equation (eq. (6)). The cyclic strain hardening coefficient of these specimens, $m' = 0.104$, was also higher than the other octahedral slip specimens.

Fractography. - Fatigue cracks usually initiated at near-surface casting micropores. These cracks propagated a small distance roughly normal to the specimen axis (mode II), then shifted to one or more {111} planes (mode I). The latter crystallographic crack propagation mode seemed to be very rapid, producing failure by tensile overload in only several fatigue cycles. This produced a small, oxidized mode II region, and a larger, relatively unoxidized mode I region, figure 55.

20

Fatigue Deformation Structure at 650 °C

General characterization. - The deformation structure of the [$\bar{2}$ 5 20], [$\bar{3}$ 6 $\bar{1}$0], and [011] LCF test specimens, which deformed by primary octahedral slip, was quite comparable, and varied as a function of the inelastic strain range incurred. Failed specimens subjected to low cyclic inelastic strains ($\Delta\gamma_{in}$ < 0.001 mm/mm on cycle 1, and < 0.0006 mm/mm at half of cyclic life) had loose, ill-defined bands of various moderate dislocation densities separated by relatively dislocation-free regions, figure 56. The band direction corresponded to the trace of the (111) primary octahedral slip plane in the foil. About 80 percent of the dislocations had the Burgers vectors corresponding to primary octahedral slip, b = ±1/2[$\bar{1}$01]. A majority of the dislocations were in the γ phase and were bowed on the (111) plane to give various characters. A smaller number of dislocations were in the γ' precipitates. These will be subsequently discussed in detail.

Failed specimens subjected to relatively large cyclic inelastic strains ($\Delta\gamma_{in}$ > 0.002 mm/mm on cycle 1, and > 0.001 mm/mm at half of cyclic life) had general deformation throughout the microstructure, figure 57. Where the dislocations were of a low enough density to enable counting, 95±10 percent of the dislocations observed in eight slip bands of two foils had the primary octahedral slip Burgers vectors, b = ±1/2[$\bar{1}$01]. In other slip bands the dislocations were too closely spaced to count but were still of the same Burgers vectors. A majority of these dislocations were in the γ phase, where they were of various characters and often slightly dissociated on {111} planes. These γ dislocations were often combined in nonplanar entanglements, figure 58. A smaller number of paired dislocations, near-screw in character, were in the γ' precipitates.

The deformation structure of the failed [001] LCF specimens, which deformed by multiple octahedral slip, generally consisted of relatively inhomogeneous patches of deformation. Specimens subjected to small inelastic strains, figure 59, had moderately spaced patches of dislocations and very infrequent discrete slip bands. Specimens subjected to large cyclic inelastic strains, figure 60, had much more frequent patches of higher dislocation density, with discrete slip bands again only infrequently observed. Most of the dislocations observed had Burgers vectors corresponding to octahedral slip: b = ±1/2[$\bar{1}$01], 1/2[101], 1/2[0$\bar{1}$1], and 1/2[011]. A majority of these dislocations were again in the γ phase, of various characters and often slightly dissociated on {111} planes. They were often combined in nonplanar entanglements in the specimens subjected to large cyclic inelastic strains. Additionally, dislocations were often arranged regularly at the γ-γ' interfaces, figure 61. A smaller number of paired dislocations having these Burgers vectors, near-screw in character, were in the γ' precipitates.

The deformation structure of the [$\bar{2}$ 3 4] and [$\bar{1}$11] LCF test specimens, which deformed by primary cube slip, also varied as a function of cyclic inelastic strain. Failed specimens cycled at low inelastic strains again had loose, ill-defined bands separated by relatively dislocation-free regions, figure 62. The band direction corresponded to the trace of the (001) primary cube slip plane in the foil. About 65 percent of the dislocations had the Burgers vectors corresponding to primary cube slip, b = ±1/2[$\bar{1}$10]. A majority of these dislocations were in the γ phase. When singular these γ dislocations were often bowed on and dissociated on the (111) or ($\bar{1}$11) planes. This was most clearly seen in a [$\bar{2}$ 3 4] LCF test interrupted at 10 cycles. A

typical tilting experiment of this specimen is shown in figure 63. Many curved γ dislocations became straight projected lines parallel to the (111) plane trace when this plane is tilted perpendicular to the electron beam. A smaller number of dislocations were in the γ' precipitates.

Failed [$\bar{2}$ 3 4] and [$\bar{1}$11] LCF specimens tested at large inelastic strains had very homogeneous deformation throughout the microstructure, figure 64. Over 90 percent of the dislocations observed in these specimens had the primary cube slip Burgers vectors, **b** = ±1/2[$\bar{1}$10]. A majority of the dislocations were again in the γ phase. When singular and extending between γ particles, these dislocations were again sometimes bowed on the (111) or ($\bar{1}$11) planes, and dissociated on these planes. Yet, when at the γ-γ' interfaces or within the γ' precipitates, singular dislocations were also observed on the (001) primary cube slip plane. The γ dislocations were often concentrated in the γ channels between the (001) and (00$\bar{1}$) faces of the γ' precipitates. This is shown in the tilting experiment of a [$\bar{1}$11] LCF specimen in figure 64. But the γ dislocations were quite often arranged in entanglements of nonplanar dislocations, figure 65. A smaller number of paired dislocations were in the γ' precipitates. These dislocations had various characters.

γ' dislocation pairs. - The glide and cross slip of dislocation pairs in the γ' precipitates are believed to control the yield strength and yield strength tension-compression anisotropy in superalloys. The characteristics of these dislocation pairs were therefore examined in detail. The characteristics of the γ' dislocation pairs were quite similar in all fatigue specimens displaying octahedral slip. The dislocation pairs in the [$\bar{2}$ 5 20], [$\bar{3}$ 6 10], and [011] LCF specimens shall first be discussed. A roughly equal number of dislocation pairs in these specimens were of Burgers vectors **b** = 1/2[$\bar{1}$01] and **b** = 1/2[10$\bar{1}$] in the regions examined. Several dislocation pairs sometimes extended across a γ' precipitate in a single file on the (111) plane, indicating macroscopic (111) slip. Two pairs were sometimes closely aligned as dipoles in this manner. Typical micrographs from a large angle tilting experiment on a normal foil of a [$\bar{3}$ 6 10] LCF specimen are shown in figure 66. These normal foils allowed the analysis of short segments of numerous γ' dislocation pairs at high magnifications. The dislocation pairs are here oriented as shown in figure 67, case B. These dislocation pair segments were predominantly near-screw in character, having line directions **u** near [$\bar{1}$01]. The lines of intersection **L** of the pairs' planes with the foil surface were near [100]. These two directions defined the (010) cube cross slip plane as the plane of these dislocation pairs. This was confirmed by the increased projected pair spacing when tilting from the [112] zone axis to the [$\bar{1}$21] zone axis, figure 66, and by stereo viewing of the pairs in various foil tilting positions. To determine the generality of these findings, the above tilting experiment was utilized to briefly characterize the dislocation pairs in 52 γ' precipitates of three TEM foils. Using the change in the projected line direction and spacing of the dislocations in a pair as approximate indications, 80±11 percent of the dislocation pairs were in majority near-screw in character and roughly on the (010) plane.

Micrographs from a (111) "slip plane" foil of a [$\bar{3}$ 6 10] LCF specimen are shown in figure 68. These slip plane foils enabled the analysis of much longer segments of γ' dislocation pairs at high magnifications, (fig. 67, case A). The predominance of near-screw dislocations in the γ' precipitates is clearly evident. Dislocation pair segments were sometimes slightly bowed on the (111)

22

plane, and could not be individually resolved. But very many pairs were of relatively constant near-screw character through the entire γ' precipitate, figure 68, and were again confirmed to lie in the (010) plane in these foils. These results were obtained for the γ' dislocation pairs of LCF specimens subjected to both large and small inelastic strains. The average distance between the dislocations of a pair on the (010) plane was approximately 4±0.5 nm.

The γ' dislocation pairs of the [001] LCF specimens had Burgers vectors of $b = \pm1/2[\bar{1}01]$, $1/2[101]$, $1/2[0\bar{1}1]$, and $1/2[011]$. These dislocations were again predominantly near-screw in character, and roughly equal numbers of dislocations had positive and negative Burgers vectors. These dislocation pairs were again each on their respective cube cross slip plane. Therefore the pairs of $b = 1/2[\bar{1}01]$ and $1/2[101]$ were on the (010) plane, while the pairs having $b = 1/2[0\bar{1}1]$ and $1/2[011]$ were on the (100) plane. This is shown in the tilting experiment of a normal foil of an [001] LCF specimen in figure 69.

The characteristics of the γ' dislocation pairs in the two specimens deforming by primary cube slip, $[\bar{2} 3 4]$ and $[\bar{1}11]$, were comparable and differed from that for octahedral slip. A roughly equal number of these dislocation pairs were of Burgers vectors $b = 1/2[\bar{1}10]$ and $1/2[1\bar{1}0]$ in the regions examined. Micrographs from a normal foil of a $[\bar{2} 3 4]$ LCF specimen are shown in figure 70. The dislocation pair segments had various line directions usually parallel to the (001) plane. The lines of intersection of the pairs' planes with the foil surface were near [110]. This indicated the pairs lay on the (001) primary cube slip plane. This fact was reaffirmed by the observed increased pair spacing when tilting towards the [001] zone axis, figure 70, and the stereo viewing of the pairs in numerous foil tilting positions. These dislocation pairs were often extensively bowed on this (001) plane, producing segments of various characters. For the normal foils of the $[\bar{1}11]$ and $[\bar{2} 3 4]$ LCF specimens, this gave long near-edge segments with u near [110] corresponding to figure 67, case A, and shorter mixed character and near-screw (u near $[\bar{1}10]$) segments corresponding to case B. Sometimes relatively straight, mixed-character dislocation pairs extended across the entire γ' precipitate, as shown in the (001) plane foil of a $[\bar{2} 3 4]$ LCF specimen in figure 71.

The generation of deformation structures. - In order to gain further understanding on how these deformation structures are generated and their correlation with cyclic stress hardening response, several further mechanical tests were performed for TEM analysis. The primary octahedral slip specimens were selected for this investigation because: (1) their cyclic hardening curves had the interesting initial easy glide regions, (2) these cyclic hardening curves resembled that of the monotonic tensile tests of these specimens, and (3) the confinement of slip to a single system allowed more detailed analysis and comparisons.

Both LCF and tensile tests were interrupted at a cumulative shear strain of less than 0.007 mm/mm, near the maximum easy glide strain γ_g, and analyzed. Both LCF and tensile deformation during this stage I easy glide hardening was confined to bands parallel to the (111). The bands were of varying width and dislocation density. At least nine slip bands of each specimen were analyzed in standard, near-identical brief tilting experiments to determine the Burgers vector and plane of the dislocations. Micrographs from typical tilting experiments of the $[\bar{3} 6 10]$ LCF and tensile specimens are shown in figures 72

to 74. The γ dislocations were mostly on the (111) plane during this stage, with no significant nonplanar entanglements observed. The curved γ dislocations clearly became nearly straight projected lines parallel to the (111) plane trace when the foil was tilted so that the (111) plane was brought nearly on edge to the electron beam. This was the case for both broad, high-density bands, figures 72 and 74, and narrow, low-density bands, figures 73 and 75, in the LCF and tensile specimens. The γ' dislocation pairs in this stage were already cross slipped onto the (010) plane, figure 75.

These characteristics were different from that observed in specimens tested to failure. As already mentioned, failed [$\bar{3}$ 6 10] LCF specimens had dislocations throughout the microstructure. This was also the case for [$\bar{3}$ 6 10] tensile specimens tested to failure. As expected, the failed tensile specimen had a higher dislocation density than the LCF specimen. But in both specimens, the dislocations in the γ phase were no longer predominantly on the (111) plane. Portions of these dislocations were often on various other planes and were often combined in nonplanar entanglements. This was determined for the LCF and tensile specimens in the same standard tilting experiments previously employed and is illustrated in the typical micrographs of these tilting experiments in figures 76 and 77. While the singular γ dislocations were sometimes still on the (111) plane, when combined in entanglements the dislocations were on various planes. These dislocations were often dissociated on {111} planes, figure 58. The dislocation pairs in the γ' precipitates remained predominantly screw in character, lying on the (010) plane. Several were sometimes entangled together within a precipitate, but this was not a predominant feature.

In order to learn more about when these changes in deformation structure occurred, an LCF test of an [011] specimen was interrupted at a cumulative shear strain of 0.096 mm/mm, where stage II strain hardening occurred. TEM analysis of this specimen disclosed that deformation was still confined to bands to some extent. In briefly examining several foils, the bands were sometimes very broad and of a relatively constant dislocation density. But narrow slip bands and undeformed areas of the microstructure still remained. Nine of these slip bands were analyzed with the standard tilting experiment. Several of the narrower bands had the characteristics of bands observed in specimens interrupted at a cumulative shear strain of less than 0.07 mm/mm, with the γ dislocations on the (111) plane. But other bands of higher dislocation density additionally had some areas where the γ dislocations were somewhat entangled and no longer on the (111) plane. One of the latter bands is shown in the typical micrographs of a tilting experiment in figure 78. The dislocation segments in the entanglements were locally dissociated on {111} planes, figure 80.

LOW CYCLE FATIGUE AT 1050 °C

Mechanical Response

Operative slip systems at 1050 °C. - Tensile tests were performed at 1050 °C to aid in slip system determinations. The 1050 °C tensile test results are presented in table 9. The axial stress-strain curves for these tests are given in figure 81, while the corresponding crystallographic rotations of the tensile specimens are shown in figure 82. Slip traces were not discernible in

24

these tests, because of the more homogeneous deformation common at this temper-
ature. Therefore only the tensile test crystallographic rotations and trans-
mission electron microscopy could be utilized in slip system determination.
The [001] and [$\bar{2}$ 5 20] specimens did not rotate appreciably, apparently indi-
cating homogeneous slip on several octahedral slip systems. The [$\bar{1}$11], [$\bar{2}$ 3 4],
and [3 6 10] specimens rotated appreciably towards the [$\bar{1}$10] direction, indicat-
ing primary cube slip. The [011] specimens rotated very slightly, (2.5°),
towards the [$\bar{1}$10] direction. But this angular rotation approached the observed
experimental error of the Laue x-ray technique of determining crystallographic
orientation (~2°), therefore the rotation could not be considered statistically
significant and the slip systems of the [011] specimen remained unknown. In
later TEM analysis of both tensile and LCF [001] and [$\bar{1}$11] specimens tested at
1050 °C, both the [001] and [$\bar{1}$11] specimens contained dislocations with Burgers
vectors of several cube and octahedral slip systems. The lack of agreement
between dislocation Burgers vectors and the operative slip systems indicated
from the tensile tests suggests that while slip may initially be dominant on
one or more preferred systems, dislocation reactions and high temperature
recovery processes activate slip to some extent on other slip systems.

Initial yield strength. - The initial axial yield strengths at an inelas-
tic strain of 0.0005 mm/mm in tension and compression are listed in table 10.
The slip system analysis suggested the [001] and [$\bar{2}$ 5 20] specimens deformed
more on the octahedral slip systems in the tensile tests. Therefore the ini-
tial yield strength results of these specimens were analyzed on the octahedral
slip system of highest Schmid factor (primary octahedral slip system). These
specimens were significantly stronger in compression than tension. The best
fit of these results in tension using Schmid's Law with least squares analysis
(appendix, table A16) produced the equation:

$$\frac{1}{\sigma_y} = 0.00816 \cos \phi \cos \lambda = 0.00816 \, S \, MPa^{-1} \qquad (21)$$

This indicated τ_{crss} was 1/0.00816 = 123 MPa, with a 70 percent confidence
interval of 120 MPa < τ_{crss} < 126 MPa, for octahedral slip in tension. The
best fit of the [001] and [$\bar{2}$ 5 20] results in compression with least squares
analysis (appendix, table A17) produced the equation:

$$\frac{1}{\sigma_y} = 0.00711 \, S \, MPa^{-1} \qquad (22)$$

This indicated τ_{crss} = 141 MPa, with a 70 percent confidence interval of
134 MPa < τ_{crss} < 148 MPa, for octahedral slip in compression. As indicated by
the confidence intervals, the results in tension and compression differed by a
statistically significant amount.

The initial yield strength results of the [$\bar{1}$11], [$\bar{2}$ 3 4], and [$\bar{3}$ 6 10]
specimens were analyzed on the primary cube slip system. The best fit with
least squares analysis of the combined data (appendix, table A18) gave the
equation:

$$\frac{1}{\sigma_y} = 0.00680 \, S \, MPa^{-1} \qquad (23)$$

This indicated τ_{crss} = 147 MPa, with a 70 percent confidence interval of
144 MPa < τ_{crss} < 150 MPa, on the primary cube slip system. But an improved

fit was obtained by analyzing the results of the [111] specimens alone (appendix, table A19):

$$\frac{1}{\sigma_y} = 0.00659 \text{ S MPa}^{-1} \tag{24}$$

This indicated τ_{crss} = 152 MPa, with a 70 percent confidence interval of 150 MPa $< \tau_{crss} <$ 154 MPa, on the primary cube slip system. The [$\bar{2}$ 3 4] and [$\bar{3}$ 6 10] results show significantly more variation when analyzed separately. The best fit of the [$\bar{2}$ 3 4] results (appendix, table A20) gave:

$$\frac{1}{\sigma_y} = 0.00734 \text{ S MPa}^{-1} \tag{25}$$

This indicated τ_{crss} = 136 MPa, with a 70 percent confidence interval of 131 MPa $< \tau_{crss} <$ 142 MPa, for these specimens. The single [$\bar{3}$ 6 10] test indicated τ_{crss} = 132 MPa. Because the slip system of the [011] specimens was not conclusively known, the [011] results were analyzed on both the octahedral and the cube slip systems. The best fit (appendix, table A21) of this data on the octahedral slip system produced the equation:

$$\frac{1}{\sigma_y} = 0.00750 \text{ S MPa}^{-1} \tag{26}$$

suggesting τ_{crss} = 133 MPa, with a 70 percent confidence interval of 129 MPa $< \tau_{crss} <$ 137 MPa, for these specimens on this slip system. This value is near the τ_{crss} of the specimens conclusively deforming by initial octahedral slip. The best fit (appendix, table A22) of the data on the primary cube slip system produced the equation:

$$\frac{1}{\sigma_y} = 0.00894 \text{ S MPa}^{-1} \tag{27}$$

suggesting τ_{crss} = 112 MPa, with a 70 percent confidence interval of 108 MPa $< \tau_{crss} <$ 116 MPa, for these specimens on the cube slip system. This value is significantly lower than the τ_{crss} of the specimens conclusively deforming by initial cube slip. Therefore this analysis suggested the [011] specimens initially deform by octahedral slip.

LCF cyclic hardening response. - Initial single LCF tests were performed at $\Delta\varepsilon_{in}$ = 0.0025 to 0.003 mm/mm on [001], [$\bar{1}$11], [011], and [$\bar{3}$ 6 10] specimens. The results of these tests are listed in table 11, while the cyclic stress and inelastic strain response of these tests are compared in figures 83 to 85. Typical hysteresis loops from these tests are depicted in figures 86 to 89. These specimens all displayed very slight cyclic stress softening of less than 4 percent from cycle 1 to half life. The [011] and [$\bar{3}$ 6 10] specimens had higher cyclic stress amplitudes. But these specimens had foreshortened fatigue lives, consistent with their lower tensile ductilities (table 8). The [001] and [$\bar{1}$11] specimens had lower stress response and longer fatigue lives consistent with their higher ductilities.

The [001] and [$\bar{1}$11] specimens were chosen for detailed characterization in further LCF tests. The results of all [001] and [$\bar{1}$11] LCF tests are listed in

table 12. The cyclic stress and inelastic strain responses in these tests are given in figures 90 to 95, while additional typical hysteresis loops from tests of these specimens at $\Delta\varepsilon_{in}$ = 0.001 mm/mm are given in figures 96 and 97. In these figures, the responses of the LCF tests performed with $\Delta\varepsilon_{in,1}$ ~ 0.001, 0.002, and 0.0027 mm/mm are indicated with open, half-filled, and filled symbols, respectively. The [001] and [$\bar{1}$11] specimens had comparable gradual cyclic softening response. In LCF tests of large inelastic strains, $\Delta\varepsilon_{in}$ = 0.0025 to 0.003 mm/mm, only very slight cyclic stress softening of 3 percent occurred between cycle 1 and half of cyclic life. In tests at smaller inelastic strains, $\Delta\varepsilon_{in}$ = 0.0009 to 0.002 mm/mm, moderate cyclic stress softening of 8 to 13 percent occurred between cycle 1 and half of cyclic life.

While the [001] and [$\bar{1}$11] specimens both displayed cyclic stress amplitude softening, the effect of fatigue cycling on their initial tension-compression anisotropies was significantly different. The [001] specimens, which initially were stronger in compression, displayed a decreased magnitude of anisotropy after appreciable fatigue cycling. This is evident in the small cyclic mean stress magnitudes depicted in figure 92 and in the hysteresis loops of figures 86 and 96. The tension-compression anisotropy of the [$\bar{1}$11] specimens, initially negligible, increased in fatigue cycling, becoming stronger in tension. This produced a sustained tensile cyclic mean stress, as shown in figure 93 and in the hysteresis loops of figures 87 and 97.

Cyclic stress-strain curves. - The cyclic stress-inelastic strain results at half of cyclic life is shown in figure 98. The [001] and [$\bar{1}$11] specimens had comparable cyclic stress-strain response in test of large inelastic strains, $\Delta\varepsilon_{in}$ ~ 0.0027 mm/mm. But in tests of small inelastic strains, $\Delta\varepsilon_{in}$ ~ 0.001 mm/mm, the [$\bar{1}$11] specimens had higher cyclic stress response. The results, when modeled by least squares analysis with the standard cyclic stress-strain equation (eq. (6)) produced, table 13, the equation (appendix, table A23):

$$\frac{\Delta\sigma}{2} = 14486 \left(\frac{\Delta\varepsilon_{in}}{2}\right)^{0.586} \quad \text{MPa} \tag{28}$$

for the [001] specimens and the equation (appendix, table A24):

$$\frac{\Delta\sigma}{2} = 682 \left(\frac{\Delta\varepsilon_{in}}{2}\right)^{0.128} \quad \text{MPa} \tag{29}$$

for the [$\bar{1}$11] specimens. The 70 percent confidence intervals of the K' constants were 9113 MPa < K' < 23026 MPa and 646 MPa < K' < 719 MPa for the [001] and [$\bar{1}$11] specimens, respectively. The 70 percent confidence intervals of the m' constants of the [001] and [$\bar{1}$11] specimens were 0.517 < m' < 0.655 and 0.121 < m' < 0.136, respectively. Therefore both K' and m' were significantly different for the [001] and [$\bar{1}$11] specimens.

Fractography. - For all the LCF specimens tested at 1050 °C, fatigue cracks usually initiated at near-surface microporosity. These cracks appeared to have initiated relatively early in the fatigue tests. In order to confirm this, several [001] specimens were fatigue tested at $\Delta\varepsilon_{in,1}$ ~ 0.0027 mm/mm and interrupted at 10, 25, 50, and 75 percent of the expected fatigue life (N_f) of

500 to 700 cycles. Optical examination at magnifications of up to 80X disclosed no clearly defined surface cracks at 10 percent N_f, although some surface oxide scale was present. At 25 percent N_f, shallow surface oxide scale ruptures were observed (fig. 99), along with a single surface crack of 0.075 mm in length with evident surface penetration. At 50 percent N_f about 20 to 30 surface cracks of about 0.45 mm length and appreciable depth were observed (fig. 100). The cracks at 75 percent N_f were often appreciably longer, 0.63 mm as shown in figure 101.

Subsequent crack growth was predominantly normal to the stress axis (mode II) in the [001] specimens (fig. 102). The crack growth in the [$\bar{1}$11] specimens was usually inclined to the stress axis and more crystallographic in nature (mode II), generally favoring the (001) plane (fig. 103).

Fatigue Deformation Structure at 1050 °C

The dislocation structure produced by exposure at 1050 °C. - In order to first characterize the microstructural effects of exposure at 1050 °C, unloaded specimens were aged at 1050 °C in an argon atmosphere for times of 2, 5, 10, 50, 100, and 500 hr and air quenched. Only the specimen aged for 500 hr consistently had dislocations at most of the γ-γ' interfaces indicating some loss in coherency; this specimen was therefore selected for analysis. The γ' precipitates in this specimen had an irregular morphology. In some regions the precipitates were still fairly regular, rounded cuboids of increased width (0.7 to 0.9 μm). In other regions the precipitates were larger and more irregular in shape, exceeding 1 μm in minimum width.

The dislocation structure in this specimen was also quite irregular. In regions where the precipitates were still fairly regular cuboids, single randomly-oriented dislocations were present. Single dislocations often extended across several γ' precipitates, figure 104. The Burgers vectors of the dislocations labelled "a" and "b" in figure 104 are about 45° out of the interface plane, and therefore relieve misfit strain inefficiently. Therefore, these dislocations did not appear to have been generated at the interfaces where they were observed. In the other regions of larger, more irregular precipitates, a greater number of dislocations, arranged in networks were present. The dislocations were here concentrated at the γ-γ' interfaces. One of these latter regions was analyzed in some detail. As shown in figure 105(a), the dislocations were arranged in somewhat irregular networks with varying dislocation spacing. Dislocations arranged in a hexagonal array lying on an interface approximately parallel the (001) plane, and in a square array lying on an interface approximately parallel to the (101) plane were analyzed to determine their Burgers vectors and line directions. The results of this analysis are given in figure 105(b). These networks were not very efficient in relieving misfit strains. In the hexagonal network on the (001) plane interface, four of the six dislocations had Burgers vectors 35° to 65° out of the interface plane. These dislocations were often evenly mixed rather than edge in character (the angle β = 90° for an edge dislocation). The square network on the (101) plane interface had dislocations with Burgers vectors within 30° of the interface plane. These dislocations ranged from mixed to edge in character. The dislocation spacing in these networks ranged from 0.13 to 0.22 μm. Employing an approximate lattice parameter of 0.359 nm and the equation $\delta = |\mathbf{b}|/p$, this spacing corresponded to a very low misfit magnitude of $|\delta| = 0.001$ to 0.002.

The generality of these findings was tested by examining the γ-γ' inter-
faces in another foil. Brief tilting experiments were devised to enable the
identification of interfaces parallel to several {001} and {111} planes and the
determination (by **g · b** = 0 image analysis) of the Burgers vectors of the dis-
locations at these interfaces. These experiments were performed on a total of
69 different γ-γ' interfaces. The results of this analysis are listed in
table 14. The dislocations had similar inefficient characteristics on these
interfaces. The micrographs of a typical tilting experiment are shown in
figure 106. Only 13±16 percent of the 223 dislocations analyzed on interfaces
approximately parallel (±15°) to the {100} planes had Burgers vectors in this
plane. But 84±19 percent of the 78 dislocations which could be analyzed on
interfaces approximately parallel (±15°) to the {111} planes had Burgers
vectors in this plane. The dislocations were often singular and separated,
but were sometimes in near-hexagonal networks on the {001} and {111} planes.

The LCF deformation structure at 1050 °C. - The γ' precipitates in the
[001] LCF specimens were moderately coarsened. Failed [001] LCF specimens were
sectioned longitudinally on the (010) plane in order to check for directional
coarsening with respect to the applied load. No appreciable consistent coar-
sening of this type was observed in these specimens. Now the γ' intercept
length of unloaded specimens sectioned in this manner was 0.56 μm with a stand-
ard deviation of 0.17 μm, (0.56±0.17 μm). The [001] LCF specimen tested at low
inelastic strains ($\Delta\varepsilon_{in}$ on cycle 1 ($\Delta\varepsilon_{in\ 1}$) ~ 0.001 mm/mm) had a γ' size of
0.76±0.25 μm, figure 107. The [001] specimen tested at high inelastic strains
($\Delta\varepsilon_{in\ 1}$ ~ 0.0027 mm/mm) had a γ' size of 0.62±0.21 μm. The γ' precipitates
were more spherical after testing, particularly in the low strain test
specimens.

The [$\bar{1}$11] LCF specimens were sectioned longitudinally on the (011) plane.
No significant directional coarsening was observed here either. Now untested
specimens sectioned on the (011), rather than the (010) planes had reduced γ'
intercept lengths. This was due to crystallographic alignment of the cuboidal
γ' precipitates. Therefore the γ' intercept lengths of the [$\bar{1}$11] LCF speci-
mens were compared to that of unloaded specimens also sectioned on the (011)
plane, figure 108. The unloaded specimens had a γ' intercept length of
0.52±0.16 μm. The [$\bar{1}$11] LCF specimens tested at $\Delta\varepsilon_{in\ 1}$ ~ 0.001 mm/mm to
failure had a γ' intercept length of 0.55±0.18 μm. The [$\bar{1}$11] LCF specimen
tested at $\Delta\varepsilon_{in\ 1}$ ~ 0.0027 mm/mm had a γ' intercept length of 0.52±0.18 μm.
The γ' precipitates were more spherical here also.

The deformations structures of the [001] and [$\bar{1}$11] LCF specimens were gen-
erally similar. The dislocations in these specimens were quite homogeneously
distributed with no evidence of slip bands. These dislocations were almost
exclusively in the γ phase, quite often lying at the γ-γ' interfaces. The
general appearance of the dislocation structures of the [001] and [$\bar{1}$11] LCF
specimens can be compared in figure 109. These micrographs are from TEM foils
prepared parallel to the (011) plane in these specimens, enabling direct com-
parisons. The [001] specimens appeared to have more well-arranged dislocation
networks than the [$\bar{1}$11] specimens at $\Delta\varepsilon_{in\ 1}$ ~ 0.001 mm/mm. The networks of
both the [001] and [$\bar{1}$11] LCF specimens tested at $\Delta\varepsilon_{in\ 1}$ ~ 0.0027 mm/mm were
more irregular. The dislocation density of the [001] LCF specimens appeared
somewhat higher than that of the [$\bar{1}$11] specimens at both strain levels.

In comparing the dislocation structures of the [001] and [$\bar{1}$11] specimens
in detail, an obvious aspect to consider is the proportion of dislocations

having Burgers vectors which correspond to the initially active octahedral or cube slip systems. Of the six possible $1/2\langle 110\rangle$ Burgers vectors, four of these or 66 percent of a random distribution can be associated with octahedral slip in an [001] specimen: $1/2[1\bar{0}1]$, $1/2[101]$, $1/2[0\bar{1}1]$, and $1/2[011]$. In a [$\bar{1}11$] specimen, three of these or 50 percent of a random distribution can be associated with cube slip: $1/2[\bar{1}10]$, $1/2[\bar{1}01]$, and $1/2[011]$.

Typical micrographs of the deformation structure observed in these [001] and [$\bar{1}11$] LCF specimens tested at $\Delta\varepsilon_{in\ 1} \sim 0.0027$ mm/mm are presented, along with the results of an extensive analysis of these dislocations, in figures 110 and 111. Dislocations of all Burgers vectors were observed, with no predominance of either octahedral or cube slip dislocations. These dislocations were predominantly at the γ-γ' interfaces. As illustrated in the analysis results, dislocations of various Burgers vectors were present at various interface planes. These dislocations were at times of the proper Burgers vectors to relieve the misfit strain at an interface, but not as a general rule. They were mixed to near-edge in character, with the angle ß between the dislocations' Burgers vector and line direction sometimes approaching 90°.

The variability of these results suggested that the analysis of many more dislocations was required to reach general conclusions. Brief tilting experiments, which identified several interfaces approximately parallel to {100} and {111} planes and the Burgers vectors of dislocations, were therefore performed as for the unloaded specimen. The results of these experiments, performed on these [001] and [$\bar{1}11$] LCF specimens subjected to large inelastic strains, are presented in tables 15 and 16. A total of 45 γ-γ' interfaces of 45 γ' precipitates were analyzed from two [001] specimen foils. A total of 53 γ-γ' interfaces of portions of 46 γ' precipitates were analyzed from two [$\bar{1}11$] foils. No variations in deformation structure between the two foils of each specimen were evident. The micrographs of typical tilting experiments on each of these specimens are shown in figures 112 and 113. In both the [001] and [$\bar{1}11$] specimens, a predominance of neither octahedral, nor cube slip dislocations was observed. In both specimens, the dislocation networks were usually irregular to near-hexagonal on interfaces approximately parallel to {100} planes. The dislocations on these interfaces had Burgers vectors randomly in or not in the plane of the interfaces. The dislocation networks were usually roughly hexagonal on interfaces approximately parallel to {111} planes. Over 90 percent of the dislocations on these interfaces had Burgers vectors in the plane of the interfaces. The dislocations were spaced 0.09 to 0.14 μm apart.

The deformation structure of specimens tested at low inelastic strains, $\Delta\varepsilon_{in\ 1} \sim 0.001$ mm/mm, was also examined in this manner. The standard tilting experiments were performed on these specimens as before. A total of 43 γ-γ' interfaces were analyzed in an [001] specimen foil. A total of 52 γ-γ' interfaces were analyzed in a [$\bar{1}11$] specimen foil. The results of this analysis are also listed in tables 15 and 16. The micrographs of typical tilting experiments on these [001] and [$\bar{1}11$] LCF specimens are presented in figures 114 and 115. There was again no predominance of dislocations having Burgers vectors resulting from octahedral, or cube slip. Compared to the specimens subjected to large inelastic strains, slightly more variability was observed in the interface plane-dislocation Burgers vector analysis, with larger standard deviations evident. But again the dislocations on interfaces approximately parallel to {100} planes had random Burgers vectors at various

30

angles to the interface plane. The dislocations on interfaces parallel to {111} planes again had Burgers vectors more often in the interface plane.

The generation of deformation structures at 1050 °C. - In order to learn more about the generation of these deformation structures, additional [001] and [$\bar{1}$11] specimens were LCF tested at $\Delta\varepsilon_{in\,1} \sim 0.0027$ mm/mm for 50 cycles, which was less than 10 percent of the expected fatigue life of about 700 cycles. The deformation structures of these specimens were then examined utilizing the tilting experiments as before. A total of 50 γ-γ' interfaces were analyzed in an [001] specimen foil. A total of 40 interfaces were analyzed in an [$\bar{1}$11] foil. The results of this analysis are listed in tables 15 and 16, while the micrographs of typical tilting experiments are presented in figures 116 and 117. The general characteristics of their dislocation structures were similar to that observed before. There was again no predominance of octahedral, or cube slip dislocations. The dislocations were again usually at the γ-γ' interfaces. On the interfaces approximately parallel to {100} planes, the dislocations again had random Burgers vectors lying at various angles to the interface planes. These dislocations were irregularly arranged. On the interfaces approximately parallel to {111} planes, the dislocations again usually had Burger vectors lying in the interface planes. When a sufficient number of dislocations were present, these latter dislocations were sometimes arranged in roughly hexagonal networks.

These results suggested that dislocation recovery occurs rapidly in these tests. Therefore additional [001] and [$\bar{1}$11] specimens were given 1/2 of an LCF cycle and then examined. The [001] specimen had inhomogeneous deformation with frequent patches of dislocations separated by undeformed regions. The dislocations in the patches were sometimes singular dislocations aligned in parallel fashion as shown at "a" in figure 118. These dislocations did not lie on a single plane, but appeared to undulate between the γ' precipitates. Therefore significant cross slip and climb apparently occurred during the bypassing of the γ' precipitates. The dislocations in these rows usually all had the same Burgers vector, corresponding to octahedral slip; $b = 1/2[\bar{1}01]$, $1/2[101]$, $1/2[0\bar{1}1]$, or $1/2[011]$; ($b = 1/2[011]$ at "a", $b = 1/2[101]$ at "b"). They were predominantly edge in character ($u \sim [\bar{1}00]$ at "a", $u \sim [010]$ at "b"). Even after only 1/2 of an LCF cycle, different rows of dislocations often intersected, beginning to knit into networks. As shown at "c" in figure 118, long near-edge dislocations having $b = 1/2[011]$ and $1/2[101]$ have formed irregular, roughly square networks. This process sometimes resulted in the patches having high dislocation density, considering the small amount of inelastic strain imposed.

The [$\bar{1}$11] specimen given 1/2 of an LCF cycle had homogeneous deformation, with dislocations scattered throughout the microstructure, figure 119. But these dislocations were not regularly aligned in rows and had no preferred character. No patches of higher dislocation density were observed. The dislocations principally had primary cube slip Burgers vectors of $b = 1/2[\bar{1}01]$, $1/2[\bar{1}10]$, and $1/2[011]$. In different regions, dislocations of one of these three Burgers vectors were sometimes more predominant. Dislocation networks had sometimes begun to form here also. This is shown at "a" and "b" in figure 119. The network at "a" had several dislocation segments with $b = 1/2[110]$, $1/2[101]$, and $1/2[0\bar{1}1]$, along with those for primary cube slip. Therefore some dislocation reactions have apparently already occurred.

31

NONISOTHERMAL LOW CYCLE FATIGUE

In order to examine the stability of the studied deformation structures to subsequent LCF of different conditions, the effects of prior deformation on cyclic stress-strain response and deformation structure, and the dependence of operative deformation mechanisms on initial microstructure, several very simple nonisothermal fatigue tests were performed. Several [001] and [$\bar{3}$ 6 10] specimens were LCF tested at 650 °C with $\Delta\varepsilon_{in\,1} \sim 0.002$ mm/mm for 20 cycles, where a large part of the cyclic hardening had taken place, and then interrupted. These specimens were subsequently tensile and LCF tested at 1050 °C with $\Delta\varepsilon_{in\,1} \sim 0.0027$ mm/mm. Conversely, several [001] and [011] specimens were first LCF tested at 1050 °C with $\Delta\varepsilon_{in\,1} \sim 0.0025$ mm/mm for 50 cycles and then removed. The accumulated oxide on these specimens was removed by grinding 0.15 mm off the gage diameter. The gage sections were then mechanically polished just as in the original specimen machining process. These specimens were then tensile tested and LCF tested at 650 °C.

650 to 1050 °C Low Cycle Fatigue

Mechanical response. - A single [001] specimen, first LCF tested at 650 °C, was subsequently tensile tested at 1050 °C. The results of this test are compared to that of a conventional [001] tensile test at 1050 °C in table 17. The axial stress-strain response of these tests are compared in figure 120. The mechanical responses of these tests were quite comparable. The crystallographic rotation in this test, figure 121, was also comparable, again indicating homogeneous octahedral slip.

The initial axial yield strengths at an inelastic strain of 0.0005 mm/mm of [001] and [$\bar{3}$ 6 10] specimens previously cycled at 650 °C are listed in table 18. Also listed are the predicted yield strengths from equations (10) and (21), generated from conventional tests at 1050 °C. The prior deformation at 650 °C moderately reduced the yield strength of the [001] specimens, but apparently did not change that of the single [$\bar{3}$ 6 10] specimen.

Single [001] and [$\bar{3}$ 6 10] specimens given this prior deformation were tested in LCF at 1050 °C. The results of these tests are listed with comparative conventional tests in table 19. The cyclic stress and inelastic strain responses of these tests are presented with comparative conventional tests at 1050 °C in figures 122 to 127, while typical hysteresis loops at cycle 1 and half of cyclic life in the two tests are shown in figures 128 and 129. After allowing for the lower initial yield strengths, the cyclic hardening response of these tests was quite comparable to the conventional tests of specimens of these orientations at this inelastic strain level. Very slight cyclic stress softening of less than 5 percent from cycle 1 to half life was observed. Although only two LCF tests were performed, the cyclic stress-strain data from these tests at half of cyclic life fit well on the cyclic stress-strain curves of the conventional tests, figure 130.

Deformation structure. - The deformation structure of the [001] LCF specimen given the prior LCF at 650 °C was analyzed. This deformation structure was quite comparable to that of the conventional [001] LCF specimens tested at 1050 °C. The size of the γ' precipitates in this specimens was comparable to that of the conventional [001] LCF specimens tested at $\Delta\varepsilon_{in\,1} \sim 0.0027$ mm/mm.

32

The dislocations were again usually in the γ phase at the γ-γ, interfaces. These dislocations were analyzed with the same tilting experiments employed on the conventionally tested [001] specimen. The results of this analysis are presented in table 20 with the comparative results of a conventional [001] specimen tested in LCF at 1050 °C at this strain range. The micrographs from a typical tilting experiment are shown in figure 131. These results are essentially the same. There was again no predominance of dislocations with Burgers vectors corresponding to octahedral slip. On interfaces approximately parallel to {100} planes, the dislocations again had Burgers vectors randomly oriented with respect to the interface plane. These dislocations were usually irregularly arranged on these interfaces. On interfaces approximately parallel to {111} planes, the dislocations again usually had Burgers vectors lying in the plane of the interfaces. These dislocations were often arranged in roughly hexagonal networks here.

1050 to 650 °C Low Cycle Fatigue

Mechanical response. - Several [001] and [011] specimens were LCF tested at 1050 °C and then tensile tested at 650 °C. The results of these tests are compared to that of conventional [001] and [011] tensile tests at 650 °C in table 21. The axial stress-strain response of these tests are compared to conventional tests in figures 132 and 133. The crystallographic rotations in these tests are shown in figure 134.

The prior LCF cycling at 1050 °C appeared to encourage subsequent deformation at 650 °C to be more heterogeneous and more nearly confined to a single slip system. Whereas the conventional [001] tensile specimens only displayed rare faint slip traces, the [001] specimens subjected to prior 1050 °C LCF had clear slip offsets parallel to the (111) primary octahedral slip plane, figure 135, and a few offsets parallel to another {111} octahedral slip plane. The axial stress-strain response of the [001] specimens was transformed from the steep severe strain hardening response of conventional [001] specimens to the flat yielding, moderate strain hardening characteristic of the single slip response of the [2 5 20], [3 6 10] and [011] specimens at 650 °C. The axial elongation, reduction in area, and corresponding true fracture strain of the specimen subjected to prior 1050 °C LCF were somewhat increased over that of the conventional [001] test. The [011] specimen subjected to prior cycling at 1050 °C displayed flat yielding, as in conventional [011] tensile tests. However, strain softening rather than hardening subsequently occurred. While the axial elongations were comparable, the [011] specimen subjected to previous cycling had a greater reduction in area and corresponding true fracture strain.

The initial axial yield strengths at an inelastic strain of 0.0005 mm/mm of the [001] and [011] specimens subjected at prior 1050 °C LCF are listed in table 22. Accompanying these values are the predicted yield strengths from equation (13), generated from conventional tests at 650 °C. The effect of the prior 1050 °C LCF on subsequent yield strength at 650 °C varied according to tension-compression anisotropy. The yield strengths were consistently increased by 10 percent over the predicted values in the direction of higher yield strength, but were unchanged in the low yield strength direction. Therefore the [001] specimens, which are in all cases stronger in tension than compression, have increased yield strength in tension after the prior 1050 °C LCF, but unchanged yield strength in compression. It should be noted that at large

inelastic strains exceeding 0.03 mm/mm, the steep strain hardening of conventional [001] specimens, figure 132, would produce higher strengths in both directions for the conventional specimens. The [011] specimens, which are in all cases stronger in compression than tension, had increased yield strength in compression, but unchanged yield strength in tension.

Several [001] specimens and a single [011] specimen given the prior 1050 °C LCF were tested in LCF at 650 °C. The results of these tests are listed in table 23. The cyclic stress and inelastic strain hardening responses of these tests are presented and then compared to comparative conventional tests at 650 °C in figures 136 to 144, while typical hysteresis loops at cycle 1 and half of cyclic life are shown in figures 145 and 146. Both the [001] and [011] specimens displayed "jerky" flow which persisted to some extent throughout the LCF tests. These tests all had short lives of less than 60 cycles; comparable conventional tests of [$\bar{2}$ 5 20] and [011] specimens still displayed some remnants of jerky flow at this number of cycles. While this jerky flow was initially present in both tension and compression, it persisted in the direction of lower yield strength, as shown in figures 145 and 146. Therefore, the jerky flow continued in tension for the [011] specimen, but continued in compression for the [001] specimens.

This tension-compression anisotropy of the jerky flow (which was not observed in conventional tests at 650 °C) and yield strength effect was examined in more detail in the several tests of [001] specimens. This unusual behavior was not dependent on initial loading direction, as tests started in tension and compression produced the same results. This behavior was also not highly dependent on crystallographic orientation near the [001] direction. Specimens oriented about 2° and about 8° from the [001] direction had the same behavior.

Beyond the higher tensile yield strength and resulting higher cyclic mean stresses, the cyclic stress amplitude as a function of fatigue cycles of the [001] specimens subjected to prior 1050 °C LCF was similar to conventional [001] LCF tests, figures 139. The [011] specimen subjected to prior 1050 °C LCF displayed more cyclic strain hardening early in the test than the conventional [011] LCF tests, but the total stress hardening eventually attained was comparable, figure 140. The [001] and [011] specimens subjected to prior 1050 °C LCF displayed no stage I easy glide region of negligible strain hardening. Rather significant strain hardening occurred from the beginning of the tests, during the pronounced jerky flow. This differed from the conventional LCF tests of the [$\bar{2}$ 5 20], [$\bar{3}$ 6 10], and [011] specimens, where significant strain hardening began as the jerky flow abated.

The cyclic stress-strain response at half of cyclic life for the [001] and [011] specimens subjected to prior 1050 °C LCF is depicted with that of conventional tests in figures 147 and 148. The [001] specimens subjected to prior 1050 °C LCF had higher cyclic stress response at small inelastic strains, and lower cyclic stress response at large inelastic strains, than that of conventional tests. The results of these [001] tests, when modeled by least squares analysis (appendix, table A25) with the standard cyclic stress-strain equation (eq. (6)) produced the equation:

$$\frac{\Delta\sigma}{2} = 1082 \left(\frac{\Delta\varepsilon_{in}}{2}\right)^{0.020} \quad \text{MPa} \tag{30}$$

The response of the [011] specimen subjected to prior 1050 °C LCF was apparently in line with conventional [011] tests, but outside their range.

Deformation structure. - The deformation structure of one of these [001] LCF specimens was examined. This deformation structure was significantly different from that of conventional specimens LCF tests at 650 °C. This deformation structure consisted of very planar highly deformed slip bands superimposed on general deformation throughout the microstructure. Brief tilting experiments, similar to those performed on the slip bands of the [3 $\bar{6}$ 10] specimens tested at 650 °C, were utilized to characterize the slip bands. Micrographs of a typical tilting experiment are shown in figure 149. These slip bands were much narrower, with much more intense, localized deformation than those of any specimen conventionally tested at 650 °C. A large majority of the dislocations in these slip bands had the Burgers vectors corresponding to primary octahedral slip, $b = \pm 1/2[\bar{1}01]$. The dislocations outside of the slip bands also often had Burgers vectors corresponding to the other octahedral slip systems, $b = \pm 1/2[101]$, $1/2[0\bar{1}1]$, and $1/2[011]$, just as in the conventionally tested [001] LCF specimens. These bands had a very high dislocation density, indicating intense deformation, which produced excessive strain contrast in TEM imaging.

V. DISCUSSION

LCF MECHANICAL RESPONSE AND DEFORMATION STRUCTURE AT 650 °C

Single crystal specimens deforming by octahedral slip, [001], [$\bar{2}$ 5 20], [$\bar{3}$ 6 10], and [011], displayed a significant yield strength tension-compression anisotropy at 650 °C. The [001] and [$\bar{2}$ 5 20] specimens were stronger in tension, while the [011] and [$\bar{3}$ 6 10] specimens were stronger in compression. These results have been reported on other studies of PWA 1480 (refs. 32 and 46), and Rene N4 (ref. 60). Comparable tension-compression anisotropies have also been observed in single phase γ'. The anisotropy was therefore associated with the shearing of γ' precipitates by dislocation pairs. The specific mechanism proposed concerned the effect of the applied stress in promoting the cross slip of the lead dislocation from the (111) plane to the (010) cube cross slip plane. An analysis of these dislocation pairs in specimens deforming by octahedral slip by transmission electron microscopy (TEM) has shown that a large majority of these dislocations do indeed lie on the (010) cube cross slip plane and remained near-screw in character because of this. The state of these stored dislocation pairs corresponded to that suggested by Kear and Wilsdorf (ref. 11) in figure 150, case B, in which the lead dislocation of the pairs has glided on the (010) plane (thereby reducing the APB energy) to the maximum extent possible, while the trailing dislocation, presumably still dissociated on the (111) plane, acts as a pinning point. A schematic illustration of this cross slip process during deformation is shown in figure 151. The initial yield strength of this single crystal superalloy therefore seems to be controlled here by the shearing of the γ' precipitates by dislocation pairs.

The specimens deforming by primary cube slip, [$\bar{2}$ 3 4] and [$\bar{1}$11], displayed no significant yield strength tension-compression anisotropy. The γ' dislocation pairs remained on the (001) primary cube slip plane, often bowed on this plane indicating continued (001) plane glide.

Unlike initial yield strength, the subsequent cyclic hardening was comparable in tension and compression for the conventional total-strain-controlled LCF tests at 650 °C. This cyclic hardening was associated with changes in the dislocation structure in the γ_ phase. When slip was confined to the primary octahedral slip system in the [$\bar{2}$ 5 20], [$\bar{3}$ 6 10], and [011] specimens, the initial hardening response in monotonic tensile deformation and in LCF deformation was similar. In both tensile and LCF tests these specimens initially displayed stage I Easy Glide behavior, with "jerky" flow and little strain hardening. This type of "jerky" flow has been associated with interactions between gliding dislocations and solute atoms (ref. 62). This behavior continued to a cumulative shear strain of about γ_g = 0.071 mm/mm. Over the range of these tests, this maximum easy glide strain value γ_g was relatively independent of unidirectional or reversed loading path, LCF inelastic strain range, and specific crystallographic orientation. This suggested that some aspect of this deformation was relatively irreversible, as a characteristic, direction-independent amount of slip was necessary to initiate increased strain hardening (stage II strain hardening). Analysis of the deformation structures generated in these specimens during the stage I glide indicated this deformation was confined to slip bands and planar, with most of the dislocations in the γ phase confined to the (111) plane. After the onset of stage II strain hardening, the dislocations had accumulated in the γ phase and begun to combine in nonplanar entanglements in the bands, becoming sessile there and providing barriers to other gliding dislocations. The γ' dislocations also sometimes intersected to provide additional barriers in this phase. Perhaps due to this hardening of the slip bands, deformation spread to some extent to the weaker, undeformed regions between the slip bands. In tensile tests and LCF tests of sufficiently large inelastic strains, this resulted in deformation throughout the microstructure at failure. But in all LCF tests of these specimens the dislocations in the γ phase were often in nonplanar entanglements, with individual dislocation segments dissociated on {111} planes. Therefore the irreversible aspect of the stage I Easy Glide deformation appeared to be the accumulation of dislocations in the γ phase. This accumulation may have been driven by the cube cross slip of the portions of these dislocations penetrating the γ' precipitates. These cross slipped segments would act as pinning points, hindering the free glide of the adjoining segments in the γ phase. In this manner the effective free glide distance of entire dislocations would be continually reduced, resulting in accumulation. The accumulation of dislocations in the γ phase could encourage more cross slip here, driven by the repulsive forces between dislocations of the same Burgers vectors. Dislocation intersections could then occur to produce the nonplanar entanglements.

When slip occurred on several octahedral slip systems, strain hardening quickly occurred in LCF tests, approaching a saturation in 20 to 30 cycles. This appeared related to the intersection, principally in the γ phase, of dislocations of the different octahedral slip systems. These dislocations formed nonplanar, sessile entanglements in the γ phase after only 10 to 20 LCF cycles. These dislocations of various Burgers vectors also were often observed in sessile orientations at the γ-γ' interfaces, as reported in other studies (refs. 55 and 56), sometimes intersecting to form rectangular networks. Each of these dislocation arrangements in the γ phase act as barriers to dislocation glide in addition to the γ' precipitates.

The primary cube slip specimens, [$\bar{2}$ 3 4] and [$\bar{1}$11], displayed immediate gradual strain hardening in LCF tests. This cyclic strain hardening continued

for nearly one third of the fatigue test. TEM analysis of the deformation structure disclosed that while dislocations in the γ' precipitates were on the primary cube slip plane, in the γ phase they were often on the (111) and ($\bar{1}$11) planes early in the LCF tests. This suggested that primary cube slip occurred in the γ' phase, while there was some tendency in the γ phase for dislocations to cross slip from the (001) plane to the (111) or ($\bar{1}$11) planes. Glide on {111} planes would occur more easily in this FCC phase. These conflicting processes may account for the gradual continual cyclic strain hardening. The glide of dislocation pairs on the primary cube slip plane in the γ' precipitates may have produced some glide of the dislocations on the (001) plane in the γ phase. But some portion of the dislocations may have locally cross slipped onto octahedral cross slip planes in the γ phase. The cross slipped segments could thereafter glide on these octahedral planes to the next γ-γ' interface. Now the likelihood of two of these cross slipped dislocations arriving at the same interface location in this manner and orientation is relatively small, preventing the easy pairing of dislocations for γ' shearing. Therefore these cross slipped segments would be pinned at the γ-γ' interfaces (fig. 63), where they would act as barriers. These barriers would increase in number in direct proportion to the amount of γ' shearing which has occurred. Additionally, the dislocations gliding on the {111} planes in the γ phase would intersect with dislocations still on the (001) plane, encouraging the formation of nonplanar entanglements. These entanglements, already evident in some places after only 10 LCF cycles in figure 63, were quite common in the failed LCF specimens, figure 64.

The cyclic stress strain curves of all specimens tested at 650 °C displayed low cyclic strain hardening response. This was especially evident for the primary octahedral slip specimens, [$\bar{2}$ 5 20], [$\bar{3}$ 6 10], and [011]. These specimens had cyclic strain hardening coefficients of less than 0.1. The specimens displaying primary cube slip, [2 3 4] and [$\bar{1}$11], also had low cyclic strain hardening coefficients of only 0.071 and 0.116. Even when slip was operative on several slip systems, the cyclic strain hardening coefficient was only 0.104. While the initial yield strength appears to be controlled by the act of dislocations shearing γ' precipitates, cyclic hardening appears to be associated with the dislocation structure in the γ phase. As dislocations accumulate in the γ phase, the free planar glide of dislocations between γ' precipitates becomes more difficult. The dislocations become locally entangled in the γ phase, providing sessile barriers to dislocation glide. This region can then be considered "hardened".

The cyclic stress-strain curve of single crystal copper also displays little or no strain hardening in this strain regime. The constant cyclic stress observed was associated with the stress required to generate a persistent slip band in the undeformed microstructure (ref. 35). This explanation appears to be also applicable here. In tests of low inelastic strains, the dislocations were in loose bands of deformation separated by undeformed regions. In tests of high inelastic strain, deformation occurred throughout the microstructure. Therefore it would seem that after the formation of the nonplanar entanglements, only a limited amount of inelastic strain can be taken up by the dislocations of a slip band. If this is not equal to externally imposed inelastic strain, further slip bands are nucleated at the same or a slightly increased stress level. In tests of sufficiently large inelastic strains, this results in deformation spread throughout the entire microstructure. Any further inelastic strain must be taken up within this deformed microstructure. This

did occur, at somewhat higher stress levels, producing the dense pileups of dislocations in the γ phase as shown in figure 65.

The LCF tests of constant inelastic strain range were performed in order to examine the path dependence of the cyclic hardening and cyclic stress-strain response and to compare the cyclic response of PWA 1480 and single phase γ'. The response of the PWA 1480 specimens deforming by octahedral slip was similar to that reported for single phase γ', with greater cyclic hardening in the high strength direction. But these PWA 1480 results are deceiving. This anisotropic cyclic hardening was due to the fact that the cyclic mean stress increased with increasing total strain range, figures 20 to 22. This was because the first LCF cycle in tests of low $\Delta\varepsilon_t$ only produced yielding in the weak strength direction, while tests of large $\Delta\varepsilon_t$ produced yielding in both directions. This produced different resulting mean stresses. In tests of constant inelastic strain range, $\Delta\varepsilon_t$ was increased as cyclic hardening occurred, increasing the cyclic mean stresses. The deformation concurrently spread throughout the microstructure. The [$\bar{3}$ 6 10] and [011] specimens continued to display "jerky" flow much longer in these tests, indicating that planar slip was being initiated in undeformed regions. The stabilized cyclic stress-strain response (including mean stress) displayed by these octahedral slip specimens corresponded to that of conventionally tested specimens with $\Delta\varepsilon_{in} \sim 0.001$ at half of cyclic life, as did their deformation structures. Therefore the stabilized cyclic stress-strain response and deformation structures of the [001], [$\bar{3}$ 6 10], and [011] specimens were not significantly path dependent in these tests.

The constant inelastic strain tests of the [$\bar{2}$ 3 4] and [$\bar{1}$11] specimens produced larger negative mean stresses at saturation than that of any conventional tests of these specimens. Therefore some path dependence of the stabilized cyclic stress-strain response of these specimens seemed indicated. The deformation structures of these specimens were quite similar to those of the conventionally tested specimens, and offered no explanations for this response.

LCF MECHANICAL RESPONSE AND DEFORMATION STRUCTURE AT 1050 °C

Tensile test crystallographic rotations indicated that the [001] and [$\bar{2}$ 5 20] specimens initially deformed on several octahedral slip systems, while the [$\bar{1}$11], [$\bar{2}$ 3 4], and [$\bar{3}$ 6 10] specimens initially deformed on the primary cube slip system. The [001] and [$\bar{2}$ 5 20] specimens had higher initial critical resolved shear strengths in compression than in tension. The [$\bar{1}$11] specimens, initially deforming by primary cube slip, had equal strength in tension and compression. In yielding, the [001] specimens displayed significantly more strain hardening than the [$\bar{1}$11] specimens. This may be due to the activation of the many octahedral slip systems in the [001] specimens, compared to only three possible cube slip systems in the [111] specimens. The few tests of the [$\bar{2}$ 3 4] and [$\bar{3}$ 6 10] specimens suggested less tension-compression anisotropy in yield strengths and a somewhat lower critical resolved shear strength on the primary cube slip system.

In terms of tension-compression anisotropy, the [001] and [$\bar{1}$11] specimens displayed the extremes of response of PWA 1480 at 1050 °C in this study. Unlike the present results, [$\bar{1}$11]-oriented specimens tested at high temperatures at other strain rates have had higher yield strength in tension than

compression in other studies of PWA 1480 (ref. 32) and Rene N4 (ref. 30). Therefore this anisotropy may be temperature and strain rate dependent. The higher strength in compression than tension of the [001]-oriented specimens was also observed in Rene N4 (ref. 60). The mechanisms producing these anisotropies have not been conclusively determined. During octahedral slip at high temperatures such as 1050 °C, cube cross slip is believed to occur quite easily irrespective of the effect of applied stress in extending or constricting dissociated $a/2[\bar{1}01]$ dislocations. In any event this mechanism would predict higher yield strength in tension for [001] specimens.

LCF tests of [001] and [$\bar{1}$11] specimens produced different initial LCF response on cycle 1. The initial cyclic stress ranges of the [001] and [$\bar{1}$11] LCF tests were significantly different as a function of inelastic strain range. This was due to their dissimilar monotonic strain hardening response. As shown in the [001] specimen hysteresis loops of figures 86 and 96, the [001] cyclic stress range on cycle 1 produced at $\Delta\varepsilon_{in} = 0.0027$ mm/mm was much larger than that at $\Delta\varepsilon_{in} = 0.0010$ mm/mm. But the [$\bar{1}$11] specimen hysteresis loops of figures 87 and 97 display more comparable stress ranges on cycle 1. These initial hysteresis loops also displayed differing mean stresses due to the different initial tension-compression anisotropies. The [001] specimens had initial negative mean stresses, while the [$\bar{1}$11] specimens had initial negligible mean stresses.

The subsequent cyclic response of the [001] and [$\bar{1}$11] specimens was similar in several respects with comparable gradual cyclic softening response. The amount of softening as a function of initial cyclic stress amplitude varied inversely with inelastic strain range. LCF tests of low inelastic strains had the most cyclic softening; while those of large inelastic strains had only slight softening. This response was accompanied by a very homogeneous deformation structure where recovery enabled many of the dislocations to rearrange to form networks at the γ-γ' interfaces. In addition the γ' precipitates were somewhat coarsened.

In all [001] and [$\bar{1}$11] LCF test specimens most of the dislocations were arranged in networks at the γ-γ' interfaces. Far fewer dislocations were observed extending in the γ phase between the γ' precipitates. The Burgers vectors of the dislocations did not primarily correspond to the slip systems indicated in monotonic tensile tests. Rather dislocations of all Burgers vectors were present in both the [001] and [$\bar{1}$11] failed LCF specimens. Therefore the processes of dislocation reaction and rearrangement associated with recovery have occurred in both the [001] and [$\bar{1}$11] specimens.

The dislocations were most regularly arranged in hexagonal networks for the [001] LCF specimens tested at $\Delta\varepsilon_{in\ 1} \sim 0.001$ mm/mm. The [$\bar{1}$11] specimens and the [001] specimens tested at $\Delta\varepsilon_{in\ 1} \sim 0.0027$ mm/mm had somewhat less well arranged dislocation networks, but they still tended to be roughly hexagonal on {111} interfaces. The [001] LCF specimens appeared to have a qualitatively higher dislocation density than the [$\bar{1}$11] LCF specimens. This may be due to the different initially operative slip systems. The [001] specimens had initial octahedral slip on several systems. Therefore dislocations of several Burgers vectors were initially generated. The [$\bar{1}$11] specimens predominantly had initial cube slip. Therefore, dislocations of one to three Burgers vectors were initially generated. Dislocation multiplication through reactions could conceivably occur at a higher rate in the [001] specimen due to the greater

rate of intersections of dissimilar dislocations, as seemed indicated in the [001] LCF specimen interrupted after 1/2 of an LCF cycle.

Unloaded specimens exposed at 1050 °C for the times of these LCF tests had very few dislocations. So the numerous dislocations at the $\gamma-\gamma'$ interfaces in the LCF specimens were due to the cyclic deformation rather than just the exposure at 1050 °C. These interfacial dislocations can relieve strains at the $\gamma-\gamma'$ interfaces due to lattice mismatch and modulus mismatch. The dislocations are therefore at minimum energy positions when they take on the characteristics of misfit dislocations: having Burgers vectors in the plane of the interface and near-edge character. Collectively, if a sufficient number of dislocations of these characteristics are present, they would presumably tend to form hexagonal networks on {111} interfaces and square networks on {010} interfaces. Therefore a reasonable indication of the degree of recovery which has occurred is the extent to which the interface dislocations have the characteristics of misfit dislocations. The relative proportion of dislocations having Burgers vectors (**b**) in the planes of interfaces parallel to several {100} and {111} planes was employed as one quantitative measure of the degree of recovery which has occurred.

The [001] and [$\bar{1}$11] LCF specimens had comparable degrees of recovery on this basis. About two-thirds of the total number of interfacial dislocations analyzed in these specimens had **b** in the planes of the interfaces. But the characteristics of the dislocations on the {100} interfaces differed from those on the {111} interfaces. Less than half of the total number of dislocations analyzed on {100} interfaces had **b** in the interface planes, with large variability between different interfaces. These results were obtained for both [001] and [$\bar{1}$11] specimens LCF tested at $\Delta\varepsilon_{in\,1} \sim 0.001$ and 0.0027 mm/mm. The dislocations on these {100} interfaces were frequently arranged in networks of irregular geometry. Conversely, over 80 percent of the total number of dislocations analyzed on the {111} interfaces had **b** in the interface planes. On these interfaces, the variability was reduced and inversely dependent on $\Delta\varepsilon_{in}$. These dislocations were often arranged in roughly hexagonal networks. These properties were attained early in the LCF tests. TEM analysis of [001] and [$\bar{1}$11] LCF specimens interrupted at 50 cycles produced quite similar results although the number of dislocations at the interfaces was reduced. Now the regularity of the dislocation networks is an additional qualitative indication of the degree of recovery which has occurred. The very slight cyclic softening observed in tests at $\Delta\varepsilon_{in\,1} \sim 0.0027$ mm/mm was associated with less recovery on this basis (somewhat irregular dislocation network arrangements) and only slight coarsening of the γ' precipitates. The more substantial cyclic softening in LCF tests at $\Delta\varepsilon_{in\,1} \sim 0.001$ mm/mm was associated with more recovery (more regular networks) and more substantial γ' coarsening. These trends were more noticeable for the [001] specimens.

The difference of the results on the {100} and {111} interfaces was most consistent, even in specimens only aged 500 hr at 1050 °C. This may be related to the fact that the {111} planes are the usual glide planes for the FCC γ phase. The glide of dislocations on {111} planes (with **b** therefore lying in the planes) to interfaces parallel to these planes may therefore occur more easily, resulting in the depositing at {111} interfaces of dislocations with **b** in the plane of the interface. Alternatively, shear loops may nucleate preferentially at these interfaces for similar reasons (ref. 63).

The extent of cyclic softening in high temperature LCF of nickel-base superalloys has been more closely attributed to the degree of γ' coarsening occurring during an LCF test (refs. 38 and 42). In the present study, the degree of γ' coarsening was inversely dependent on inelastic strain range and accentuated in tests of [001] specimens. Now in an LCF test at the same inelastic strain range, the [001] specimens had approximately twice the elapsed time per cycle of the [$\bar{1}$11] specimens, due to the large difference in their elastic moduli. The fatigue lives of the [001] and [$\bar{1}$11] specimens at 1050 °C were comparable as a function of inelastic strain range, (appendix, fig. A2). Therefore for LCF tests at comparable $\Delta\varepsilon_{in}$ and fatigue lives, the [001] specimens were exposed to LCF at 1050 °C for over twice the time of the [$\bar{1}$11] specimens. The [$\bar{1}$11] and [001] LCF tests at $\Delta\varepsilon_{in\ 1} \sim 0.0027$ mm/mm lasted about 1.2 and 2.7 hr, respectively. The [$\bar{1}$11] and [001] tests at $\Delta\varepsilon_{in\ 1} \sim 0.001$ mm/mm lasted about 2.6 and 8.6 hr, respectively. Therefore the change in γ' size of the failed LCF specimens was roughly proportional to the time of the LCF tests, indicating the coarsening during LCF loading was still in some respects a time-dependent process. This may help explain the increased γ' coarsening of the [001] over [$\bar{1}$11] specimens. It should also be noted that in creep tests of another single crystal superalloy at 980 °C, [001]-oriented specimens had higher γ' coarsening rates than [$\bar{1}$11] specimens (ref. 64). Therefore, the basic stress-assisted γ' coarsening rates of [001] and [$\bar{1}$11] specimens may differ.

The effect of the γ-γ' interfacial dislocations on the γ' coarsening rate is unclear. In the present study, the γ' size was relatively stable, with only a moderate amount of coarsening evident. But the specimen with the most regularly hexagonal dislocation networks, [001] tested at $\Delta\varepsilon_{in\ 1} \sim 0.001$ mm/mm, had the most coarsening. These dislocations may enhance precipitate coarsening by providing shorter diffusion paths (refs. 41 and 42). Conversely, they may slow the advance of the γ-γ' interfaces, slowing precipitate coarsening (ref. 65). Experiments involving the extended high temperature aging of specimens previously loaded to produce the interfacial dislocation networks could perhaps resolve this question.

To summarize, the cyclic softening of both the [001] and [$\bar{1}$11] specimens at 1050 °C appeared to be directly associated with the dislocation recovery at the γ-γ' interfaces and indirectly related to the γ' precipitate coarsening. In particular, the storage of dislocations at the γ-γ' interfaces and their rearrangement and reactions to form networks there played a major role in the cyclic softening, with more efficient interfacial dislocation arrangements associated with more cyclic softening. The degree of γ' precipitate coarsening varied with cyclic response and LCF test time in a more complex manner.

The build-up of the tension-compression anisotropy of the [$\bar{1}$11] specimens in high temperature LCF has been reported in other studies of PWA 1480 (ref. 46) and Rene N4 (ref. 30). The relaxation of the tension-compression anisotropy-induced negative cyclic mean stresses of the [001] specimens and the persistence of the positive mean stresses of the [$\bar{1}$11] specimens may be related to differences observed in the high temperature creep properties of specimens of these orientations, which has been reported elsewhere for PWA 1480 (ref. 66). No consistent differences in deformation structures were observed in the LCF test specimens which could explain this dissimilar response.

NONISOTHERMAL LCF MECHANICAL RESPONSE AND DEFORMATION STRUCTURES

The simple nonisothermal tests were primarily performed in order to learn more about the generation of the deformation structures at 650 and 1050 °C, their dependence on initial conditions, and their stability in subsequent deformation. These tests did aid in the understanding of these structures, but they also introduced many new questions. These relatively simple nonisothermal tests served to illustrate the complexities which can be introduced by nonisothermal deformation.

Prior LCF deformation at 650 °C had little effect on subsequent LCF at 1050 °C. The initial yield strength of [001] specimens at 1050 °C was moderately reduced by the prior deformation. This may have been due to the ready supply of dislocations preexistent in the microstructure, enabling flow at lower stresses. But continued LCF cycling produced response quite comparable to conventional tests, with slight cyclic softening. This appeared to be due to the high mobility of dislocations in LCF at 1050 °C, where enhanced recovery occurs. The dislocations were readily attracted to the γ-γ' interfaces, where the rearrangements and dislocation reactions resulted in a deformation structure very similar to that of specimens conventionally LCF tested at 1050 °C. Therefore this experiment illustrated the dominance of recovery processes in LCF at 1050 °C, which negated the effects of prior deformation at 650 °C.

Prior LCF deformation at 1050 °C greatly affected subsequent LCF at 650 °C. The initial yield strength at 650 °C was significantly increased by the prior deformation. But the initial yield strengths of the [001] and [011] specimens were curiously only increased in their higher strength directions: tension for the [001] specimens and compression for the [011] specimens. Subsequent LCF deformation was heterogeneous and more nearly confined to a single slip system for both the [011] and [001] specimens, with sharp slip offsets evident. "Jerky" flow curiously persisted only in the low strength directions of these specimens: compression for the [001] specimens and tension for the [011] specimens. Further investigation would be required to fully understand this complex response; this was clearly beyond the intent of this brief look at nonisothermal LCF.

The deformation structure associated with this response was complex. The dislocations introduced at the γ-γ' interfaces by the LCF at 1050 °C (fig. 115) apparently remained quite sessile at 650 °C, and did not rearrange. Instead they remained held as networks at the γ-γ' interfaces, as can be seen below the slip band in figure 145. These interfacial networks were in different configurations from those sometimes observed in conventionally tested specimens at 650 °C, figure 61. The networks produced at 1050 °C apparently strengthen the interfaces to increase the stress required for precipitate shearing. As shown in figure 145, planar, very narrow slip bands of intense deformation were produced, along with minor, more homogeneous deformation on several octahedral slip systems in the [001] specimen. These slip bands were more narrow and intense than those observed in any specimens conventionally tested at 650 °C.

The complex mechanical behavior observed with respect to anisotropy in tension and compression is quite difficult to explain in terms of deformation structure. A much more extensive series of mechanical tests and deformation

studies would be required to fully understand this response. But several aspects deserve consideration. The increased intensity of slip may be due to the increased strength of the γ-γ' interfaces. Slip may tend to continue to be localized at locations where the dislocation-strengthened interfaces have been penetrated rather than spreading to other areas where the interface structure is still intact. This may play a role in the increased tension-compression anisotropy. As shown in the mechanical tests and deformation structure studies at 650 °C, the tension-compression anisotropy is dependent on γ' shearing. Now at very small inelastic strains where yielding first begins ("micro-yielding"), single phase γ' single crystals do not display tension-compression anisotropy in yield strength (ref. 3). But at larger inelastic strains the anisotropy becomes quite evident, as more extensive γ' shearing occurs, somehow promoting the cross slip of more dislocations onto the (010) plane. The highly localized, excessive γ' shearing which occurs in the slip bands of the specimens subjected to prior LCF at 1050 °C may in a similar manner induce more tension-compression anisotropy.

The anisotropy in "jerky" flow was not present in conventionally tested specimens at 650 °C. In the conventional LCF tests at 650 °C, the jerky flow occurred in both tension and compression in the stage I easy glide portion of the hardening curve. The jerky flow was not observed in conventionally tested [001] specimens at 650 °C. Now in the low strength direction of single crystals specimens tested at 650 °C, dislocations are believed to glide easily over longer distances, as pinning by way of cube cross slip in the γ' precipitates is minimized. So the jerky flow in the low strength direction of the specimens subjected to prior LCF deformation could be somehow related to the easier glide of dislocations possible in the low strength direction. As jerky flow is often attributed to the breakaway of gliding dislocations from hindering groups of solute atoms, the prior LCF at 1050 °C could possibly have affected the distributions of these solute atoms.

VI. CONCLUSIONS

1. Initial yield strength at 650 °C was controlled by the shearing of γ' precipitates by dislocation pairs. Single crystals deforming by octahedral slip at 650 °C, [001], [2 5 20], [3 6 10], and [011], have a yield strength tension-compression anisotropy. This response was due to the effect of applied stress on the dominant cube cross slip pinning of dislocation pairs in the γ' precipitates. Single crystals deforming primarily by primary cube slip at 650 °C, [2 3 4] and [111], had evidence of primary cube slip in the γ' precipitate phase and some octahedral slip in the γ phase.

2. Cyclic hardening at 650 °C was associated with dislocation interactions in the γ phase. The specimens deforming by primary octahedral slip at 650 °C displayed classic single crystal hardening response in both LCF and tensile tests. While the stage I easy glide response was controlled by the planar shearing of the γ' precipitates in slip bands, the stage II and stage III hardening to saturation conditions was related to the formation of dislocation entanglements in the γ phase and the spreading of deformation on the same slip system in the microstructure.

3. Specimens deforming by octahedral slip on several slip systems at 650 °C, [001], had rapid cyclic hardening to a saturation, related to the

intersection in the γ phase of dislocations of different operative octahedral slip systems. Specimens deforming by primary cube slip at 650 °C, [$\bar{2}$ 3 4] and [$\bar{1}$11], had gradual continued cyclic hardening, with the early formation of nonplanar dislocation entanglements in the γ phase, possibly related to the different slip processes in the γ and γ' phases.

4. The cyclic stress-strain curves of all specimens tested at 650 °C had low cyclic strain hardening. This was consistent with the fact that deformation spread throughout the microstructure only in the tests of largest inelastic strains.

5. The [001] and [$\bar{2}$ 5 20] specimens had initial octahedral slip on numerous slip systems, producing high monotonic strain hardening rates, at 1050 °C. The [$\bar{3}$ 6 10], [$\bar{2}$ 3 4], and [$\bar{1}$11] specimens had initial cube slip on fewer slip systems, producing lower monotonic strain hardening rates at 1050 °C. But dislocations of all possible 1/2<110> Burgers vectors were observed in failed [001] and [$\bar{1}$11] LCF specimens, indicating that dislocation reactions occur readily in these conditions.

6. The [001], [$\bar{3}$ 6 10], [011], and [$\bar{1}$11] specimens all had slight cyclic softening in LCF tests at 1050 °C. This response was associated with extensive dislocation recovery, producing dislocation networks at the γ-γ' interfaces, and some coarsening of the γ' precipitates.

7. The LCF deformation at 650 °C was significantly affected by prior deformation at 1050 °C, but had minimal effects on subsequent LCF deformation at 1050 °C. LCF deformation at 1050 °C was not significantly affected by prior deformation at 650 °C, and had major effects on subsequent LCF deformation at 650 °C.

REFERENCES

1. Decker, R.F.: Strengthening Mechanisms in Nickel-Base Superalloys. Steel-Strengthening Mechanisms, Climax Molybdenum Co., Greenwich, CT, 1970, pp. 147-170.

2. Sims, C.T.; and Hagel, W.C., eds.: The Superalloys. Wiley, 1972.

3. Pope, D.P.; and Ezz, S.S.: Mechanical Properties of Ni_3Al and Nickel-Base Alloys With High Volume Fraction of q'. Int. Met. Rev., vol. 29, no. 2, 1984, pp. 136-167.

4. Guard, R.W.; and Westbrook, J.H.: Studies of the Compound Ni_3Al by High-Temperature X-Ray Methods. Trans. AIME, vol. 215, no. 5, Oct. 1959, pp. 871-872.

5. Flinn, P.A.: Theory of Deformation in Superlattices. Trans. AIME, vol. 218, no. 1, Feb. 1960, pp. 145-154.

6. Mihalisin, J.R.; and Decker, R.F.: Phase Transformations in Nickel-Rich Nickel-Titanium-Aluminum Alloys. Trans. AIME, vol. 218, no. 3, June 1960, pp. 507-515.

7. Grose, D.A.; and Ansell, G.S.: The Influence of Coherency Strain on the Elevated Temperature Tensile Behavior of Ni-15Cr-Al-Ti-Mo Alloys. Metall. Trans. A, vol. 12, no. 9, Sept. 1981, pp. 1631-1645.

8. Reppich, B.; Schepp, P.; and Wehner, B.: Some New Aspects Concerning Particle Hardening Mechanisms in γ' Precipitating Nickel-Base Alloys - II. Experiments. Acta Met., vol. 30, no. 1, 1982, pp. 95-104.

9. Gleiter, H.; and Hornbogen, E.: Precipitation Hardening by Coherent Particles. Mater. Sci. Eng., vol. 2, 1968, pp. 285-302.

10. Copley, S.M.; and Kear, B.H.: Temperature and Orientation Dependence of the Flow Stress in Off-Stoichiometric Ni_3Al (γ' Phase). Trans. AIME, vol. 239, no. 7, July 1967, pp. 977-984.

11. Kear, B.H.; and Wilsdorf, H.G.F.: Dislocation Configurations in Plastically Deformed Polycrystalline Cu_3Au Alloys. Trans. AIME, vol. 224, no. 2, Apr. 1962, pp. 382-386.

12. Leverant, G.R.; and Kear, B.H.: The Mechanics of Creep in Gamma Prime Precipitation-Hardenened Nickel-Base Alloys at Intermediate Temperatures. Metall. Trans. A, vol. 1, no. 2, Feb. 1970, pp. 491-498.

13. Leverant, G.R.; Gell, M.; and Hopkins, S.W.: The Effect of Strain Rate on the Flow Stress and Dislocation Behavior of a Precipitation-Hardened Nickel-Base Alloy. Mater. Sci. Eng., vol. 8, 1971, pp. 125-133.

14. Foreman, A.J.E.; and Makin, M.J.: Dislocation Movement Through Random Arrays of Obstacles. Phil. Mag., vol. 14, no. 131, Nov. 1966, pp. 911-924.

15. Weertmann, J.: Creep of Indium, Lead, and Some of Their Alloys with Various Metals. Trans. AIME, vol. 218, no. 2, Apr. 1960, pp. 207-218.

16. Herring, C.: Diffusional Viscosity of a Polycrystalline Solid. J. Appl. Phys., vol. 21, no. 5, May 1950, pp. 437-445.

17. Couts, W.H.: Mechanical Processing. The Superalloys, C.T. Sims and W.C. Hagel, eds., John Wiley and Sons, 1972, pp. 451-478.

18. Cole, G.S.; and Cremisio, R.S.: Solidification and Structure Control in Superalloys. The Superalloys, C.T. Sims and W. C. Hagel, eds., John Wiley and Sons, 1972, pp. 479-508.

19. Strangman, T.E., et al.: Development of Exothermically Cast Single-Crystal MAR-M 247 and Derivative Alloys. Superalloys 1980, J.K Tien, et al., eds., American Society for Metals, Metals Park, OH, 1980, pp. 215-224.

20. Gell, M.D.; Duhl, N.; and Giamei, A.F.: The Development of Single Crystal Superalloy Turbine Blades. Superalloys 1980, J.K. Tien, et al., eds., American Society for Metals, Metals Park, OH, 1980, pp. 205-214.

21. Decker, R.F.; and Sims, C.T.: The Metallurgy of Nickel-Base Alloys. The Superalloys, C.T. Sims and W.C. Hagel, eds., John Wiley and Sons, 1972, pp. 33-77.

22. Hertzberg, R.W.: Deformation and Fracture Mechanics of Engineering Materials. John Wiley and Sons, 1976, pp. 442-443.

23. Stoltz, R.E.; and Pineau, A.G.: Dislocation-Precipitate Interaction and Cyclic Stress-Strain Behavior of a γ' Strengthened Superalloy. Mater. Sci. Eng., vol. 34, 1978, pp. 275-284.

24. Anton, D.L.; and Fine, M.E.: Cyclic Hardening of an Ni-14.4 At. Pct Al Alloy Containing Coherent Precipitates. Metall. Trans. A, vol. 13, no. 7, July 1982, pp. 1187-1198.

25. Wells, C.H.; and Sullivan, C.P.: The Low-Cycle Fatigue Characteristics of a Nickel-Base Superalloy at Room Temperature. Trans. ASM, vol. 57, no. 4, Dec. 1964, pp. 841-855.

26. Wells, C.H.; and Sullivan, C.P.: Low-Cycle Fatigue Damage of Udimet 700 at 1400°F. Trans. ASM, vol. 58, no. 3, Sept. 1965, pp. 391-402.

27. Miner, R.V.; Gayda, J.: and Maier, R.D.: Fatigue and Creep-Fatigue Deformation of Several Nickel-Base Superalloys at 650°C. Metall. Trans. A, vol. 13, no. 10, Oct. 1982, pp. 1755-1765.

28. Horibe, S.; and Laird, C.: Orientation and History Dependence of Cyclic Deformation in Al-Cu Single Crystals Containing θ' Precipitates. Acta Met., vol. 31, no. 10, Oct. 1983, pp. 1567-1579.

29. Schmid, E.; and Boas, W.: Plasticity of Crystals. F.A. Hughes and Co. Limited, London, 1960, pp. 57-69.

30. Gabb, T.P.; Gayda, J.; and Miner, R.V.: Orientation and Temperature Dependence of Some Mechanical Properties of the Single-Crystal Nickel-Base Superalloy Rene N4: Part II. Low Cycle Fatigue Behavior. Metall. Trans. A, vol. 17, no. 3, Mar. 1986, pp. 497-505.

31. Jablonski, D.A.; and Sargent, S.: Anisotropic Fatigue Hardening of a Nickel-Base Single Crystal at Elevated Temperature. Scr. Met., vol. 15, no. 9, Sept. 1981, pp. 1003-1006.

32. Shah, D.M.; and Duhl, D.N.: The Effect of Orientation, Temperature, and Gamma Prime Size on the Yield Strength of a Single Crystal Nickel Base Superalloy. Superalloys 1984, M. Gell, et al., eds., The Metallurgical Society of AIME, Warrendale, PA, 1984, pp. 105-114.

33. Paidar, V.; Pope, D.P.; and Vitek, V.: A Theory of the Anomalous Yield Behavior in Ll_2 Ordered Alloys. Acta Met., vol. 32, no. 3, Mar. 1984, pp. 435-448.

34. Pak, H.-R.; Hsiung, L.-M.; and Kato, M.: Cyclic Deformation Behavior of Ni_3Ge Single Crystals at Room Temperature. High Temperature Ordered Intermetallic Alloys, C.C. Koch, C.T. Liu, and N.Ş. Stoloff, eds., The Materials Research Society, Pittsburg, PA, 1985, pp. 239-246.

35. Cheng, A.S.; and Laird, C.: Mechanisms of Fatigue Hardening in Copper Single Crystals: The Effects of Strain Amplitude and Orientation. Mater. Sci. Eng., vol. 51, 1981, pp. 111-121.

36. Fritzemeier, L.G.: The Cyclic Stress-Strain Behavior of Nickel-Base Superalloy Poly- and Single Crystals. Ph.D. Thesis, Columbia University, 1984.

37. Milligan, W.M.; Jayaraman, N.; and Bill, R.C.: Low Cycle Fatigue of MAR-M 200 Single Crystals with a Bimodal γ' Distribution at 760 and 870°C. Mater. Sci. Eng., vol. 82, 1986, pp. 127-139.

38. Antolovich, S.D.; Liu, S.; and Baur, R.: Low Cycle Fatigue Behavior of Rene 80 at Elevated Temperature. Metall. Trans. A, vol. 12, no. 3, Mar. 1981, pp. 473-481.

39. Stoloff, N.S.: Fundamentals of Strengthening. The Superalloys, C.T. Sims and W.C. Hagel, eds., John Wiley and Sons, 1972, pp. 79-111.

40. Pineau, A.: High Temperature Fatigue Behavior of Engineering Materials in Relation to Microstructure. Fatigue at High Temperatures, R. P. Skelton, ed., Applied Science Publishers, 1983, pp. 305-364.

41. Carry, C.; and Strudel, J.L.: Apparent and Effective Creep Parameters in Single Crystals of a Nickel Base Superalloy - I. Incubation Period. Acta Met., vol. 25, no. 7, July 1977, pp. 767-777.

42. Antolovich, S.D.; Rosa, E.; and Pineau, A.: Low Cycle Fatigue of Rene 77 at Elevated Temperatures. Mater. Sci. Eng., vol. 47, 1981, pp. 47-57.

43. Raguet, M.; Antolovich, S.D.; and Payne, R.K.: Fatigue and Deformation Behavior of Directionally Solidified Rene 80. Superalloys 1984, M. Gell, et al., eds., The Metallurgical Society of AIME, Warrendale, PA, 1984, pp. 231-241.

44. Miner, R.V.; Gayda, J.; and Hebsur, M.: Creep-Fatigue Behavior of NiCoCrAlY Coated PWA 1480 Superalloy Single Crystals. NASA TM-87110, 1985.

45. Gabb, T.P.; Miner, R.V.; and Gayda, J.: The Tensile and Fatigue Deformation Structures in a Single Crystal Ni-Base Superalloy. Scr. Met., vol. 20, no. 4, Apr. 1986, pp. 513-518.

46. Swanson, G.A., et al.: Life Prediction and Constitutive Models for Engine Hot Section Anisotropic Materials Program. (PWA-5968-19, Pratt and Whitney Aircraft; NASA Contract NAS3-23939) NASA CR-17495, 1986.

47. van der Merwe, J.H.: Crystal Interfaces. Part I. Semi-Infinite Crystals. J. Appl. Phys., vol. 34, no. 1, Jan. 1963, pp. 117-122.

48. Jesser, W.A.; and Kuhlmann-Wilsdorf, D.: On the Theory of Interfacial Energy and Elastic Strain of Epitaxial Overgrowths in Parallel Alignment on Single Crystal Substrates. Phys. Stat. Sol., vol. 19, 1967, pp. 95-105.

49. Shiflet, G.J.: Low Energy Dislocation Structures Caused By Phase Transformations. Mater. Sci. Eng., vol. 81, 1986, pp. 61-100.

50. Lasalmonie, A.; and Strudel, J.L.: Interfacial Dislocation Networks Around γ' Precipitates in Nickel-Base Alloys. Phil. Mag., vol. 32, no. 5, Nov. 1975, pp. 937-949.

51. Ference, T.G.; and Allen, S.M.: Dislocation/Precipitate Interactions during Coarsening of a Plastically Strained High-Misfit Nickel-Base Superalloy. Metall. Trans. A, vol. 17, no. 12, Dec. 1986, pp. 2239-2247.

52. Fredholm, A.; and Strudel, J.L.: On the Creep Resistance of Some Nickel Base Single Crystals. Superalloys 1984, M. Gell, et al., eds., The Metallurgical Society of AIME, Warrendale, PA, 1984, pp. 211-220.

53. Weatherly, G.C.; and Nicholson, R.B.: An Electron Microscope Investigation of the Interfacial Structure of Semi-Coherent Precipitates. Phil. Mag., vol. 17, no. 148, Apr. 1968, pp. 801-831.

54. Antolovich, S.D.; Domas, P.; and Strudel, J.L.: Low Cycle Fatigue of Rene 80 as Affected By Prior Exposure. Metall. Trans. A, vol. 10, no. 12, Dec. 1979, pp. 1859-1868.

55. Huron, E.: High Temperature Monotonic and Cyclic Deformation in a Directionally Solidified Nickel-Base Superalloy. NASA CR-175101, 1986.

56. Milligan, W.M.; and Antolovich, S.D.: Yielding and Deformation Behavior of the Single Crystal Superalloy PWA 1480. Metall. Trans. A, vol. 18, no. 1, Jan. 1987, pp. 85-95.

57. Edington, J.W.: Interpretation of Transmission Electron Micrographs. Macmillan, London, 1975, pp. 10-25.

58. Kear, B.H.; and Hornbecker, M.F.: Deformation Structures in Polycrystalline Ni_3Al. Trans ASM, vol. 59, no. 2, June 1966, pp. 155-161.

59. Drabik, W.; and Torun, J.: On the Analytical Methods of Line Defect and Beam Direction Determinations. Phys. Stat. Sol. A, vol. 77, 1983, pp. 513-519.

60. Miner, R.V., et al.: Orientation and Temperature Dependence of Some Mechanical Properties of the Single Crystal Nickel-Base Superalloy Rene N4: Part III. Tension-Compression Anisotropy. Metall. Trans. A, vol. 17, no. 3, Mar. 1986, pp. 507-512.

61. Paterson, M.S.: Plastic Deformation of Copper Crystal Under Alternating Tension and Compression. Acta Met., vol. 3, no. 5, Sept. 1955, pp. 491-500.

62. Jensen, R.R.; and Tien, J.K.: Temperature and Strain Rate Dependence of Stress-Strain Behavior in a Nickel-Base Superalloy. Metall. Trans. A, vol. 16, no. 6, June 1985, pp. 1049-1068.

63. Nathal, M.V.: private communication. NASA Lewis Research Center, Cleveland, OH.

64. Nathal, M.V.; and MacKay, R.A.: The Stability of Lamellar $\gamma-\gamma'$ Structures. Mater. Sci. Eng., vol. 85, no. 1-2, Jan. 1987, pp. 127-138.

65. Yu, K.: Anisotropic Deformation of IN-100 Nickel Base Superalloy Single Crystals. Ph.D. Thesis, Massachusetts Institute of Technology, 1985.

66. Duhl, D.N.: Directionally Solidified Superalloys. Superalloys II, C.T. Sims, N.S. Stoloff, and W.C. Hagel, eds., John Wiley and Sons, 1987, pp. 189-214.

BIBLIOGRAPHY

1. R. F. Decker. "Strengthening Mechanisms in Nickel-Base Superalloys." In Symposium: Steel-Strengthening Mechanisms: Proceedings of the Symposium in Zurich, Switzerland, May 5-6, 1969, by the Climax Molybdenum Co. Greenwich, Conn.: Climax Molybdenum Co., Greenwich, Conn., 1970, 147-170.

2. C. T. Sims and W. C. Hagel, ed. The Superalloys. New York: John Wiley and Sons, 1972.

3. D. P. Pope and S. S. Ezz. "Mechanical Properties of Ni_3Al and Nickel-Base Alloys With High Volume Fraction of γ'." Int. Metals Reviews 29 (1984): 136-167.

4. R. W. Guard and J. H. Westbrook. "Studies of the Compound Ni_3Al by High-Temperature X-Ray Methods." Trans. AIME, 215 (1959): 871-872.

5. P. A. Flinn. "Theory of Deformation in Superlattices." Trans. AIME 218 (1960): 145-154.

6. J. R. Mihalisin and R. F. Decker. "Phase Transformations in Nickel-Rich Nickel-Titanium-Aluminum Alloys." Trans. AIME 218 (1960): 507-515.

7. D. A. Gross and G. S. Ansell. "The Influence of Coherency Strain on the Elevated Temperature Tensile Behavior of Ni-15Cr-Al-Ti-Mo Alloys." Met. Trans. A 12A (1981): 1631-1645.

8. B. Reppich, P. Schepp, and B. Wehner. "Some New Aspects Concerning Particle Hardening Mechanisms in γ' Precipitating Nickel-Base Alloys - II. Experiments." Acta Met. 30 (1982): 95-104.

9. H. Gleiter and E. Hornbogen. "Precipitation Hardening by Coherent Precipitates." Mat. Sci. Eng. 2 (1968): 285-302.

10. S. M. Copley and B. H. Kear. "Temperature and Orientation Dependence of the Flow Stress in Off-Stoichiometric Ni_3Al (γ' Phase)." Trans. AIME 239 (1967): 977-984.

11. B. H. Kear and H. G. F. Wilsdorf. "Dislocation Configurations in Plastically Deformed Polycrystalline Cu_3Au Alloys." Trans. TMS-AIME 224 (1962): 382-386.

12. G. R. Leverant and B. H. Kear. "The Mechanics of Creep in Gamma Prime Precipitation-Hardenened Nickel-Base Alloys at

Intermediate Temperatures." Met. Trans. A 1A (1970): 491-498.

13. G. R. Leverant, M. Gell, and S. W. Hopkins. "The Effect of Strain Rate on the Flow Stress and Dislocation Behavior of a Precipitation-Hardened Nickel-Base Alloy." Mat. Sci. Eng. 8 (1971): 125-133.

14. A. J. E. Foreman and M. J. Markin. "Dislocation Movement Through Arrays of Obstacles." Phil. Mag 14 (1966): 911-924.

15. J. Weertmann. "Creep of Indium, Lead, and Some of Their Alloys with Various Metals." Trans. AIME 218 (1960): 207-218.

16. C. Herring. "Diffusional Viscosity of a Polycrystalline Solid." J. Appl. Phys. 21 (1950): 437-445.

17. W. H. Couts. "Mechanical Processing." In The Superalloys, ed. by C. T. Sims and W. C. Hagel, 451-478. New York: John Wiley and Sons, 1972.

18. G. S. Cole and R. S. Cremisio. "Solidification and Structure Control in Superalloys." In The Superalloys, ed. by C. T. Sims and W. C. Hagel, 479-508. New York: John Wiley and Sons, 1972.

19. T. E. Strangman, G. S. Hoppin, C. M. Phipps, and K. Harris. "Development of Exothermically Cast Single-Crystal MAR-M 247 and Derivative Alloys." In Superalloys 1980, ed. by J. K Tien, S. T. Wlodek, H. Murrow, M. Gell, and G. E. Maurer, 215-224. Metals Park: American Society for Metals, 1980.

20. M. Gell, D. N. Duhl, and A. F. Giamei. "The Defeclopment of Single Crystal Superalloy Turbine Blades." In Superalloys 1980, ed. by J. K. Tien, S. T. Wlodek, J. Murrow, M. Gell, and G. E. Maurer, 205-214. Metals Park: American Society for Metals, 1980.

21. R. F. Decker and C. T. Sims. "The Metallurgy of Nickel-Base Alloys". In The Superalloys, ed. by C. T. Sims and W. C. Hagel, 33-77. New York: John Wiley and Sons, 1972.

22. R. W. Hertzberg. Deformation and Fracture Mechanics of Engineering Materials, 442-443. New York: John Wiley and Sons, 1976.

23. R. E. Stoltz and A. G. Pineau. "Dislocation-Precipitate Interactions and Cyclic Stress-Strain Behavior of a γ' Strengthened Superalloy." Mat. Sci. Eng. 34 (1978): 275-284.

24. D. L. Anton and M. E. Fine. "Cyclic Hardening of an Ni-14.4 Atomic Percent Aluminum Alloy Containing Coherent Precipitates." Met. Trans. A 13A (1982): 1187-1198.

25. C. H. Wells and C. P. Sullivan. "The Low-Cycle Fatigue Characteristics of a Nickel-Base Superalloy at Room Temperature." Trans. ASM 57 (1965): 841-855.

26. C. H. Wells and C. P. Sullivan. "Low-Cycle Fatigue Damage of Udimet 700 at 1400°F." Trans. ASM 58 (1965): 391-402.

27. R. V. Miner, J. Gayda and R. D. Maier. "Fatigue and Creep-Fatigue Deformation of Several Nickel-Base Superalloys at 650°C." Met. Trans. A 13A (1982): 1755-1765.

28. S. Horibe and C. Laird. "Orientation and History Dependence of Cyclic Deformation in Al-Cu Single Crystals Containing ' Precipitates." Acta Met. 31 (1983): 1567-1579.

29. E. Schmid and W. Boas. Plasticity of Crystals, 57-69. London: F. A. Hughs and Co. Limited, 1960.

30. T. P. Gabb, J. Gayda and R. V. Miner. "Orientation and Temperature Dependence of Some Mechanical Properties of the Single-Crystal Nickel-Base Superalloy Rene N4: Part II. Low Cycle Fatigue." Met. Trans. A 17A (1986): 497-506.

31. D. A. Jablonski and S. Sargent. "Anisotropic Fatigue Hardening of a Nickel-Base Single Crystal at Elevated Temperature." Scripta Met. 15 (1981): 1003-1006.

32. D. M. Shah and D. N. Duhl. "The Effect of Orientation, Temperature, and Gamma Prime Size on the Yield Strength of a Single Crystal Nickel Base Superalloy." In Superalloys 1984, ed. by M. Gell, C. S. Kortovich, R. H. Bricknell and W. B. Kent, 105-114. Warrendale,PA: The Metallurgical Society of AIME, 1984.

33. V. Paidar, D. P. Pope and V. Vitek. "A Theory of the Anomalous Yield Behavior in $L1_2$ Ordered Alloys." Acta Met. 32 (1984): 435-448.

34. H.-R. Pak, L.-M. Hsiung and M. Kato. "Cyclic Deformation Behavior of Ni_3Ge Single Crystals at Room Temperature." In High Temperature Ordered Intermetallic Alloys, ed. by C. C. Koch, C. T. Liu and N. S. Stoloff, 239-246. Pittsburg, PA: The Materials Research Society, 1985.

35. A. S. Cheng and C. Laird. "Mechanisms of Fatigue Hardening in Copper Single Crystals: The Effects of Strain Amplitude

and Orientation." Mat. Sci. Eng. 51 (1981): 111-121.

36. L. G. Fritzemeier. The Cyclic Stress-Strain Behavior of
     Nickel-Base Superalloy Poly- and Single Crystals, Ph.D.
     Thesis, Columbia University, 1984.

37. W. M. Milligan, N. Jayaraman, and R. C. Bill. "Low Cycle
     Fatigue of MAR-M 200 Single Crystals with a Bimodal γ'
     Distribution at 760 and 870°C." Mat. Sci. Eng. 82 (1986):
     127-139.

38. S. D. Antolovich. S. Liu and R. Baur. "Low Cycle Fatigue
     Behavior of Rene 80 at Elevated Temperature." Met. Trans. A
     12A (1981): 473-481.

39. N. S. Stoloff. "Fundamentals of Strengthening." In The
     Superalloys, ed. by C. T. Sims and W. C. Hagel, 79-111. New
     York: John Wiley and Sons, 1972.

40. A. Pineau. "High Temperature Fatigue Behavior of Engineering
     Materials in Relation to Microstructure." In Fatigue at High
     Temperatures, ed. by R. P. Skelton, 305-364. New York:
     Applied Science Publishers, 1983.

41. C. Carry and J. L. Strudel. "Apparent and Effective Creep
     Parameters in Single Crystals of a Nickel Base Superalloy -
     I. Incubation Period." Acta Met. 25 (1977): 767-777.

42. S. D. Antolovich, E. Rosa, and A. Pineau. "Low Cycle Fatigue
     of Rene 77 at Elevated Temperatures." Mat. Sci. Eng. 47
     (1981): 47-57.

43. M. Raguet, S. D. Antolovich, and R. K. Payne. "Fatigue and
     Deformation Behavior of Directionally Solidified Rene 80."
     In Superalloys 1984, ed. by M. Gell, C. S. Kortovich, R. H.
     Bricknell, and W. B. Kent, 231-241. Warrendale, PA: The
     Metallurgical Society of AIME, 1984.

44. R. V. Miner, J. Gayda, and M. Hebsur. Creep-Fatigue Behavior
     of NiCoCrAlY Coated PWA 1480 Superalloy Single Crystals,
     NASA TM-87110. Washington, D.C.: National Aeronautics and
     Space Administration, 1985.

45. T. P. Gabb, R. V. Miner, and J. Gayda. "The Tensile and
     Fatigue Deformation Structures in a Single Crystal Ni-Base
     Superalloy." Scripta Met. 20 (1986): 513-518.

46. G. A. Swanson, I. Linask, K. M. Nissley, P. P. Norris, T. G.
     Meyer, and K. P. Walker. Life Prediction and Constitutive
     Models for Engine Hot Section Anisotropic Materials Program,

NASA CR-17495. Washington, D.C.: National Aeronautics and Space Administration, 1986.

47. J. H. van der Merwe. "Crystal Interfaces. Part I. Semi-Infinite Crystals." J. Appl. Phys. 34 (1963): 117-122.

48. W. A. Jesser and D. Kuhlmann-Wilsdorf. "On the Theory of Interfacial Energy and Elastic Strain of Epitaxial Overgrowths in Parallel Alignment on Single Crystal Substrates." Phys. Stat. Sol. 19 (1965): 95-105.

49. G. J. Shiflet. "Low Energy Dislocation Structures Caused By Phase Transformations." Mat. Sci. Eng. 81 (1986): 61-100.

50. A. Lasalmonie and J. L. Strudel. "Interfacial Dislocation Networks Around γ' Precipitates in Nickel-Base Alloys." Phil. Mag. 32 (1975): 937-949.

51. T. G. Ference and S. M. Allen. "Dislocation/Precipitate Interactions during Coarsening of a Plastically Strained High-Misfit Nickel-Base Superalloy." Met. Trans. A 17A (1986): 2239-2247.

52. A. Fredholm and J. L. Strudel. "On the Creep Resistance of Some Nickel Base Single Crystals." In Superalloys 1984. ed. by M. Gell, C. S. Kortovich, R. H. Bricknell, and W. B. Kent, 211-220. Warrendale, PA: The Metallurgical Society of AIME, 1984.

53. G. C. Weatherly and R. B. Nicholson. "An Electron Microscope Investigation of the Interfacial Structure of Semi-Coherent Precipitates." Phil. Mag. 17 (1968): 801-831.

54. S. D. Antolovich, P. Domas, and J. L. Strudel. "Low Cycle Fatigue of Rene 80 as Affected By Prior Exposure." Met. Trans. A 10A (1979): 1859-1868.

55. E. Huron. High Temperature Monotonic and Cyclic Deformation in a Directionally Solidified Nickel-Base Superalloy, NASA CR-175101. Washington, D.C.: National Aeronautics and Space Administration, 1986.

56. W. M. Milligan and S. D. Antolovich. "Yielding and Deformation Behavior of the Single Crystal Superalloy PWA 1480." Met. Trans. A 18A (1987): 85-95.

57. J. W. Eddington. Practical Electron Microscopy in Materials Science: 3. Interpretation of Transmission Electron Micrographs, Philips Technical Library, N. V. Philips' Gloeilampenfabrieken, Einhoven, 10-25. East Kilbride,

Scotland: Thomson Litho Ltd., 1975.

58. B. H. Kear and M. F. Hornbecker. "Deformation Structures in Polycrystalline Ni_3Al." Trans ASM 59 (1966): 155-161.

59. W. Drabik and J. Torun. "On the Analytical Methods of Line Defect and Beam Direction Determinations." Phys. Stat. Sol. 77 (1983): 513-519.

60. R. V. Miner, T. P. Gabb, J. Gayda, and K. J. Hemker. "Orientation and Temperature Dependence of Some Mechanical Properties of the Single Crystal Nickel-Base Superalloy Rene N4: Part III. Tension-Compression Anisotropy." Met. Trans. A 17A (1986): 507-512.

61. M. S. Patterson. "Plastic Deformation of Copper Crystal Under Alternating Tension and Compression." Acta Met. 3 (1955): 491-500.

62. R. R. Jenson and J. K. Tien. "Temperature and Strain Rate Dependence of Stress-Strain Behavior in a Nickel-Base Superalloy." Met. Trans. A 16A (1985): 1049-1068.

63. M. V. Nathal, private communication.

64. M. V. Nathal and R.A. MacKay. "The Stability of Lamellar γ-γ' Structures." Mat. Sci. Eng. 85 (1987): 127-138.

65. K. Yu. Anisotropic Deformation of IN-100 Nickel Base Superalloy Single Crystals. Ph'D Thesis, Massachusetts Institite of Technology, 1985.

66. D. N. Duhl. "Directionally Solidified Superalloys." In Superalloys II, ed. by C. T. Sims, N. S. Stoloff, and W. C. Hagel, 189-214. New York: John Wiley and Sons, 1987.

55

Table 1. LCF Test Matrix.

Test Temperature	650°C	1050°C
Specimens	$[001],[\bar{2}\ 5\ 20],[\bar{3}\ 6\ 10],[011]$	$[001]$
	$[\bar{2}\ 3\ 4],[\bar{1}11]$	$[\bar{1}11]$
Approximate Inelastic Strain Range on Cycle 1 $\Delta\varepsilon_{in\ 1}$ (mm/mm)	.0008,.0017,.0025	.001,.002,.0027

Table 2. Composition of the PWA 1480 test material in weight %.

Element	Al	C	Co	Cr	S	Si	Ta	Ti	W	Ni
Nominal	5	<.02	5	10	-	-	12	1.5	4	Bal.
Slabs	4.7	.005	4.8	9.4	.001	.9	11	1.0	5.2	Bal.
Bars	5.3	.003	5.3	10.3	-	-	11.9	1.3	4.0	Bal.

Table 3. Tensile test results at 650°C

Nominal Orient. [hkl]	Measured Orient. [hkl]	Symbol	Elastic Modulus E (GPa)	Yield Strength .2 % Offset σ_y (MPa)	Ultimate Strength σ_u (MPa)	True Fracture Strain ε_{tf} (mm/mm)
0 0 1	$\bar{1}$ 1 100	■	103	963	1343	.033
$\bar{2}$ 5 20	$\overline{14}$ 33 100	◆	133	855	992	.112
$\bar{3}$ 6 10	$\overline{21}$ 63 100	●	177	742	951	.149
0 1 1	$\bar{1}$ 81 100	⬬	184	841	983	.112
$\bar{2}$ 3 4	$\overline{33}$ 97 100	⬠	238	755	1159	.232
$\bar{1}$ 1 1	$\overline{78}$ 82 100	▲	257	747	1180	.245

Table 4a. Initial Yield Strengths of Octahedral Slip Specimens.

Nom. Orient. [hkl]	Actual Orient. [hkl]	Tens.(t) Comp.(c)	Yield Strength ε_{in}=.0005mm/mm σ_y (MPa)	Predicted Strength Equ. 11 σ_{11} (MPa)	Equ. 13 c_{13} (MPa)
0 0 1	$\bar{4}$ 7 100	t	892	872	907
	$\bar{2}$ 6 100	t	894	874	912
	$\bar{2}$ 6 100	t	914	874	912
	$\bar{3}$ 14 100	t	853	830	859
	$\bar{5}$ 12 100	c	832	838	810
	$\bar{5}$ 7 100	t	852	874	909
	$\bar{5}$ 14 100	t	905	827	853
	$\bar{3}$ 16 100	t	857	818	844
	$\bar{1}$ 1 100	t	899	915	966
$\bar{2}$ 5 20	$\overline{14}$ 30 100	t	840	778	786
	$\overline{14}$ 33 100	t	848	771	777
	$\bar{7}$ 21 100	t	859	797	816
	$\bar{8}$ 25 100	c	817	786	771
	$\overline{10}$ 13 100	c	814	841	817
$\bar{3}$ 6 10	$\overline{22}$ 63 100	t	749	778	762
	$\overline{22}$ 61 100	t	740	776	762
	$\overline{19}$ 57 100	c	785	768	779
	$\overline{19}$ 58 100	t	742	770	758
	$\overline{32}$ 61 100	c	789	802	818
	$\overline{28}$ 59 100	t	762	789	775

Table 4a. (cont.)

Nom. Orient. [hkl]	Actual Orient. [hkl]	Tens.(t) Comp.(c)	Yield Strength ε_{in}=.0005 mm/mm σ_y (MPa)	Predicted Strength Equ. 11 σ_{11} (MPa)	Equ. 13 σ_{13} (MPa)
0 1 1	$\bar{4}$ 88 100	t	805	863	830
	$\bar{8}$ 91 100	t	796	861	826
	0 92 100	t	848	889	853
	0 93 100	c	919	897	936
	$\bar{1}$ 84 100	t	841	855	827
	$\bar{1}$ 81 100	t	826	845	820
	$\bar{2}$ 89 100	t	836	870	837

Table 4b. The initial axial yield strengths for the cube slip specimens at 650°C.

Nom. Orient. [hkl]	Actual Orient. [hkl]	Tens.(t) Comp.(c)	Yield Strength at ε_{in} =.0005mm/mm σ_y (MPa)	Predicted Strength (Eq.14) σ_{14} (MPa)
$\bar{2}$ 3 4	$\overline{48}$ 82 100	t	731	734
	$\overline{46}$ 79 100	t	738	734
	$\overline{45}$ 75 100	t	735	737
	$\overline{40}$ 66 100	c	749	754
	$\overline{43}$ 68 100	t	731	743
$\bar{1}$ 1 1	$\overline{78}$ 80 100	t	739	714
	$\overline{88}$ 100 100	t	746	740
	$\overline{89}$ 100 100	c	719	742
	$\overline{82}$ 86 100	t	746	719
	$\overline{87}$ 94 100	t	747	731

Table 5. Results of the LCF tests at 650°C.

Nom. Orient. [hkl]	Actual Orient. [hkl]	Sym.	Schmid Factor S	Total Strain $\Delta\varepsilon_t$ mm/mm	Cycle 1			Cycle .5 N_f			Fatigue Life N_f cycles
					Inelas. Strain $\Delta\varepsilon_{in}$ mm/mm	Max. Stress σ_{max} MPa	Min. Stress σ_{min} MPa	Inelas. Strain $\Delta\varepsilon_{in}$ mm/mm	Max. Stress σ_{max} MPa	Min. Stress σ_{min} MPa	
001	$\bar{5}$ 8 100	□	.436	.0145	.00026	798	798	.0002	825	782	1455
	$\bar{4}$ 5 100	⊟	.427	.0164	.00055	851	853	.00040	870	848	1228
	$\bar{2}$ 6 100	■	.433	.0179	.00200	900	860	.00093	974	911	215
$\bar{2}$ 5 20	$\bar{7}$ 22 100	◇	.478	.0142	.00033	848	818	.0002	855	816	872
	$\bar{8}$ 25 100	◑	.482	.0149	.00093	878	822	.00055	889	841	427
	$\overline{14}$ 30 100	◈	.487	.0146	.00152	846	805	.00082	879	829	237
	$\overline{19}$ 13 100	◆	.450	.0171	.00266	881	824	.00130	962	881	165
$\bar{3}$ 6 10	$\overline{19}$ 57 100	○	.493	.0092	.00128	758	784	.00069	764	807	1171
	$\overline{19}$ 58 100	◒	.492	.0097	.00170	743	777	.00087	789	827	971
	$\overline{32}$ 61 100	●	.472	.0105	.00249	775	793	.00123	856	889	180

Table 5.(cont).

					Cycle 1			Cycle .5 N_f			
Nom. Orient. [hkl]	Actual Orient. [hkl]	Sym.	Schmid Factor S	Total Strain $\Delta\varepsilon_t$ mm/mm	Inelas. Strain $\Delta\varepsilon_{in}$ mm/mm	Max Stress σ_{max} MPa	Min. Stress σ_{min} MPa	Inelas. Strain $\Delta\varepsilon_{in}$ mm/mm	Max. Stress σ_{max} MPa	Min. Stress σ_{min} MPa	Fatigue Life N_f cycles
011	$\bar{3}$ 94 100	◯	.426	.0089	.00035	830	897	.00025	851	884	1546
	$\bar{2}$ 86 100	◑	.441	.0092	.00059	854	894	.00038	861	916	824
	$\bar{2}$ 89 100	⊖	.435	.0105	.00150	841	930	.00080	887	967	862
	$\bar{4}$ 88 100	●	.439	.0115	.00289	816	896	.00111	917	1049	555
$\bar{2}$ 3 4	$\overline{42}$ 80 100	△	.475	.0074	.00082	741	755	.00034	784	818	2063
	$\overline{40}$ 66 100	◖	.470	.0077	.00119	738	747	.00040	795	834	1440
	$\overline{43}$ 68 100	⬠	.477	.0087	.00220	732	790	.00090	863	912	281
$\bar{1}$11	$\overline{75}$ 81 100	△	.497	.0063	.00089	739	732	.00023	810	821	1884
	$\overline{82}$ 86 100	▲	.493	.0072	.00164	747	744	.00056	867	889	1010
	$\overline{87}$ 94 100	▲	.485	.0080	.00249	749	771	.00111	917	956	338

Table 6. Glide Strain Values in Tensile and LCF Tests at 650°C.

Tensile	Nom. Orient. [hkl]	Actual Orient. [hkl]	Glide Strain γ_g mm/mm
Tensile	$\bar{2}$ 5 20	$\overline{14}$ 33 100	.065
	$\bar{3}$ 6 10	$\overline{21}$ 63 100	.077
	0 1 1	$\bar{1}$ 81 100	.069
	0 1 1	$\bar{3}$ 77 100	.055
	$\bar{2}$ 3 4	$\overline{33}$ 97 100	–
	$\bar{1}$ 1 1	$\overline{78}$ 82 100	–
LCF	$\bar{2}$ 5 20	$\bar{8}$ 25 100	.054
		$\overline{14}$ 30 100	.033
		$\overline{10}$ 13 100	.066
	$\bar{3}$ 6 10	$\overline{19}$ 57 100	.100
		$\overline{19}$ 58 100	.063
		$\overline{32}$ 61 100	.072
		$\overline{37}$ 66 100	.082
	0 1 1	$\bar{2}$ 89 100	.081
		$\bar{4}$ 88 100	.078
		$\bar{3}$ 97 100	.093

$$\overline{\gamma}_g = .071 \pm .017 \text{ mm/mm.}$$

Table 7. Results of the LCF tests performed at constant inelastic strain
range at 650°C.

| | | | | Cycle 1 | | | | Cycle .5 N_f | | | |
Nom. Orient. [hkl]	Actual Orient. [hkl]	Sym.	Schmid Factor S	Total Strain $\Delta\varepsilon_t$ * mm/mm	Inelas. Strain $\Delta\varepsilon_{in}$ mm/mm	Max. Stress σ_{max} MPa	Min. Stress σ_{min} MPa	Inelas. Strain $\Delta\varepsilon_{in}$ mm/mm	Max. Stress σ_{max} MPa	Min. Stress σ_{min} MPa	Fatigue Life N_f cycles
001	$\bar{3}$ 3 100	⊟	.419	.0191	.0010	893	865	.0010	1001	923	192
$\bar{3}$ 6 10	$\overline{37}$ 66 100	⊘	.458	.0108	.0010	760	792	.0010	826	906	723
011	$\bar{3}$ 97 100	⊘	.421	.0111	.0010	836	917	.0010	884	1032	577
$\bar{2}$ 3 4	$\overline{35}$ 83 100	△	.462	.0090	.0010	735	764	.0010	848	946	215
$\bar{1}$11	$\overline{73}$ 83 100	△	.496	.0079	.0010	745	730	.0010	879	948	413

* $\Delta\varepsilon_t$ at .5 N_f

Table 8. The Cyclic Stress-Strain Constants for LCF at 650°C.

Nom. Orient. [hkl]	Cyclic Strength Constant K' (MPa)	Cyclic Strain Hardening Coefficient m'
0 0 1	2091	.104
$\bar{2}$ 5 20	480	.021
$\bar{3}$ 6 10	514	.036
0 1 1	780	.091
$\bar{2}$ 3 4	951	.116
$\bar{1}$ 1 1	736	.071

Table 9. The tensile tests results at 1050°C.

Nom. Orient. [hkl]	Actual Orient. [hkl]	Sym.	Elastic Modulus E GPa	Yield Strength at $\varepsilon_{in}=.002$ mm/mm σ_y MPa	Ultimate Strength σ_u MPa	True Fracture Strain ε_{tf} mm/mm
001	$\bar{1}$ 4 100	■	78	393	603	.343
$\bar{2}$ 5 20	$\bar{1}\bar{7}$ 34 100	◆	97	429	623	.178
$\bar{3}$ 6 10	$\bar{3}\bar{2}$ 61 100	●	146	444	553	.141
011	$\bar{1}$ 91 100	⬬	152	469	579	.187
$\bar{2}$ 3 4	$\bar{3}\bar{5}$ 40 100	⬠	135	452	577	.116
$\bar{1}$11	$\bar{7}\bar{6}$ 90 100	▲	205	402	497	.228

Table 10. Initial Yield Strength Results at 1050°C.

Nom. Orient. [hkl]	Actual Orient. [hkl]	Tens.(t) Comp.(c)	Yield Strength .0005 Offset σ_y MPa
001	$\overline{10}$ 16 100	t	262
	$\overline{11}$ 13 100	t	279
	$\overline{1}$ 10 100	t	254
	$\overline{1}$ 15 100	t	277
	$\overline{1}$ 14 100	t	250
	$\overline{11}$ 14 100	c	308
	$\overline{5}$ 17 100	c	290
$\overline{2}$ 5 20	$\overline{12}$ 27 100	t	261
	$\overline{14}$ 29 100	t	272
	$\overline{13}$ 29 100	c	303
$\overline{1}$11	$\overline{68}$ 88 100	t	324
	$\overline{73}$ 83 100	t	315
	$\overline{75}$ 85 100	t	313
	$\overline{98}$ 100 100	t	319
	$\overline{74}$ 99 100	t	308
	$\overline{66}$ 85 100	t	301
	$\overline{93}$ 96 100	c	303
	$\overline{68}$ 86 100	c	301
	$\overline{77}$ 85 100	c	495

Table 10. (cont.)

Nom. Orient. [hkl]	Actual Orient. [hkl]	Tens.(t) Comp.(c)	Yield Strength .0005 Offset σ_y MPa
$\bar{2}$ 3 4	$\bar{3}\bar{6}$ 41 100	t	316
	$\bar{3}\bar{5}$ 40 100	t	325
	$\bar{3}\bar{3}$ 41 100	t	346
$\bar{3}$ 6 10	$\bar{3}\bar{5}$ 65 100	t	288
011	$\bar{1}$ 89 100	t	313
	$\bar{5}$ 99 100	t	319
	$\bar{1}$ 89 100	t	321
	$\bar{2}$ 90 100	t	291

Table 11. Results of the initial LCF tests at 1050°C.

| Nom. Orient. [hkl] | Actual Orient. [hkl] | Sym. | Cycle 1 | | | | Cycle .5 N_f | | | Fatigue Life |
			Total Strain $\Delta\varepsilon_t$	Inelas. Strain $\Delta\varepsilon_{in}$	Max. Stress σ_{max}	Min. Stress σ_{min}	Inelas. Strain $\Delta\varepsilon_{in}$	Max. Stress σ_{max}	Min. Stress σ_{min}	N_f
001	$\bar{8}$ 7 100	■	.0114	.00280	332	348	.00310	333	317	804
$\bar{1}$11	$\overline{74}$ 95 100	▲	.0053	.00261	303	301	.00274	301	285	750
$\bar{3}$ 6 10	$\overline{35}$ 64 100	●	.0076	.00305	321	328	.00295	316	309	374
011	$\bar{5}$ 99 100	⬬	.0076	.00270	362	378	.00270	365	364	191

Table 12. Results of the LCF tests of the [001] and [Ī1Ī] specimens at 1050°C.

Nom. Orient. [hkl]	Actual Orient. [hkl]	Sym.	Cycle 1				Cycle .5 N_f			Fatigue Life
			Total Strain $\Delta\varepsilon_t$ mm/mm	Inelas. Strain $\Delta\varepsilon_{in}$ mm/mm	Max. Stress σ_{max} MPa	Min. Stress σ_{min} MPa	Inelas. Strain $\Delta\varepsilon_{in}$ mm/mm	Max. Stress σ_{max} MPa	Min. Stress σ_{min} MPa	N_f cycles
001	Ī0 16 100 □		.00755	.00105	258	263	.00172	233	228	3878
	Ī1 14 100 ▬		.00980	.00185	315	333	.00240	288	282	1226
	8̄ 7 100 ■		.01140	.00280	332	348	.00310	333	317	804
Ī11	6̄3 88 100 △		.00340	.00090	311	296	.00125	276	254	2560
	6̄1 85 100 ▲		.00470	.00200	315	301	.00220	295	272	700
	7̄4 95 100 ▲		.00530	.00261	303	301	.00274	301	285	750

Table 13. The LCF cyclic stress-strain constants in tests at
1050°C, Equations 28 and 29.

Specimen Orient. [h k l]	Cyclic Strength Constant K' MPa	Cyclic Strain Hardening Coefficient m'
[001]	14486	.586
[$\bar{1}$11]	682	.128

Table 14. Results of the TEM analysis of unloaded PWA 1480 exposed 500 hours at 1050°C.

No. of dislocations analyzed	Proportion of dislocations on an interface with $\vec{b}$ in the interface plane		
	{010} and {111}	{010}	{111}
	% in (_) interfaces		
373	28 ± 38 (60)	9 ± 18 (44)	82 ± 25 (16)

Table 15. Results of the TEM analysis of the [001] specimens tested in LCF at 1050°C.

Inelastic Strain on Cycle 1 $\Delta\varepsilon_{in 1}$ (mm/mm)	No. Disl. Analyzed	Prop. of Disl. in a Region With an an Oct. Slip $\vec{b}$ % in (_) regions	Prop. of Disl. on an Interface With $\vec{b}$ in the Interface Plane		
			{010} and {111}	{010}	{111}
			% in (_) interfaces		
.00270	232	77 ± 12 (9)	66 ± 37 (45)	39 ± 33 (23)	95 ± 10 (22)
.00085	193	72 ± 14 (9)	66 ± 36 (43)	40 ± 36 (18)	85 ± 21 (25)
.00245*	239	62 ± 11 (9)	56 ± 36 (50)	38 ± 30 (33)	93 ± 12 (17)

* LCF test interrupted at 50 cycles.

Table 16. Results of the TEM analysis of the [$\bar{1}$11] specimens tested in LCF at 1050°C.

Inelastic Strain on Cycle 1 $\Delta\varepsilon_{in\ 1}$ (mm/mm)	No. Disl. Analyzed	Prop. of Disl. in a Region With an a Cube Slip $\vec{b}$ % in (_) regions	Prop. of Disl. on an Interface With $\vec{b}$ in the Interface Plane		
			{010} and {111}	{010}	{111}
			% in (_) interfaces		
.00280	399	50 ± 11 (9)	76 ± 39 (52)	47 ± 42 (24)	100 ± 0 (28)
.00090	309	72 ± 9 (9)	65 ± 44 (52)	31 ± 39 (21)	88 ± 31 (31)
.00275*	210	42 ± 31 (9)	72 ± 31 (40)	48 ± 28 (20)	94 ± 11 (20)

* LCF test interrupted at 50 cycles.

Table 17. Results of the tensile tests of [001] specimens at 1050°C with and without prior LCF cycling at 650°C.

Measured Orient. [hkl]	Symbol	Elastic Modulus E (GPa)	Yield Strength at ε_{in}=.002 mm/mm σ_y (MPa)	Ultimate Strength σ_u (MPa)	True Fracture Strain ε_{tf} (mm/mm)
$\bar{6}$ 10 100 p	▯	80	438	653	.254
$\bar{1}$ 9 100 c	▩	85	426	635	.170

p - with prior LCF; c - conventionally tested.

Table 18. Initial axial tensile yield strengths at 1050°C
of specimens with prior LCF cycling at 650°C.

Nom. Orient. [hkl]	Measured Orient. [hkl]	Yield Strength at ε_{in}=.0005 mm/mm σ_y (MPa)	Predicted Strength Equ. 21 σ_{21} (MPa)	Equ. 10 σ_{10} (MPa)
0 0 1	$\bar{5}$ 12 100	226	271	
	$\bar{3}$ 14 100	230	269	
$\bar{3}$ 6 10	$\overline{28}$ 59 100	279		275

Table 19. Results of LCF tests at 1050°C of specimens with and without prior LCF cycling at 650°C.

Nom. Orient. [hkl]	Measured Orient. [hkl]	Sym-bol	Cycle 1				Cycle .5 N_f			Fatigue Life
			Total Strain $\Delta\varepsilon_t$ mm/mm	Inelas. Strain $\Delta\varepsilon_{in}$ mm/mm	Max. Stress σ_{max} MPa	Min. Stress σ_{min} MPa	Inelas. Strain $\Delta\varepsilon_{in}$ mm/mm	Max. Stress σ_{max} MPa	Min. Stress σ_{min} MPa	N_f cycles
0 0 1	$\bar{5}$ 12 100 p	▯	.0110	.00275	293	341	.00305	303	299	776
	0 0 1 c	▮	.0114	.00280	332	348	.00310	333	317	804
$\bar{3}$ 6 10	$\bar{2}$8 59 100p	◑	.0072	.00240	326	329	.00255	320	307	450
	$\bar{3}\bar{5}$ 64 100c	●	.0076	.00305	321	328	.00295	316	309	374

p - with prior LCF; c - conventionally tested.

Table 20. Results of the TEM analysis of [001] specimens tested in LCF at 1050°C with and without prior LCF cycling at 650°C.

Inelastic Strain on Cycle 1 $\Delta\varepsilon_{in\ 1}$ (mm/mm)	No. Disl. Analyzed	Prop. of Disl. in a Region With an Oct. Slip $\vec{b}$ % in (_) regions	Prop. of Disl. on an Interface With $\vec{b}$ in the Interface Plane % in (_) interfaces		
			{010} and {111}	{010}	{111}
.00270 p	210	66 ± 13 (9)	60 ± 39 (53)	39 ± 36 (31)	92 ± 13 (22)
.00270 c	232	77 ± 12 (9)	66 ± 37 (45)	39 ± 33 (23)	95 ± 10 (22)

p - with prior LCF; c - conventional test

Table 21. Results of the tensile tests at 650°C of specimens with and without prior LCF cycling at 1050°C.

Nom. Orient. [hkl]	Measured Orient. [hkl]	Sym-bol	Elastic Modulus E (GPa)	Yield Strength at ε_{in}=.002 mm/mm σ_y (MPa)	Ultimate Strength σ_u (MPa)	True Fracture Strain ε_{tf} (mm/mm)
0 0 1	$\bar{1}$ 14 100p	▭	108	969	1007	.050
	$\bar{5}$ 7 100c	▪	107	922	1186	.075
0 1 1	$\bar{1}$ 89 100p	⬭	196	838	838	.250
	$\bar{1}$ 81 100c	⬮	184	841	983	.112

p - with prior LCF; c - conventionally tested.

Table 22. Initial axial yield strengths at 650°C of specimens with prior LCF cycling at 1050°C.

Nom. Orient. [hkl]	Measured Orient. [hkl]	Yield Strength at ε_{in}=.0005 mm/mm σ_y (MPa)	Predicted Strength Equ. 13 σ_{13} (MPa)
0 0 1	$\bar{1}$ 14 100	962 (t)	860
	$\bar{1}$ 15 100	791 (c)	797
	$\bar{1}$ 10 100	786 (c)	817
0 1 1	$\bar{1}$ 89 100	833 (t)	840
	$\bar{2}$ 90 100	1014 (c)	910

t - tension; c - compression.

Table 23. Results of the LCF tests at 650°C of specimens with and without prior LCF cycling at 1050°C.

Nom. Orient. [hkl]	Measured Orient. [hkl]	Sym-bol	Cycle 1				Cycle .5 N_f			Fatigue Life
			Total Strain ε_t mm/mm	Inelas. Strain ε_{in} mm/mm	Max. Stress σ_{max} MPa	Min. Stress σ_{min} MPa	Inelas. Strain ε_{in} mm/mm	Max. Stress σ_{max} MPa	Min. Stress σ_{min} MPa	N_f cycles
0 0 1	$\bar{1}$ 10 100p	⊞	.0173	.00124	971	813	.00046	995	829	55
	0 0 1 p	■	.0182	.00160	973	835	.00104	1031	846	44
	$\bar{1}$ 15 100p	⊞	.0191	.00326	978	819	.00198	1028	848	34
	$\bar{2}$ 6 100c	▦	.0179	.00200	900	860	.00093	974	911	215
0 1 1	$\bar{2}$ 90 100p	◯	.0118	.00282	823	1005	.00215	935	1144	28
	$\bar{4}$ 88 100c	◕	.0115	.00290	816	896	.00111	917	1049	555

p - with prior LCF; c - conventional test.

Table A1. Statistical analysis of the initial yield strength of the $[\bar{2}\ 5\ 20]$,

$[\bar{3}\ 6\ 10]$, [011], and [001] specimens at 650°C, Equ. 11: $1/\sigma_y = .00264\ S$ 1/MPa.

Analysis of Variance (ANOVA)

Due To	Degrees of Freedom (D.F.)	Sum of Squares (S.S.)	Mean Square (M.S.)=SS/DF
Regression	1	4.0997×10^{-5}	4.0997×10^{-5}
Residual	27	9.3969×10^{-8}	$s^2 = 3.4803 \times 10^{-9}$
Total	28	4.109×10^{-5}	

Coefficient	Standard Deviation (S.D.)	70% Confidence Interval (70% C.I.)
$1/\tau = .00264$	.000024	$.00261 < 1/\tau < .00267$

Table A2. Statistical analysis of the initial yield strength of the $[\bar{2}\ 5\ 20]$, $[\bar{3}\ 6\ 10]$, $[011]$, and $[001]$ specimens at 650°C, Equ. 13:   a. $1/\sigma_y = .00259\ S_1 + .00010\ S_2 - \delta\ .00017\ S_3$ 1/MPa.

ANOVA

Due to	D.F.	S.S.	M.S.
Regress.	3	4.104×10^{-5}	1.368×10^{-5}
Res.	25	5.339×10^{-8}	$s^2 = 2.135 \times 10^{-9}$
Total	28	4.109×10^{-5}	

Coeff.(C)	S.D.	t-ratio=C/S.D.	70% C.I.
.00259	.000048	53.77	.00254<C<.00264
.00010	.00008	1.22	-
-.00017	.00007	-2.46	-.00024<C<-.00010

   b. $1/\sigma_y = .00264\ S_1 - \delta\ .00023\ S_3$ 1/MPa.

ANOVA

Due to	D.F.	S.S.	M.S.
Regress.	2	4.103×10^{-5}	2.052×10^{-5}
Res.	26	5.658×10^{-8}	$s^2 = 2.176 \times 10^{-9}$
Total	28	4.109×10^{-5}	

Coeff.(C)	S.D.	t-ratio	70% C.I.
.00264	.000019	137.30	.00262<C<.00266
-.00023	.000055	-4.14	.000169<C<.000284

84

Table A3. Statistical analysis of the initial yield strength of the [$\bar{2}$ 3 4] and [$\bar{1}$11] specimens at 650°C, Equ. 14:

$$1/\sigma_y = .00282 \text{ S} \quad 1/\text{MPa}.$$

ANOVA

Due to	D.F.	S.S.	M.S.
Regress.	1	2.016×10^{-5}	2.016×10^{-5}
Res.	10	1.482×10^{-8}	$s^2 = 1.482 \times 10^{-9}$
Total	11	2.017×10^{-5}	

Coeff.	S.D.	70% C.I.
$1/\tau = .00282$	.0000242	$.00279 < 1/\tau < .00284$

Table A4. Statistical analysis of the cyclic inelastic strain response of the [$\bar{2}$ 5 20] specimens at 650°C.

a. [$\bar{8}$ 25 100]

1. Equ. 15:

$$\Delta\gamma_{in} = .001972 - 2.745 \times 10^{-5}N + 8.536 \times 10^{-8}N^2 - 4.322 \times 10^{-10}N^3$$
$$+ 6.544 \times 10^{-13}N^4 - .000236 \ln N \quad mm/mm.$$

ANOVA Due To	D.F.	S.S.	M.S.	
Regress.	5	.01581	3.162×10^{-3}	
Res.	19	4.576×10^{-4}	$s^2 = 2.408 \times 10^{-5}$	
Total	24	.01627		$R^2_{adj} = .964$

2. Equ. 16:

$$\gamma_c = .000946 + .00244N - 4.527 \times 10^{-6}N^2 + 2.597 10^{-8}N^3 - 4.312 \times 10^{-11}N^4$$
$$+ .00355 \ln N \quad mm/mm.$$

ANOVA Due To	D.F.	S.S.	M.S.	
Regress.	5	9125.74	1825.15	
Res.	19	.4600	$s^2 = .0240$	
Total	24	9126.2		$R^2_{adj} = 1.000$

3. At γ_c = .054 : S.D.($\Delta\gamma_{in}$)=.0016, S.D.(γ_c)=.0505 mm/mm.

b. [$\overline{14}$ 30 100]

1. Equ. 15 :

$$\Delta\gamma_{in} = .00322 - 5.248 \times 10^{-5}N + 8.133 \times 10^{-7}N^2 - 5.136 \times 10^{-9}N^3$$
$$+ 1.127 \times 10^{-11}N^4 - 8.182 \times 10^{-5} \ln N \quad mm/mm.$$

ANOVA Due To	D.F.	S.S.	M.S.	
Regress.	5	.06018	.01204	
Res.	16	1.472×10^{-3}	$s^2 = 9.199 \times 10^{-5}$	
Total	21	.06165		$R^2_{adj} = .969$

Table A4.b.(cont.)

2. Equ. 16:

$$\gamma_c = -6.16 \times 10^{-4} + .004762N - 2.115 \times 10^{-5}N^2 + 1.276 \times 10^{-7}N^3$$
$$- 2.747 \times 10^{-10}N^4 + .00540 \ln N \quad mm/mm.$$

ANOVA	Due To	D.F.	S.S.	M.S.
	Regress.	5	8879.01	1775.8
	Res.	16	.6820	$s^2 = .043$
	Total	21	8879.7	$R^2_{adj} = 1.000$

3. At $\gamma_c = .033$, S.D.$(\Delta\gamma_{in}) = 3.6 \times 10^{-5}$, S.D.$(\gamma_c) = .00074$ mm/mm.

c. $[\overline{10} \ 13 \ 100]$

1. Equ. 15:

$$\Delta\gamma_{in} = .00603 + 8.69 \times 10^{-6}N + 2.005 \times 10^{-7}N^2 - 2.559 \times 10^{-9}N^3$$
$$+ 8.379 10^{-12}N^4 - 9.387 \times 10^{-4} \ln N \quad mm/mm.$$

ANOVA	Due To	D.F.	S.S.	M.S.
	Regress.	5	.1715	.03429
	Res.	14	1.193×10^{-3}	$s^2 = 8.52 \times 10^{-5}$
	Total	19	.1727	$R^2_{adj} = .991$

2. Equ. 16:

$$\gamma_c = 4.94 \times 10^{-4} + 8.115 \times 10^{-3}N - 5.592 \times 10^{-5}N^2 + 5.343 \times 10^{-7}N^3$$
$$- 1.841 \times 10^{-9}N^4 + .00870 \ln N \quad mm/mm.$$

ANOVA	Due To	D.F.	S.S.	M.S.
	Regress.	5	12859.0	2571.8
	Res.	14	.930	$s^2 = .070$
	Total	19	12859.9	$R^2_{adj} = 1.000$

3. At $\gamma_c = .066$, S.D.$(\Delta\gamma_{in}) = 3.85 \times 10^{-5}$, S.D.$(\gamma_c) = .00107$ mm/mm.

Table A5. The cyclic inelastic strain response of the [$\overline{3}$ 6 10] specimens at 650°C.

a. [$\overline{19}$ 57 100]

1. Equ. 15:

$$\Delta\gamma_{in} = .00249 + 2.175 \times 10^{-6} N + 1.517 \times 10^{-9} N^2 - 7.69 \times 10^{-12} N^3$$
$$+ 5.109 \times 10^{-15} N^4 - .000303 \ln N \quad mm/mm.$$

ANOVA	Due To	D.F.	S.S.	M.S.
	Regress.	5	.02868	5.736×10^{-3}
	Res.	24	2.176×10^{-3}	$s^2 = 9.066 \times 10^{-5}$
	Total	29	.3086	$R^2_{adj} = .915$

2. Equ. 16:

$$\gamma_c = -.00574 + .00224 N + 2.368 \times 10^{-6} N^2 - 4.827 \times 10^{-9} N^3$$
$$+ 3.523 \times 10^{-12} N^4 + .001258 \ln N \quad mm/mm.$$

ANOVA	Due To	D.F.	S.S.	M.S.
	Regress.	5	162581.0	32516.2
	Res.	24	8.50	$s^2 = .40$
	Total	29	162589.5	$R^2_{adj} = 1.000$

3. At $\gamma_c = .010$, S.D.($\Delta\gamma_{in}$) = 2.7×10^{-5}, S.D.(γ_c) = .00169 mm/mm.

b. [$\overline{19}$ 58 100]

1. Equ. 15:

$$\Delta\gamma_{in} = .00409 - 1.794 \times 10^{-6} N + 1.95 \times 10^{-8} N^2 - 3.40 \times 10^{-11} N^3$$
$$+ 1.767 \times 10^{-14} N^4 - 4.946 \times 10^{-4} \ln N \quad mm/mm.$$

ANOVA	Due To	D.F.	S.S.	M.S.
	Regress.	5	.1389	.02778
	Res.	22	.01268	$s^2 = 5.765 \times 10^{-4}$
	Total	27	.1515	$R^2_{adj} = .897$

Table A5.b.(cont.)

2. Equ. 16:

$$\gamma_c = -.01268 + .003275N + 8.720 \times 10^{-7}N^2 - 1.80 \times 10^{-9}N^3$$
$$+ 1.235 \times 10^{-12}N^4 + .0248 \ln N \quad mm/mm.$$

ANOVA	Due To	D.F.	S.S.	M.S.
	Regress.	5	248758.7	49751.8
	Res.	22	45.8	$s^2 = 2.1$
	Total	27	248804.6	$R^2_{adj} = 1.000$

3. At $\gamma_c = .063$, S.D.$(\Delta\gamma_{in}) = 6.43 \times 10^{-5}$, S.D.$(\gamma_c) = .00387$ mm/mm.

c. [$\overline{32}$ 61 100]

1. Equ. 15:

$$\Delta\gamma_{in} = .00551 - 2.150 \times 10^{-4}N + 4.502 \times 10^{-6}N^2 - 4.073 \times 10^{-8}N^3$$
$$+ 1.269 \times 10^{-10}N^4 + 2.938 \times 10^{-4} \ln N \quad mm/mm.$$

ANOVA	Due To	D.F.	S.S.	M.S.
	Regress.	5	.2165	.04331
	Res.	14	3.313×10^{-3}	$s^2 = 2.366 \times 10^{-4}$
	Total	19	.2198	$R^2_{adj} = .98$

2. Equ. 16:

$$\gamma_c = 4.578 \times 10^{-4} + .009575N - 8.129 \times 10^{-5}N^2 + 6.965 \times 10^{-7}N^3$$
$$- 2.255 \times 10^{-9}N^4 + .004545 \ln N \quad mm/mm.$$

ANOVA	Due To	D.F.	S.S.	M.S.
	Regress.	5	9896.6	1979.3
	Res.	14	.200	$s^2 = .010$
	Total	19	9896.8	$R^2_{adj} = 1.000$

3. At $\gamma_c = .072$, S.D.$(\Delta\gamma_{in}) = 6.16 \times 10^{-5}$, S.D.$(\gamma_c) = 4.78 \times 10^{-4}$ mm/mm.

Table A5.(cont.)

   d. [$\overline{37}$ 66 100], constant inelastic strain range test.

    1. $\Delta\gamma_{in}$ = .01041 mm/mm, with S.D.$(\Delta\gamma_{in})$=9.8X10^{-5}.

    2. γ_c =-.001071+.00457N   mm/mm.

ANOVA	Due To	D.F.	S.S.	M.S.
	Regress.	1	70306.2	70306.2
	Res.	21	9.29	s^2=.440
	Total	22	70315.5	R^2_{adj}=1.000

    3. At γ_c = .082, S.D.$(\Delta\gamma_{in})$=9.8X10^{-5}, S.D.(γ_c)=.00169 mm/mm.

Table A6. The cyclic inelastic strain response of the [011] specimens at 650°C.

a. [$\bar{2}$ 89 100]

1. Equ. 15:

$$\Delta\gamma_{in} = .003934 - 8.15 \times 10^{-6}N + 8.93 \times 10^{-8}N^2 - 2.483 \times 10^{-10}N^3$$
$$+ 2.129 \times 10^{-13}N^4 - 4.63 \times 10^{-4} \ln N \quad \text{mm/mm.}$$

ANOVA	Due To	D.F.	S.S.	M.S.
	Regress.	5	.104	.02079
	Res.	19	.04033	$s^2 = 2.122 \times 10^{-3}$
	Total	24	.1443	$R^2_{adj} = .647$

2. Equ. 16:

$$\gamma_c = -.00135 + .00366N - 1.438 \times 10^{-6}N^2 + 4.147 \times 10^{-9}N^3$$
$$- 3.689 \times 10^{-12}N^4 + .0166 \ln N \quad \text{mm/mm.}$$

ANOVA	Due To	D.F.	S.S.	M.S.
	Regress.	5	70219.5	14043.9
	Res.	19	1.94	$s^2 = .100$
	Total	24	70221.4	$R^2_{adj} = 1.000$

3. At $\gamma_c = .081$, S.D.$(\Delta\gamma_{in}) = 1.445 \times 10^{-4}$, S.D.$(\gamma_c) = .0010$ mm/mm.

b. [$\bar{4}$ 88 100]

1. Equ. 15:

$$\Delta\gamma_{in} = .00688 - 1.491 \times 10^{-5}N + 2.117 \times 10^{-7}N^2 - 7.296 \times 10^{-10}$$
$$+ 7.561 \times 10^{-13}N^4 - 9.491 \times 10^{-4} \ln N \quad \text{mm/mm.}$$

ANOVA	Due To	D.F.	S.S.	M.S.
	Regress.	5	.368	.0736
	Res.	12	9.123×10^{-3}	$s^2 = 7.603 \times 10^{-4}$
	Total	17	.3771	$R^2_{adj} = .966$

Table A6.b.(cont.)

2. Equ. 16:

$$\gamma_c = .00196 + .00695N - 1.872 \times 10^{-5} N^2 + 6.708 \times 10^{-8} N^3$$

$$-7.688 \times 10^{-11} N^4 + .001901 \ln N \quad mm/mm.$$

ANOVA	Due To	D.F.	S.S.	M.S.
	Regress.	5	76808.4	15361.7
	Res.	11	3.42	$s^2 = .310$
	Total	16	76811.8	$R^2_{adj} = 1.000$

3. At $\gamma_c = .078$, S.D.$(\Delta\gamma_{in}) = 9.89 \times 10^{-5}$, S.D.$(\gamma_c) = .00212$ mm/mm.

c. [$\bar{3}$ 97 100] Constant inelastic strain test.

1. $\Delta\gamma_{in} = .001033$ mm/mm, with S.D.$(\Delta\gamma_{in}) = .000102$ mm/mm.

2. $\gamma_c = .001695 + .004539N$ mm/mm.

ANOVA	Due To	D.F.	S.S.	M.S.
	Regress.	1	72857.4	72857.4
	Res.	23	.020	$s^2 = 8.696 \times 10^{-4}$
	Total	24	72857.4	$R^2_{adj} = 1.000$

3. At $\gamma_c = .093$, S.D.$(\Delta\gamma_{in}) = .000102$, S.D.$(\gamma_c) = 6.5 \times 10^{-5}$ mm/mm.

Table A7. The cyclic inelastic strain response of a $[\bar{2}\ 3\ 4]$ specimen at 650°C.

  a. $[\overline{46}\ 79\ 100]$

   1. Equ. 15:

$$\Delta\gamma_{in} = .002635 + 7.994 \times 10^{-6}N - 1.728 \times 10^{-8}N^2 + 1.712 \times 10^{-11}N^3$$
$$- 5.985 \times 10^{-15}N^4 - 4.926 \times 10^{-4}\ln N \quad mm/mm.$$

ANOVA	Due To	D.F.	S.S.	M.S.
	Regress.	5	.05599	.01120
	Res.	20	.00050	$s^2 = 2.5 \times 10^{-5}$
	Total	25	.05650	$R^2_{adj} = .989$

   2. Equ. 16:

$$\gamma_c = .004776 + .00228N - 9.86 \times 10^{-7}N^2 + 1.496 \times 10^{-9}N^3$$
$$- 7.442 \times 10^{-13}N^4 + .00518\ln N \quad mm/mm.$$

ANOVA	Due To	D.F.	S.S.	M.S.
	Regress.	5	122706.8	24541.4
	Res.	20	11.900	$s^2 = 0.6$
	Total	25	122718.8	$R^2_{adj} = 1.000$

Table A8. The cyclic inelastic strain response of a $[\bar{1}11]$ specimen at 650°C.

a. $[\bar{82}\ 86\ 100]$

1. Equ. 15:

$$\Delta\gamma_{in} = .003384 + 7.133 \times 10^{-6} N - 2.152 \times 10^{-8} N^2 + 3.432 \times 10^{-11} N^3$$
$$- 2.004 \times 10^{-14} N^4 - 5.581 \times 10^{-4} \ln N \quad mm/mm.$$

ANOVA	Due To	D.F.	S.S.	M.S.
	Regress.	5	.08910	.01782
	Res.	13	2.955×10^{-4}	$s^2 = 2.273 \times 10^{-5}$
	Total	18	.08940	$R^2_{adj} = .995$

2. Equ. 16:

$$\gamma_c = .000116 + .003159 N - 3.117 \times 10^{-6} N^2 + 4.660 \times 10^{-9} N^3$$
$$- 2.489 \times 10^{-12} N^4 + .009245 \ln N \quad mm/mm.$$

ANOVA	Due To	D.F.	S.S.	M.S.
	Regress.	5	47337	9467
	Res.	13	.53	$s^2 = .04$
	Total	18	47337	$R^2_{adj} = 1.000$

Table A9. Statistical analysis of the LCF cyclic stress-strain response of the $[\bar{2}\ 5\ 20]$ specimens at 650°C, Equ. 20:

$$\Delta\tau/2 = 480(\Delta\gamma_{in}/2)^{.021} \ ; \ \ln(\Delta\tau/2) = 6.173 + .021\ \ln(\Delta\gamma_{in}/2).$$

ANOVA Due To	D.F.	S.S.	M.S.	
Regress.	1	.0008476	.0008676	
Res.	2	.0003856	s^2=.0001928	
Total	3	.001233		R^2_{adj}=.531

Coeff.	S.D.	70% C.I.
ln K'=6.1731	.07324	6.072<ln K'<6.275
m'=.0207	.00987	.007<m'<.034

Table A10. Statistical analysis of the LCF cyclic stress-strain response of the $[\bar{3}\ 6\ 10]$ specimens at 650°C, Equ. 20:

$$\Delta\tau/2 = 514(\Delta\gamma_{in}/2)^{.036} \ ; \ \ln(\Delta\tau/2) = 6.243 + .0362\ \ln(\Delta\gamma_{in}/2).$$

ANOVA Due To	D.F.	S.S.	M.S.	
Regress.	1	.005144	.005144	
Res.	2	.0007989	s^2=.0003995	
Total	3	.005943		R^2_{adj}=.798

Coeff.	S.D.	70% C.I.
ln K'=6.243	.07675	6.137<ln K'<6.349
m'=.036	.01009	.022<m'<.050

C-2

Table A11. Statistical analysis of the LCF cyclic stress-strain response of the [011] specimens at 650°C, Equ. 20:

$$\Delta\tau/2 = 780(\Delta\gamma_{in}/2)^{.091} \; ; \; \ln (\Delta\tau/2) = 6.659 + .0909 \ln (\Delta\gamma_{in}/2).$$

ANOVA Due To	D.F.	S.S.	M.S.	
Regress.	1	.011307	.011307	
Res.	2	.001115	s^2=.000558	
Total	3	.01243		R^2_{adj}=.865

Coeff.	S.D.	70% C.I.
ln K'=6.659	.1496	6.452<ln K'<6.866
m'=.091	.0202	.063<m'<.119

Table A12. Statistical analysis of the LCF cyclic stress-strain response of the [$\bar{2}$ 5 20], [$\bar{3}$ 6 10], and [011] specimens, Equ.20:

$$\Delta\tau/2 = 555(\Delta\gamma_{in}/2)^{.044} \; ; \; \ln (\Delta\tau/2) = 6.318 + .0438 \ln (\Delta\gamma_{in}/2).$$

ANOVA Due To	D.F.	S.S.	M.S.	
Regress	1	.014043	.014043	
Res.	10	.010761	s^2=.001076	
Total	11	.024804		R^2_{adj}=.523

Coeff.	S.D.	70% C.I.
ln K'=6.318	.0906	6.219<ln K'<6.417
m'=.044	.0121	.031<m'<.057

Table A13. Statistical analysis of the LCF cyclic stress-strain response of the $[\bar{2}\ 3\ 4]$ specimens at 650°C, Equ. 20:

$$\Delta\tau/2 = 951(\Delta\gamma_{in}/2)^{.116} \ ; \ \ln(\Delta\tau/2) = 6.858 + .116 \ln(\Delta\gamma_{in}/2).$$

ANOVA	Due To	D.F.	S.S.	M.S.
	Regress.	1	.00706	.00706
	Res.	1	.000111	s^2=.000111
	Total	2	.00717	R^2_{adj}=.969

Coeff.	S.D.	70% C.I.
ln K'=6.858	.1101	6.642<ln K'<7.074
m'=.116	.0146	.088<m'<.145

Table A14. Statistical analysis of the LCF cyclic stress-strain response of the $[\bar{1}11]$ specimens at 650°C, Equ. 20:

$$\Delta\tau/2 = 736(\Delta\gamma_{in}/2)^{.071} \ ; \ \ln(\Delta\tau/2) = 6.602 + .071 \ln(\Delta\gamma_{in}/2).$$

ANOVA	Due To	D.F.	S.S.	M.S.
	Regress.	1	.00654	.00654
	Res.	1	1.11×10^{-6}	s^2=1.11×10^{-6}
	Total	2	.00654	R^2_{adj}=1.000

Coeff.	S.D.	70% C.I.
ln K'=6.602	.0070	6.588<ln K'<6.616
m'=.071	.0009	.069<m'<.073

Table A15. Statistical analysis of the LCF cyclic stress-strain response of the [001] specimens at 650°C, Equ. 6:

$$\Delta\sigma/2 = 2091(\Delta\varepsilon_{in}/2)^{.104} \; ; \; \ln(\Delta\sigma/2) = 7.645 + .104\ln(\Delta\varepsilon_{in}/2).$$

ANOVA	Due To	D.F.	S.S.	M.S.	
	Regress.	1	.0128	.0128	
	Res.	1	1.78×10^{-5}	$s^2 = 1.78 \times 10^{-5}$	
	Total	2	.0128		$R^2_{adj} = .997$

Coeff.	S.D.	70% C.I.
$\ln K' = 7.645$	.0329	$7.581 < \ln K' < 7.710$
$m' = .104$	.0039	$.096 < m' < .112$

Table A16. Statistical analysis of the initial tensile yield strength at $\varepsilon_{in} = .0005$ mm/mm of the [001] and [$\bar{2}$ 5 20] specimens at 1050°C, Equ. 21: $1/\sigma_y = .00816$ S.

ANOVA	Due To	D.F.	S.S.	M.S.
	Regress.	1	9.986×10^{-5}	9.986×10^{-5}
	Res.	6	2.841×10^{-4}	$s^2 = 4.735 \times 10^{-8}$
	Total	7	1.001×10^{-4}	

Coeff.	S.D.	70% C.I.
$1/\tau = .00816$	.00018	$.00796 < 1/\tau < .00837$

Table A17. Statistical analysis of the initial compressive yield strength at ε_{in} = .0005 mm/mm of the [001] and [$\bar{2}$ 5 20] specimens at 1050°C, Equ. 22: $1/\sigma_y$ = .00711 S.

ANOVA	Due To	D.F.	S.S.	M.S.
	Regress.	1	3.328×10^{-5}	3.328×10^{-5}
	Res.	2	4.245×10^{-8}	$s^2 = 2.123 \times 10^{-8}$
	Total	3	3.332×10^{-5}	

Coeff.	S.D.	70% C.I.
$1/\tau = .00711$	.00018	$.00676 < 1/\tau < .00747$

Table A18. Statistical analysis of the initial yield strength at ε_{in} = .0005 mm/mm of the [$\bar{1}$11], [$\bar{2}$ 3 4], and [$\bar{3}$ 6 10] specimens at 1050°C, Equ. 23: $1/\sigma_y$ = .00680 S.

ANOVA	Due To	D.F.	S.S.	M.S.
	Regress.	1	1.331×10^{-4}	1.331×10^{-4}
	Res.	12	4.743×10^{-7}	$s^2 = 3.95 \times 10^{-8}$
	Total	13	1.335×10^{-4}	

Coeff.	S.D.	70% C.I.
$1/\tau = .00680$	.00012	$.00667 < 1/\tau < .00693$

Table A19. Statistical analysis of the initial yield strength at ε_{in} .0005 mm/mm of the [$\bar{1}11$] specimens at 1050°C, Equ. 24:

$$1/\sigma_y = .00659 \text{ S.}$$

ANOVA Due To	D.F.	S.S.	M.S.
Regress.	1	9.361×10^{-5}	9.361×10^{-5}
Res.	8	7.309×10^{-8}	$s^2 = 9.136 \times 10^{-9}$
Total	9	9.369×10^{-5}	

Coeff.	S.D.	70% C.I.
$1/\tau = .00659$	6.5×10^{-5}	$.00652 < 1/\tau < .00667$

Table A20. Statistical analysis of the initial yield strength at ε_{in} = .0005 mm/mm of the [$\bar{2}$ 3 4] specimens at 1050°C, Equ. 25:

$$1/\sigma_y = .00734 \text{ S.}$$

ANOVA Due To	D.F.	S.S.	M.S.
Regress.	1	2.781×10^{-5}	2.781×10^{-5}
Res.	2	2.435×10^{-8}	$s^2 = 1.217 \times 10^{-8}$
Total	3	2.783×10^{-5}	

Coeff.	S.D.	70% C.I.
$1/\tau = .00734$	$.000154$	$.00704 < 1/\tau < .00764$

Table A21. Statistical analysis on the octahedral slip system of the initial yield strength at ε_{in} = .0005 mm/mm of the [011] specimens at 1050°C, Equ. 26: $1/\sigma_y$ = .00757 S.

ANOVA	Due To	D.F.	S.S.	M.S.
	Regress.	1	4.149×10^{-5}	4.149×10^{-5}
	Res.	3	5.731×10^{-8}	$s^2 = 1.91 \times 10^{-8}$
	Total	4	4.155×10^{-5}	

Coeff.	S.D.	70% C.I.
$1/\tau = .00750$	.00016	$.00727 < 1/\tau < .00772$

Table A22. Statistical analysis on the cube slip system of the initial yield strength at ε_{in} = .0005 mm/mm of the [011] specimens at 1050°C, Equ. 27: $1/\sigma_y$ = .00894 S.

ANOVA	Due To	D.F.	S.S.	M.S.
	Regress.	1	4.146×10^{-5}	4.146×10^{-5}
	Res.	3	9.006×10^{-8}	$s^2 = 3.002 \times 10^{-8}$
	Total	4	4.155×10^{-5}	

Coeff.	S.D.	70% C.I.
$1/\tau = .00894$	.00025	$.00861 < 1/\tau < .00928$

Table A23. Statistical analysis of the LCF cyclic stress-strain response of the [001] specimens at 1050°C, Equ. 28:

$$\Delta\sigma/2 = 14486(\Delta\varepsilon_{in}/2)^{.586} \;;\; \ln(\Delta\sigma/2) = 9.581 + .586 \ln(\Delta\varepsilon_{in}/2).$$

ANOVA	Due To	D.F.	S.S.	M.S.
	Regress.	1	.05990	.05990
	Res.	1	.000213	$s^2 = .000213$
	Total	2	.06011	

Coeff.	S.D.	70% C.I.
$\ln K' = 9.581$	.2361	$9.117 < \ln K' < 10.044$
$m' = .586$	.0350	$.517 < m' < .655$

Table A24. Statistical analysis of the LCF cyclic stress-strain response of the [$\bar{1}11$] specimens at 1050°C, Equ. 29:

$$\Delta\sigma/2 = 682(\Delta\varepsilon_{in}/2)^{.128} \;;\; \ln(\Delta\sigma/2) = 6.525 + .128 \ln(\Delta\varepsilon_{in}/2).$$

ANOVA	Due To	D.F.	S.S.	M.S.
	Regress.	1	.00528	.00528
	Res.	1	4.983×10^{-6}	$s^2 = 4.983 \times 10^{-6}$
	Total	2	.00529	

Coeff.	S.D.	70% C.I.
$\ln K' = 6.525$	.02732	$6.471 < \ln K' < 6.578$
$m' = .128$	.0039	$.121 < m' < .136$

Table A25. Statistical analysis of the LCF cyclic stress-strain response of the [001] specimens at 650°C, subjected to prior LCF at 1050°C, Equ. 30:

$$\Delta\sigma/2 = 1082 \ (\Delta\varepsilon_{in}/2)^{.020} \ ; \ \ln \ (\Delta\sigma/2) = 6.985+.020 \ \ln \ (\Delta\varepsilon_{in}/2).$$

ANOVA	Due To	D.F.	S.S.	M.S.	
	Regress.	1	4.14×10^{-4}	4.14×10^{-4}	
	Res.	1	1.33×10^{-4}	$s^2 = 1.33 \times 10^{-4}$	
	Total	2	5.47×10^{-4}		$R^2_{adj} = .514$

Coeff.	S.D.	70% C.I.
$\ln$ K'=6.985	.0855	6.819<$\ln$ K'<7.151
m'=.020	.0112	.000<m'<.042

$$\delta = 2\ (\alpha_{\gamma'} - \alpha_{\gamma})/(\alpha_{\gamma'} + \alpha_{\gamma})$$
$$|p| = (\alpha_{\gamma'}\ \alpha_{\gamma})/(\alpha_{\gamma} -\ \alpha_{\gamma'})$$
$$p = |\bar{b}|/|\delta|$$

COHERENT γ - γ' INTERFACE   SEMI-COHERENT γ - γ' INTERFACE
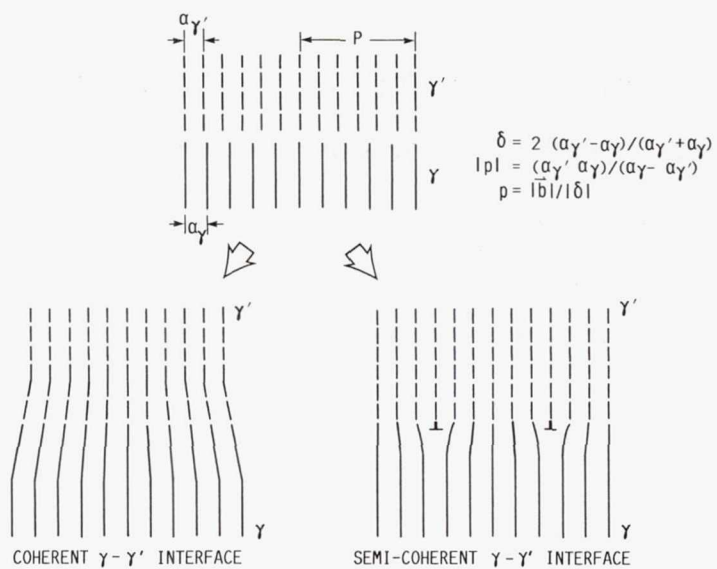
FIGURE 1. - SCHEMATIC DEPICTIONS OF INTERFACES.

CD-87-29798
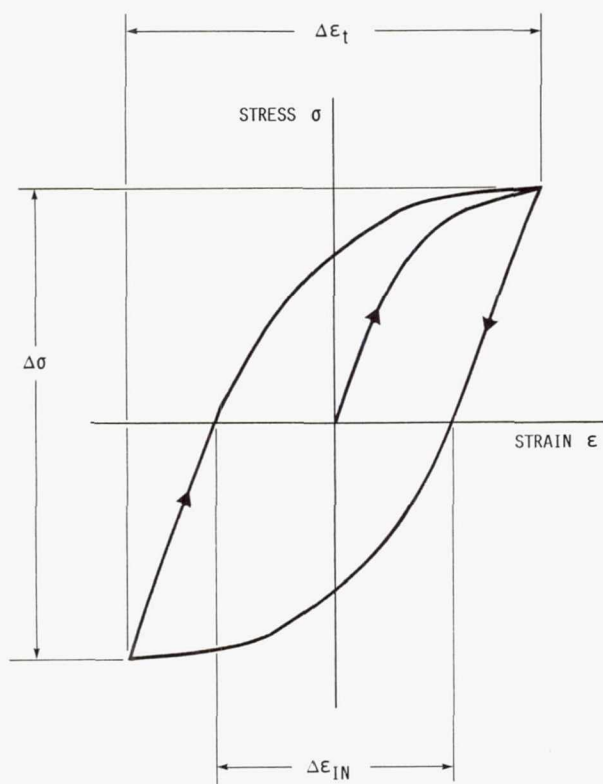
FIGURE 2. - A LOW CYCLE FATIGUE (LCF) TEST HYSTERESIS LOOP.

STRESS RESPONSE   HYSTERESIS LOOP RESPONSE

CYCLIC
HARDENING

CYCLIC
SOFTENING

CYCLE 1
CYCLE 150
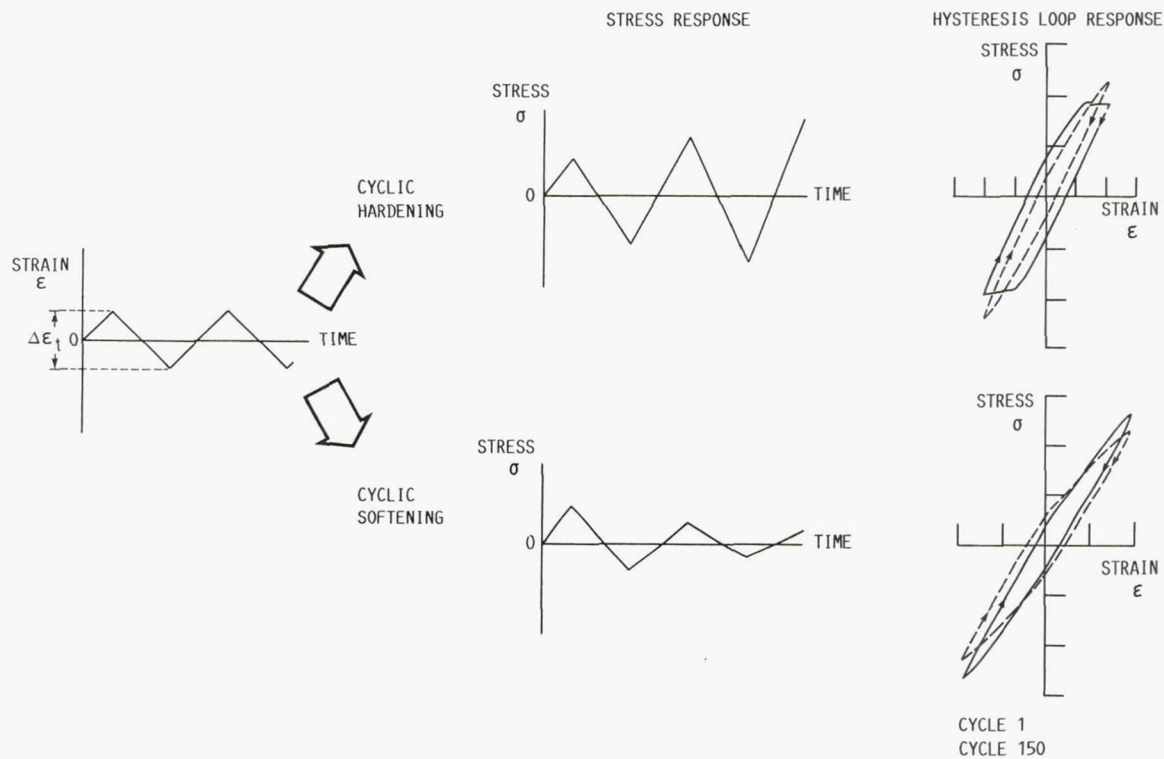
FIGURE 3. - CYCLIC HARDENING AND SOFTENING IN AN LCF TEST.

$\{111\}$
INTERFACES

$\{001\}$
INTERFACES

(111) PLANE: $\vec{b}_1 = \frac{1}{2}[\bar{1}10]$

$\vec{b}_2 = \frac{1}{2}[0\bar{1}1]$

$\vec{b}_3 = \frac{1}{2}[\bar{1}01]$

(011) PLANE: $\vec{b}_1 = \frac{1}{2}[\bar{1}10]$

$\vec{b}_2 = \frac{1}{2}[110]$
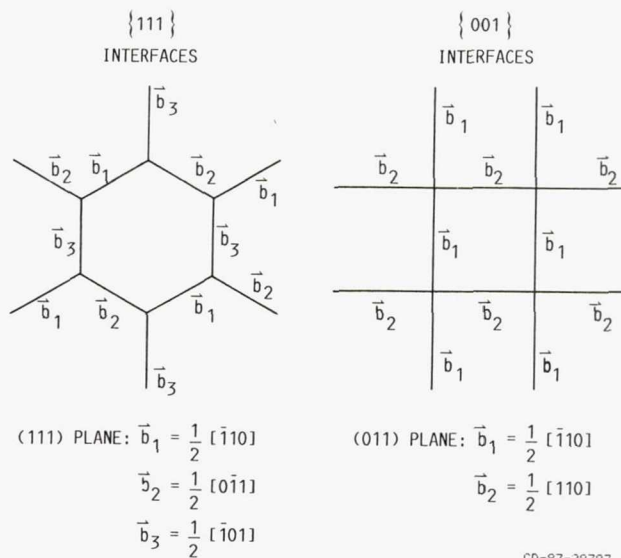
CD-87-29797

FIGURE 4. - SCHEMATIC DEPICTIONS OF MISFIT DISLOCATION NETWORKS.
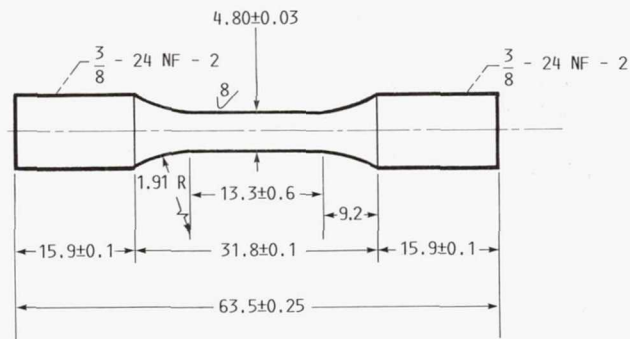
FIGURE 5. - THE LCF AND TENSILE TEST SPECIMENS' CONFIGURATION.
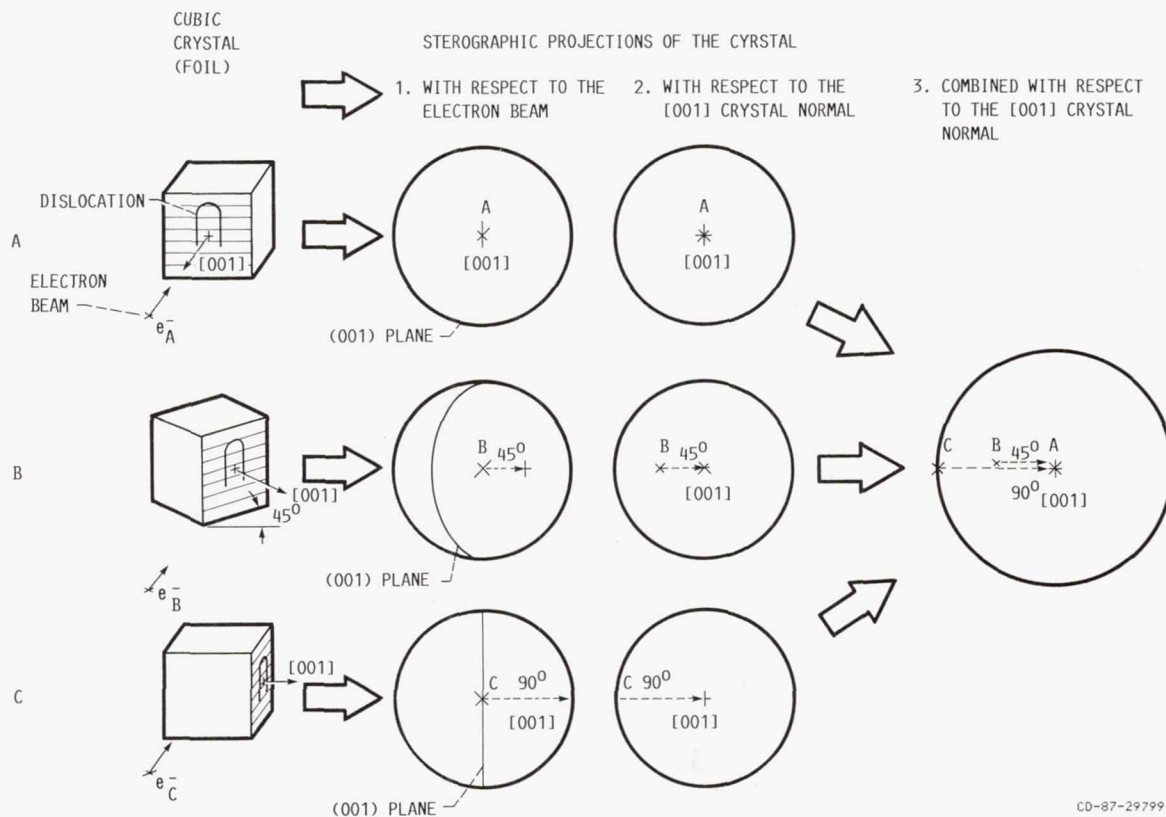
FIGURE 6. - A SCHEMATIC ILLUSTRATION OF TILTING EXPERIMENTS IN TRANSMISSION ELECTRON MICROSCOPY.
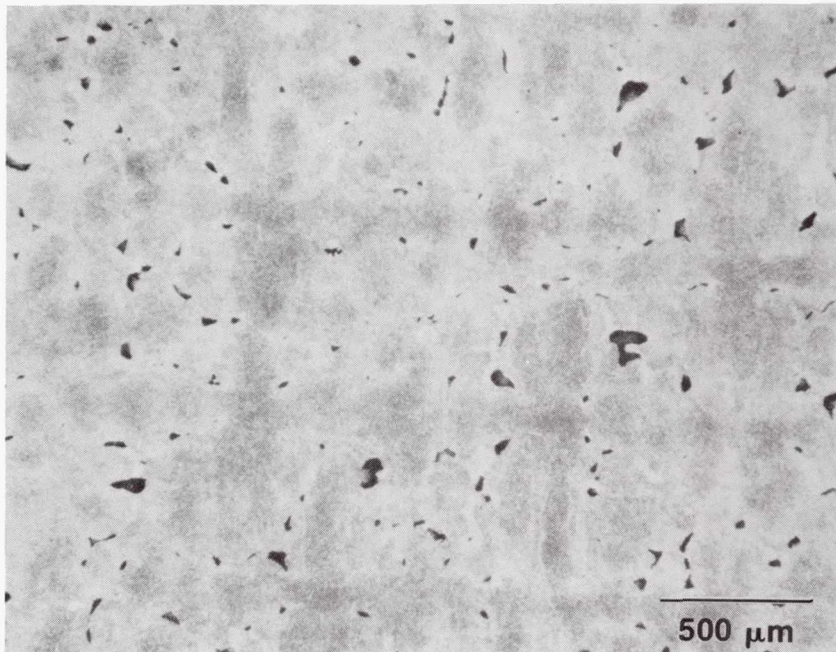
FIGURE 7. - MACROSTRUCTURE OF THE PWA 1480 SINGLE CRYSTAL SLABS.
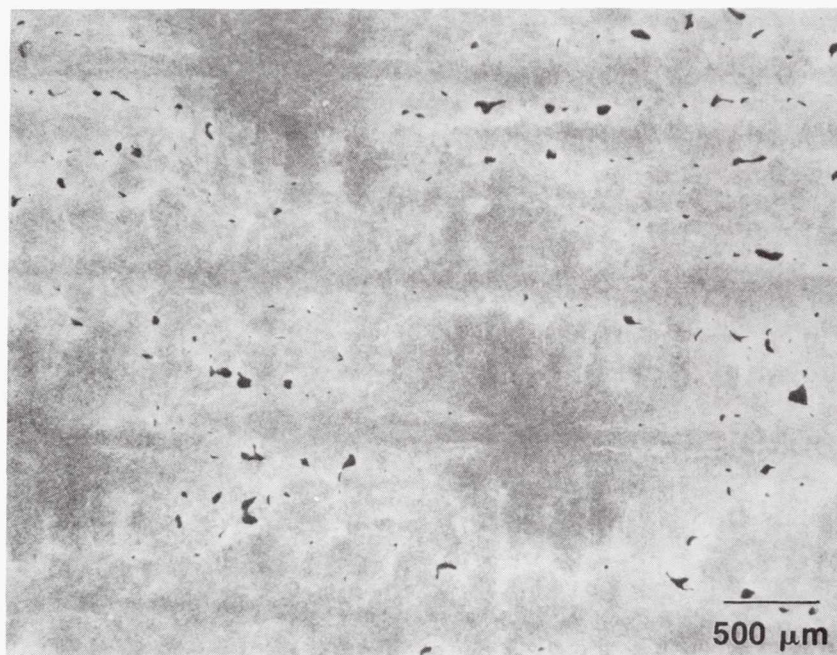
FIGURE 8. - MACROSTRUCTURE OF THE PWA 1480 SINGLE CRYSTAL BARS.

107
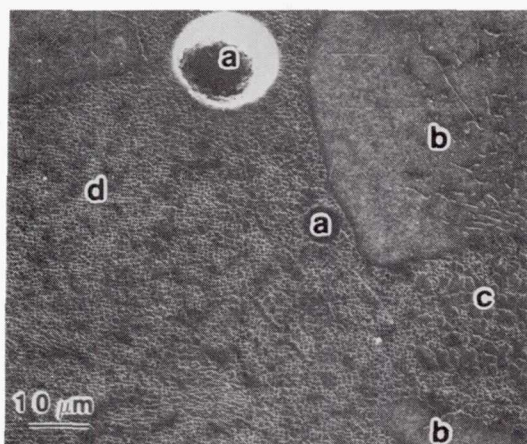
FIGURE 9. – THE VARIOUS PRIMARY MICROSTRUCTURAL FEATURES OF THE TEST MATERIAL. A: MICROPORES; B: γ-γ' EUTECTIC POOLS; C: LARGE γ' PRECIPITATES ASSOCIATED WITH THE EUTECTIC POOLS; D: CUBOIDAL γ' PRECIPITATES.
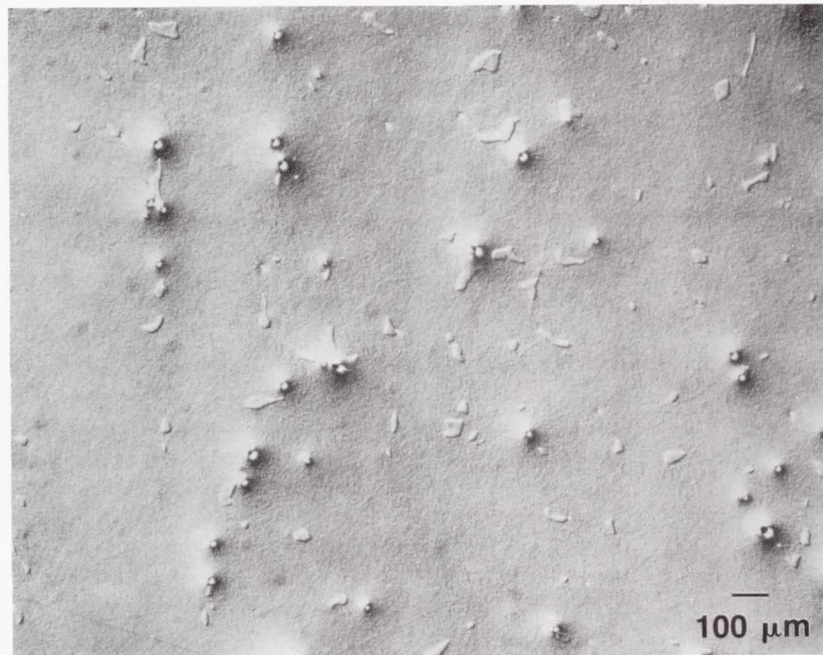
(A) NEAR A DENDRITE CORE, SINGLE CRYSTAL BAR.
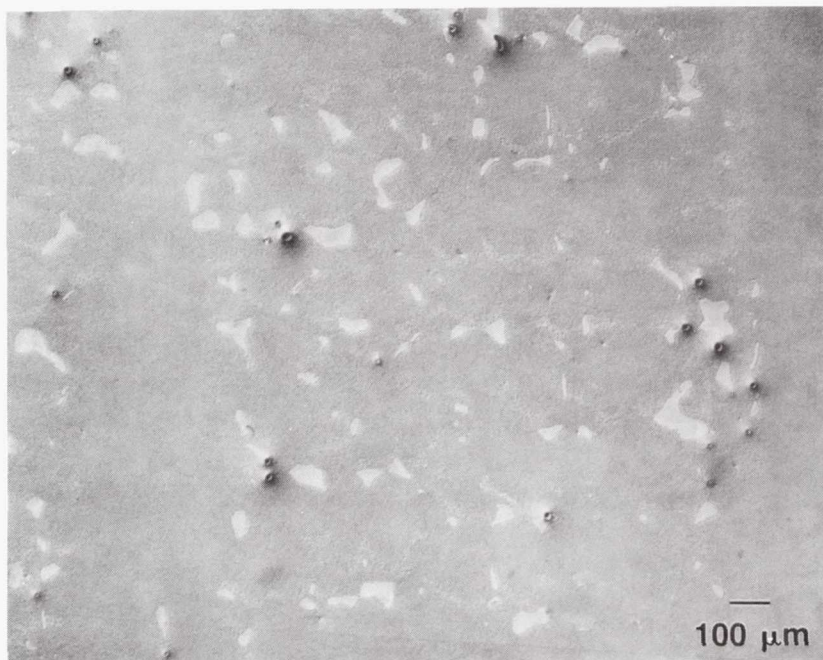
(B) IN AN INTERDENDRITIC REGION, A SINGLE CRYSTAL SLAB.

FIGURE 10. - THE $\gamma-\gamma'$ EUTECTIC POOLS IN THE TEST MATERIAL.
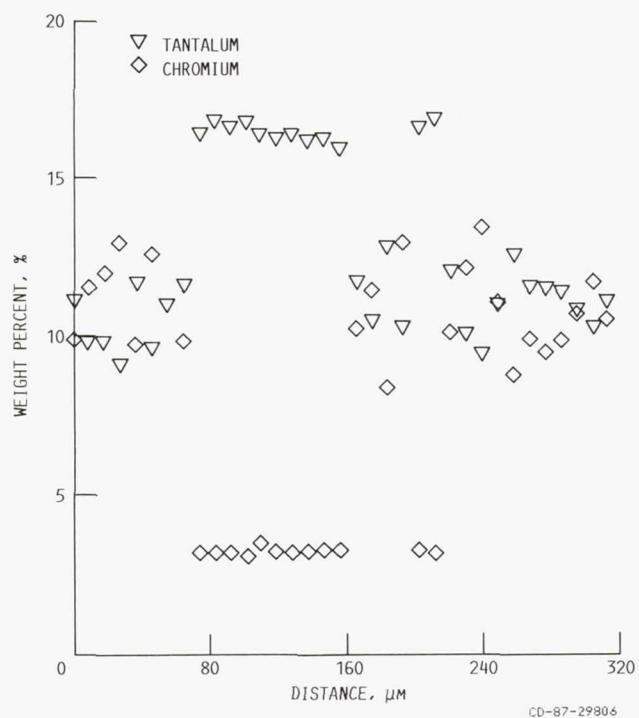
FIGURE 11. - MICROPROBE MEASUREMENTS OF THE CHROMIUM AND TANTALUM LEVELS IN THE γ-γ′ EUTECTIC POOLS.

110
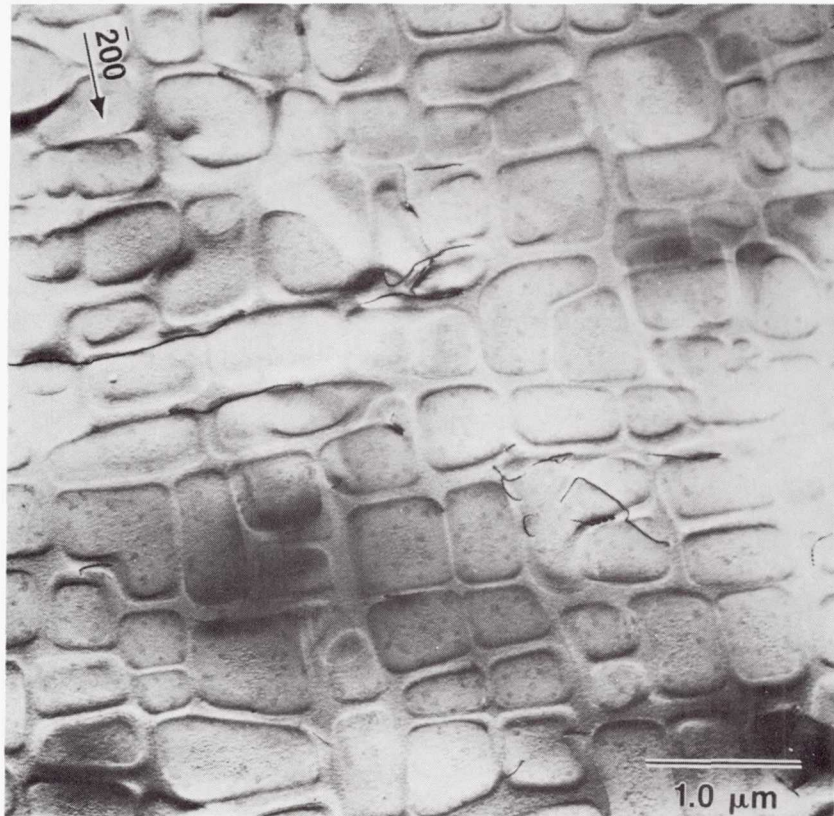
FIGURE 12. - TYPICAL MICROGRAPH OF THE TEST MATERIAL MICROSTRUCTURE, [001] ZONE AXIS
(Z.A.).
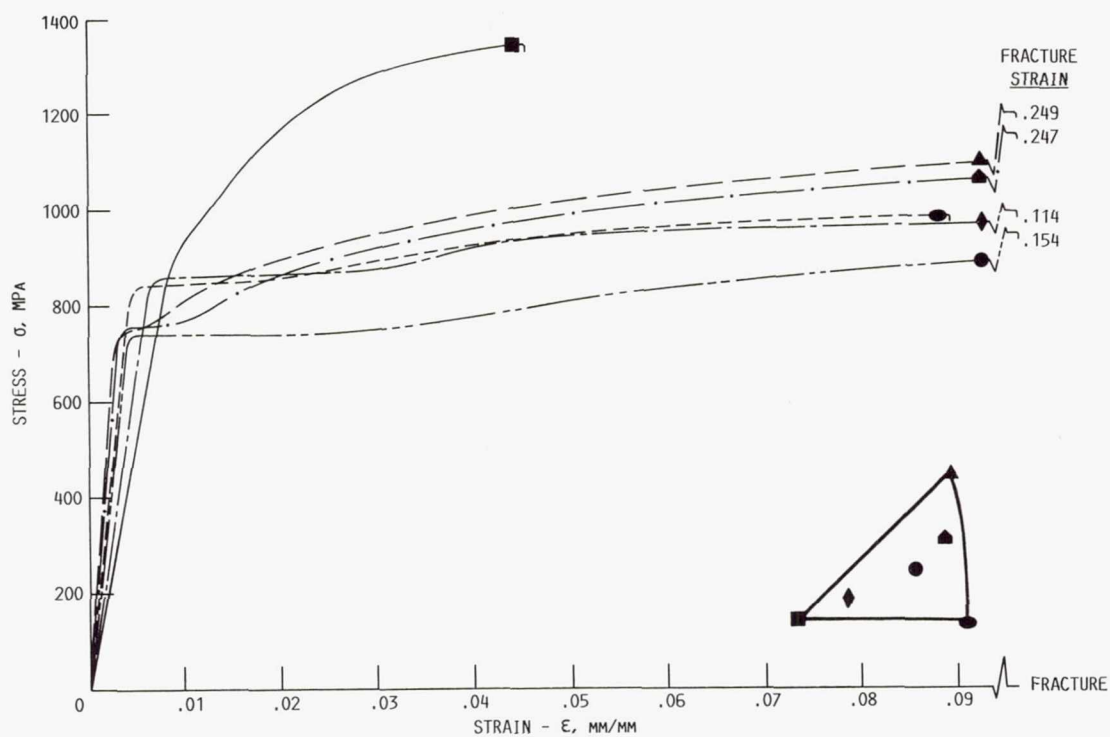
FIGURE 13. - THE AXIAL STRESS-STRAIN CURVES OF THE TENSILE TESTS AT 650 $^{\circ}$C.
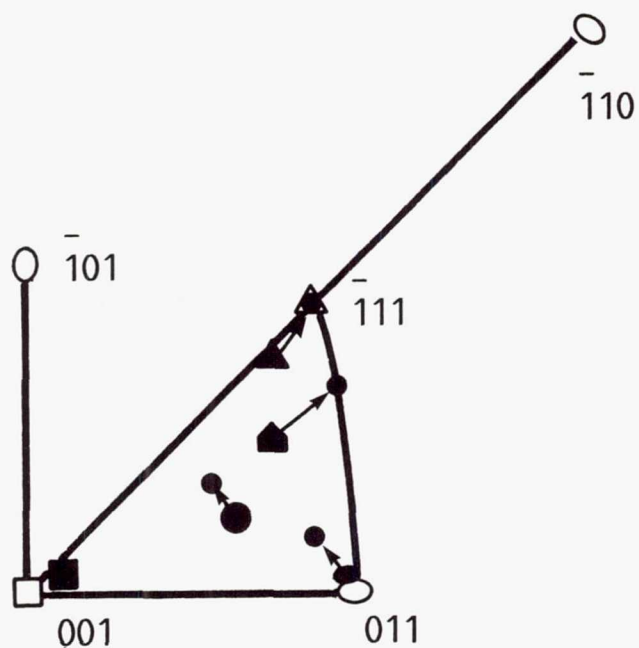
FIGURE 14. - CRYSTALLOGRAPHIC
ROTATIONS OF THE SPECIMEN
AXES IN THE TENSILE TESTS
AT 650 $^{\circ}$C.
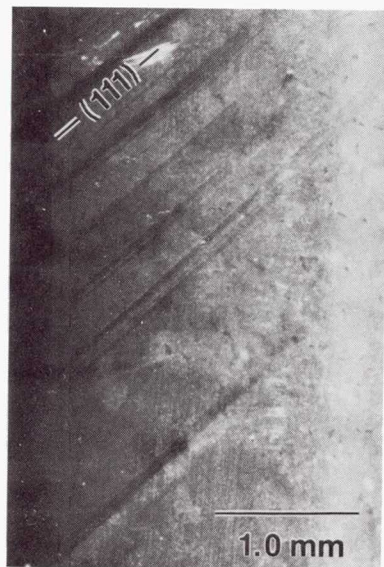
(A) [$\bar{3}$ 6 10] LCF SPECIMEN, $\Delta\varepsilon_{IN.}$
< .0010 MM/MM ON CYCLE 1.
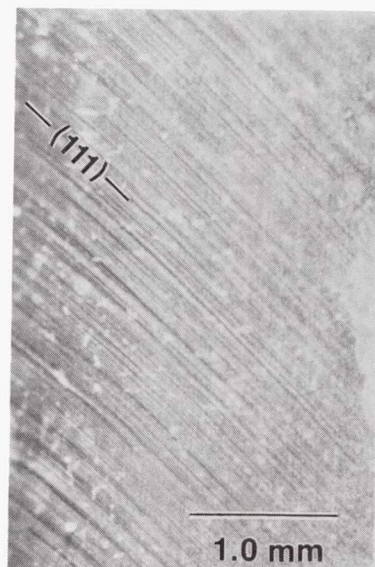
(B) [3 6 10] LCF SPECIMEN, $\Delta\varepsilon_{IN.}$
= .0017 MM/MM ON CYCLE 1.
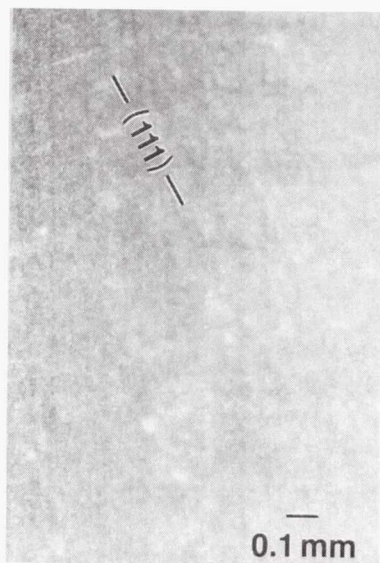
(C) [001] LCF SPECIMEN, $\Delta\varepsilon_{IN.}$
= .0020 MM/MM ON CYCLE 1.
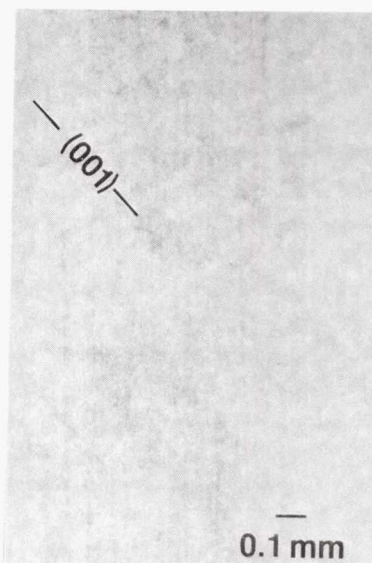
(D) [$\bar{1}$11] LCF SPECIMEN, $\Delta\varepsilon_{IN.}$
= .0017 MM/MM ON CYCLE 1.

FIGURE 15. - SLIP OFFSETS OF THE LCF TEST SPECIMENS AT 650 °C.

113
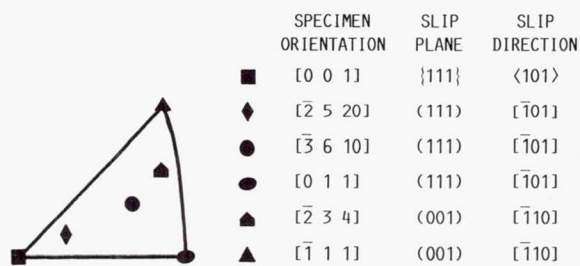
FIGURE 16. – THE OEPRATIVE SLIP SYSTEMS IN TESTS AT 650 °C.
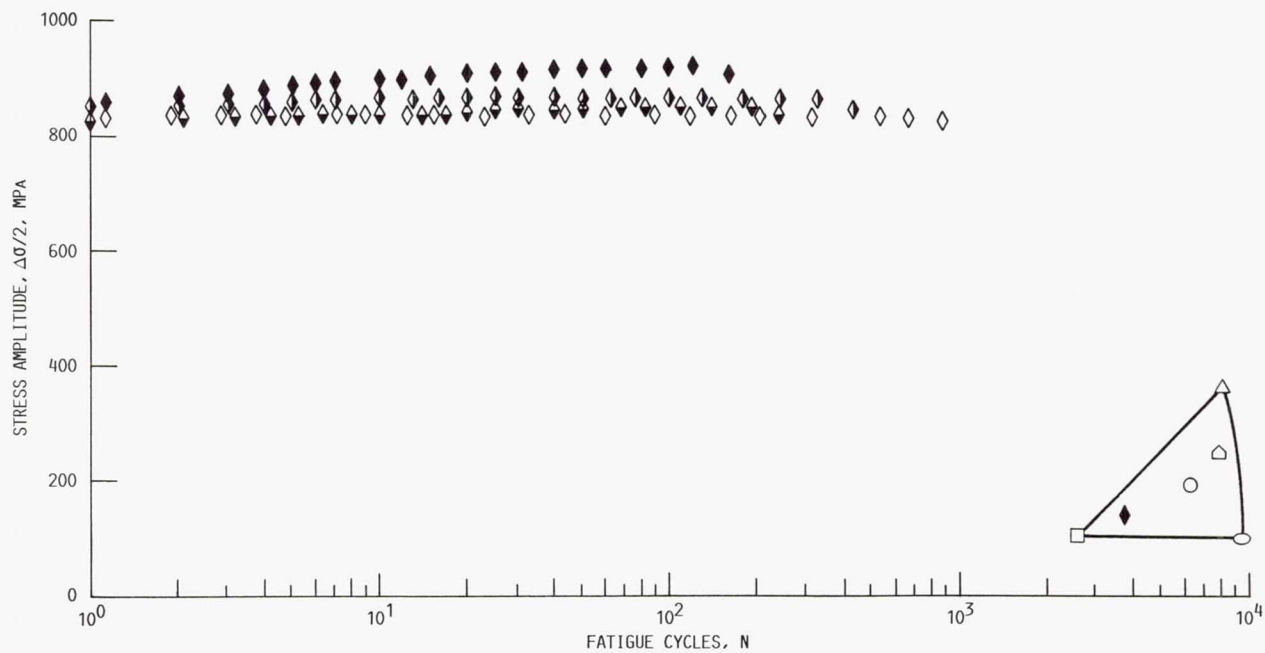
FIGURE 17. – THE LCF STRESS HARDENING RESPONSE OF THE [$\bar{2}$ 5 20] SPECIMENS AT 650 °C.
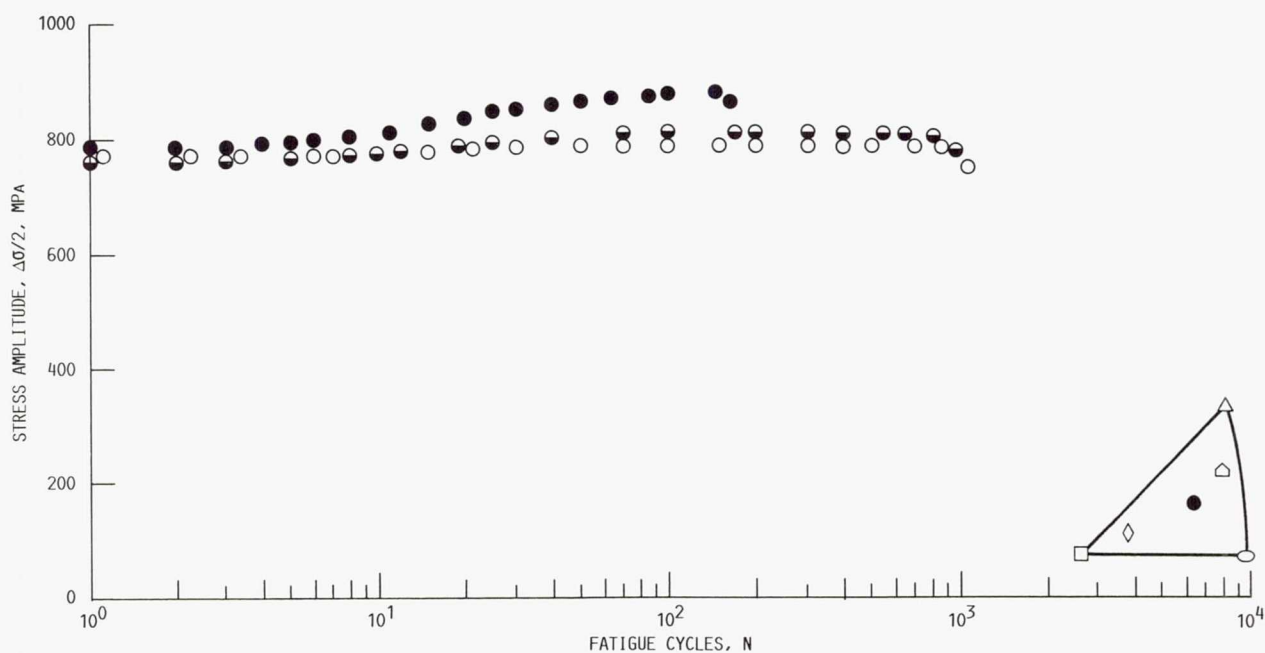
FIGURE 18. – THE LCF STRESS HARDENING RESPONSE OF THE [$\bar{3}$ 6 10] SPECIMENS AT 650 °C.

114
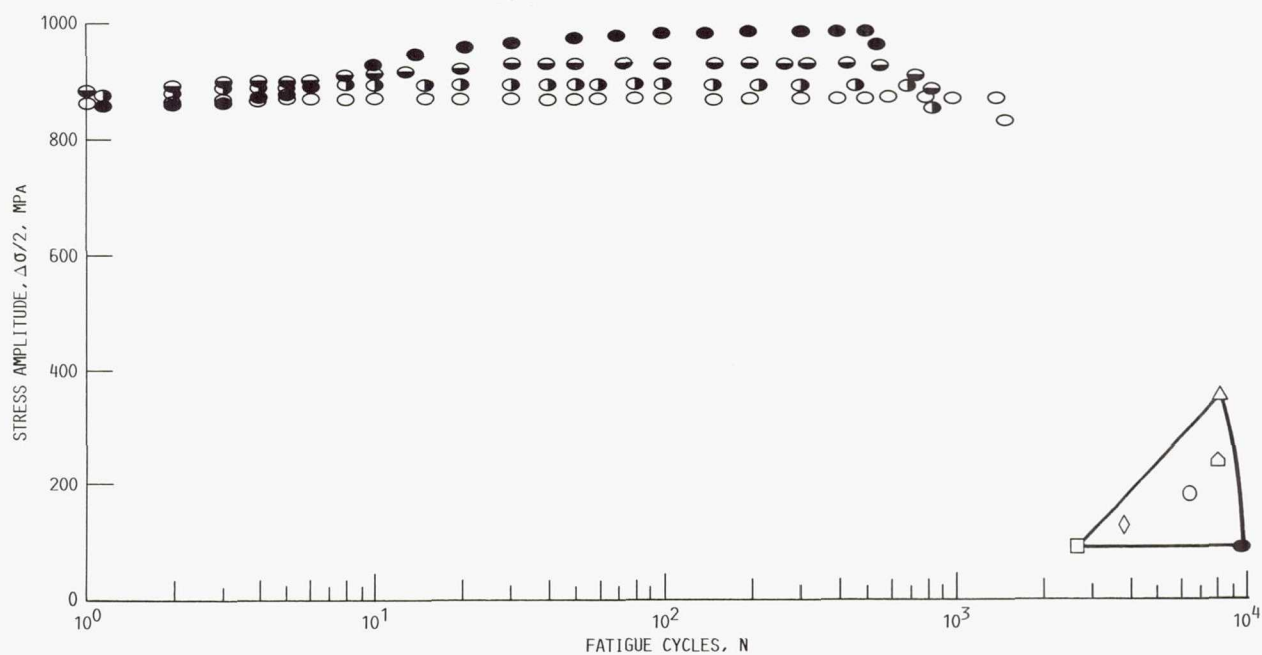
FIGURE 19. – THE LCF STRESS HARDENING RESPONSE OF THE [011] SPECIMENS AT 650 °C.
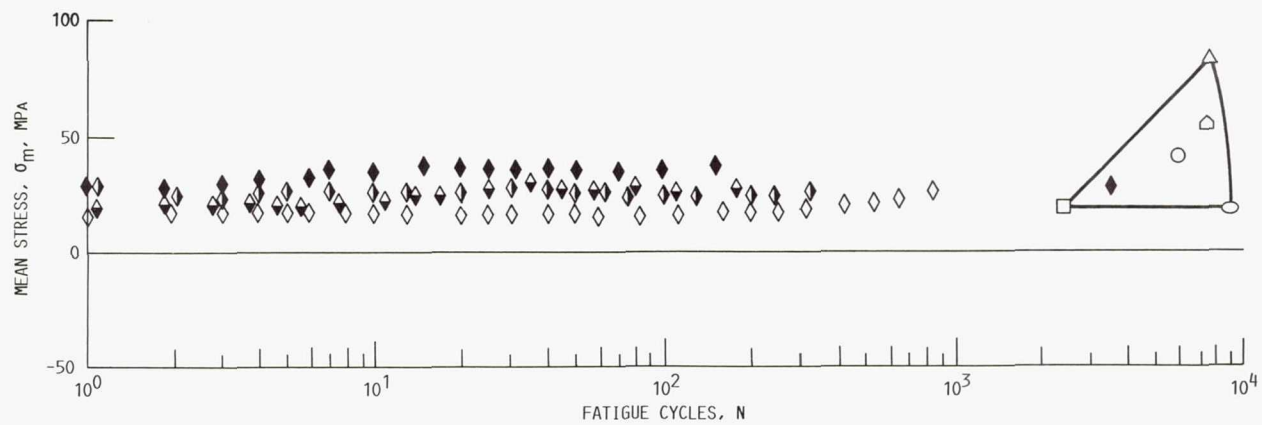
FIGURE 20. – THE LCF MEAN STRESS RESPONSE OF THE [$\bar{2}$ 5 20] SPECIMENS AT 650 °C.
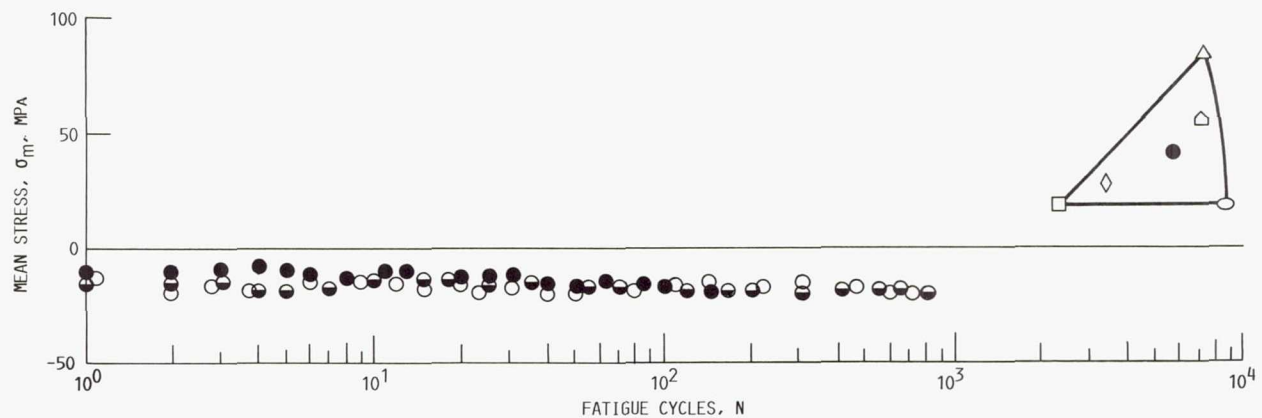
FIGURE 21. – THE LCF MEAN STRESS RESPONSE OF THE [$\bar{3}$ 6 10] SPECIMENS AT 650 °C.

115
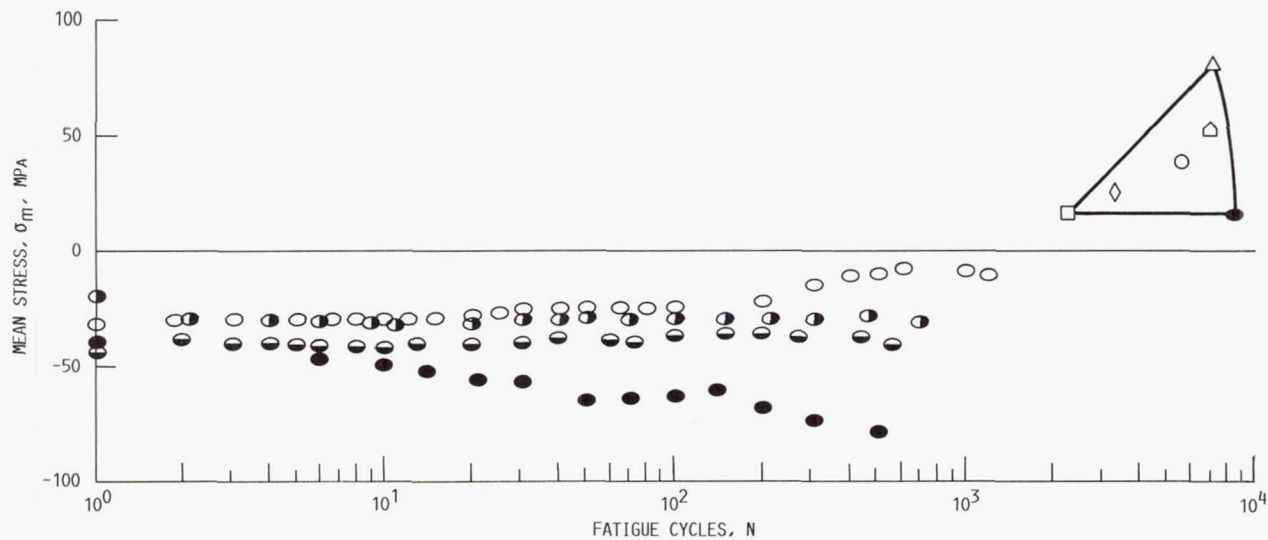
FIGURE 22. - THE LCF MEAN STRESS RESPONSE OF THE [011] SPECIMENS AT 650 °C.
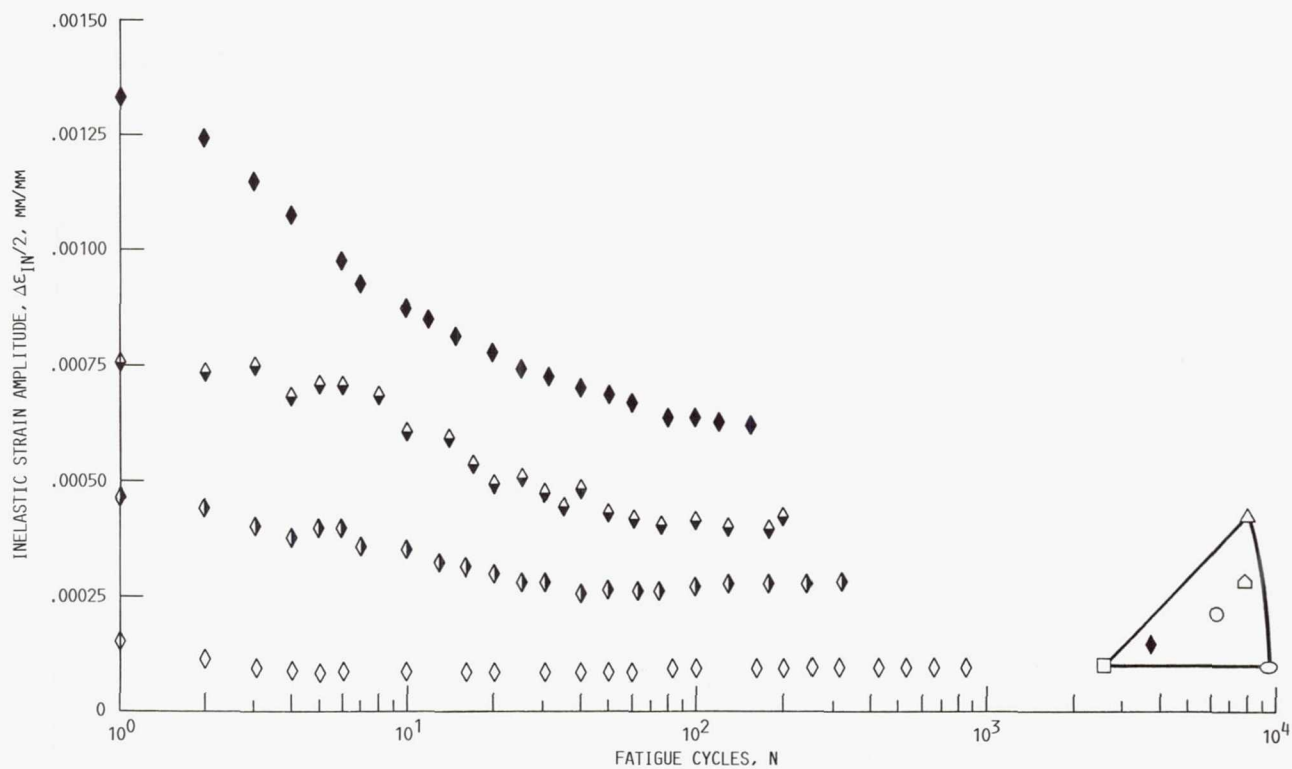
FIGURE 23. - THE LCF INELASTIC STRAIN RESPONSE OF THE [$\bar{2}$ 5 20] SPECIMENS AT 650 °C.

116
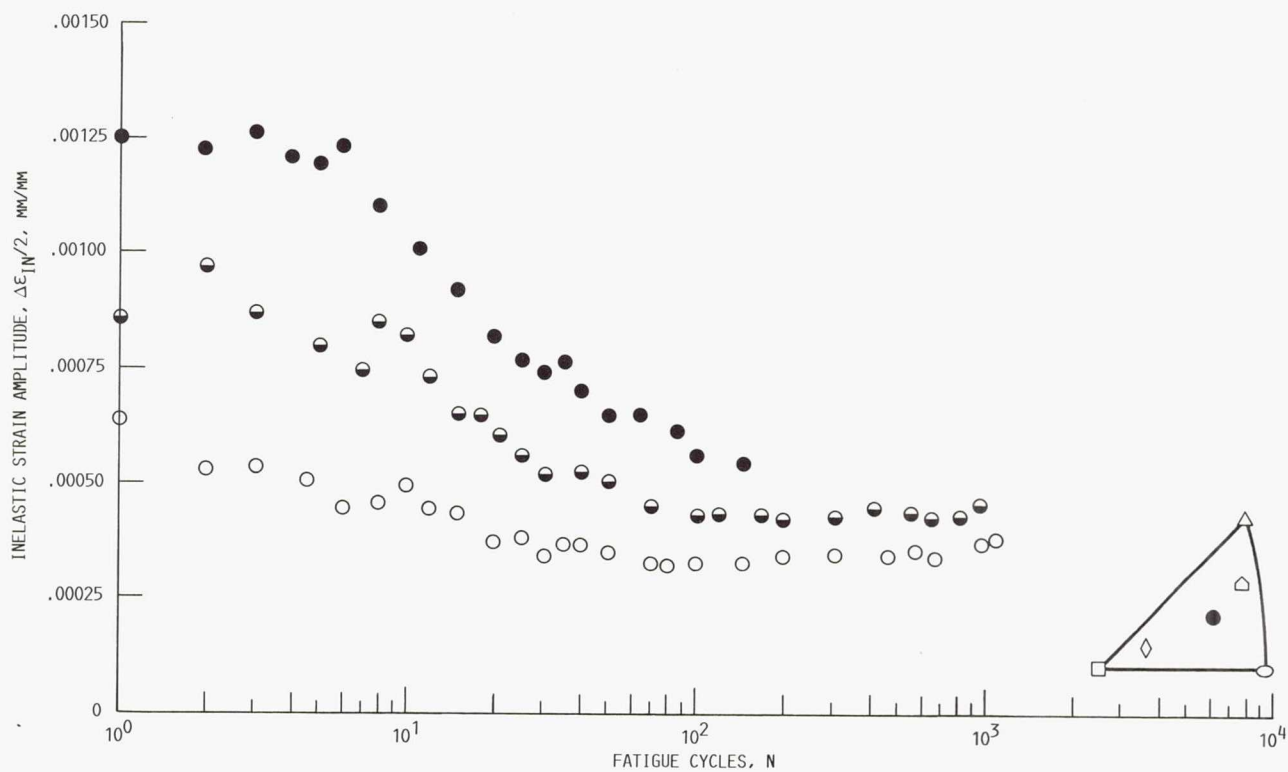
FIGURE 24. – THE LCF INELASTIC STRAIN RESPONSE OF THE [$\bar{3}$ 6 10] SPECIMENS AT 650 ^{o}C.
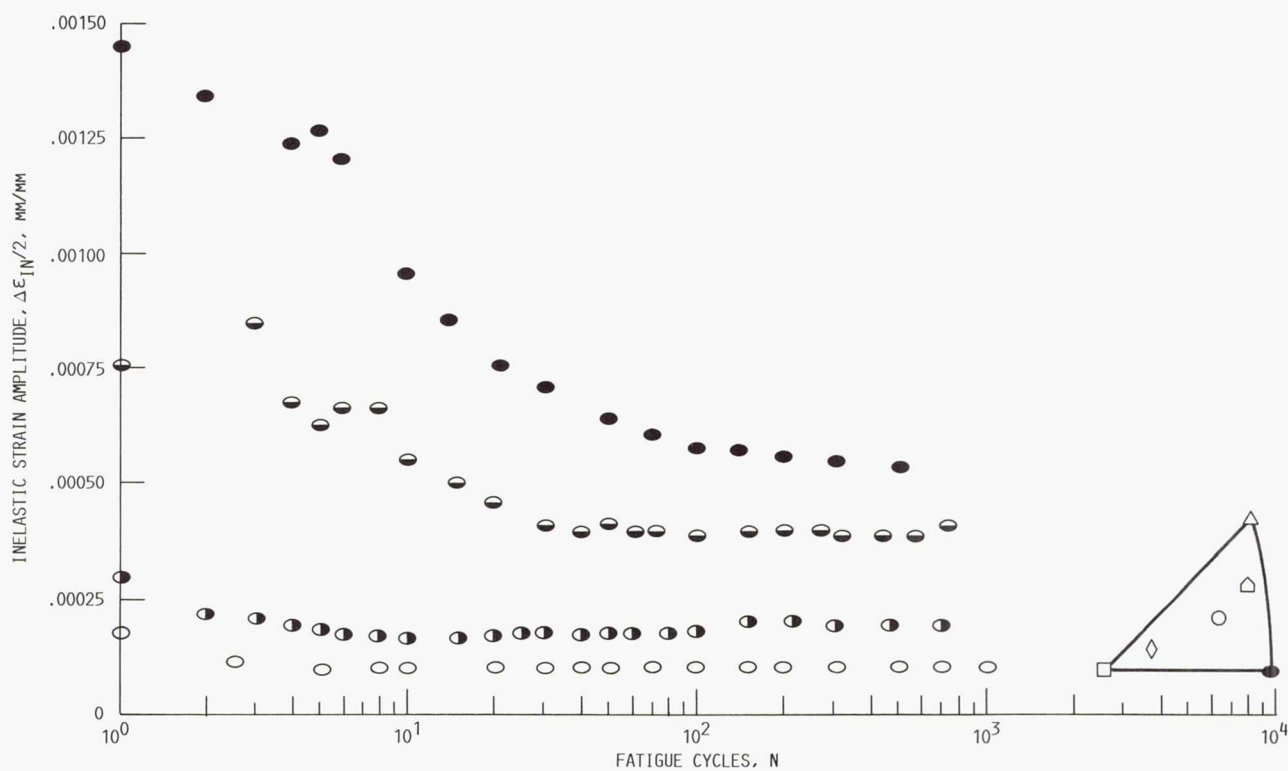
FIGURE 25. – THE LCF INELASTIC STRAIN RESPONSE OF THE [011] SPECIMENS AT 650 ^{o}C.

117
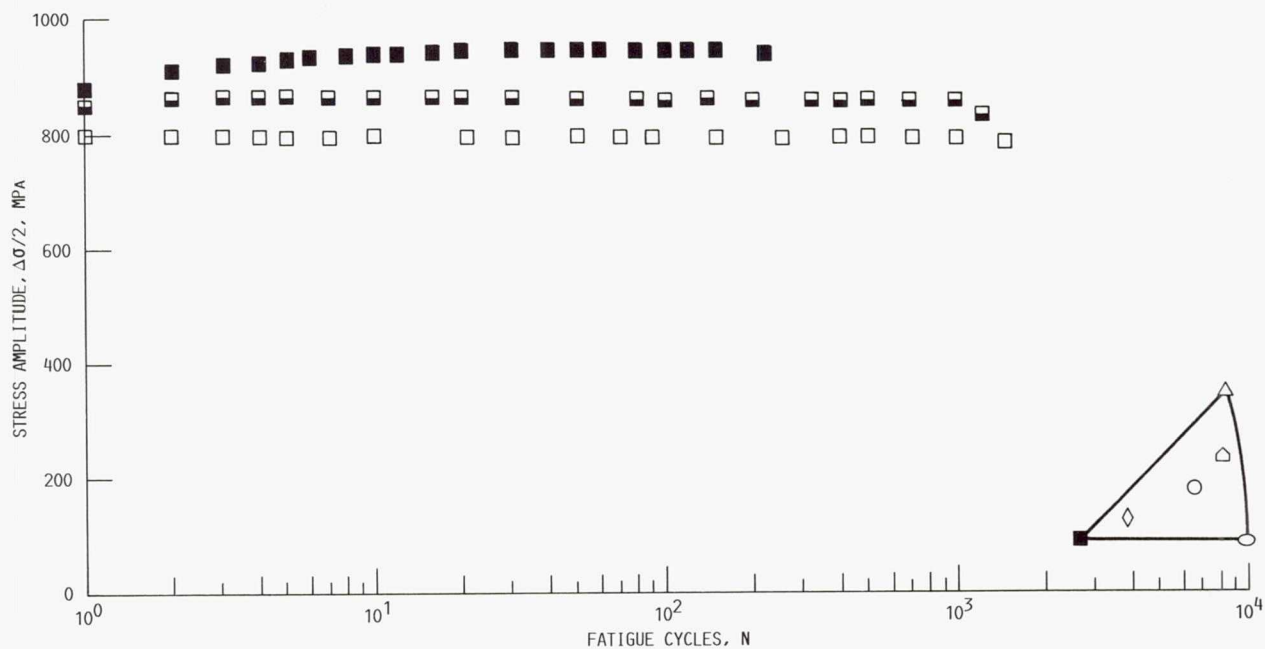
FIGURE 26. – THE LCF STRESS HARDENING RESPONSE OF THE [001] SPECIMENS AT 650 °C.
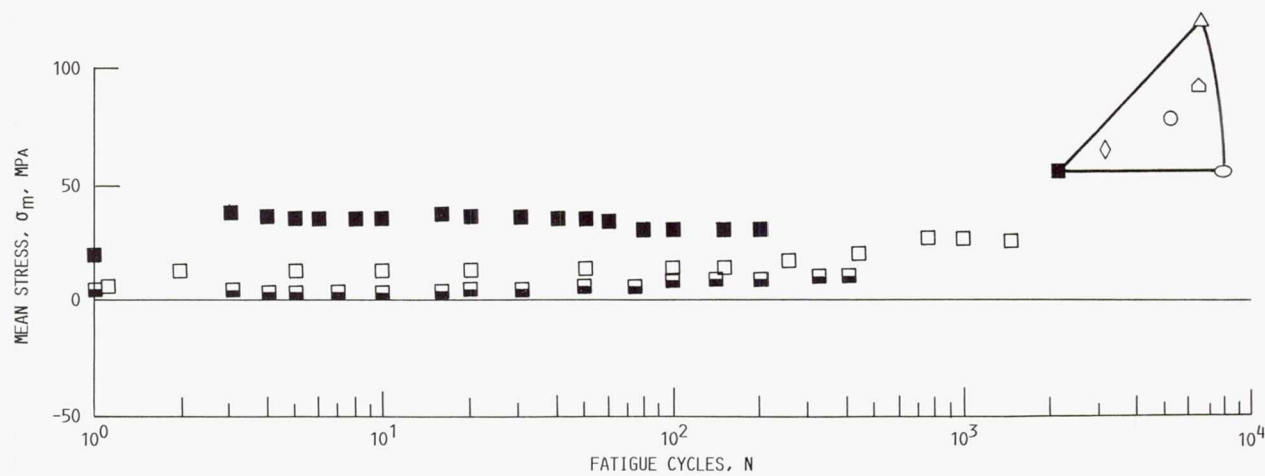
FIGURE 27. – THE LCF MEAN STRESS OF THE [001] SPECIMENS AT 650 °C.
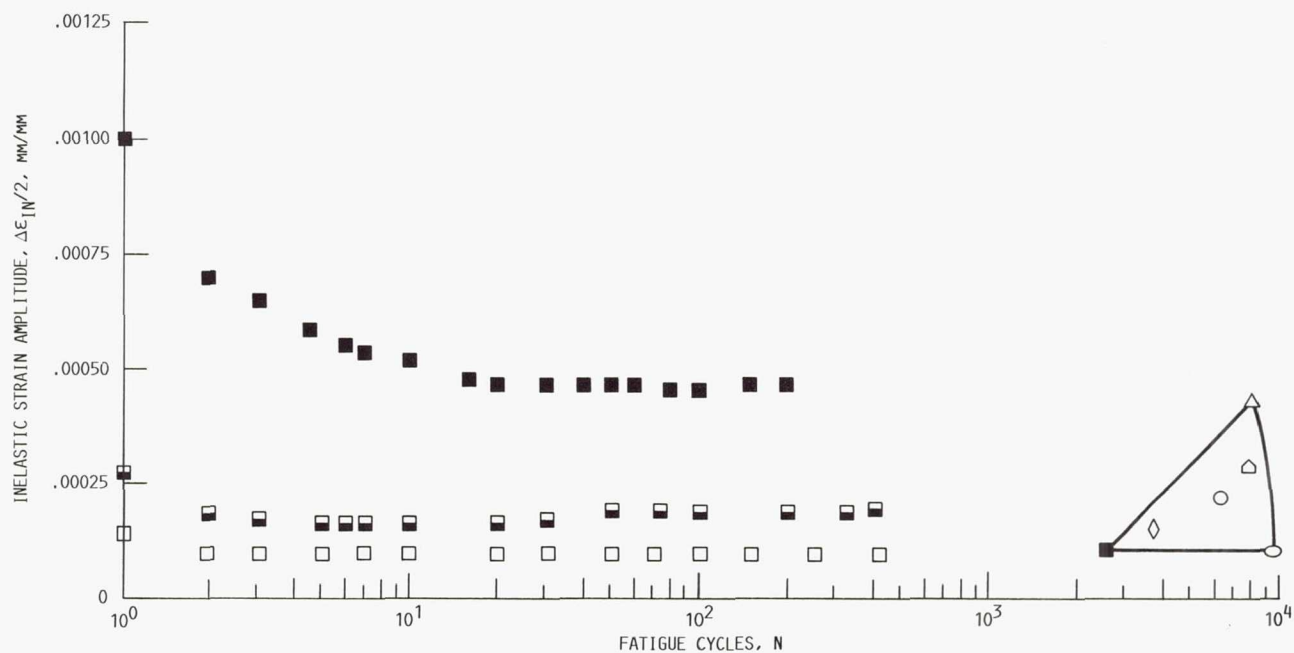
FIGURE 28. – THE LCF INELASTIC STRAIN RESPONSE OF THE [001] SPECIMENS AT 650 $^\circ$C.
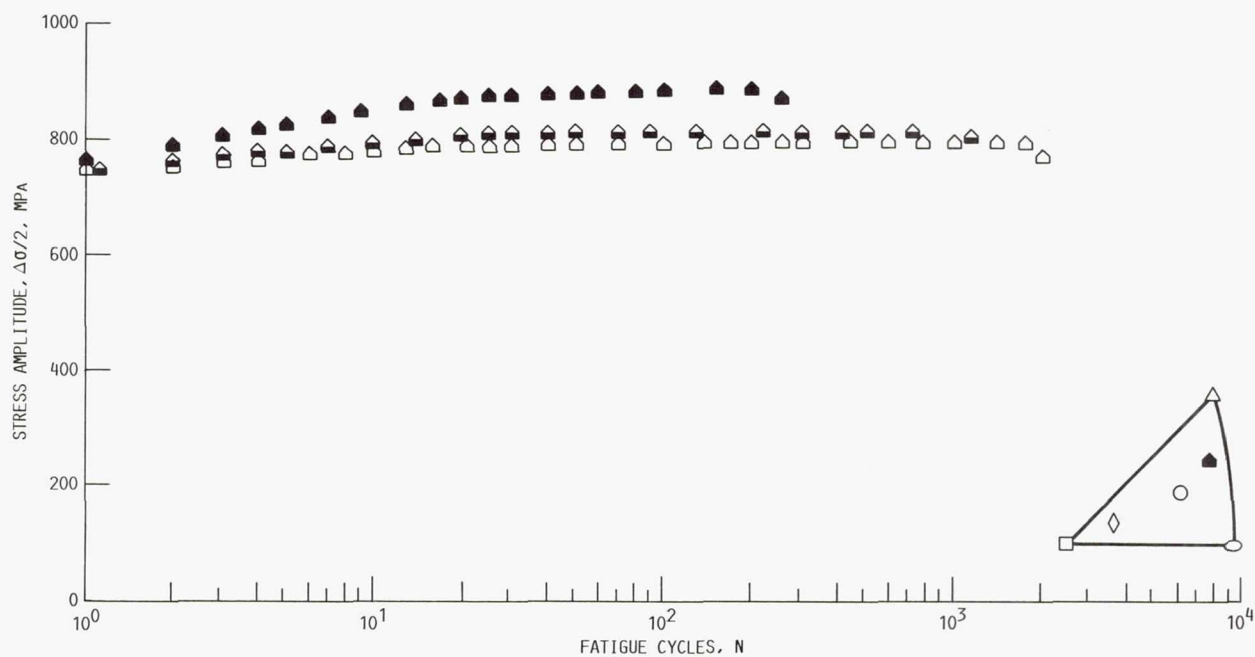
FIGURE 29. – THE LCF STRESS HARDENING RESPONSE OF THE [$\bar{2}$ 3 4] SPECIMENS AT 650 $^\circ$C.
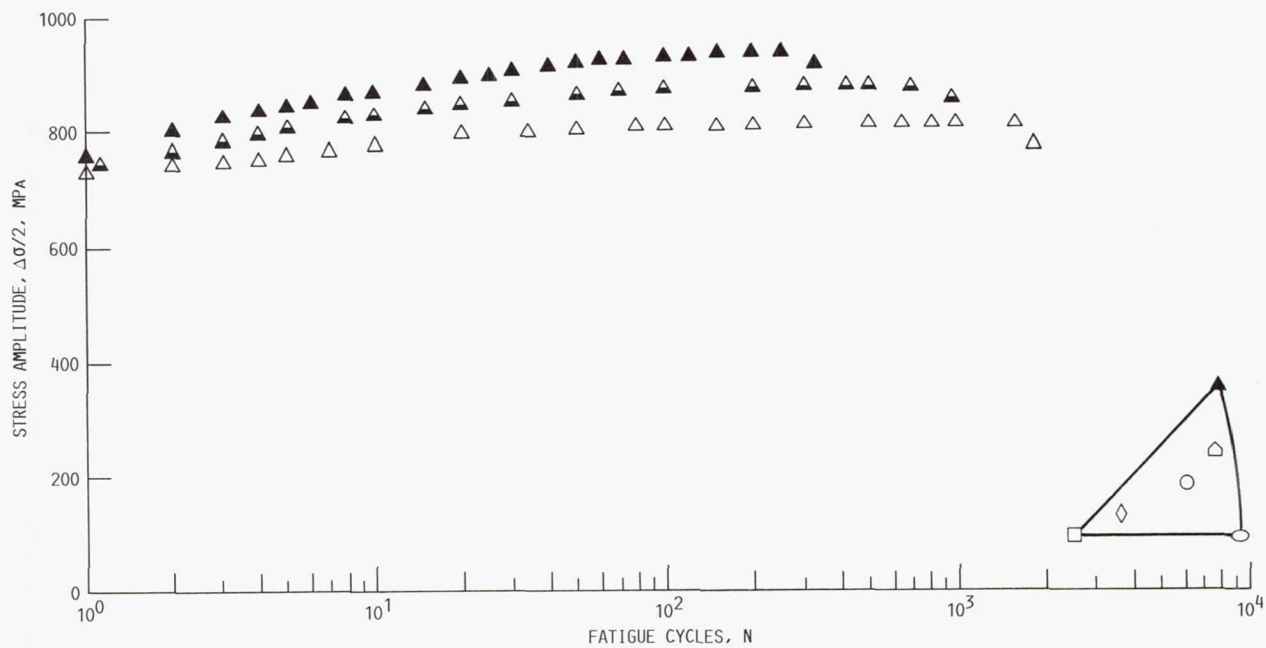
FIGURE 30. - THE LCF STRESS HARDENING RESPONSE OF THE [$\bar{1}$11] SPECIMENS AT 650 ^{o}C.
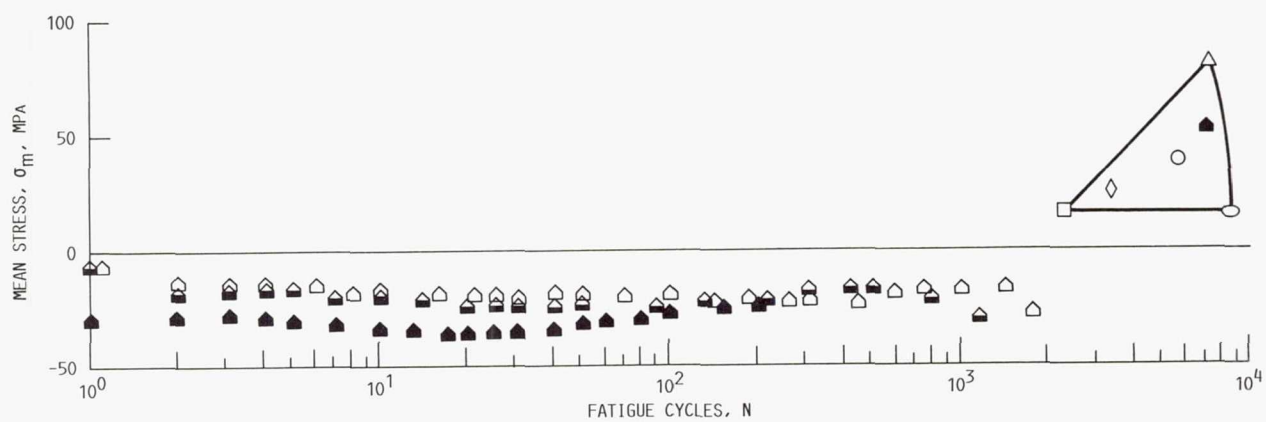
FIGURE 31. - THE LCF MEAN STRESS RESPONSE OF THE [$\bar{2}$ 3 4] SPECIMENS AT 650 ^{o}C.
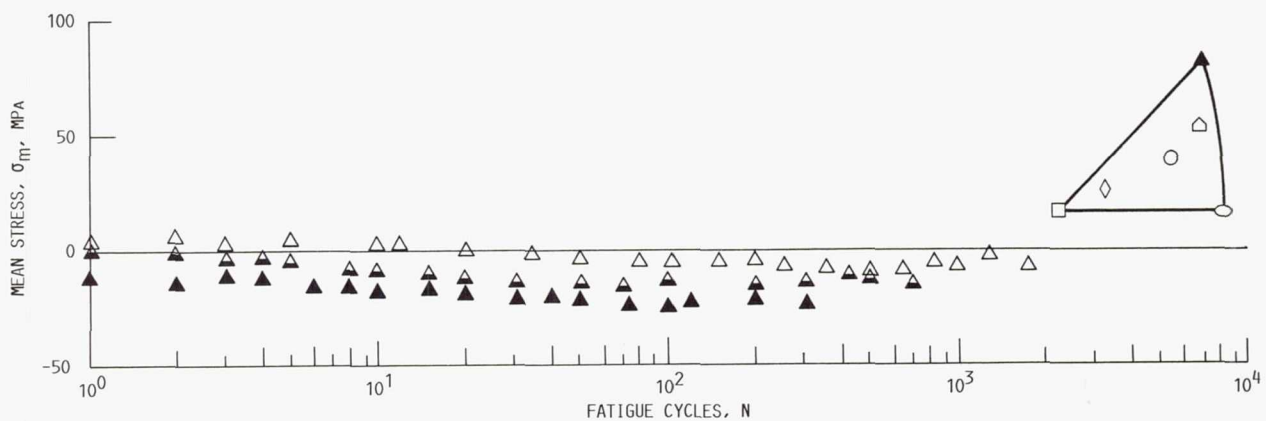
FIGURE 32. - THE LCF MEAN STRESS RESPONSE OF THE [$\bar{1}$11] SPECIMENS AT 650 ^{o}C.
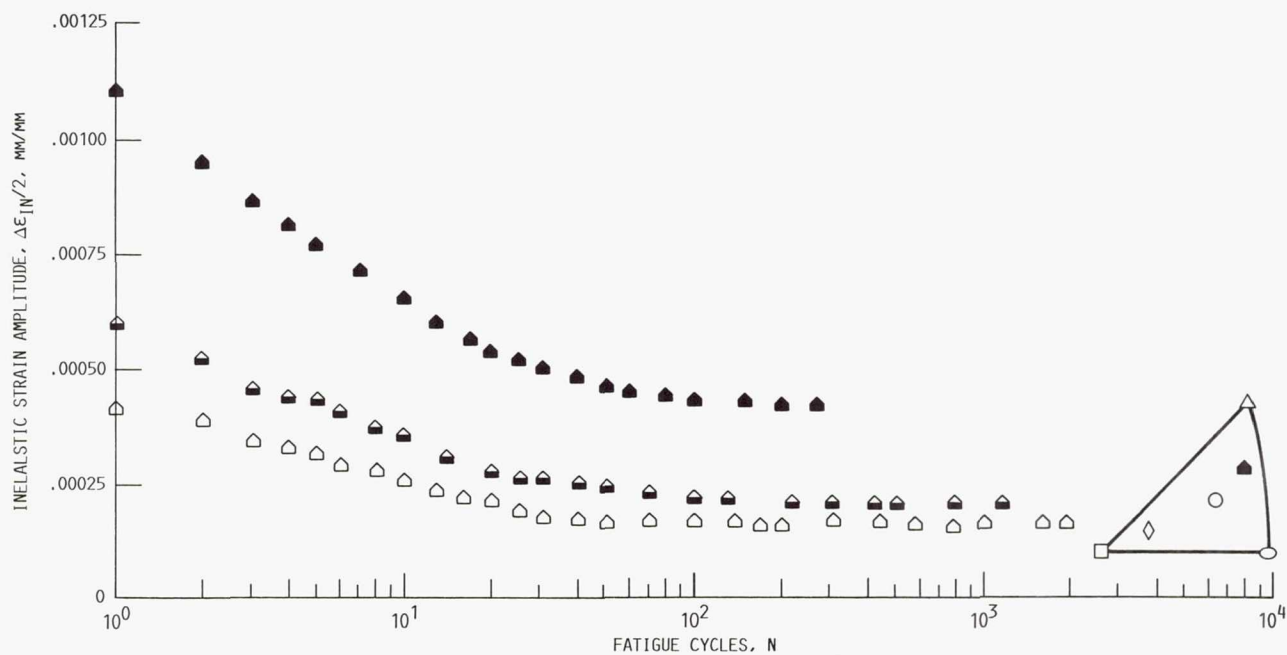
FIGURE 33. – THE LCF INELASTIC STRAIN RESPONSE OF THE [2 3 4] SPECIMENS AT 650 ^{o}C.
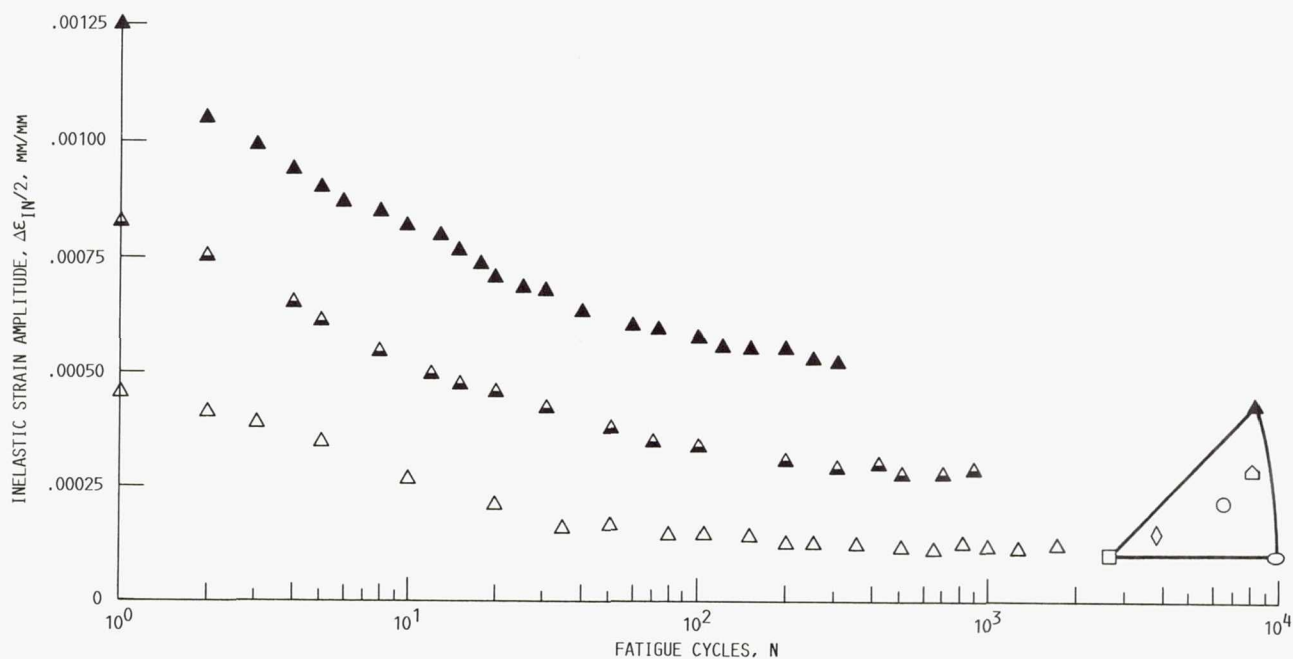
FIGURE 34. – THE LCF INELASTIC STRAIN RESPONSE OF THE [111] SPECIMENS AT 650 ^{o}C.

$[\bar{2}\ 5\ 20]$ ◈

STRESS - σ, MPa

CYCLE 1
CYCLE $N_f/2$

STRAIN - ε, MM/MM

-.01

.01

1000

-1000

$\sigma_t > \sigma_c$
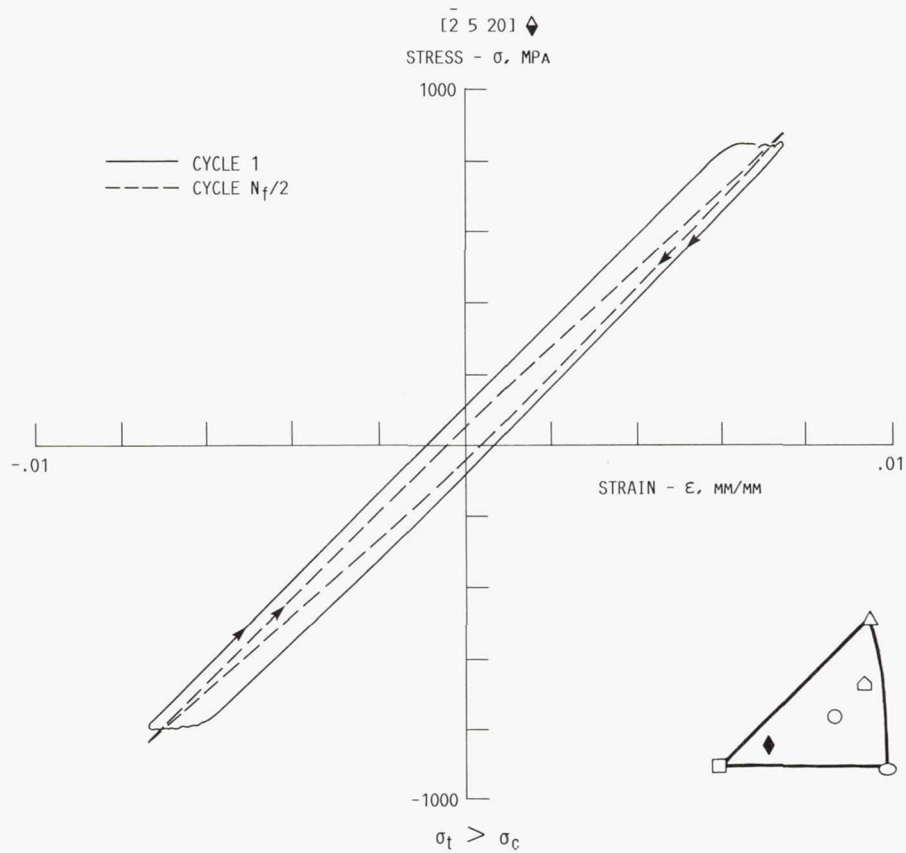
FIGURE 35. - TYPICAL LCF HYSTERESIS LOOPS OF THE $[\bar{2}\ 5\ 20]$ SPECIMENS AT 650 °C.

$[\bar{3}\ 6\ 10]$ ◓

STRESS - σ, MPa

CYCLE 1
CYCLE $N_f/2$

STRAIN - ε, MM/MM

-.01

.01

1000

-1000

$\sigma_t < \sigma_c$
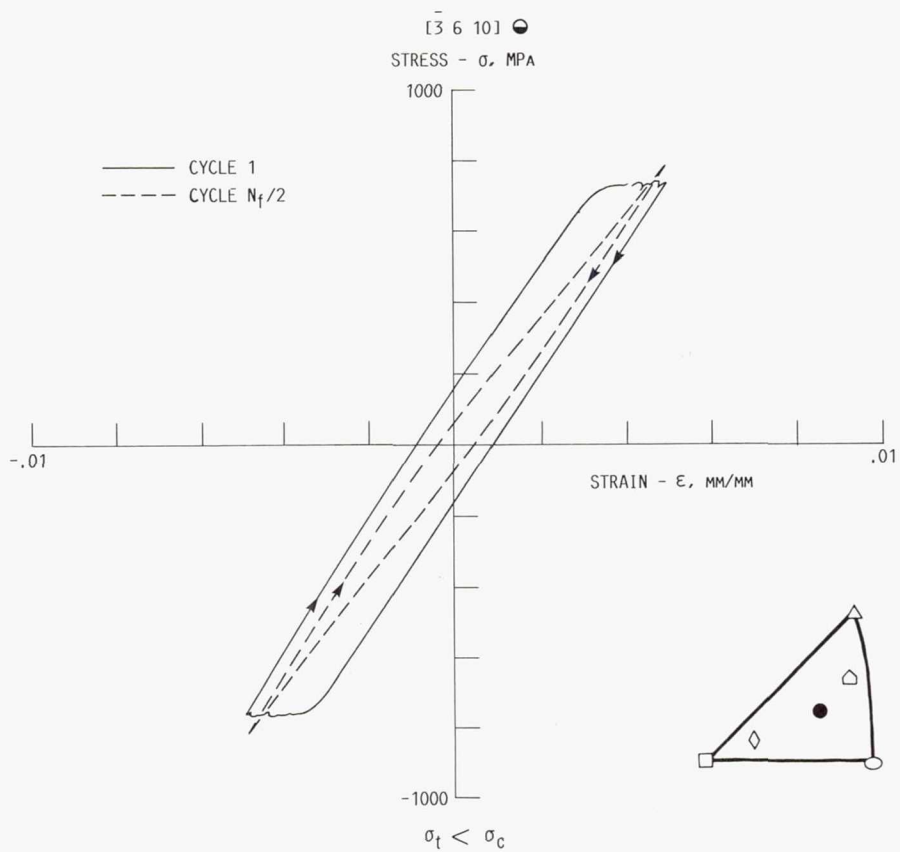
FIGURE 36. - TYPICAL LCF HYSTERESIS LOOPS OF THE $[\bar{3}\ 6\ 10]$ SPECIMENS AT 650 °C.

122

[011] ◉

STRESS - σ, MPa

CYCLE 1
CYCLE N_f/2

STRAIN - ε, MM/MM

$\sigma_t < \sigma_c$
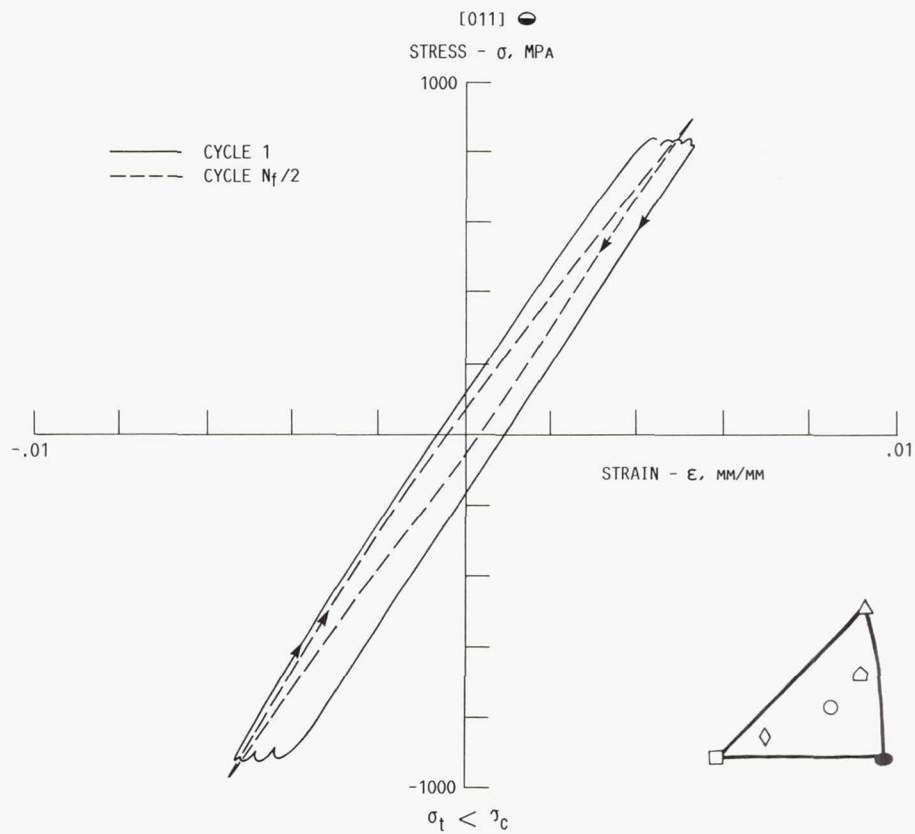
FIGURE 37. - TYPICAL LCF HYSTERESIS LOOPS OF THE [011] SPECIMENS AT 650 ^{O}C.

[001] ■

STRESS - σ, MPa

CYCLE 1
CYCLE N_f/2

STRAIN - ε, MM/MM

$\sigma_t > \sigma_c$
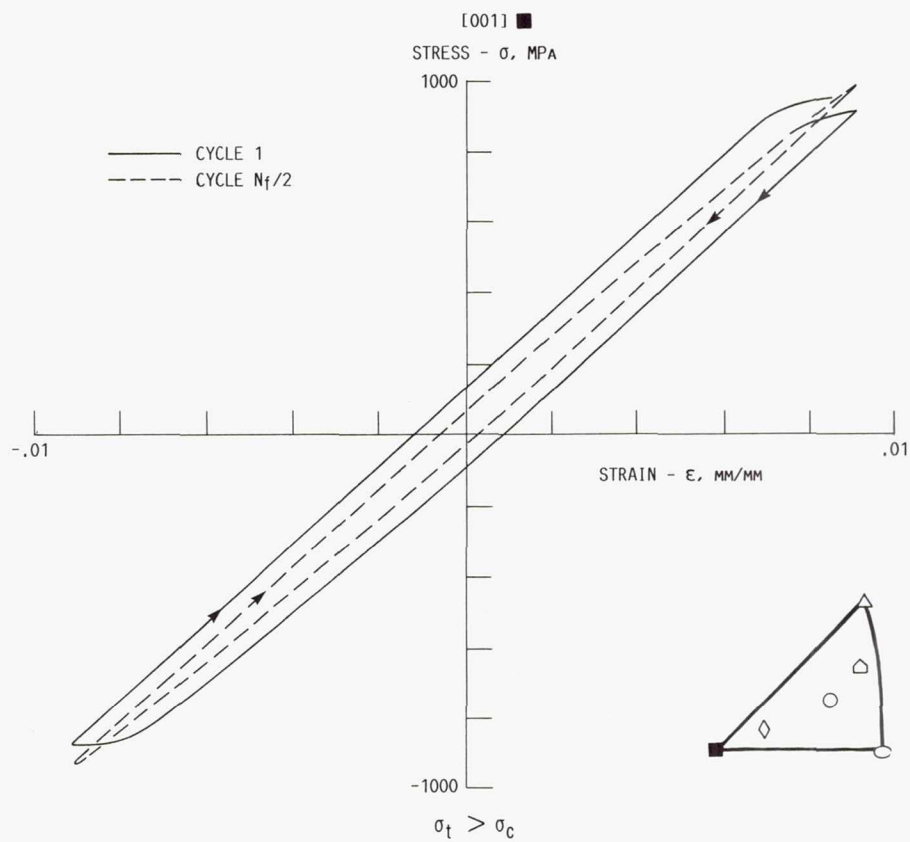
FIGURE 38. - TYPICAL LCF HYSTERESIS LOOPS OF THE [001] SPECIMENS AT 650 ^{O}C.
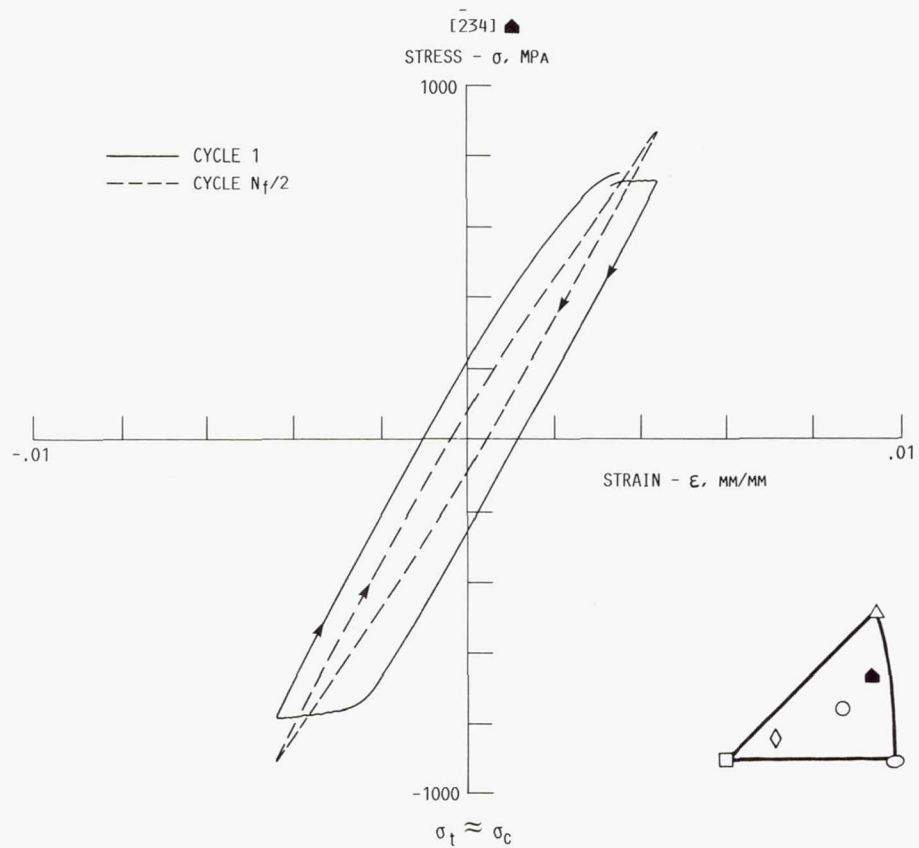
FIGURE 39. – TYPICAL LCF HYSTERESIS LOOPS OF THE [2̄ 3 4] SPECIMENS AT 650 °C.
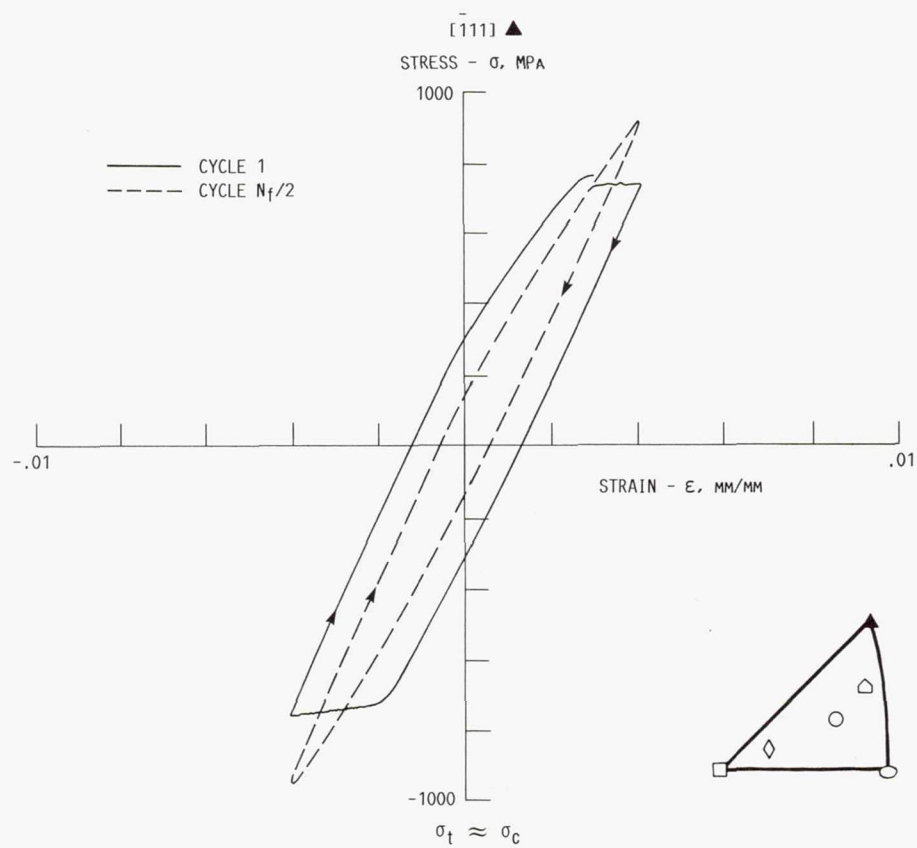
FIGURE 40. – TYPICAL LCF HYSTERESIS LOOPS OF THE [1̄11] SPECIMENS AT 650 °C.
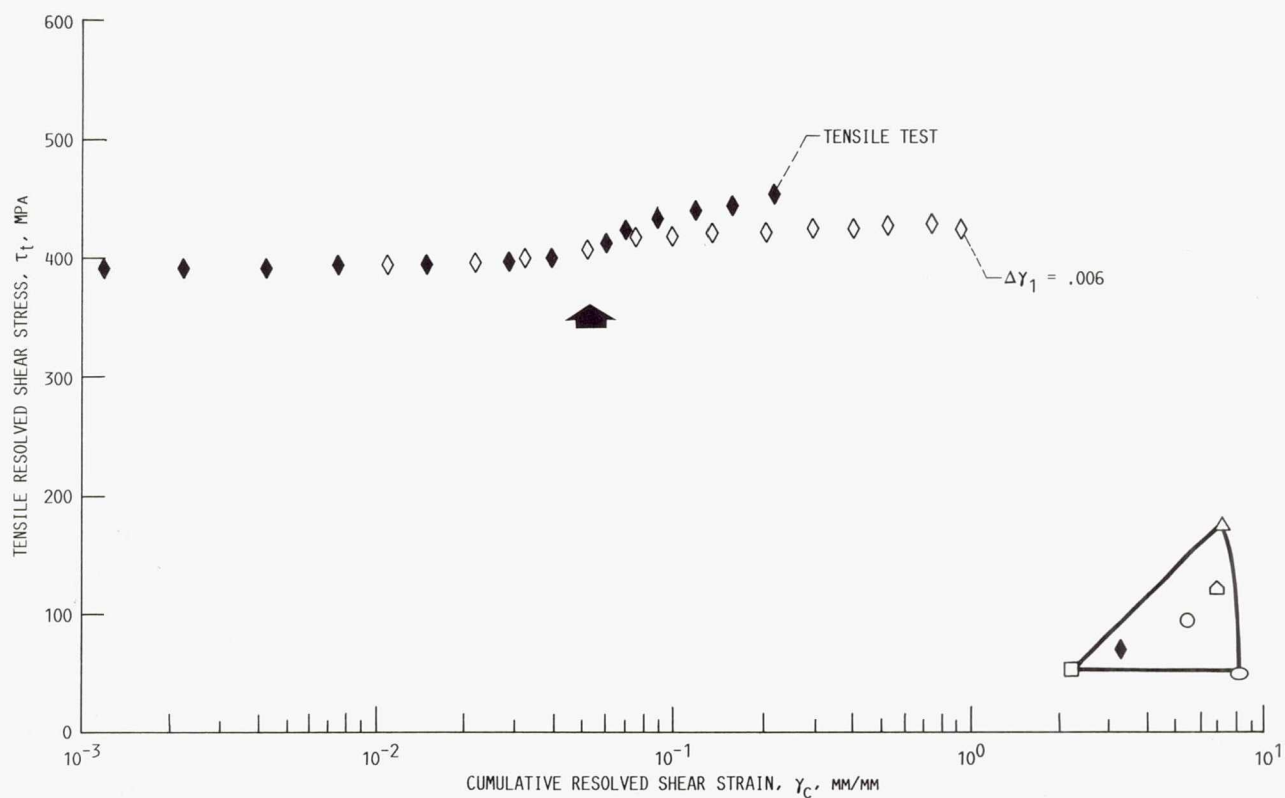
FIGURE 41. - THE TENSILE SHEAR STRESS - CUMULATIVE SHEAR STRAIN RESPONSE OF THE [$\bar{2}$ 5 20] LCF AND TENSILE TEST SPECIMENS AT 650 ^{O}C.
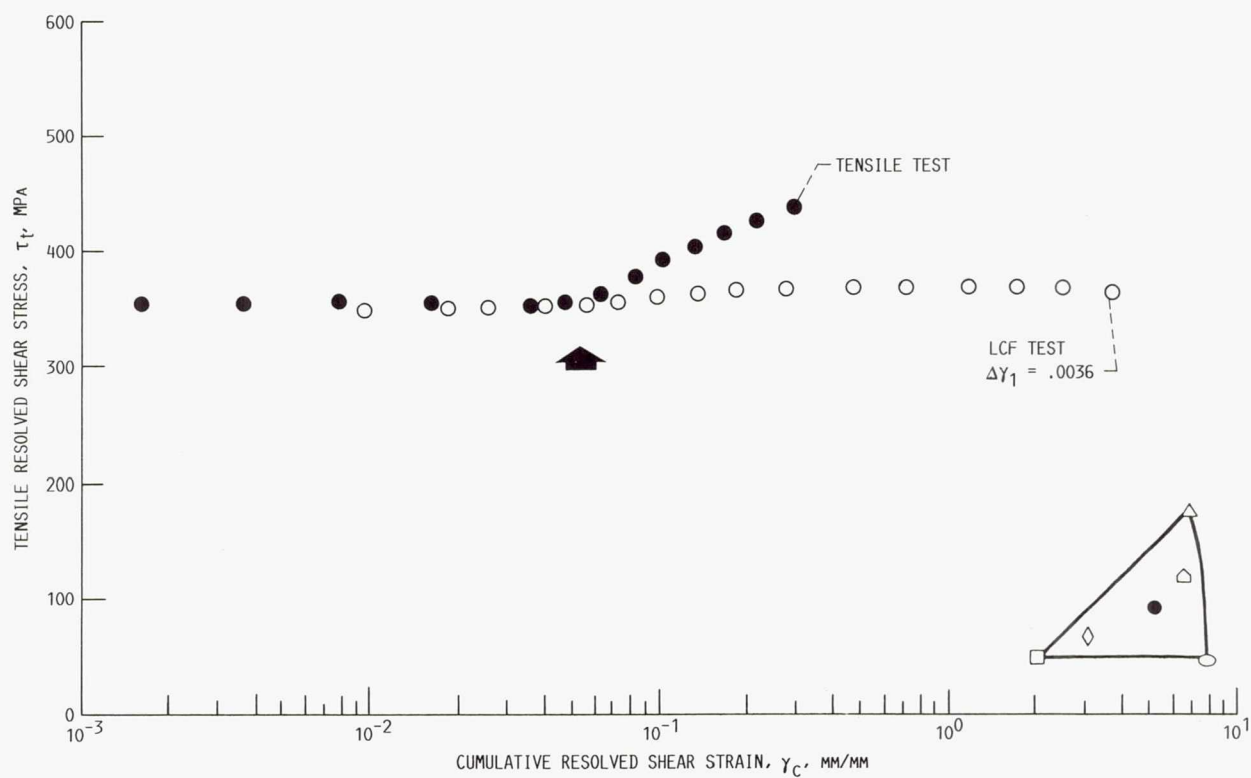
FIGURE 42. - THE TENSILE SHEAR STRESS - CUMULATIVE SHEAR STRAIN RESPONSE OF THE [$\bar{3}$ 6 10] LCF AND TENSILE TEST SPECIMENS AT 650 ^{O}C.
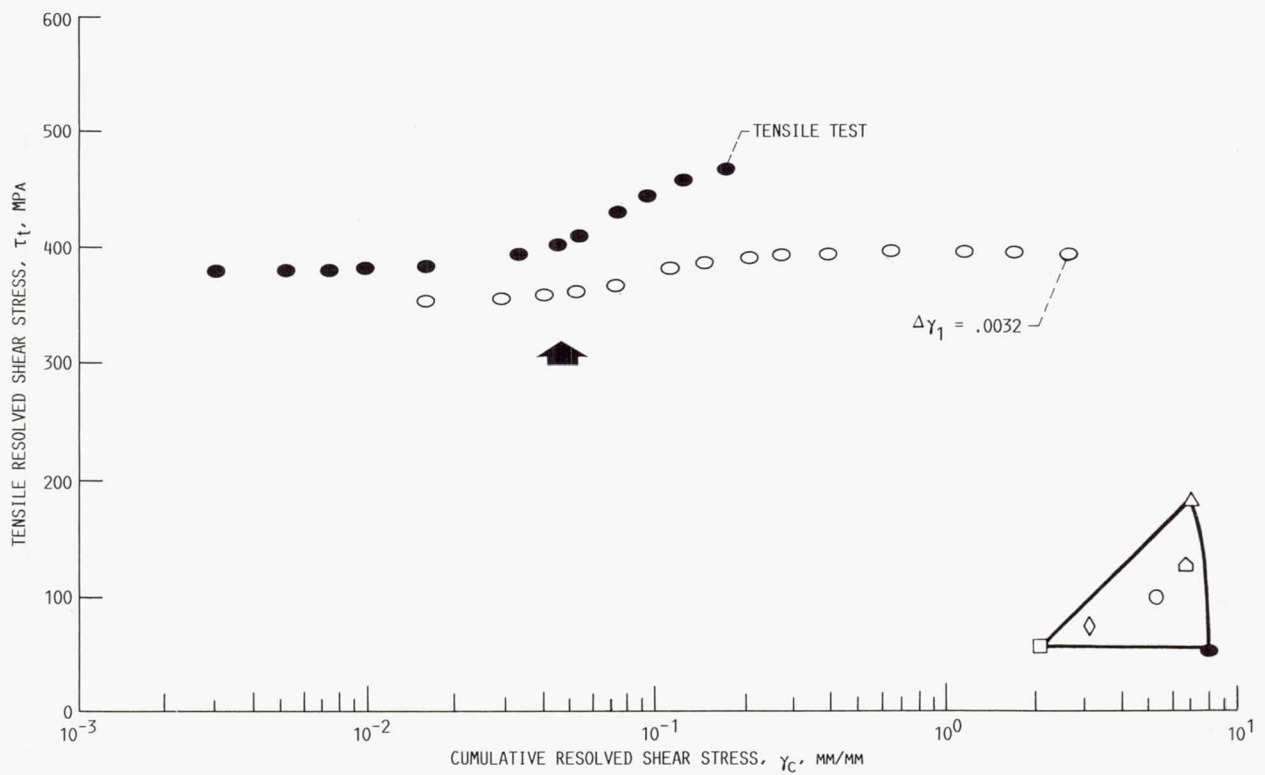
FIGURE 43. - THE TENSILE SHEAR STRESS - CUMULATIVE SHEAR STRAIN RESPONSE OF THE [011] LCF AND TENSILE TEST SPECIMENS AT 650 °C.
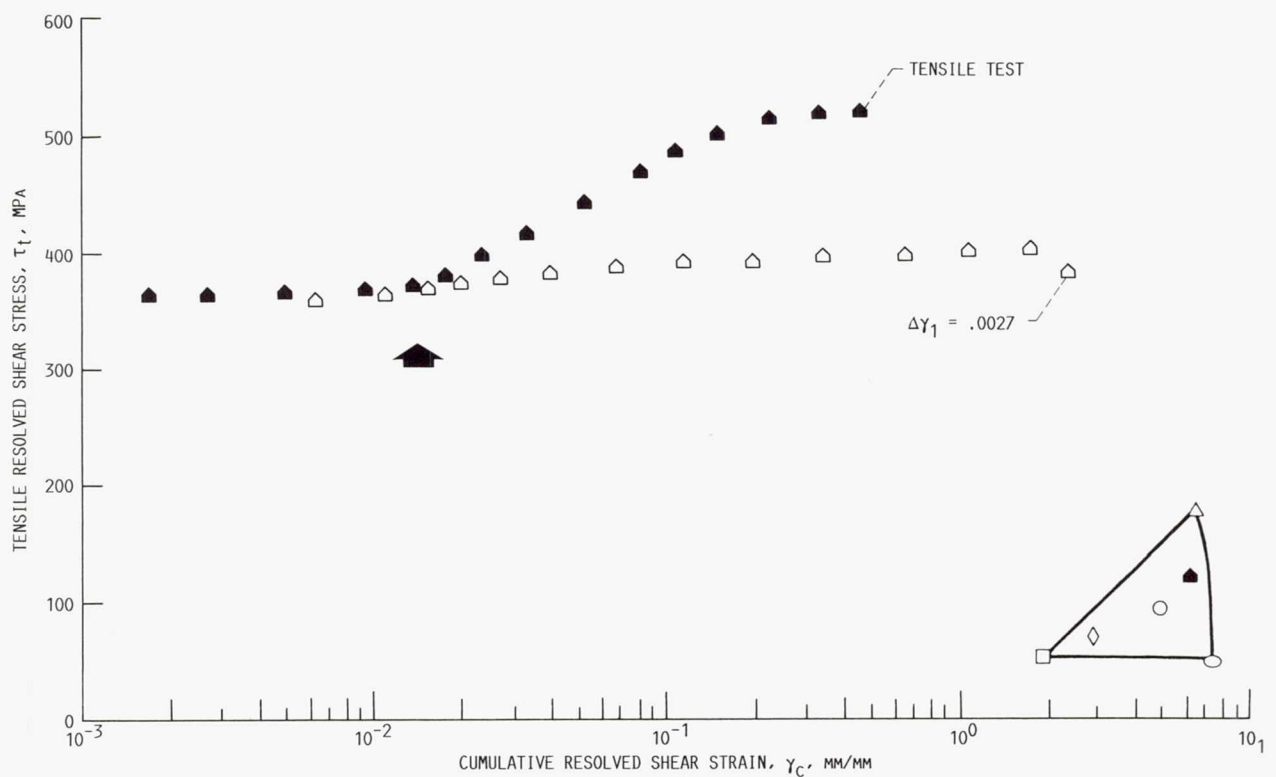
FIGURE 44. - THE TENSILE SHEAR STRESS - CUMULATIVE SHEAR STRAIN RESPONSE OF THE [$\bar{2}$ 3 4] LCF AND TENSILE TEST SPECIMENS AT 650 °C.
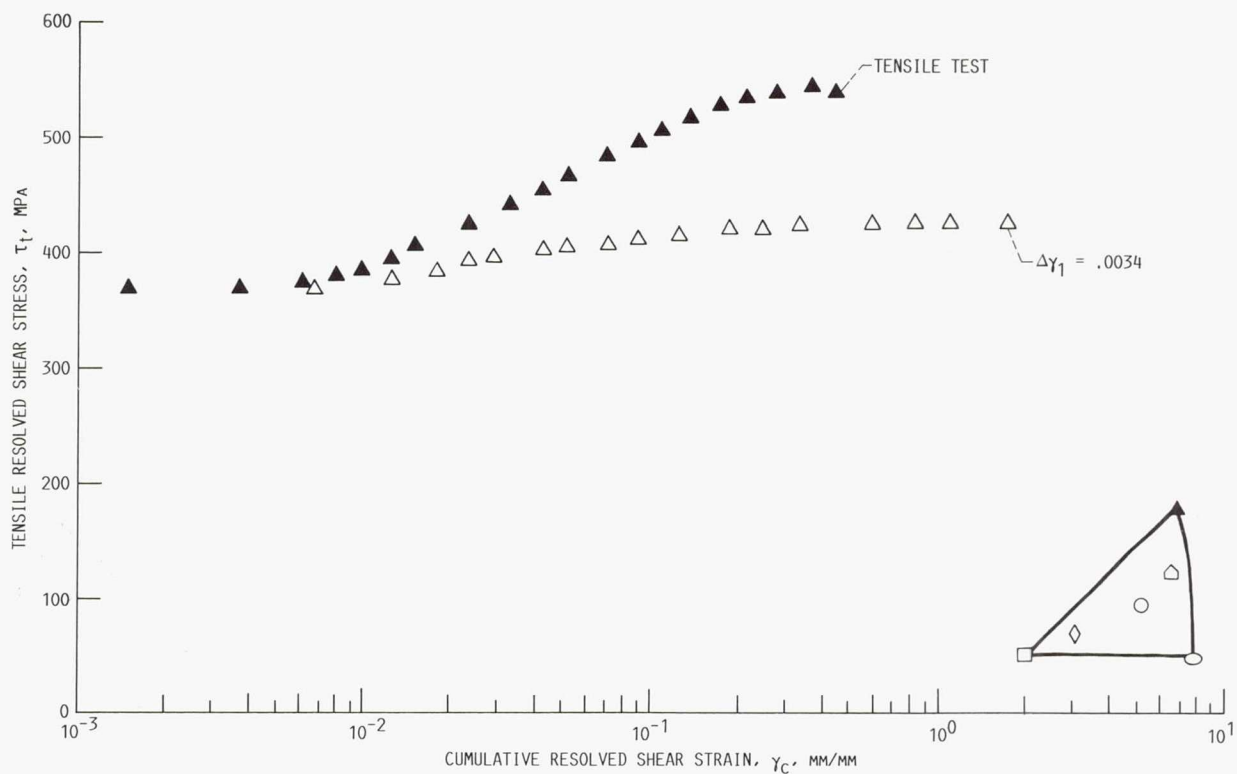
FIGURE 45. — THE TENSILE SHEAR STRESS — CUMULATIVE SHEAR STRAIN RESPONSE OF THE [$\bar{1}$11] LCF AND TENSILE SPECIMENS AT 650 $^\circ$C.
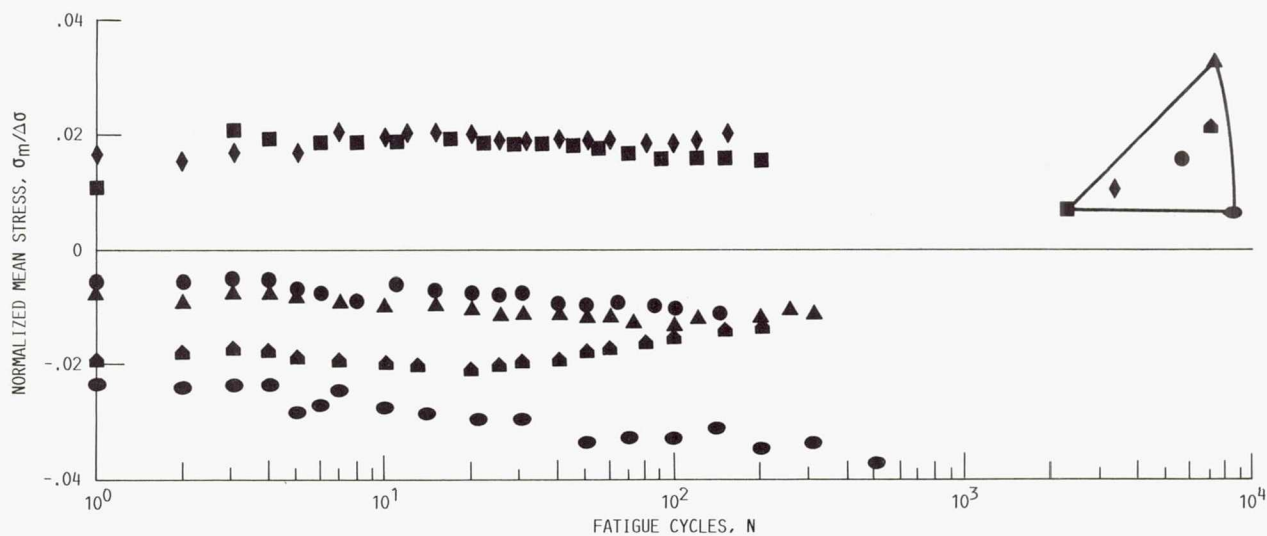
FIGURE 46. — THE LCF NORMALIZED MEAN STRESS RESPONSE IN OCTAHEDRAL SLIP AT 650 $^\circ$C.
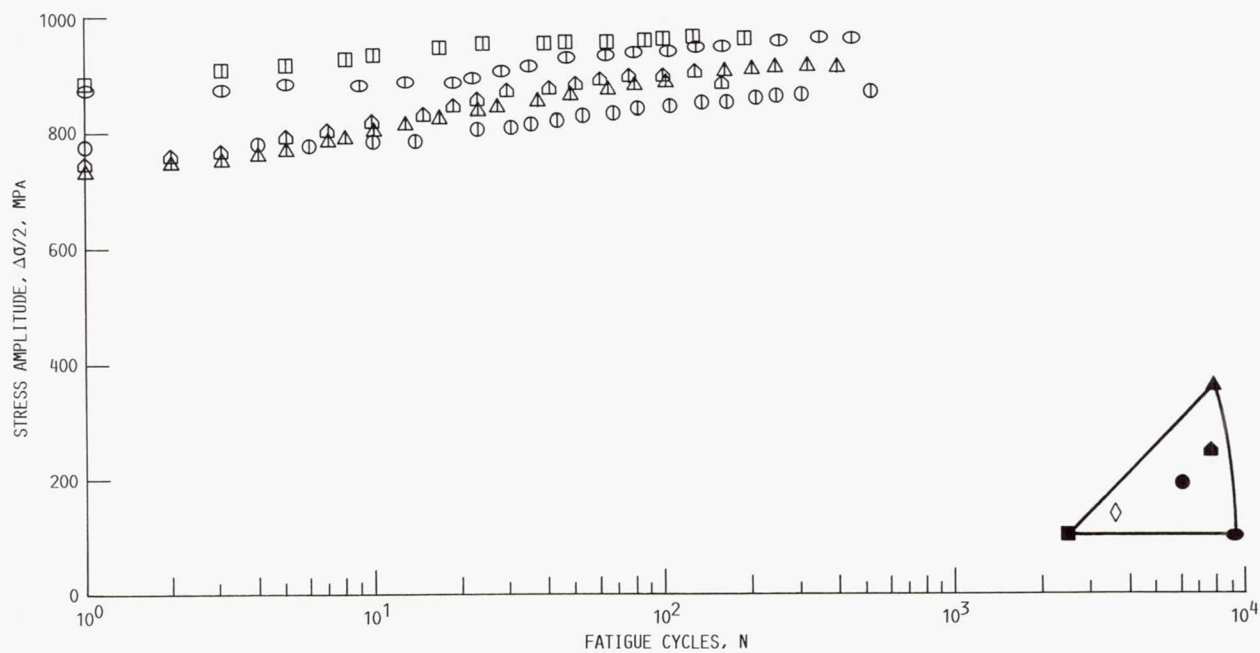
FIGURE 47. - THE LCF STRESS HARDENING RESPONSE IN TESTS OF CONSTANT INELASTIC STRAIN RANGE AT 650 ^{O}C.
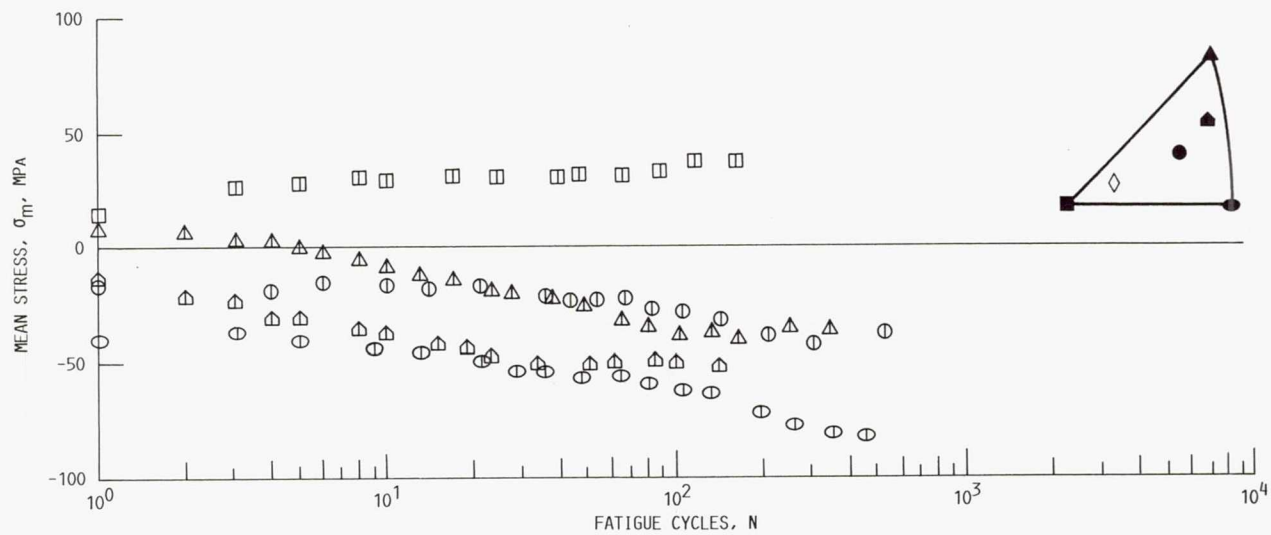
FIGURE 48. - THE LCF MEAN STRESS RESPONSE IN TESTS OF CONSTANT INELASTIC STRAIN RANGE AT 650 ^{O}C.
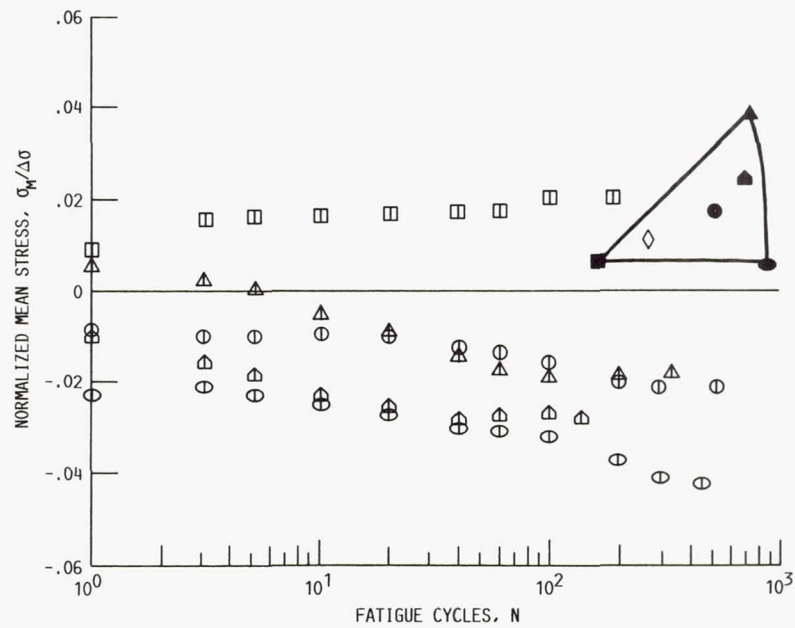
FIGURE 49. – THE LCF NORMALIZED MEAN STRESS RESPONSE IN TESTS OF CONSTANT INELASTIC STRAIN RANGE AT 650 °C.
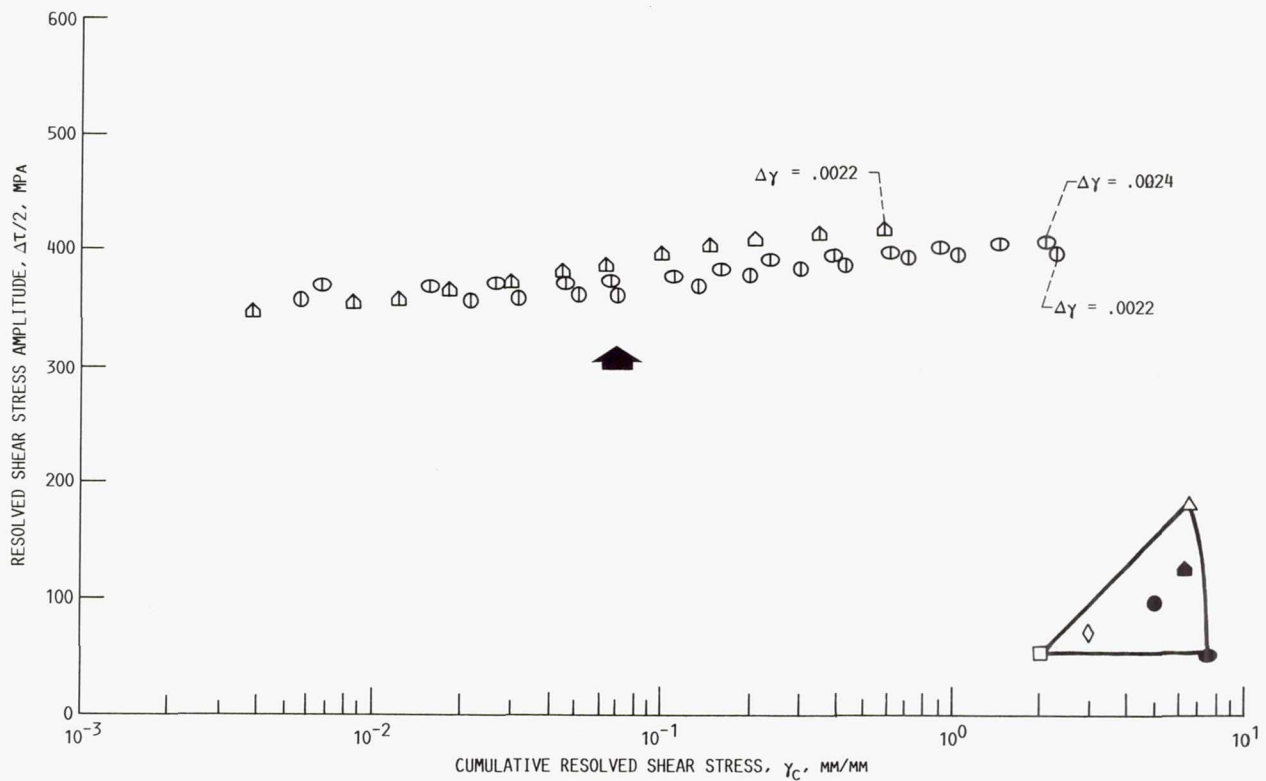
FIGURE 50. – THE SHEAR STRESS – CUMULATIVE SHEAR STRAIN RESPONSE IN TESTS OF CONSTANT INELASTIC STRAIN RANGE AT 650 °C.
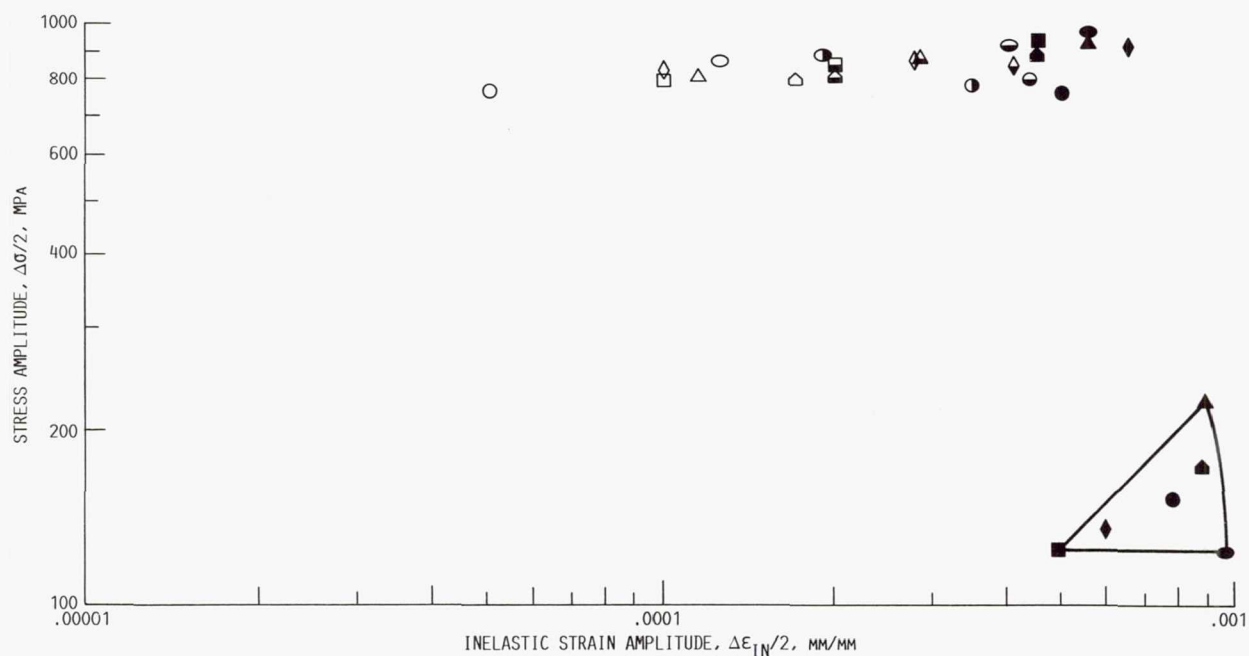
FIGURE 51. - THE LCF CYCLIC STRESS-STRAIN RESPONSE AT HALF OF CYCLIC LIFE AT 650 °C.
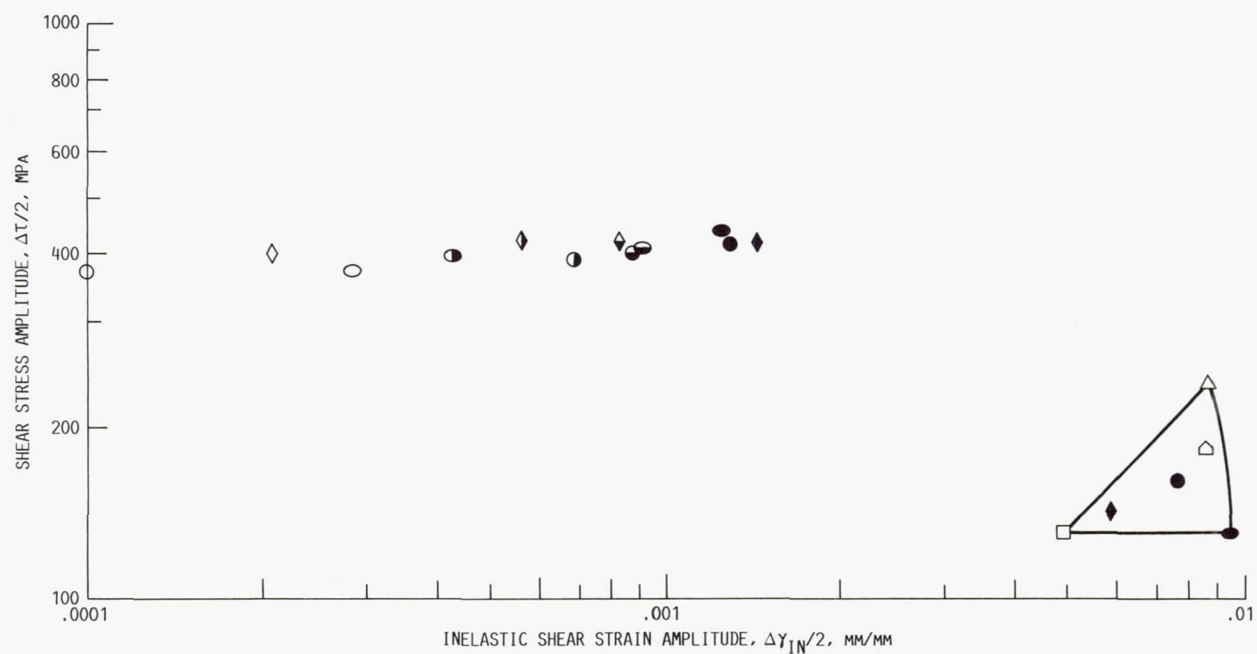
FIGURE 52. - THE RESOLVED CYCLIC STRESS-STRAIN RESPONSE AT HALF OF CYCLIC LIFE OF THE [$\bar{2}$ 5 20], [$\bar{3}$ 6 10], AND [011] SPEC-IMENS AT 650 °C.
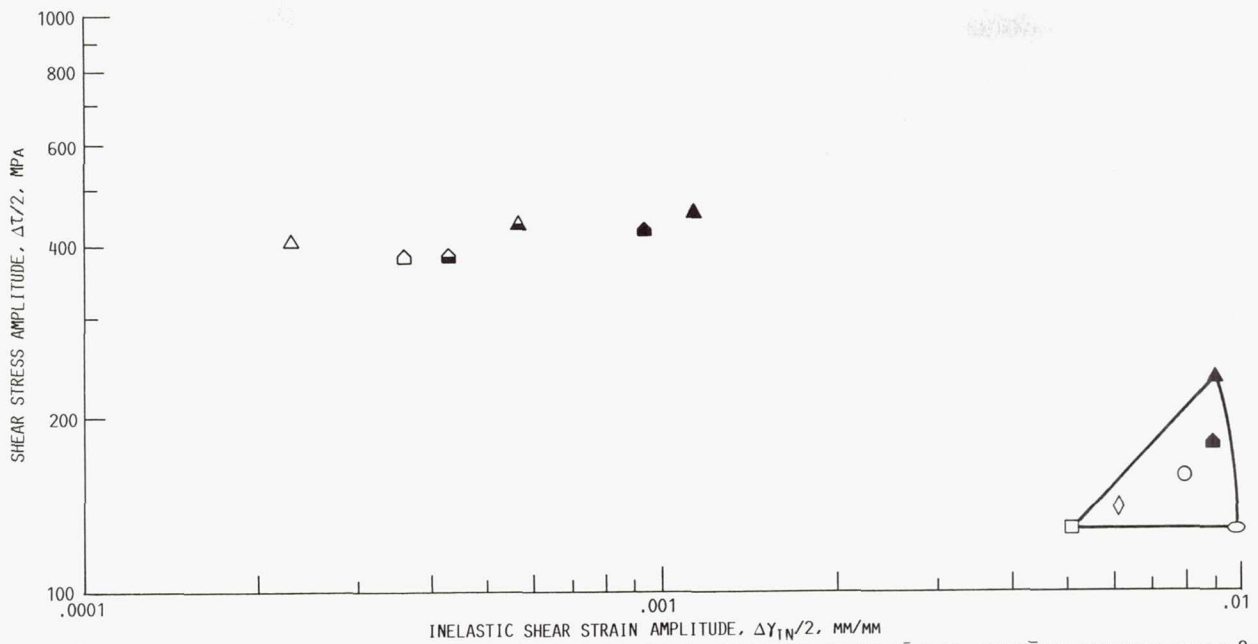
FIGURE 53. – THE RESOLVED CYCLIC STRESS-STRAIN RESPONSE AT HALF OF CYCLIC LIFE OF THE [$\bar{2}$ 3 4], AND [$\bar{1}$11] SPECIMENS AT 650 $^\circ$C.
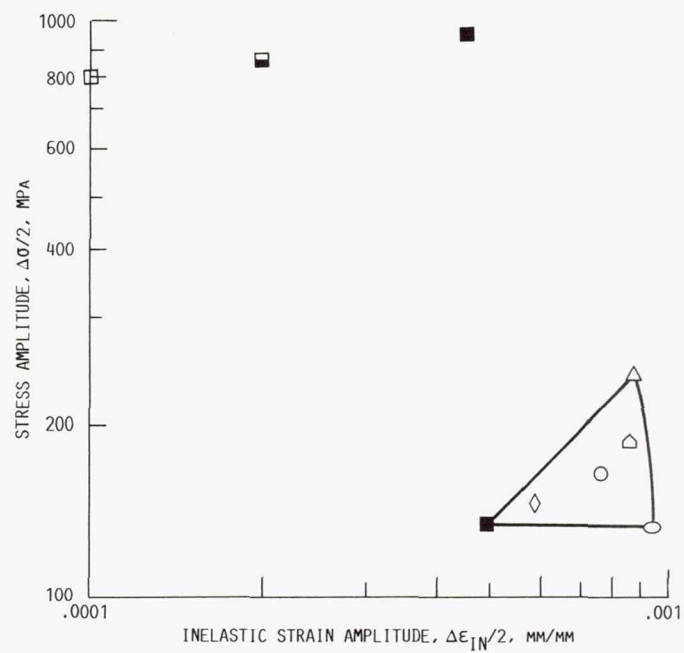
FIGURE 54. – THE LCF CYCLIC STRESS-STRAIN RESPONSE OF THE [001] SPECIMENS AT 650 $^\circ$C.
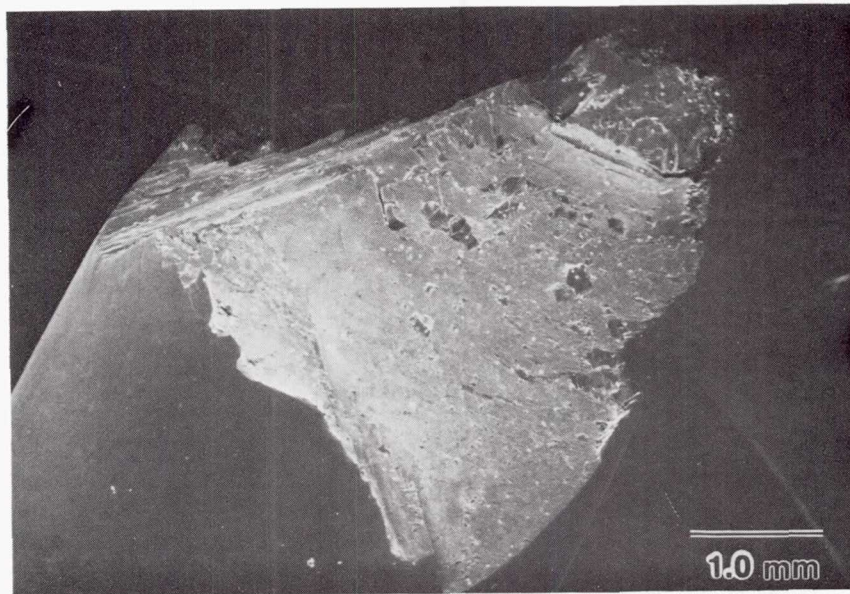
FIGURE 55. – CRYSTALLOGRAPHIC FRACTURE SURFACES OF AN [001] LCF SPECIMEN, 650 $^\circ$C.

FIGURE 56. – THE DEFORMATION STRUCTURE OF A [$\bar{3}$ 6 10] LCF SPECIMEN, 650 $^\circ$C, $\Delta\epsilon_{IN.}$ <.001 MM/MM ON CYCLE 1, [011] Z.A.
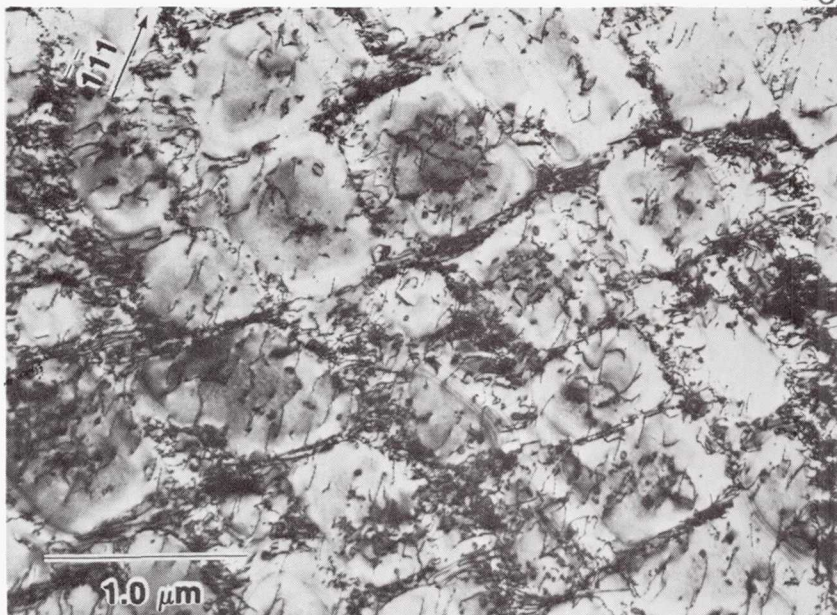
FIGURE 57. - THE DEFORMATION STRUCTURE OF A [$\bar{3}$ 6 10] LCF SPECIMEN, 650 ^{O}C, $\Delta\varepsilon_{IN.}$ > .002 MM/MM ON CYCLE 1, [011] Z.A.
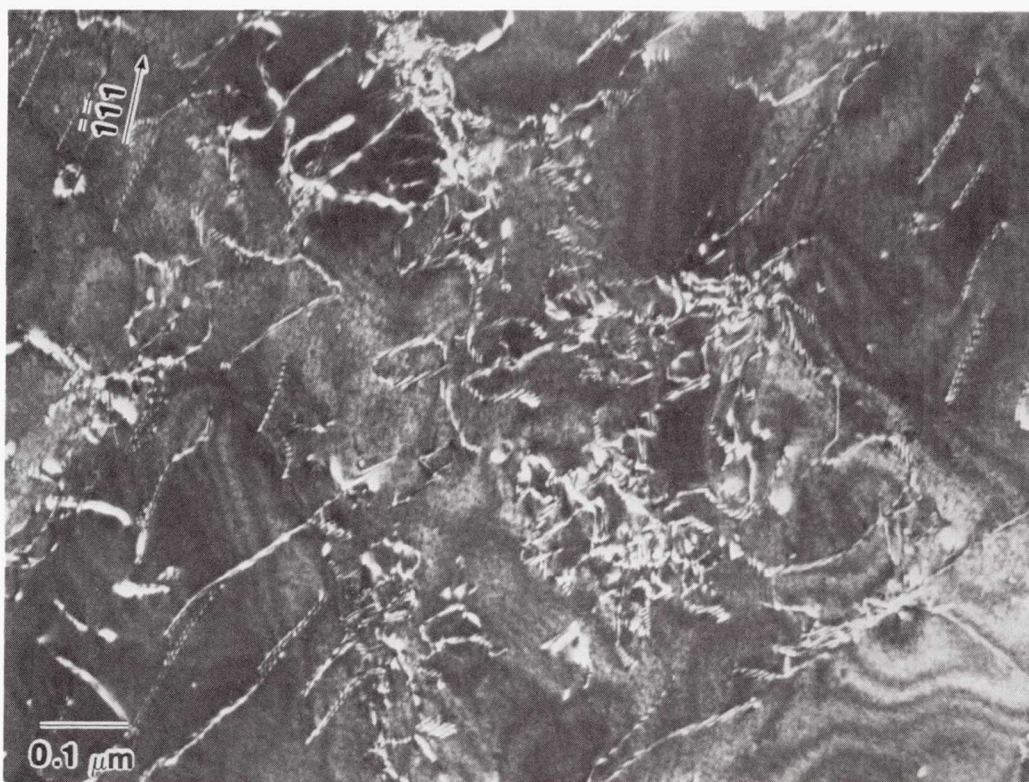
FIGURE 58. - NONPLANAR DISLOCATION ENTANGLEMENTS OF A [$\bar{3}$ 6 10] LCF SPECIMEN, 650 ^{O}C, $\Delta\varepsilon_{IN.}$ > .002 MM/MM ON CYCLE 1, g/3g WEAK BEAM DARK FIELD (WBDF), [$\bar{1}$21] Z.A.
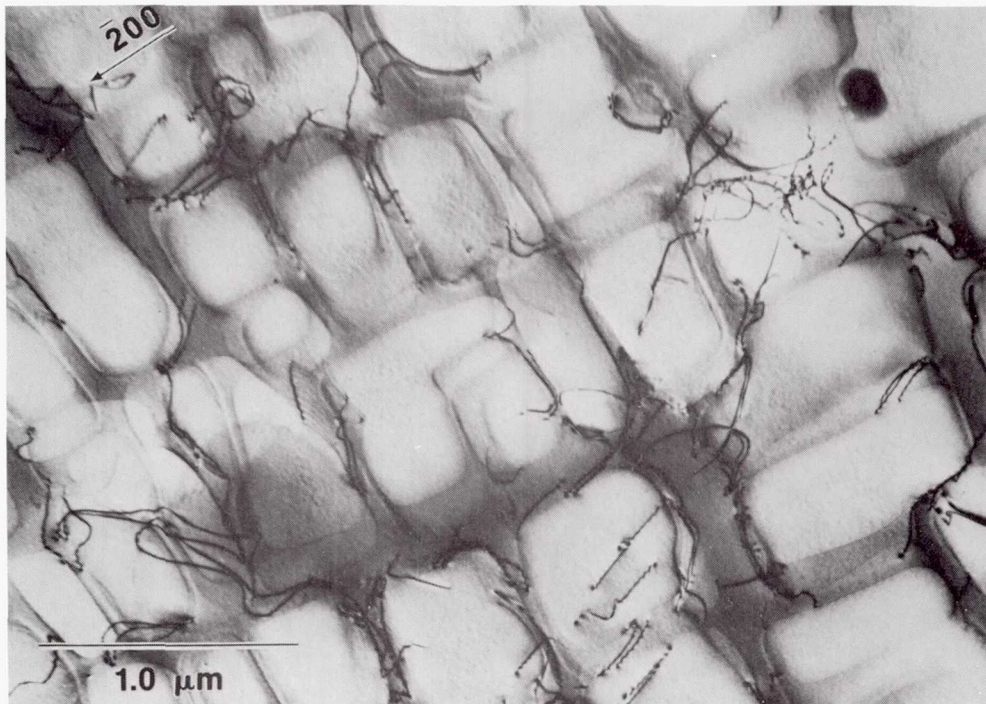
FIGURE 59. - THE DEFORMATION STRUCTURE OF AN [001] LCF SPECIMEN, 650 ^{O}C, $\Delta\varepsilon_{IN.}$ < .001 MM/MM ON CYCLE 1, [013] Z.A.
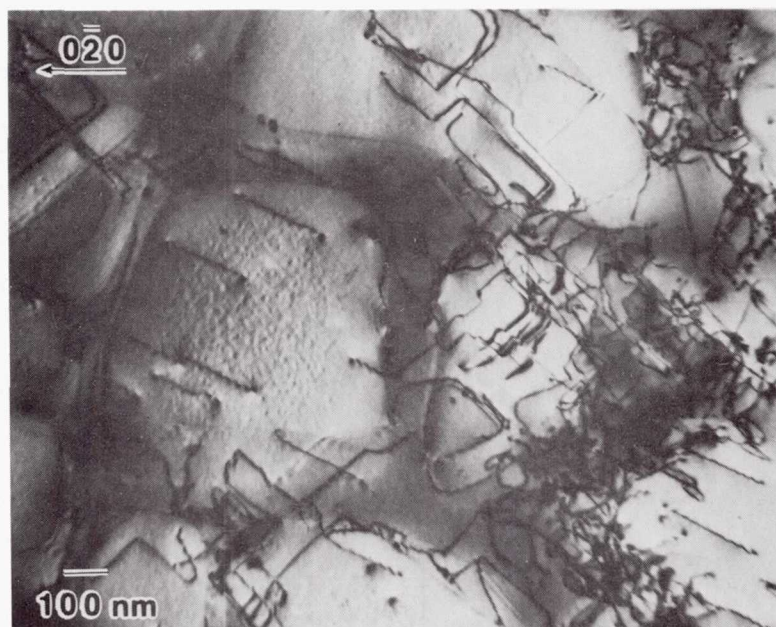
FIGURE 60. - THE DEFORMATION STRUCTURE OF AN [001] LCF SPECIMEN, 650 ^{O}C, $\Delta\varepsilon_{IN.}$ > .002 MM/MM ON CYCLE 1, [$\bar{1}$01] Z.A.
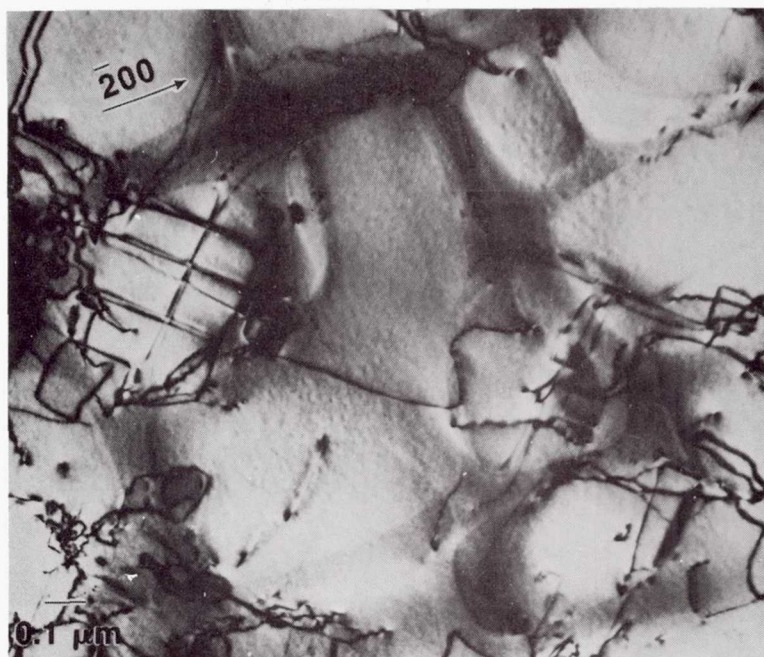
FIGURE 61. - γ-γ' INTERFACE DISLOCATIONS OF AN [001] LCF SPECIMEN, 650 °C,
$\Delta\varepsilon_{IN.}$ > .002 MM/MM ON CYCLE 1, [001] Z.A.
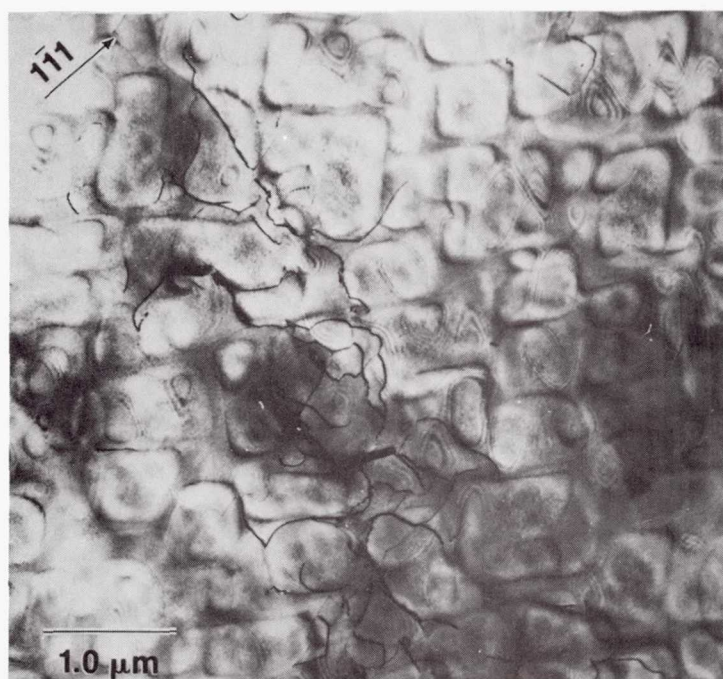
FIGURE 62. - THE DEFORMATION STRUCTURE OF A [$\bar{2}$ 3 4] LCF SPECIMEN, 650 °C,
$\Delta\varepsilon_{IN.}$ < .001 MM/MM ON CYCLE 1, [011] Z.A.

135

(A) [$\bar{2}$13] Z.A.

1.0 μm
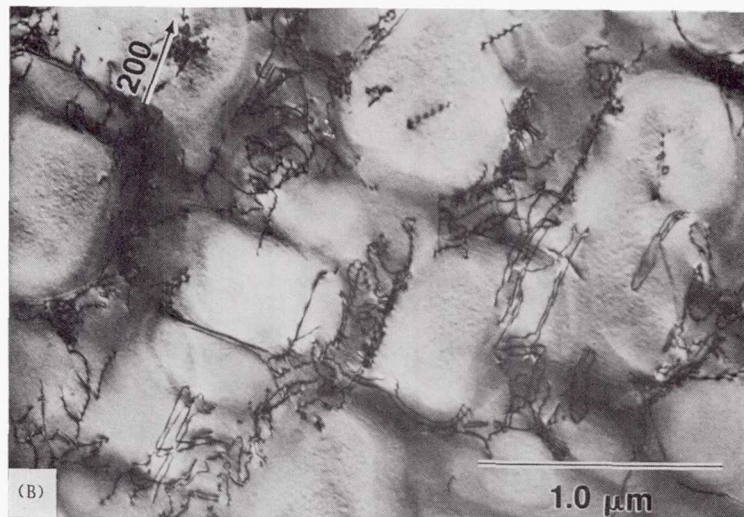
(B) [031] Z.A.

[$\bar{2}$34] 650 °C
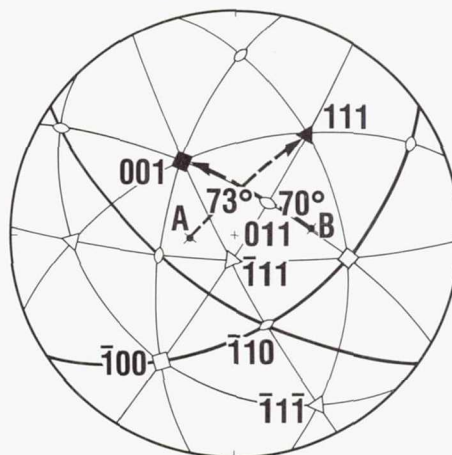
FIGURE 63. - TYPICAL MICROGRAPHS OF A TILTING EXPERIMENT OF A [$\bar{2}$ 3 4] LCF SPECIMEN, 650 °C, $\Delta\varepsilon_{IN.}$ = .0018 MM/MM ON CYCLE 1, INTERRUPTED AT 10 CYCLES.

(A) [ī01] Z.A.

(B) [041] Z.A.

[ī11] 650 °C

CD-87-29822
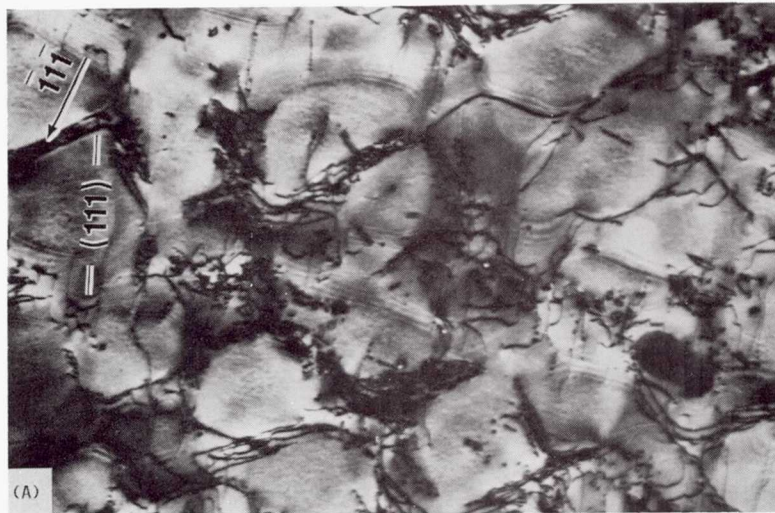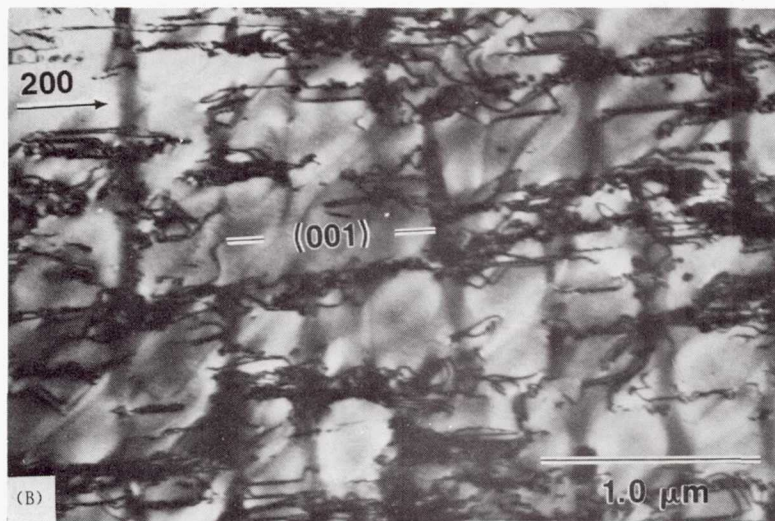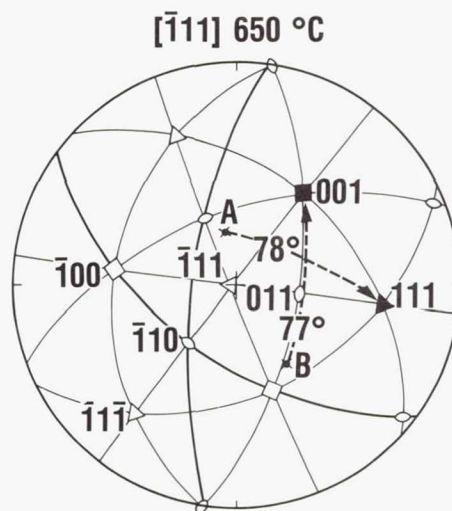
FIGURE 64. - TYPICAL MICROGRAPHS OF A TILTING EXPERIMENT OF A [ī11] LCF SPECIMEN,
650 °C, $\Delta\epsilon_{IN.} > .002$ MM/MM ON CYCLE 1.

137
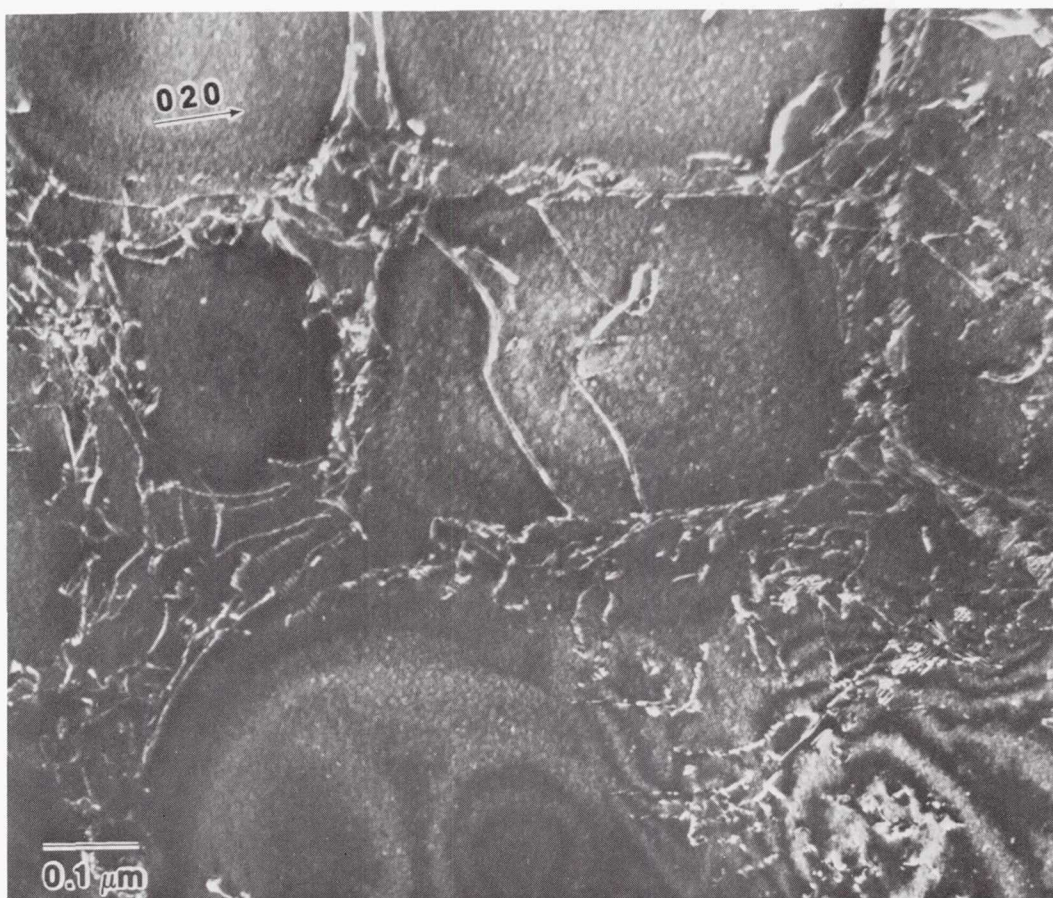
FIGURE 65. - NONPLANAR DISLOCATION ENTANGLEMENTS OF A [$\bar{2}$ 3 4] LCF SPECIMEN, 650 $^\circ$C, $\Delta\varepsilon_{IN.}$ > .002 MM/MM ON CYCLE 1, [001] Z.A.
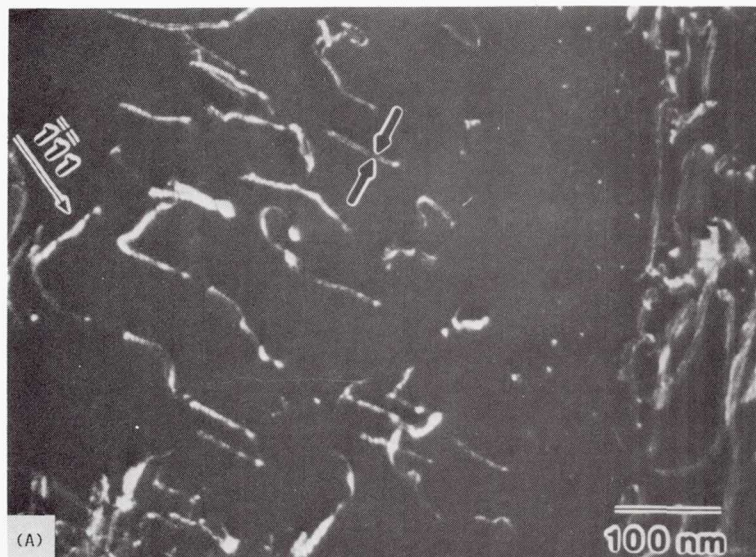
(A) [112] Z.A.

(B) [$\bar{1}$21] Z.A.

[$\bar{3}$ 6 10] 650 °C
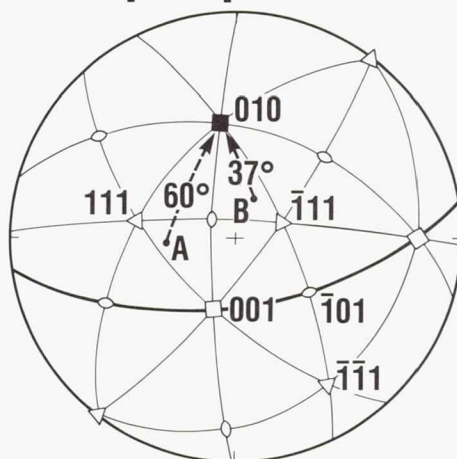
FIGURE 66. – TYPICAL MICROGRAPHS OF A TILTING EXPERIMENT OF A [$\bar{3}$ 6 10] LCF SPECI-MEN, 650 °C, $\Delta\varepsilon_{IN.} > .002$ MM/MM ON CYCLE 1, g/5g WBDF.

139

A. DISLOCATIONS PARALLEL TO FOIL PLANE.

CASE A

B. DISLOCATIONS AT AN ARBITRARY ANGLE.

CASE B

$\vec{u}$ – DISLOCATION LINE DIRECTION
$\vec{u}'$ – 2-D PROJECTION OF $\vec{u}$
$\vec{L}$ – LINE OF INTERSECTION OF THE DISLOCATION PAIR PLANE AND THE FOIL SURFACE
$\vec{L}'$ – 2-D PROJECTION OF $\vec{L}$

CD-87-23969
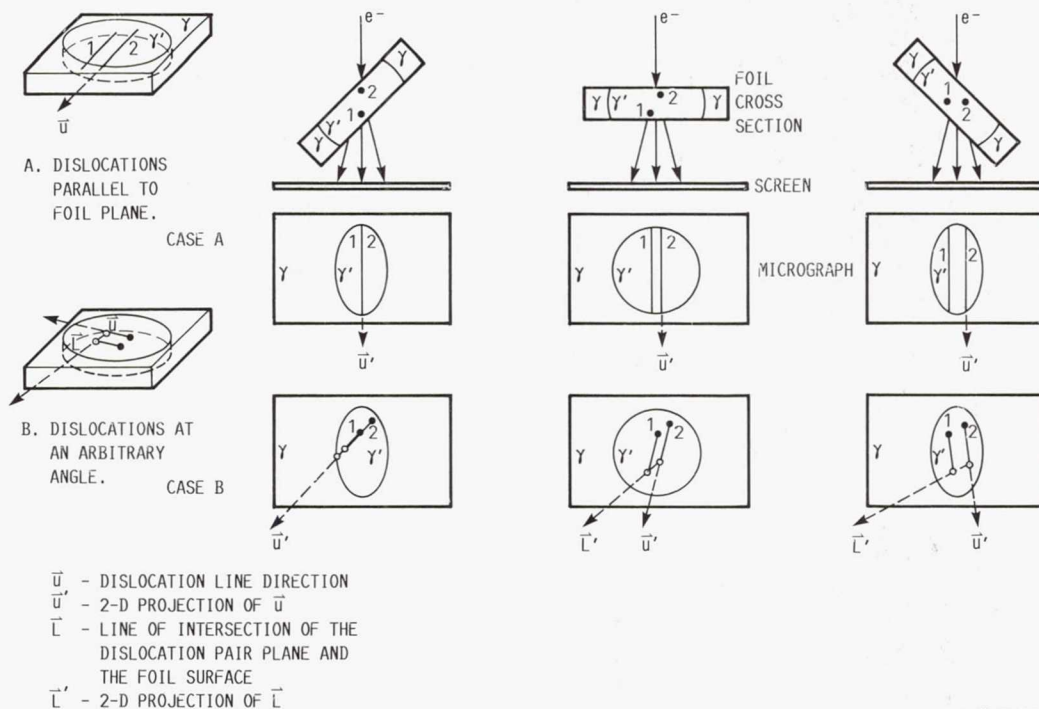
FIGURE 67. – SCHEMATIC ILLUSTRATION OF THE TILTING OF γ' DISLOCATION PAIRS.

(A) [112] Z.A.
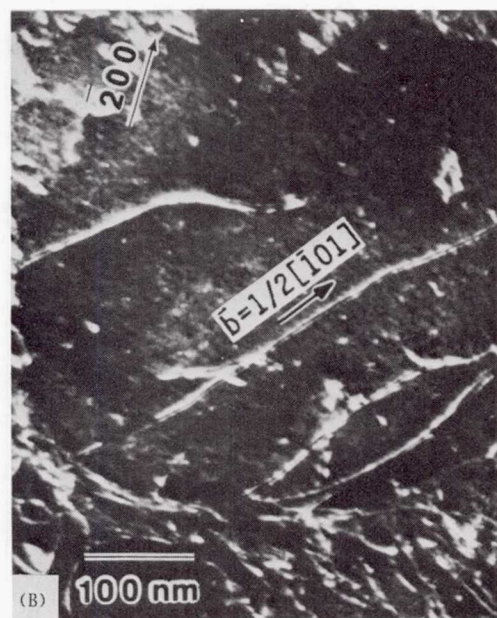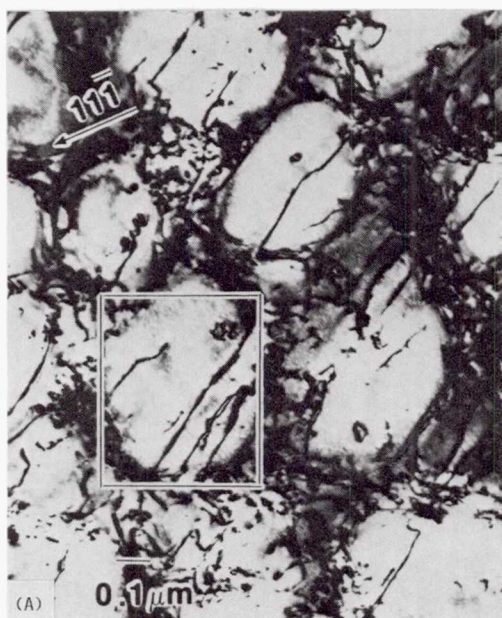
(B) [012] Z.A., g/3g WBDF.

FIGURE 68. – THE γ' DISLOCATION PAIRS OF A [$\bar{3}$ 6 10] LCF SPECIMEN, 650 $^\circ$C, $\Delta\varepsilon_{IN.}$ > .002 MM/MM ON CYCLE 1, (111) FOIL.

(A) [012] Z.A.

(B) [001] Z.A.
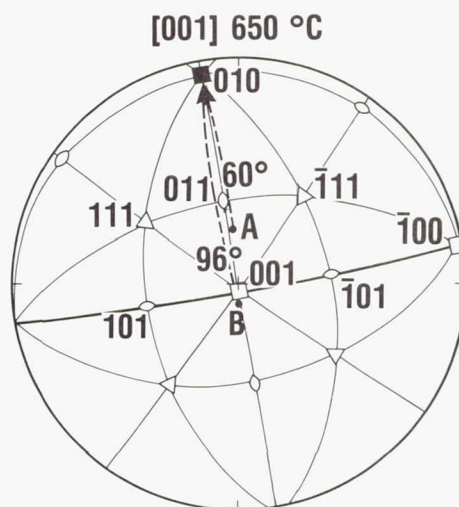
FIGURE 69. – TYPICAL MICROGRAPHS OF A TILTING EXPERIMENT OF AN [001] LCF SPECIMEN, 650 $^\circ$C, $\Delta\varepsilon_{IN.}$ > .002 MM/MM ON CYCLE 1, g/3g WBDF.
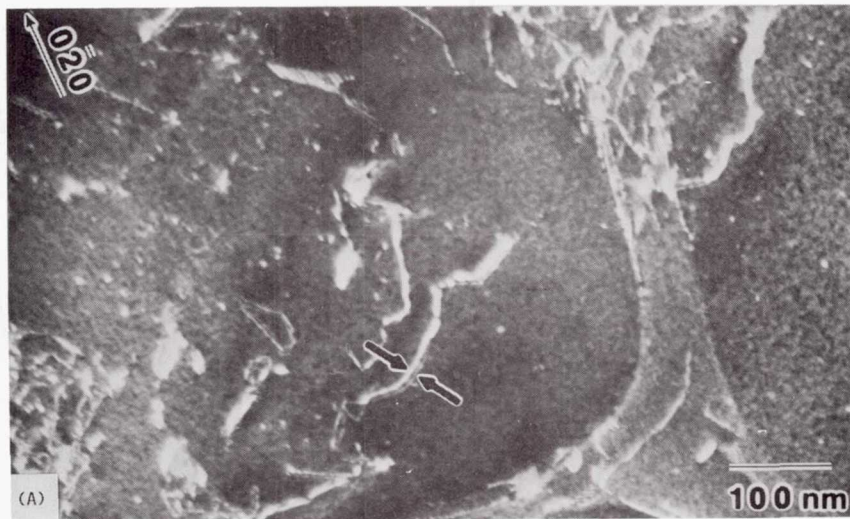
(A) [001] Z.A.

(B) [010] Z.A.

[$\bar{2}$34] 650 °C
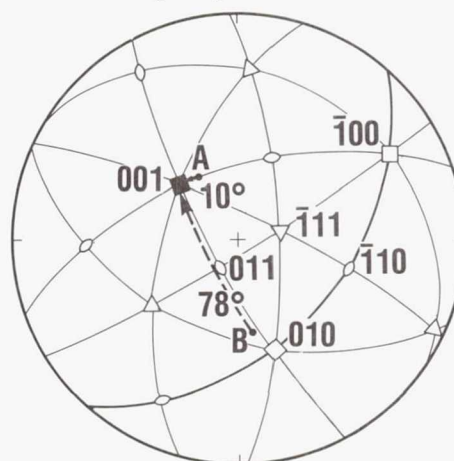
FIGURE 70.. - TYPICAL MICROGRAPHS OF A TILTING EXPERIMENT OF A [$\bar{2}$ 3 4] LCF SPECIMEN,
650 °C, $\Delta\varepsilon_{IN.} > .002$ MM/MM ON CYCLE 1, $g/3g$ WBDF.

142
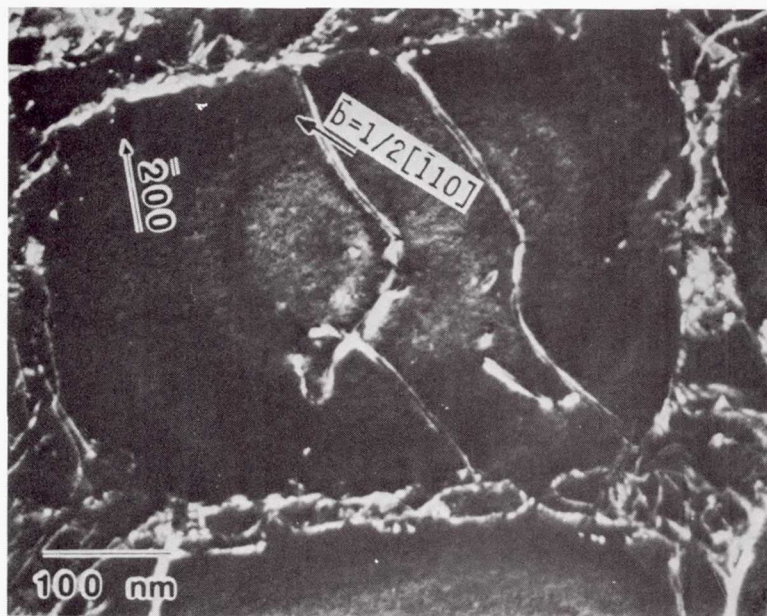
FIGURE 71. – THE γ′ DISLOCATION PAIRS OF A [$\bar{2}$ 3 4] LCF SPECIMEN, 650 °C, $\Delta\varepsilon_{IN.}$ > .002 MM/MM ON CYCLE 1, (001) FOIL, g/3g WBDF, [001] Z.A.

(A) [$\bar{2}31$] Z.A.
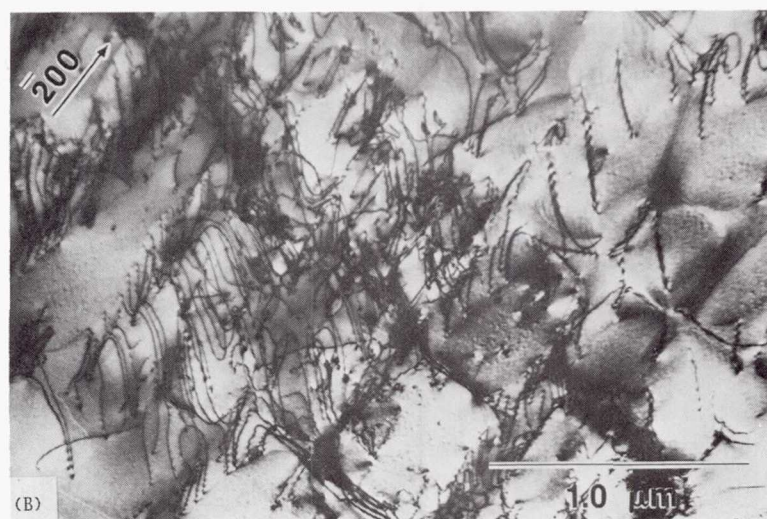
(B) [$0\bar{1}4$] Z.A.
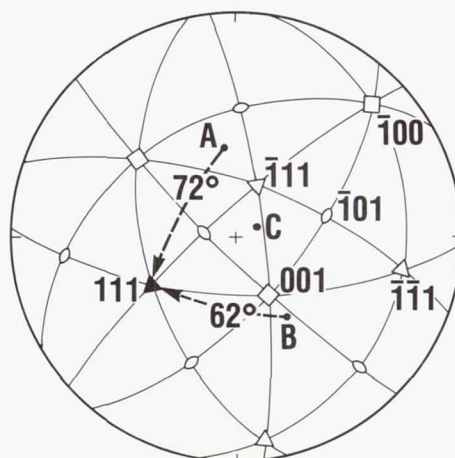
[$\bar{3}$ 6 10] 650 °C

FIGURE 72. – MICROGRAPHS OF A TYPICAL TILTING EXPERIMENT OF A [$\bar{3}$ 6 10] LCF SPECIMEN, 650 °C, γ_c = .062 MM/MM.

(C) [Ī12] Z.A.

[3̄ 6 10] 650 °C
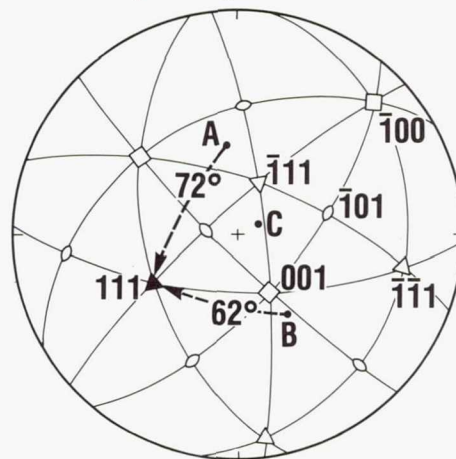
CD-87-29816

FIGURE 72. - CONCLUDED.

145
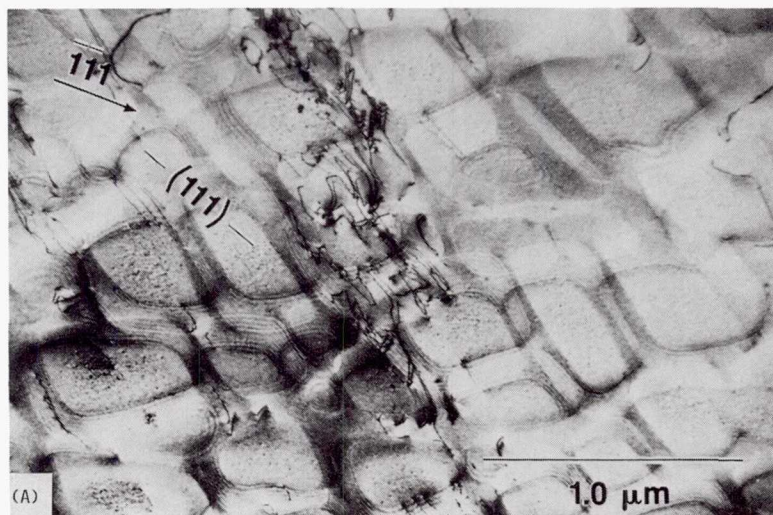
(A) [$\bar{2}31$] Z.A.

[$\bar{3}$ 6 10] 650 °C

CD-87-29816

FIGURE 73. - NARROW SLIP BAND OF A [3 6 10] LCF SPECIMEN, 650 °C, γ_C = .062 MM/MM.
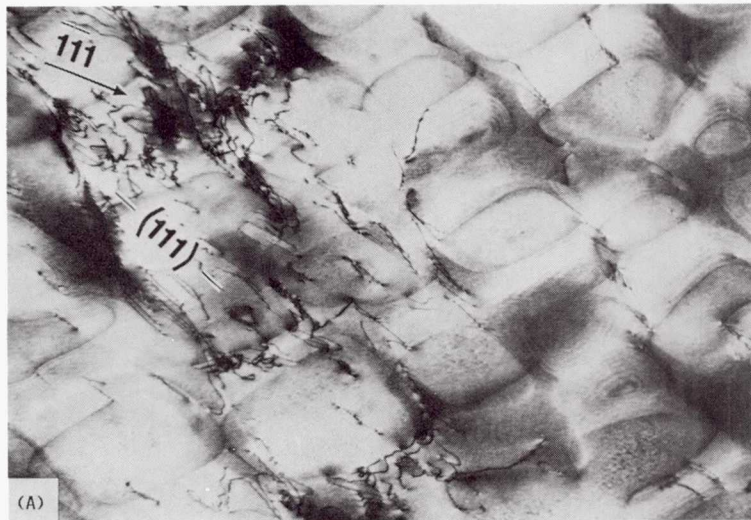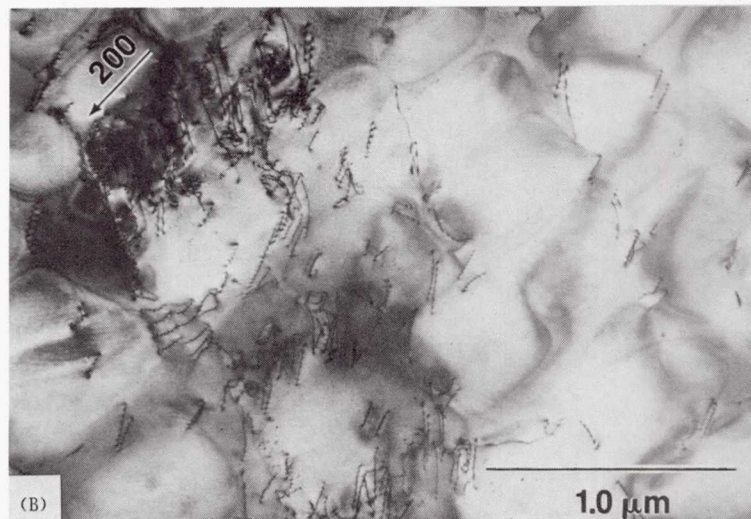
(A) [$\bar{2}$31] Z.A.

(B) [0$\bar{1}$4] Z.A.
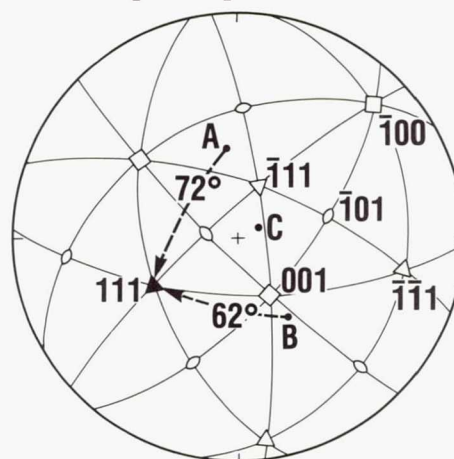
[$\bar{3}$ 6 10] 650 °C

CD-87-29816

FIGURE 74. - MICROGRAPHS OF A TYPICAL TILTING EXPERIMENT OF A [$\bar{3}$ 6 10] TENSILE
SPECIMEN, 650 °C, γ_C = .039 MM/MM.

(C) [Ī12] Z.A.
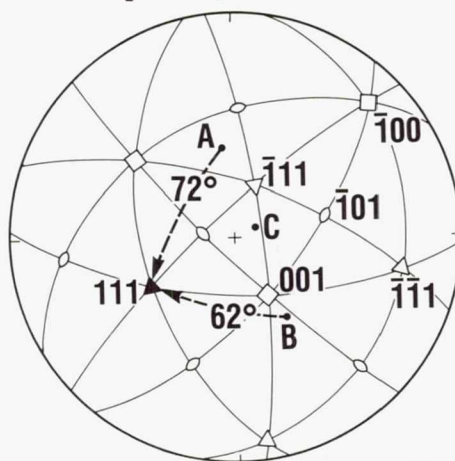
[3̄ 6 10] 650 °C

FIGURE 74. - CONCLUDED.
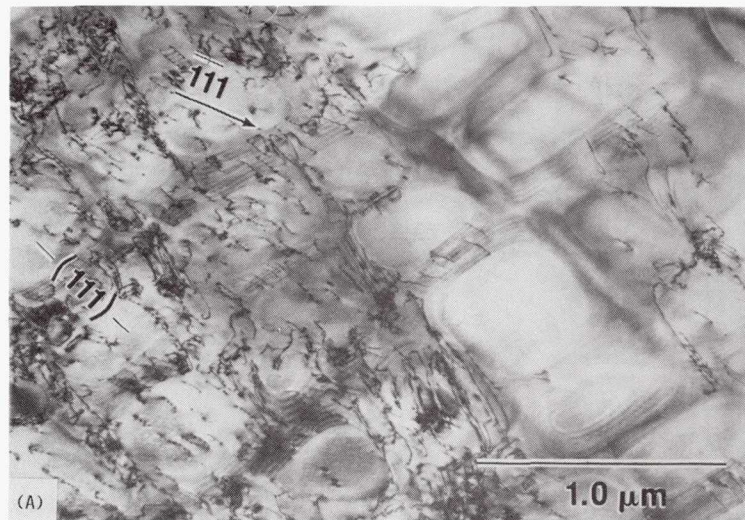
(A) [$\bar{2}$31] Z.A.

[$\bar{3}$ 6 10] 650 °C
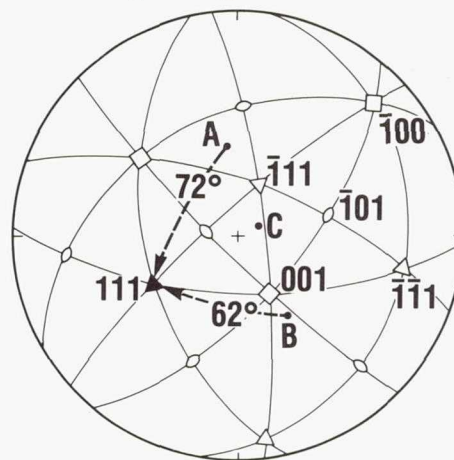
CD-87-29816

FIGURE 75. - BROAD AND NARROW SLIP BANDS OF A [$\bar{3}$ 6 10] TENSILE SPECIMEN, 650 °C, γ_C = . 039 MM/MM.
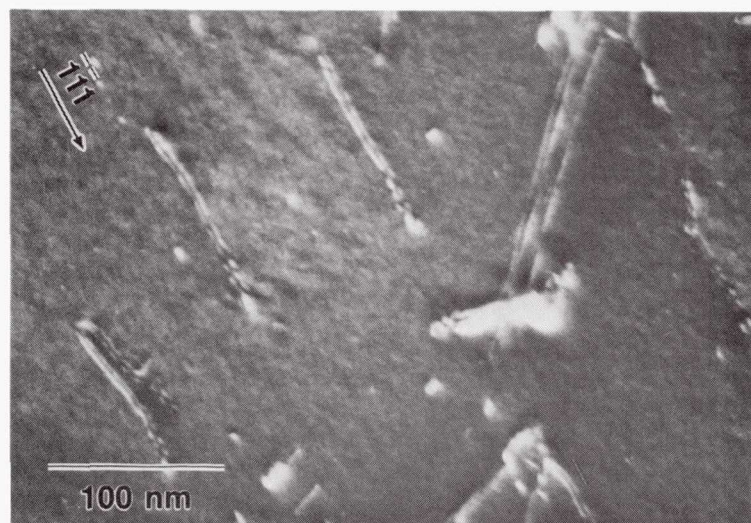
FIGURE 75. - CONCLUDED. THE γ' DISLOCATION PAIRS OF A [$\bar{3}$ 6 10] TENSILE SPECIMEN, 650 °C, γ_C = .039 MM/MM, g/3g WBDF, [$\bar{1}$21] Z.A.
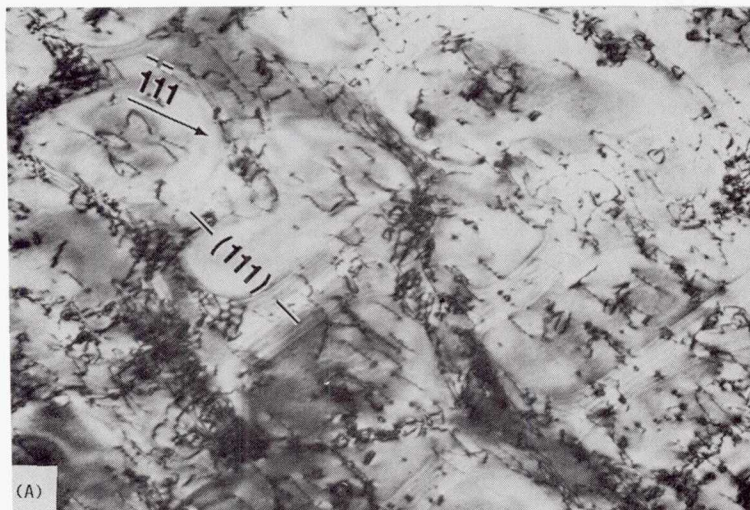
(A) [$\bar{2}31$] Z.A.
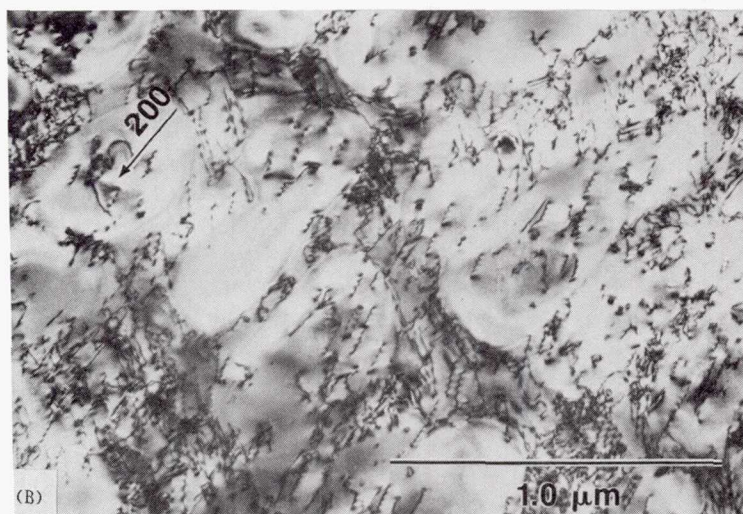
(B) [$0\bar{1}4$] Z.A.
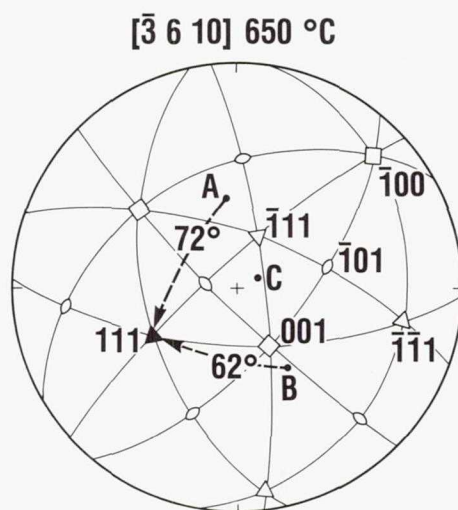
[$\bar{3}$ 6 10] 650 °C

CD-87-29816

FIGURE 76. – MICROGRAPHS OF A TYPICAL TILTING EXPERIMENT OF A [$\bar{3}$ 6 10] LCF
SPECIMEN TESTED TO FAILURE, 650 °C, $\Delta\varepsilon_{IN.1}$ >.002 MM/MM ON CYCLE 1.

(C) [$\bar{1}$12] Z.A.
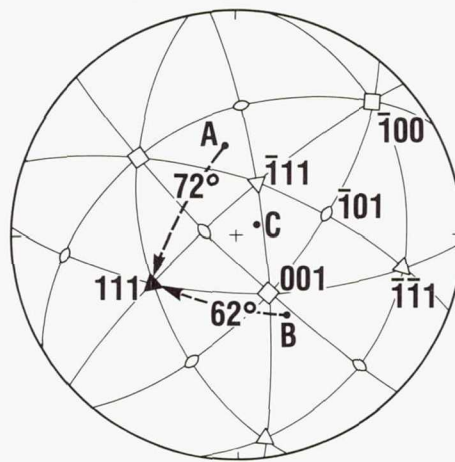
[$\bar{3}$ 6 10] 650 °C

CD-87-

FIGURE 76. - CONCLUDED.
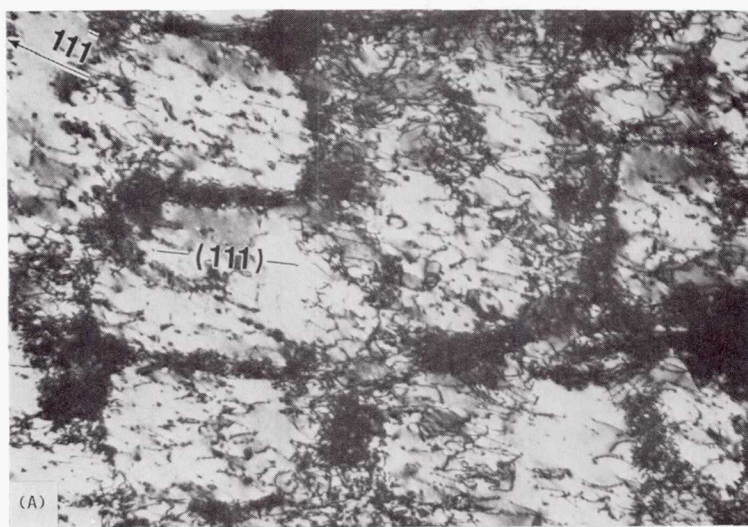
(A) [$\bar{2}$31] Z.A.
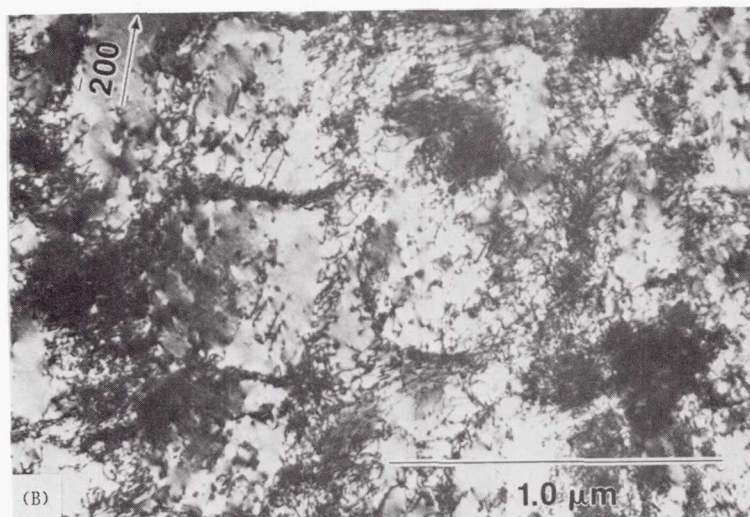
(B) [$0\bar{1}4$] Z.A.

[$\bar{3}$ 6 10] 650 °C
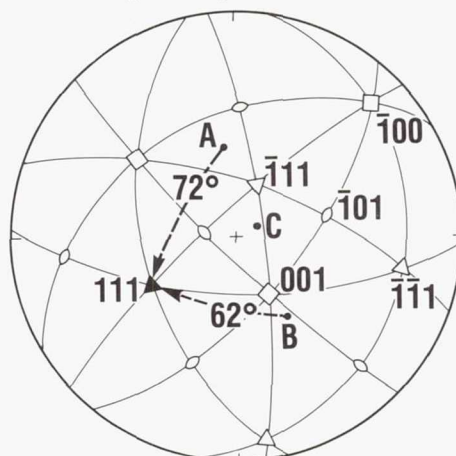
FIGURE 77. - MICROGRAPHS OF A TYPICAL TILTING EXPERIMENT OF A [$\bar{3}$ 6 10] TENSILE
SPECIMEN TESTED TO FAILURE, 650 °C.
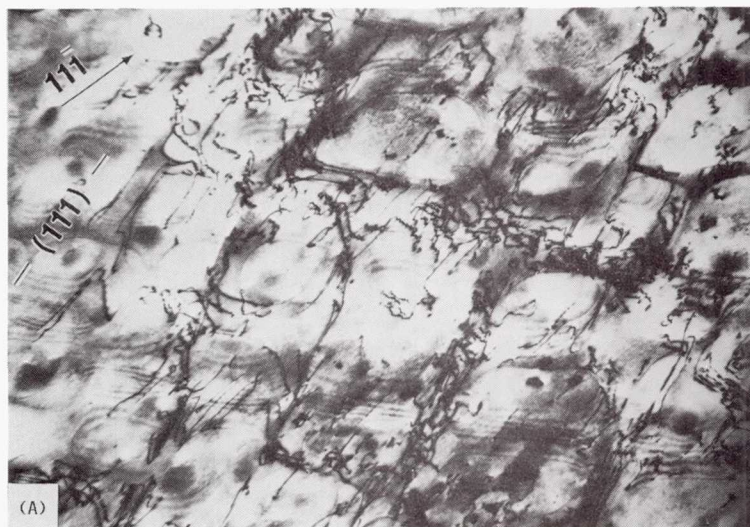
(A) [2̄31] Z.A.

(B) [012] Z.A.
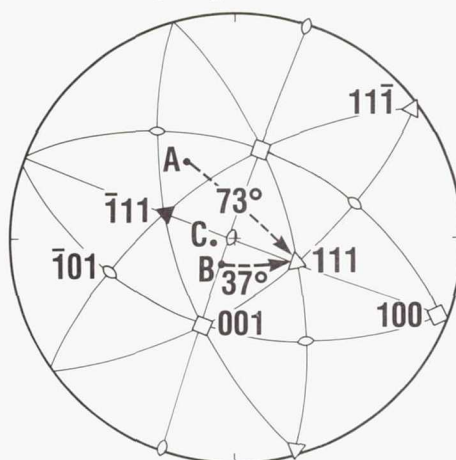
[011] 650 °C

FIGURE 78. - MICROGRAPHS OF A TYPICAL TILTING EXPERIMENT OF AN [011] LCF SPECI-
MEN, 650 °C, γ_C = .096 MM/MM.

(C) [011] Z.A.

FIGURE 78. - CONCLUDED.
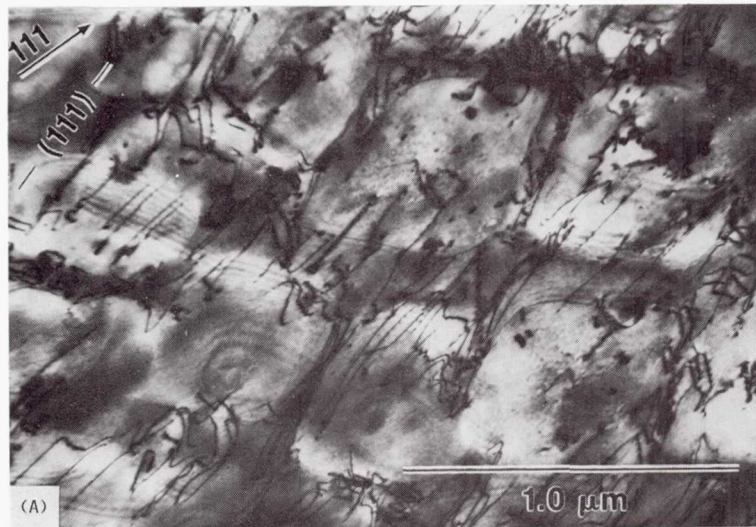
(A) [2̄31] Z.A.

[011] 650 °C
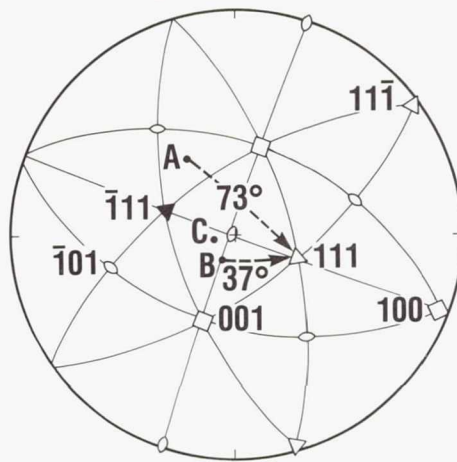
FIGURE 79. – ANOTHER SLIP BAND OF AN [011] LCF SPECIMEN, 650 °C, γ_c = .096 MM/MM.
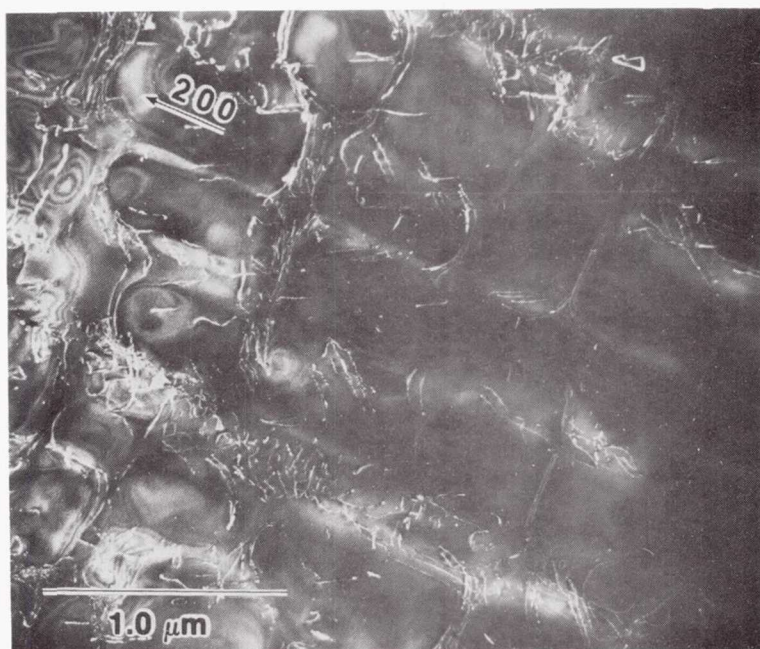
(A) LOW MAGNIFICATION.

(B) HIGH MAGNIFICATION.

FIGURE 80. – THE DISLOCATION ENTANGLEMENTS OF FIGURE 76(A), [012] Z.A., g/3g WBDF.
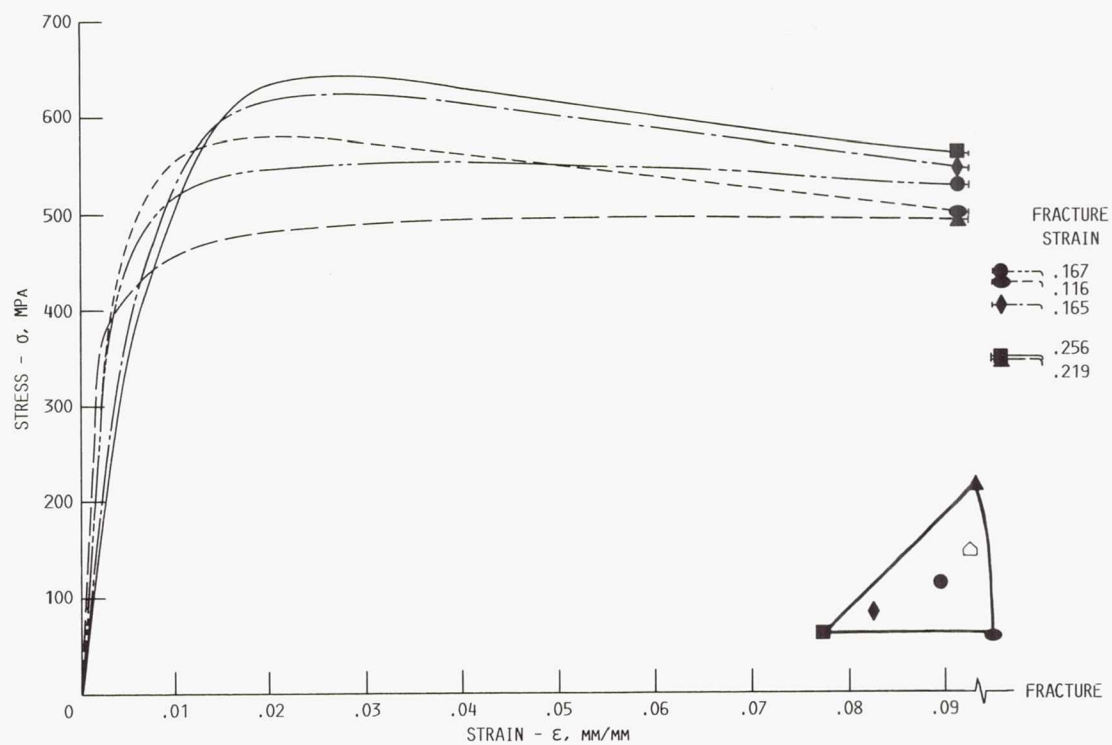
FIGURE 81. – THE AXIAL STRESS-STRAIN RESPONSE IN THE TENSILE TESTS AT 1050 °C.
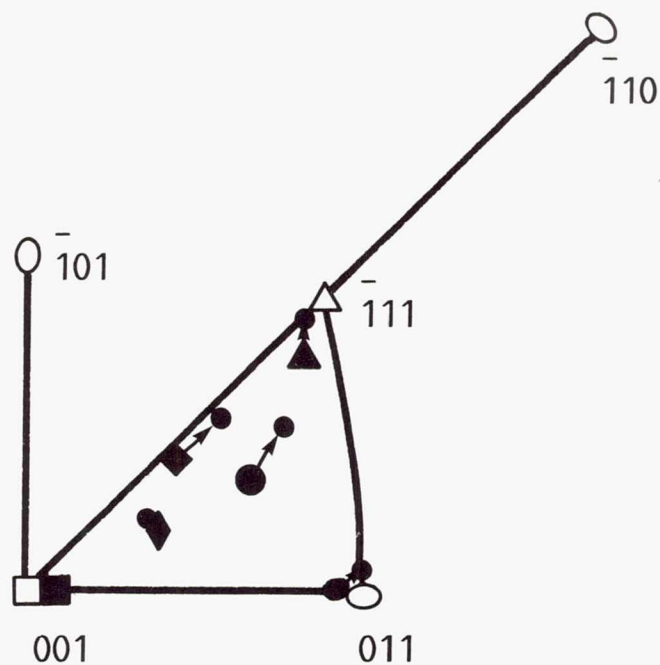
FIGURE 82. – THE CRYSTALLOGRAPHIC
ROTATIONS OF THE SPECIMEN AXES
IN TENSILE TESTS AT 1050 °C.
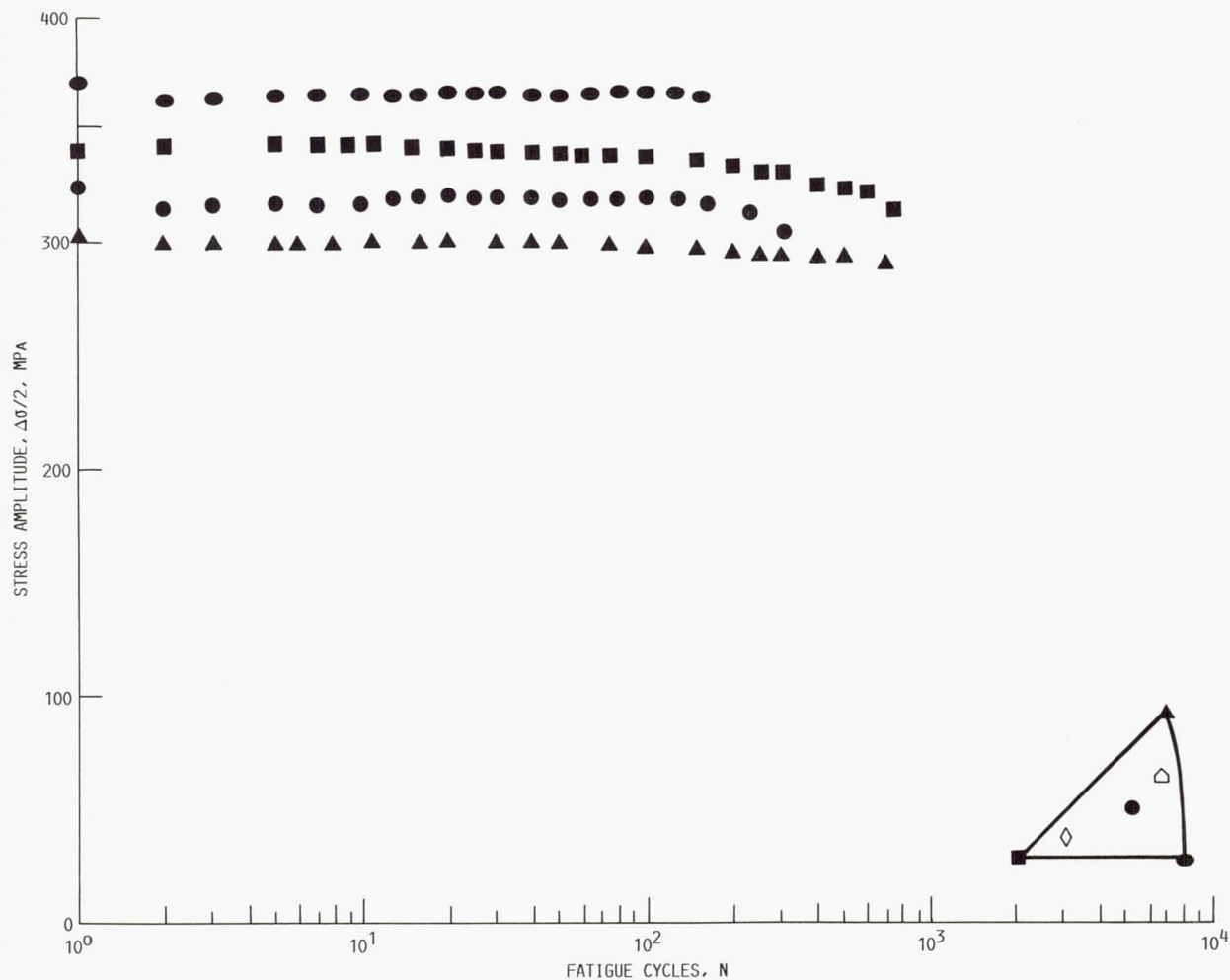
FIGURE 83. - THE LCF STRESS RESPONSE OF SPECIMENS TESTED AT $\Delta\varepsilon_{IN.1} \sim .0027$ MM/MM AT 1050 ^{O}C.
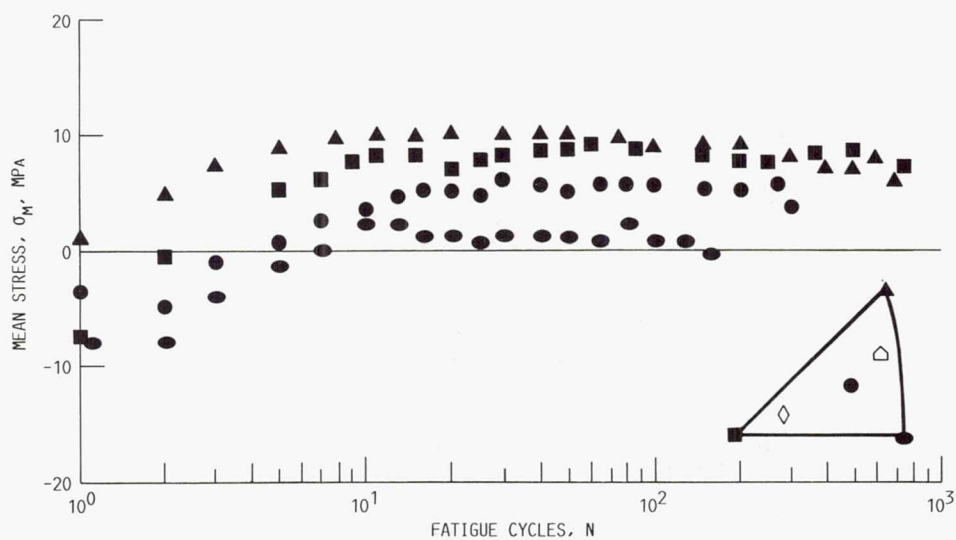
FIGURE 84. - THE LCF MEAN STRESS REPONSE OF SPECIMENS TESTED AT $\Delta\varepsilon_{IN.1} \sim .0027$ MM/MM AT 1050 ^{O}C.
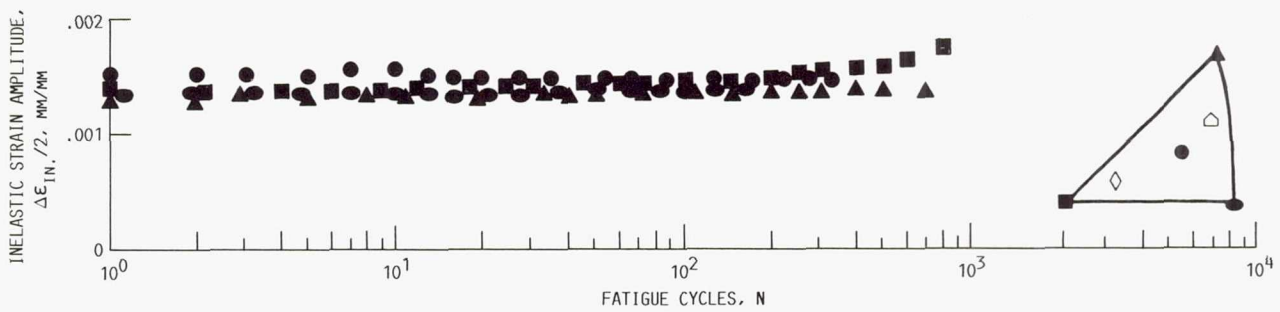
FIGURE 85. – THE LCF INELASTIC STRAIN RESPONSE OF SPECIMENS TESTED AT $\Delta\varepsilon_{IN.1} \sim .0027$ MM/MM AT 1050 ^{O}C.

[001] ■

STRESS – σ, MPA

$\sigma_t \approx \sigma_c$
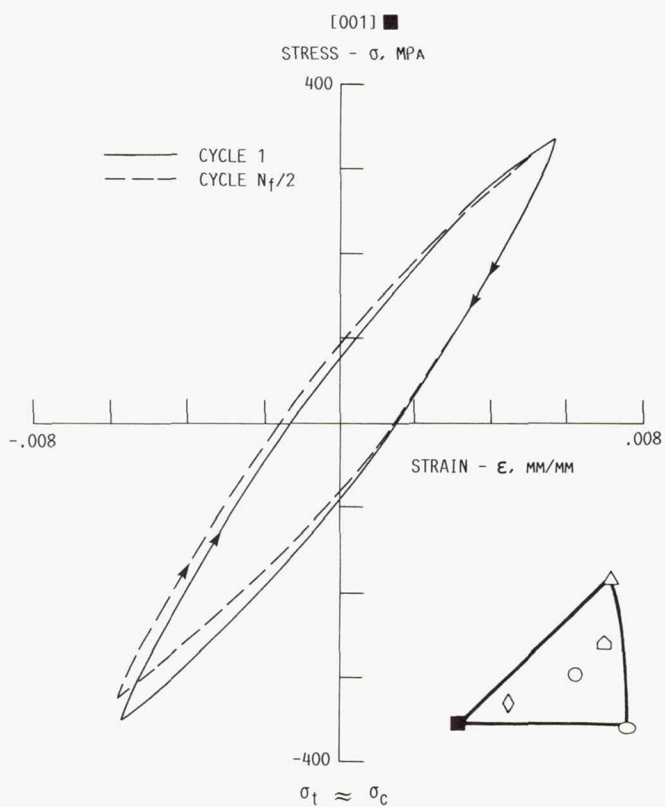
FIGURE 86. – TYPICAL LCF HYSTERESIS LOOPS OF THE [001] SPECIMEN, 1050 ^{O}C, $\Delta\varepsilon_{IN.1} \sim .0027$ MM/MM.

[$\bar{1}$11] ▲

STRESS – σ, MPA

$\sigma_t > \sigma_c$
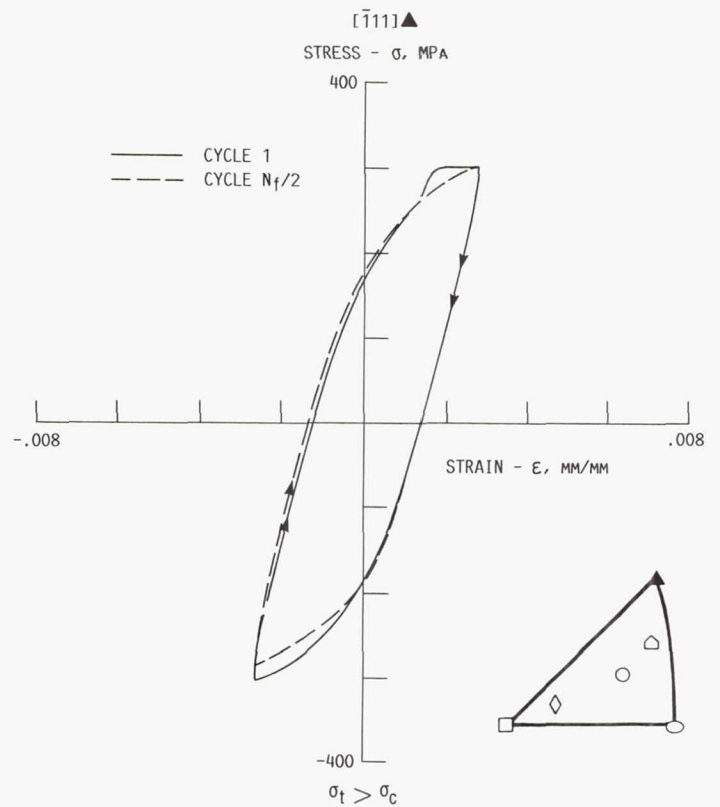
FIGURE 87. – TYPICAL LCF HYSTERESIS LOOPS OF THE [111] SPECIMEN, 1050 ^{O}C, $\Delta\varepsilon_{IN.1} \sim .0027$ MM/MM.
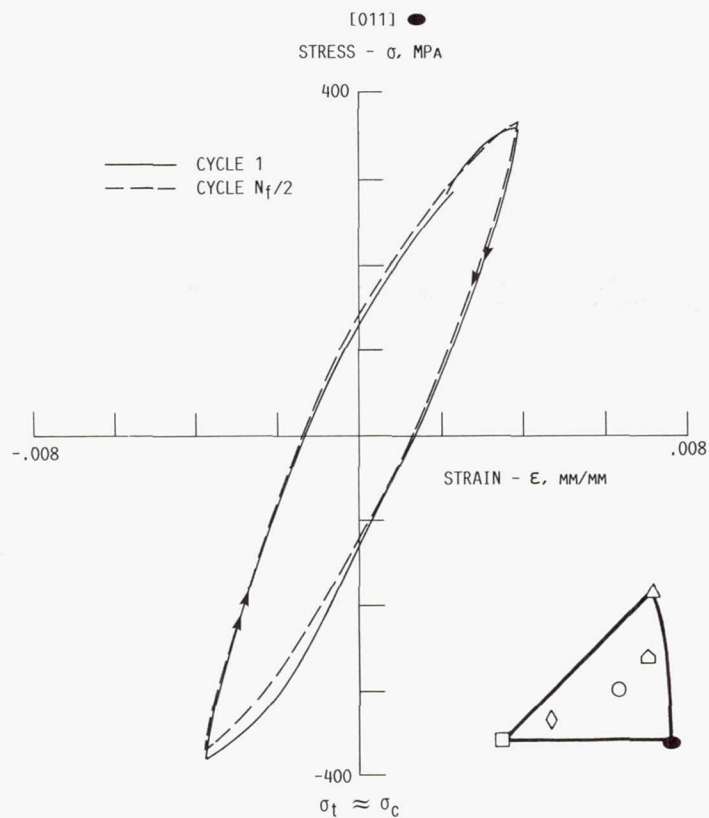
FIGURE 88. – TYPICAL LCF HYSTERESIS LOOPS OF THE [011] SPECIMEN
1050 $^{\circ}$C, $\Delta\varepsilon_{IN.1} \sim .0027$ MM/MM.
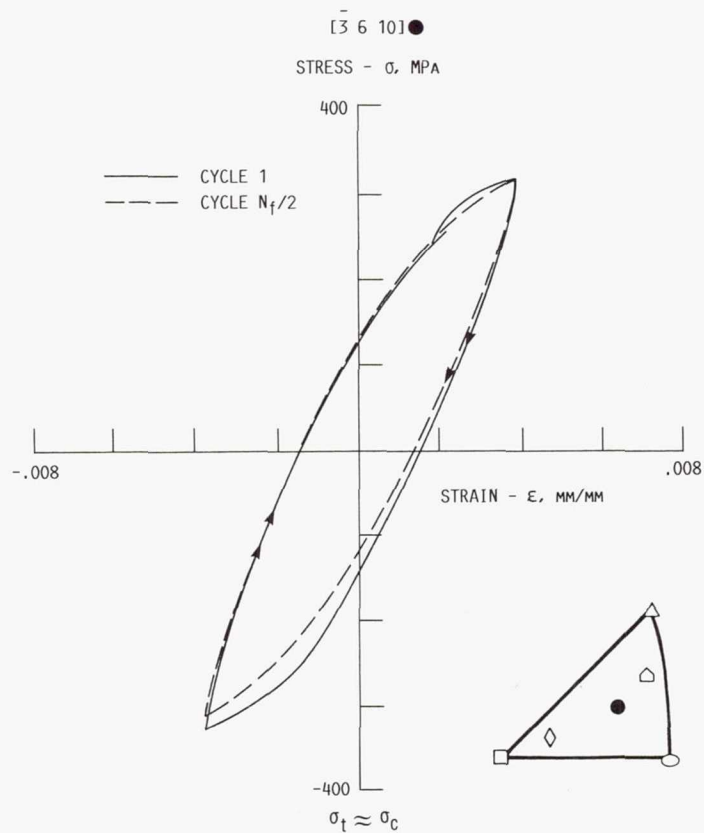
FIGURE 89. – TYPICAL LCF HYSTERESIS LOOPS OF THE [$\bar{3}$ 6 10] SPECIMEN,
1050 $^{\circ}$C, $\Delta\varepsilon_{IN.1} \sim .0027$ MM/MM.

160
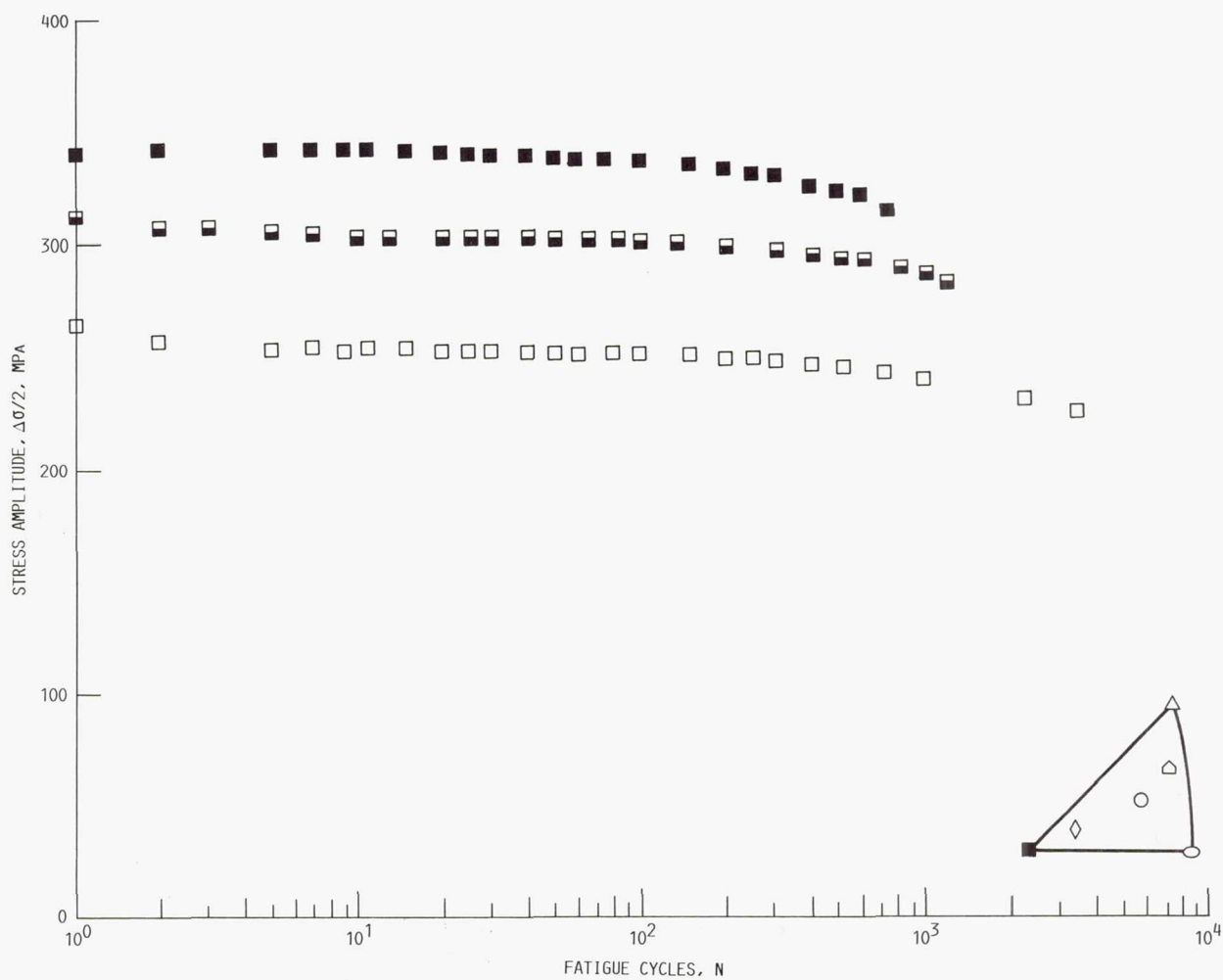
FIGURE 90. - THE LCF STRESS RESPONSE OF THE [001] SPECIMENS AT 1050 °C.
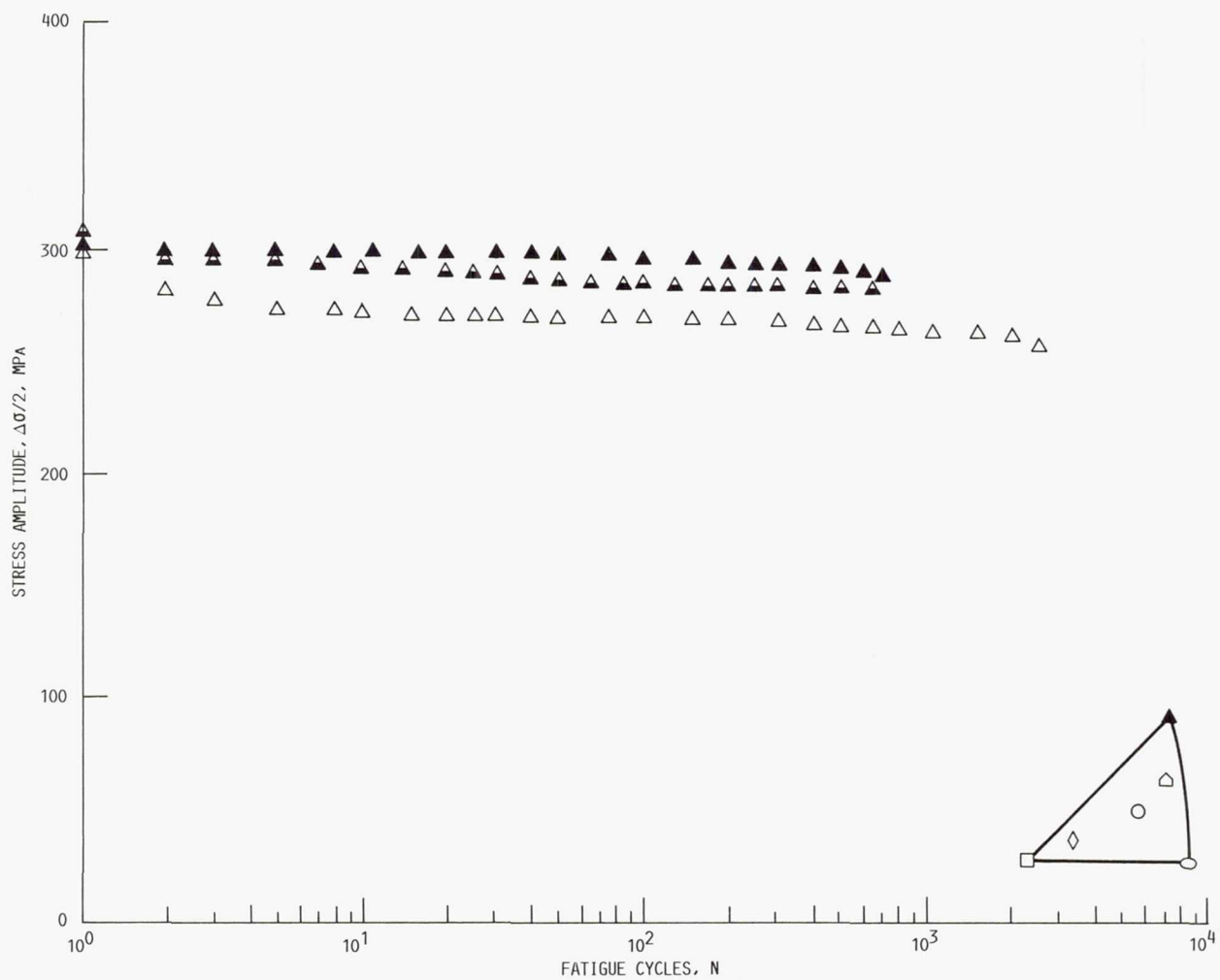
FIGURE 91. - THE LCF STRESS RESPONSE OF THE [111] SPECIMENS AT 1050 °C.
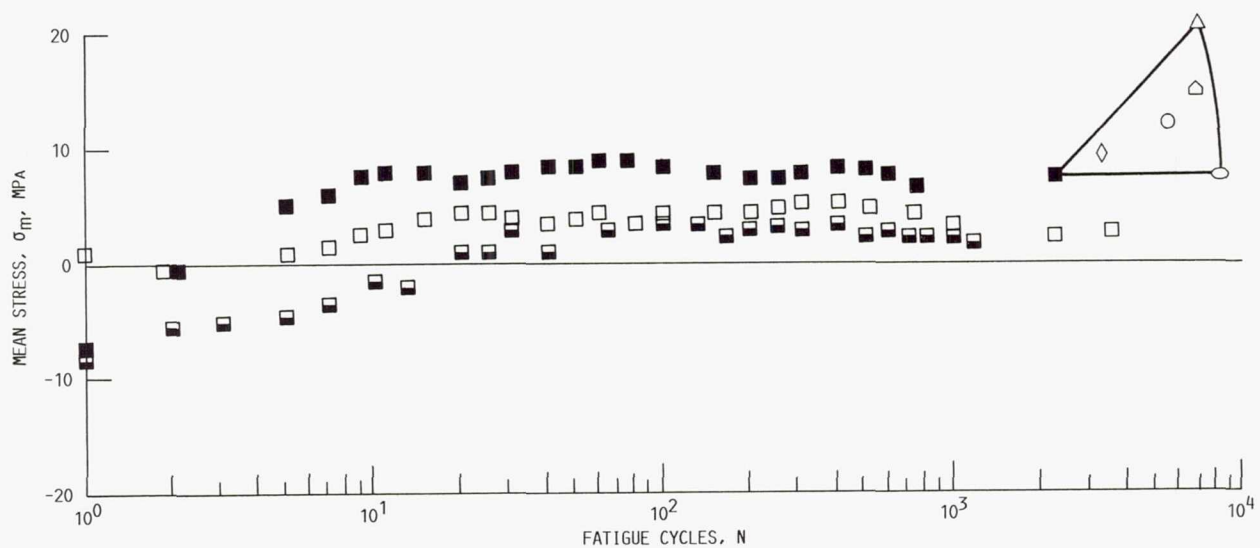
FIGURE 92. - THE LCF MEAN STRESS RESPONSE OF THE [001] SPECIMENS AT 1050 °C.
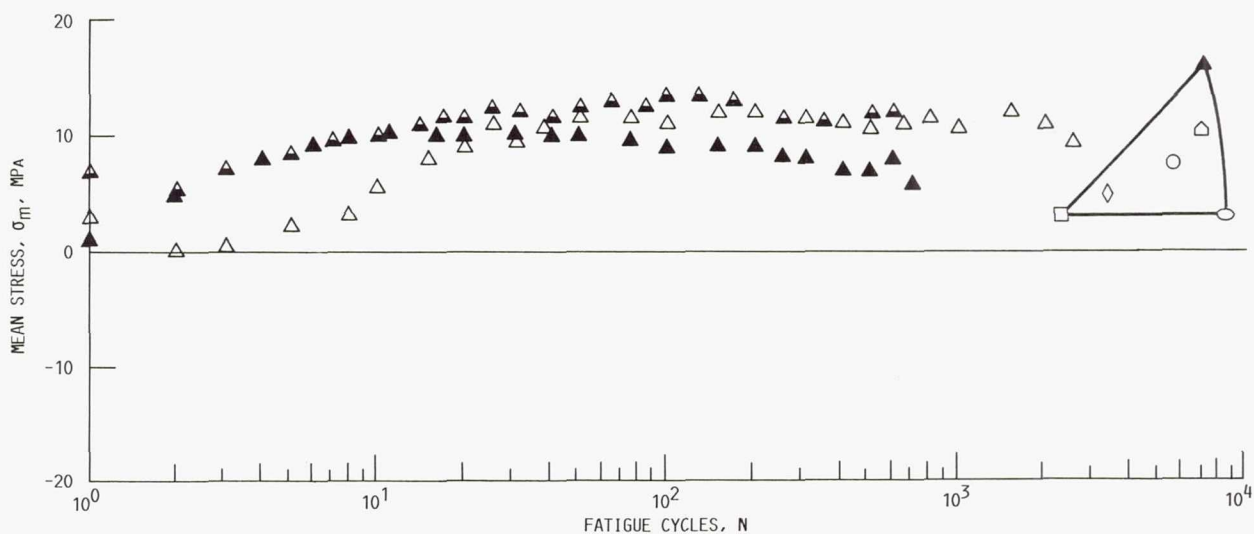
FIGURE 93. – THE LCF MEAN STRESS RESPONSE OF THE [$\bar{1}11$] SPECIMENS AT 1050 $^{\circ}$C.
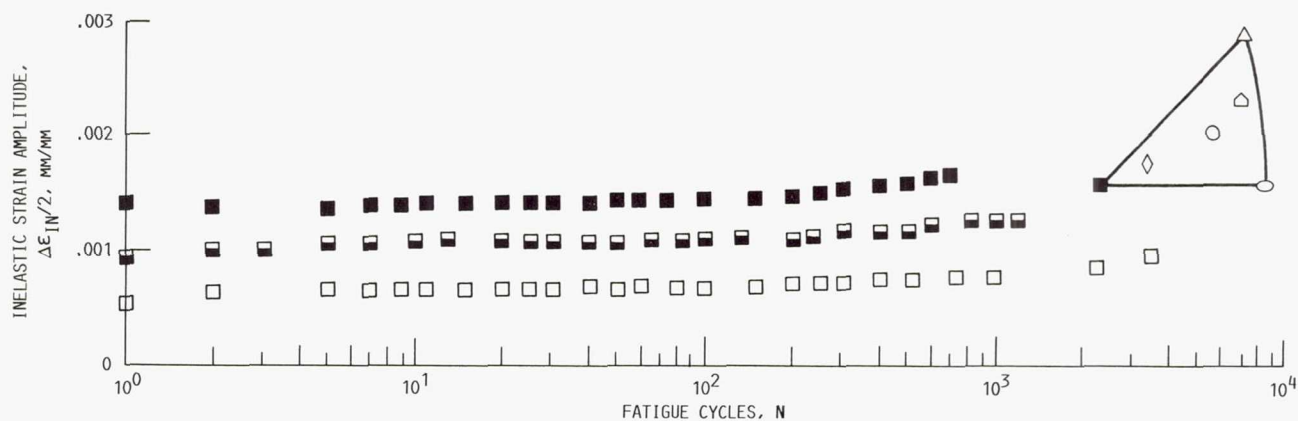
FIGURE 94. – THE LCF INELASTIC STRAIN RESPONSE OF THE [001] SPECIMENS AT 1050 $^{\circ}$C.
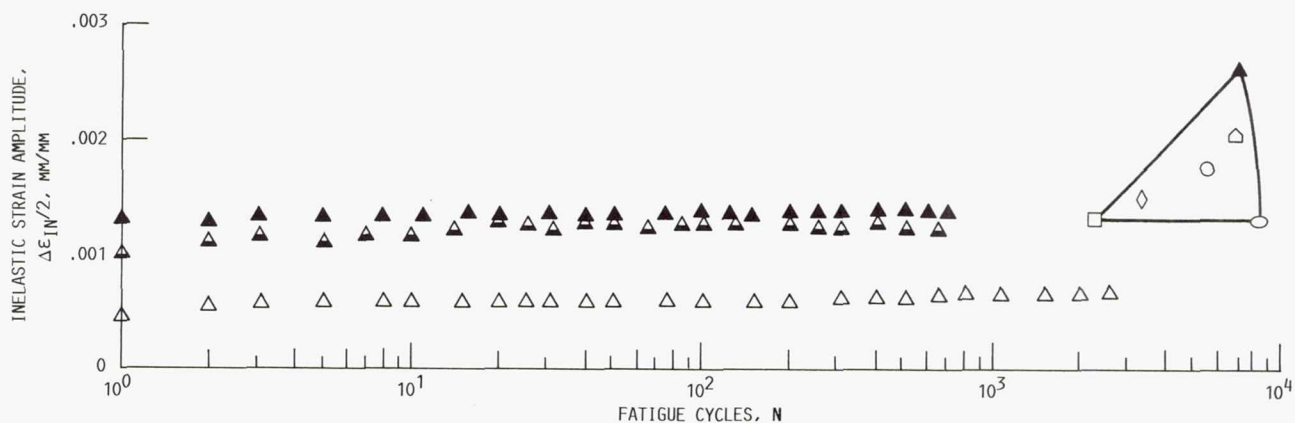
FIGURE 95. – THE LCF INELASTIC STRAIN RESPONSE OF THE [$\bar{1}11$] SPECIMENS AT 1050 $^{\circ}$C.

163

[001] □
STRESS - σ, MPA
400

CYCLE 1
CYCLE N$_f$/2

-.008
.008
STRAIN - ε, MM/MM

σ$_t$ ≈ σ$_c$

-400
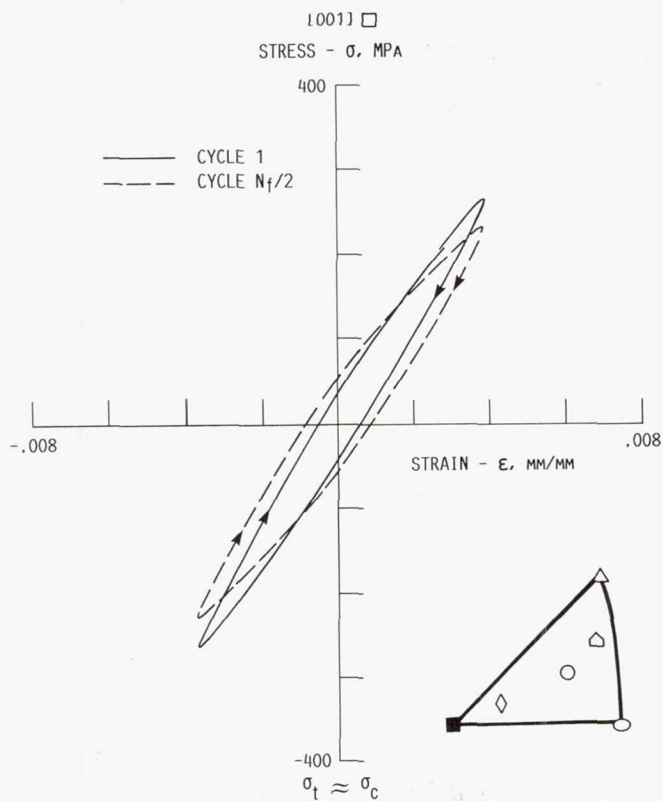
FIGURE 96. - TYPICAL LCF HYSTERESIS LOOPS OF THE [001] SPECIMEN, 1050 °C, Δε$_{IN. 1}$ ~ .001 MM/MM.

[$\overline{1}$11] △
STRESS - σ, MPA
400

CYCLE 1
CYCLE N$_f$/2

.008
STRAIN - ε, MM/MM

σ$_t$ > σ$_c$

-400
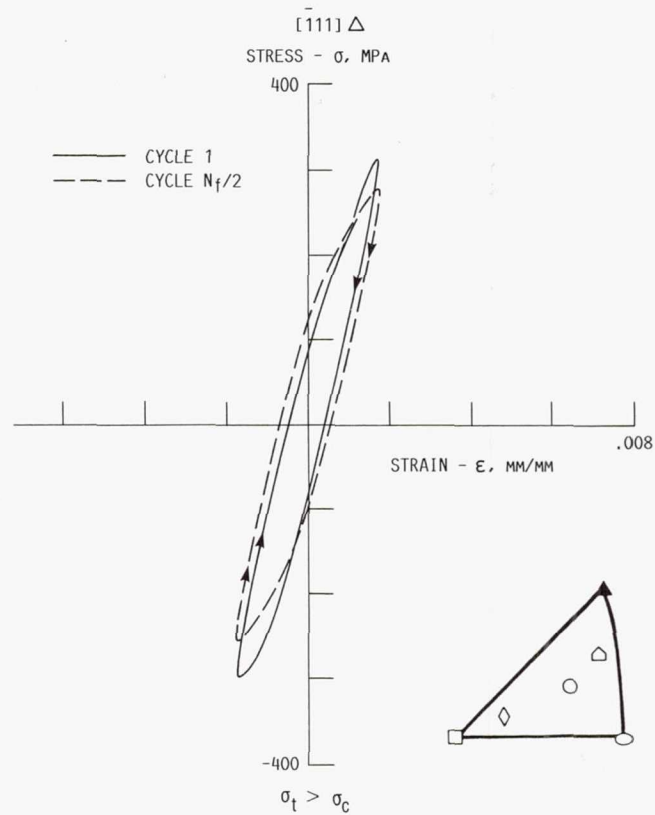
FIGURE 97. - TYPICAL LCF HYSTERESIS LOOPS OF THE [$\overline{1}$11] SPECIMEN, 1050 °C, Δε$_{IN.1}$ ~ .001 MM/MM.

1000
800
600

400

STRESS AMPLITUDE, Δσ/2, MPA

200

100
10^{-4}
10^{-3}
10^{-2}
INELASTIC STRAIN AMPLITUDE, Δε$_{IN.}$/2, MM/MM
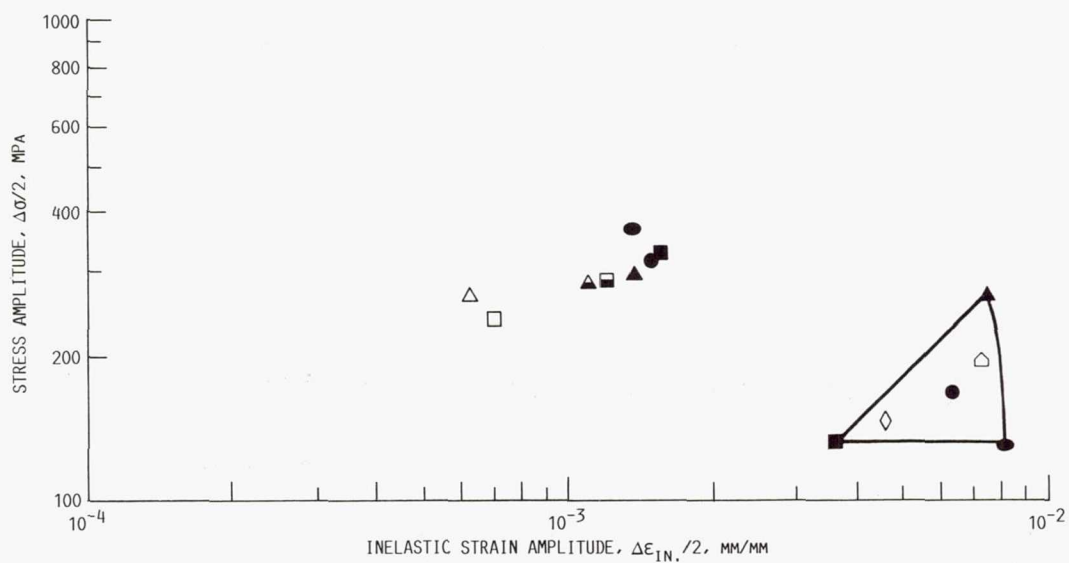
FIGURE 98. - THE CYCLIC STRESS-STRAIN RESPONSE AT HALF OF CYCLIC LIFE OF THE LCF TESTS AT 1050 °C.

164

FIGURE 100. - NUMEROUS SURFACE CRACKS OF AN [001] LCF SPECIMEN, 1050 ^{O}C, $\Delta\varepsilon_{IN.}$ ~.0027 MM/MM ON CYCLE 1, INTERRUPTED AT 400 CYCLES (0.5 N_f).
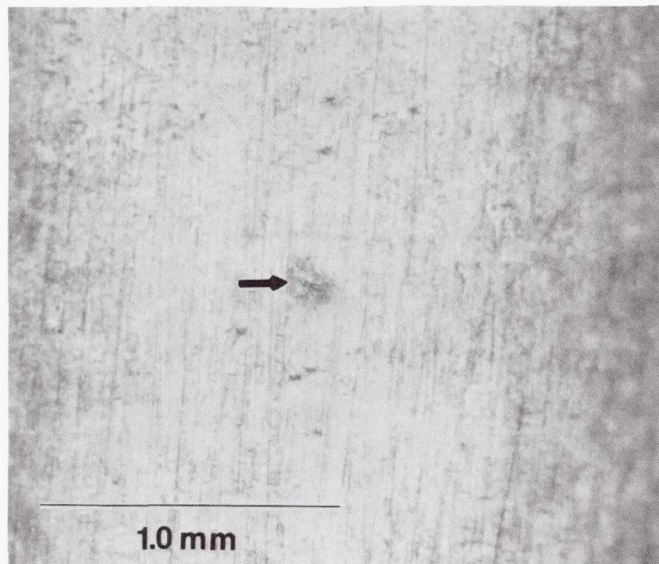
(A) SHALLOW OXIDE SCALE RUPTURE.
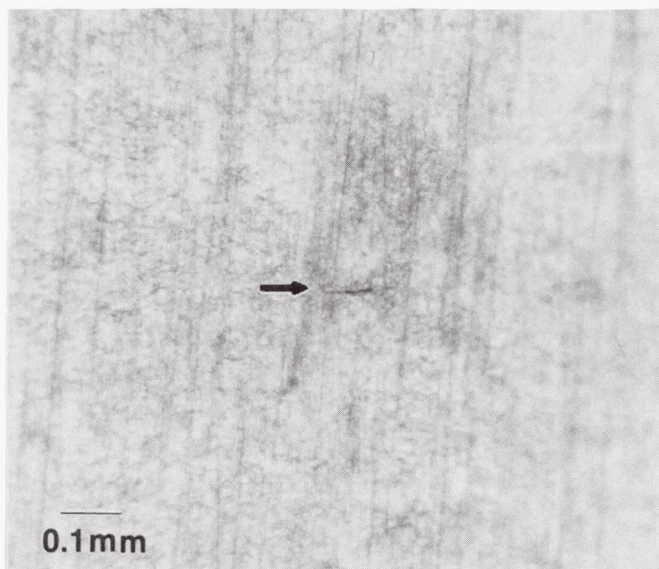
(B) SINGLE SURFACE CRACK.

FIGURE 99. - SURFACE OF AN [001] LCF SPECIMEN, 1050 ^{O}C, $\Delta\varepsilon_{IN.}$ ~ .0027 MM/MM ON CYCLE 1, INTERRUPTED AT 200 CYCLES (0.25 N_f).
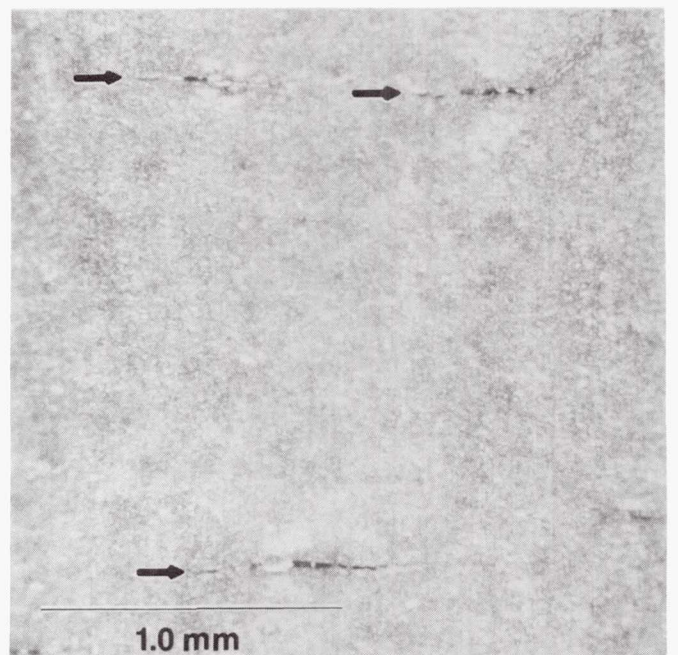
FIGURE 101. - LARGER SURFACE CRACKS OF AN [001] LCF SPECIMEN, 1050 ^{O}C, $\Delta\varepsilon_{IN.}$ ~ .0027 MM/MM ON CYCLE 1, INTERRUPTED AT 600 CYCLES (0.75 N_f).
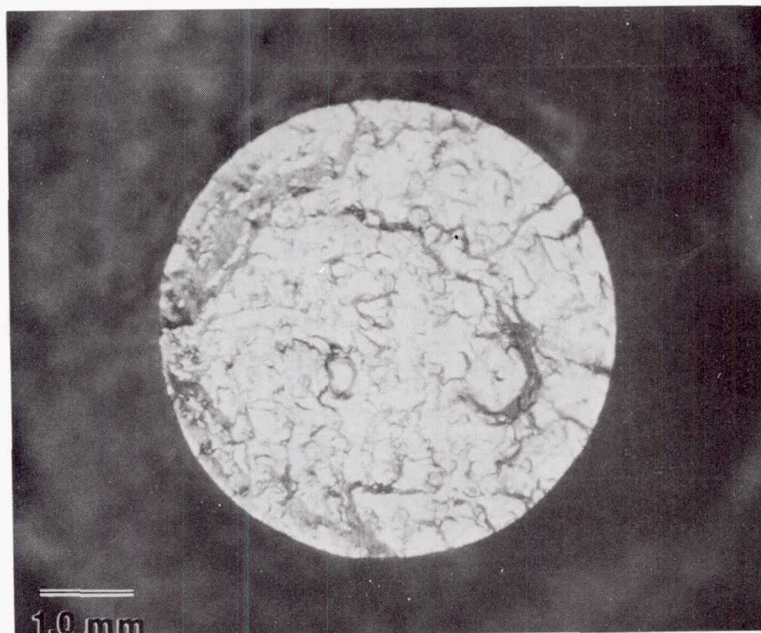
FIGURE 102. – FRACTURE SURFACE OF AN [001] LCF SPECIMEN, 1050 $^\circ$C, $\Delta\varepsilon_{IN.}$ = .0027 MM/MM ON CYCLE 1.
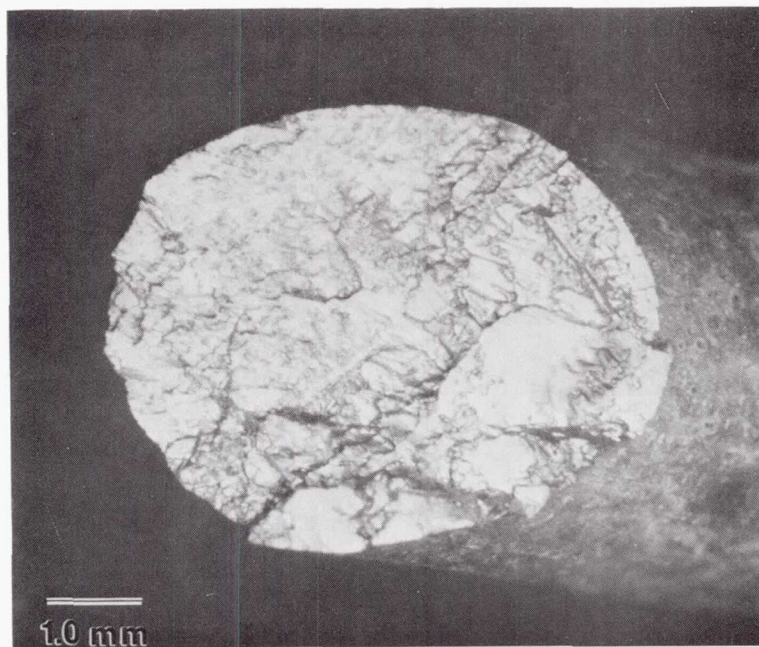
FIGURE 103. – FRACTURE SURFACE OF A [111] LCF SPECIMEN, 1050 $^\circ$C, $\Delta\varepsilon_{IN.}$ = .0027 MM/MM ON CYCLE 1.
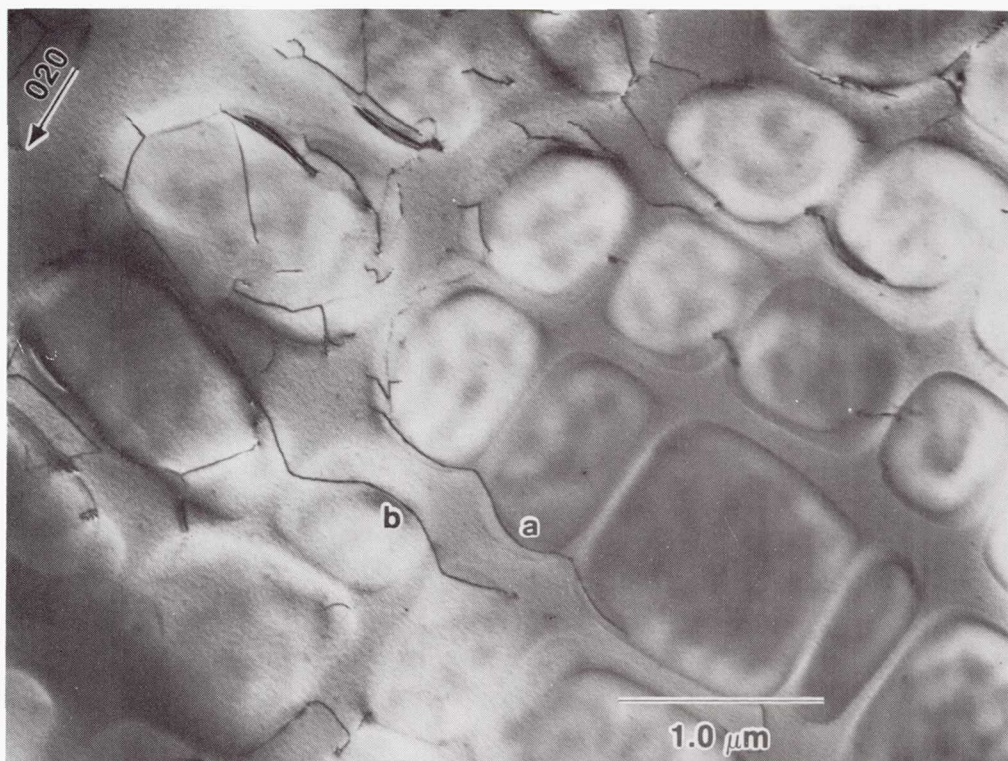
FIGURE 104. – SINGULAR RANDOM DISLOCATIONS IN UNLOADED PWA 1480 EXPOSED 500 HR AT 1050 ^{O}C, [001] Z.A.

FIGURE 105(A). – DISLOCATION NETWORKS IN UNLOADED PWA 1480 EXPOSED 500 HR AT 1050 ^{O}C, [001] Z.A.

167
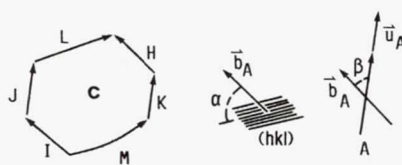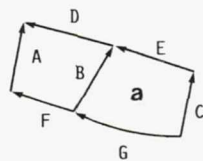
CD-87-29808

DISL.	BURGERS VECTOR	LINE DIR.	INTERF. PLANE	$\bar{B}$-(HKL) ANGLE	$\bar{B}$-$\bar{U}$ ANGLE
	$\bar{B}$	$\bar{U}$	(HKL)	α	β
A	1/2[110]	[4 7 $\bar{6}$]	(1 0 1)	30^0	39^0
B	1/2[110]	[5 $\bar{3}$ $\bar{8}$]	(1 0 1)	30^0	82^0
C	1/2[110]	[8 $\bar{2}$ $\bar{6}$]	(5 2 8)	13^0	65^0
D	1/2[$\bar{1}$10]	[4 9 $\bar{1}$]	(1 0 1)	30^0	69^0
E	1/2[$\bar{1}$10]	[4 9 $\bar{1}$]	(5 $\bar{2}$ 8)	31^0	69^0
F	1/2[$\bar{1}$10]	[4 7 $\bar{6}$]	(1 0 1)	30^0	78^0
G	1/2[$\bar{1}$10]	[4 9 $\bar{1}$]	(5 $\bar{2}$ 8)	31^0	69^0
H	1/2[01$\bar{1}$]	[8 7 0]	(0 $\bar{1}$ 10)	51^0	62^0
I	1/2[01$\bar{1}$]	[8 6 0]	(0 $\bar{1}$ 10)	51^0	65^0
J	1/2[110]	[10 1 2]	(0 $\bar{1}$ 10)	4^0	41^0
K	1/2[110]	[1 0 0]	(0 $\bar{1}$ 10)	4^0	45^0
L	1/2[101]	[2 $\bar{10}$ 0]	(0 $\bar{1}$ 10)	45^0	82^0
M	1/2[101]	[2 $\bar{10}$ $\bar{3}$]	(0 $\bar{1}$ 10)	45^0	86^0

FIGURE 105(B). - RESULTS OF THE ANALYSIS OF SELECTED DISLOCATIONS IN FIGURE 105(A).

168
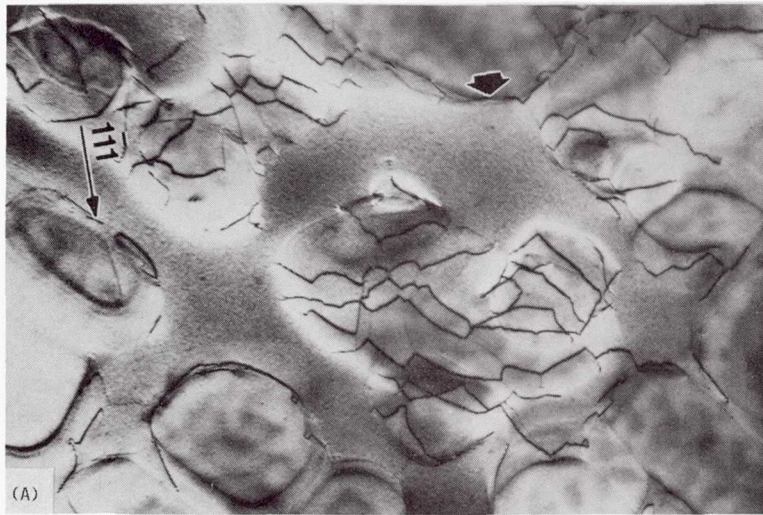
(A) [$\bar{2}13$] Z.A., ($1\bar{1}1$) INTERFACE INDICATED BY THE ARROW.

(B) [012] Z.A., ($\bar{1}00$) INTERFACE INDICATED.
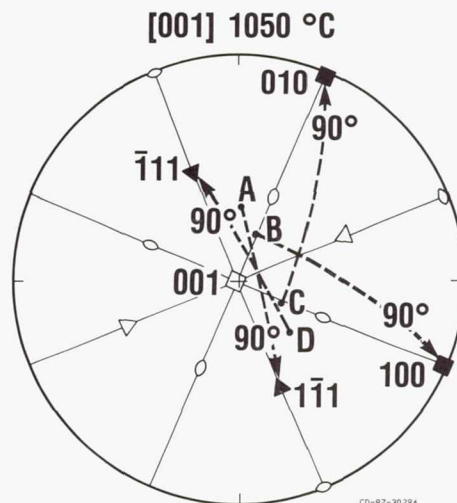
FIGURE 106. - MICROGRAPHS OF A TYPICAL TILTING EXPERIMENT OF UNLOADED PWA 1480 EXPOSED 500 HR AT 1050 °C.
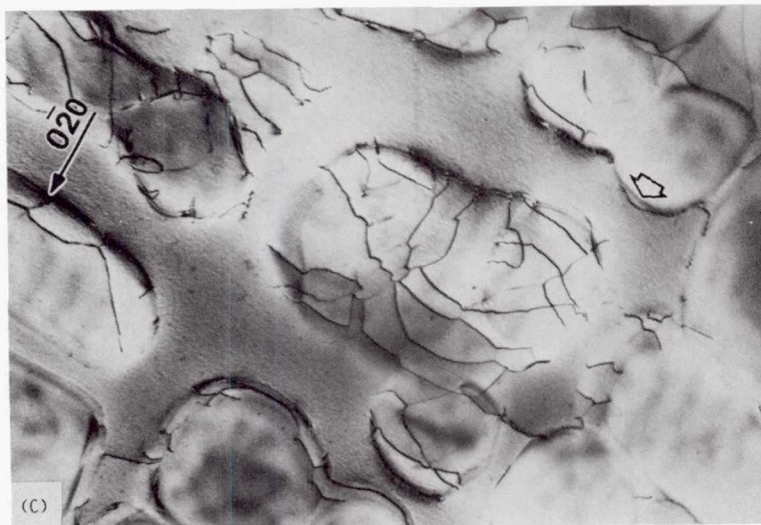
(C) [ī23] Z.A., (0ī0) INTERFACED INDICATED.
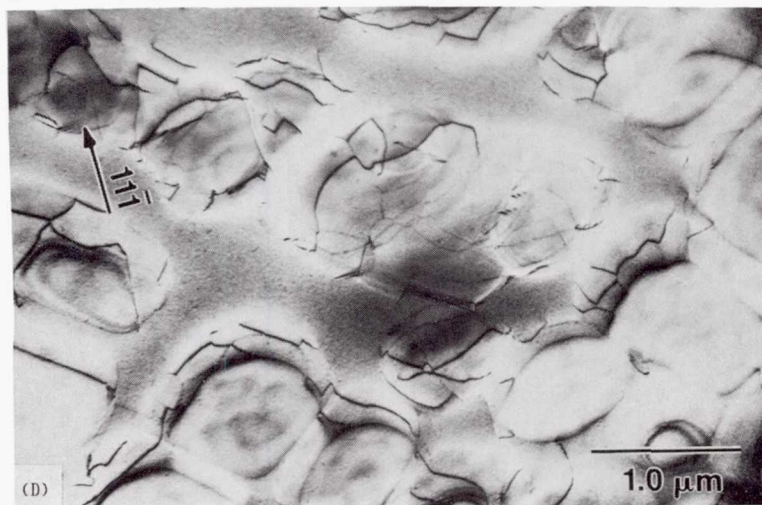
(D) [102] Z.A.
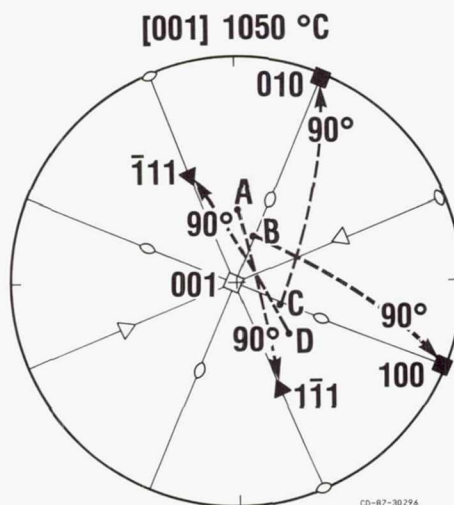
FIGURE 106. - CONCLUDED.
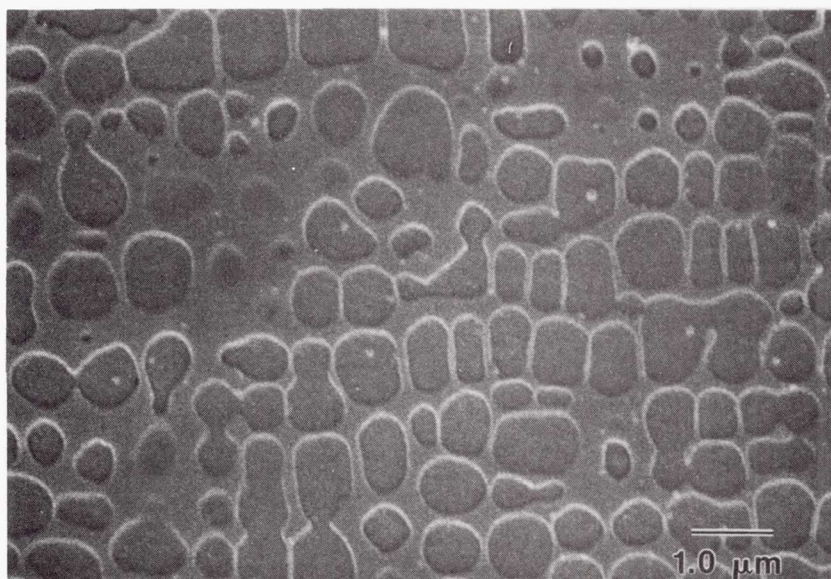
(A) $\Delta\varepsilon_{IN.}$ = .0010 MM/MM ON CYCLE 1, (010) PLANE.
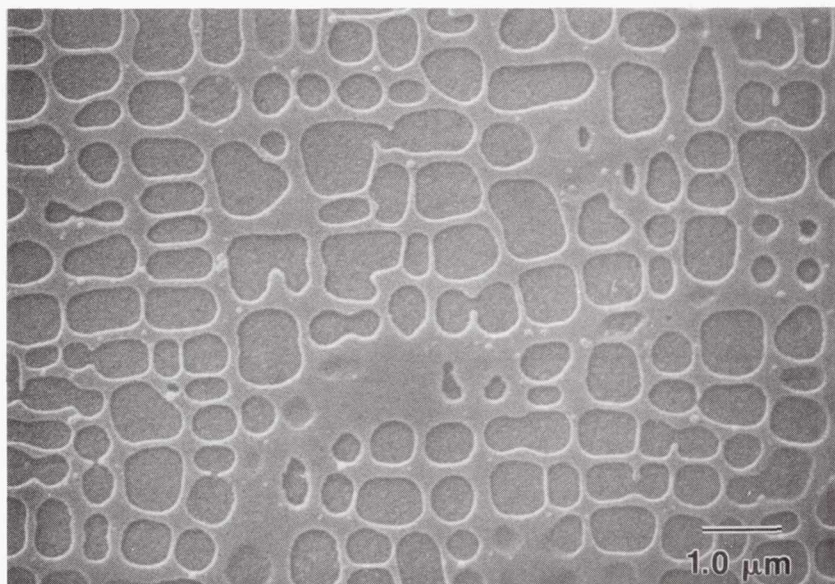
(B) $\Delta\varepsilon_{IN.}$ = .0027 MM/MM ON CYCLE 1, (010) PLANE.

FIGURE 107. - MICROGRAPH OF AN [001] LCF SPECIMEN, 1050 ^{O}C.

(A) UNTESTED.

1.0 μm
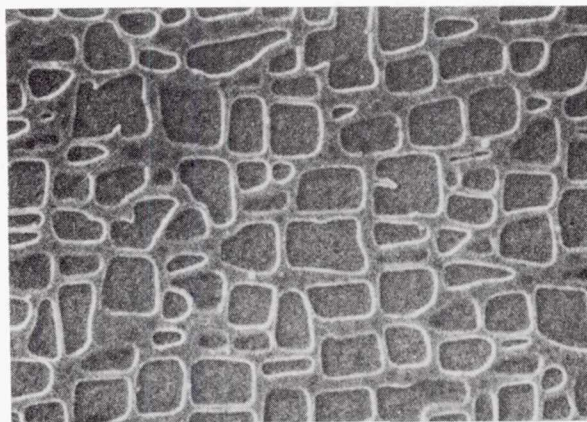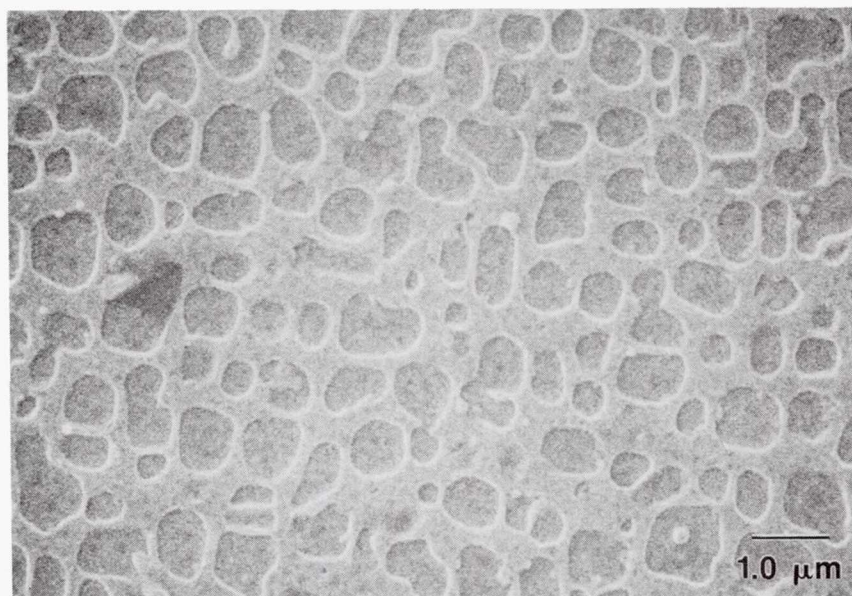
(B) LCF SPECIMEN, 1050 ^{O}C, $\Delta\varepsilon_{IN.1} \sim .001$ MM/MM.

FIGURE 108. - MICROGRAPHS OF [$\bar{1}$11] SPECIMENS, SECTIONED ON (011) PLANES.

(C) UNTESTED.

1.0 μm
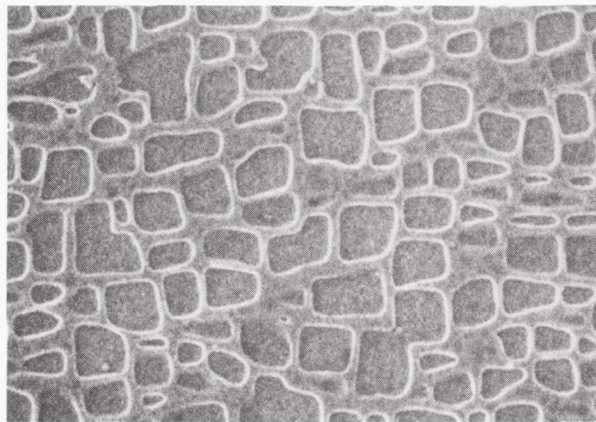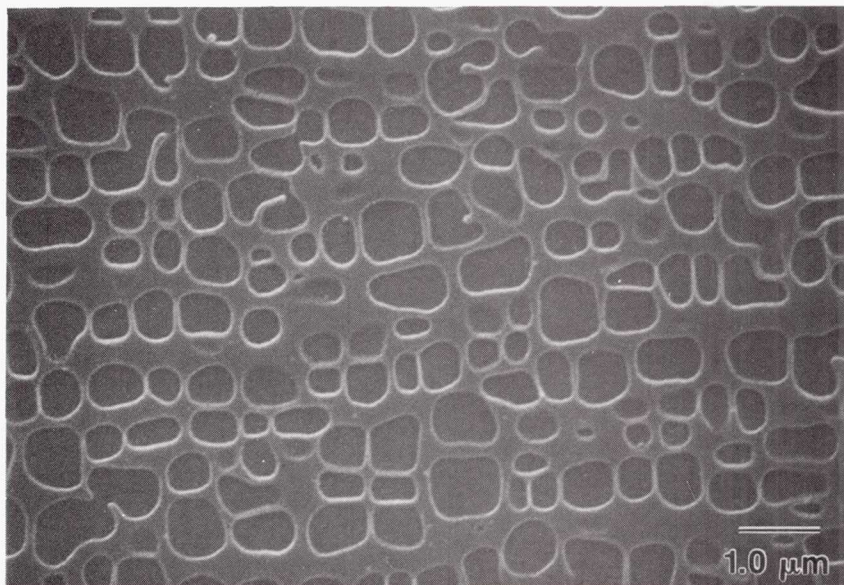
(D) LCF SPECIMEN, 1050 °C, $\Delta\varepsilon_{IN. 1} \sim .0027$ MM/MM.

FIGURE 108. - CONCLUDED.

(A) [001], $\Delta\varepsilon_{IN.} \sim .001$ MM/MM.
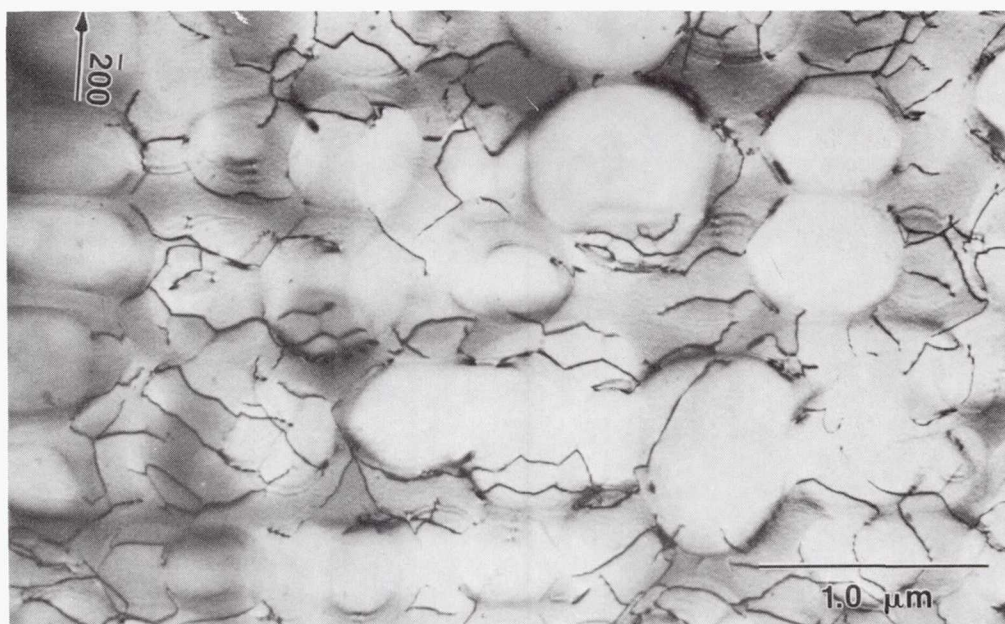
(B) [$\bar{1}$11], $\Delta\varepsilon_{IN.} \sim .001$ MM/MM.

FIGURE 109. - COMPARATIVE DEFORMATION STRUCTURES OF THE [001] AND [$\bar{1}$11] LCF SPECIMENS, 1050 ^{O}C, $\Delta\varepsilon_{IN.1} \sim$ .001 MM/MM, [011] Z.A., (011) FOILS.
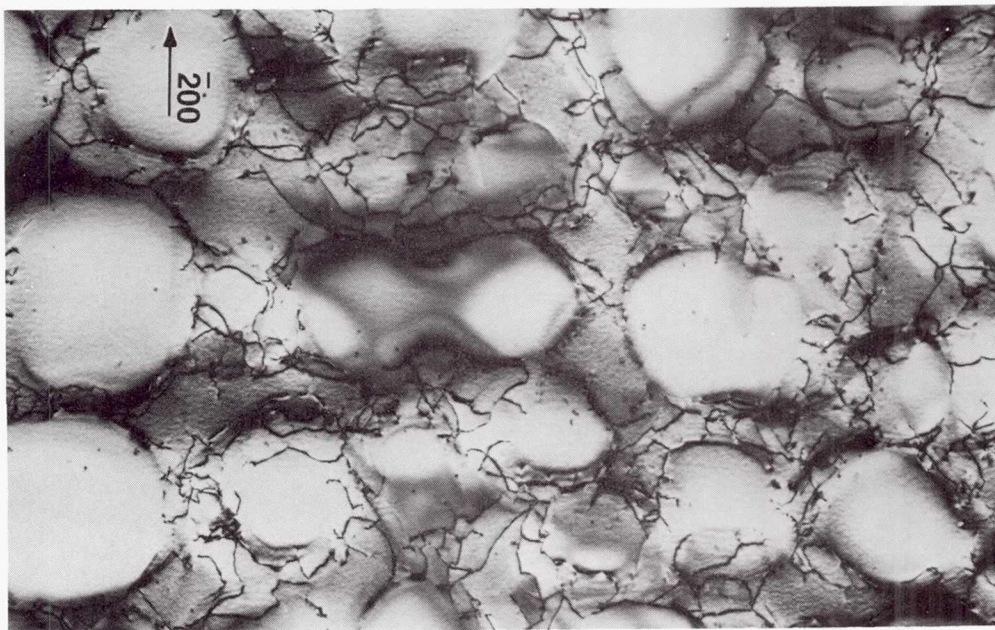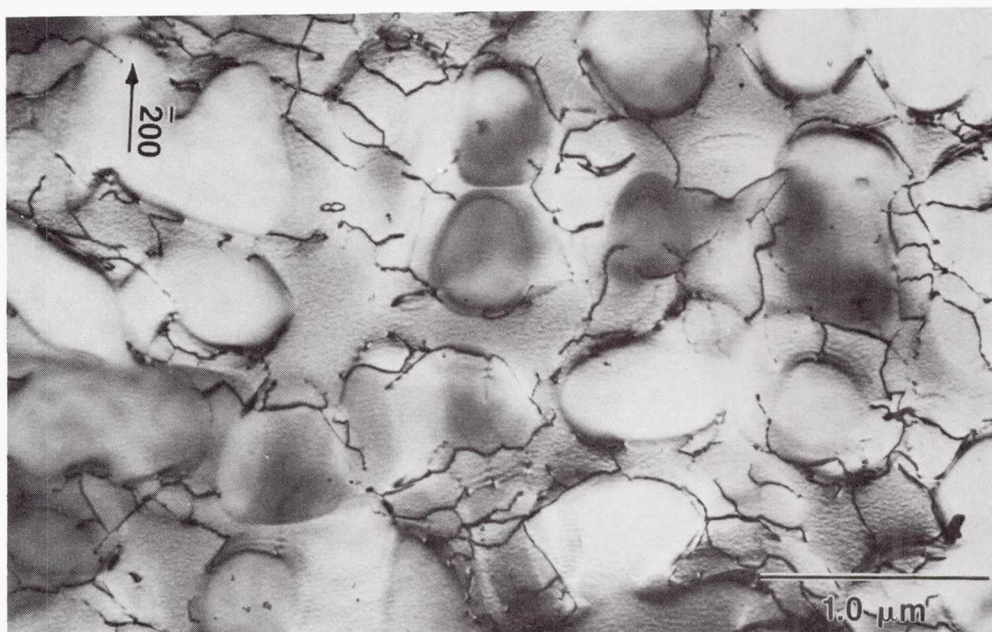
(C) [001], $\Delta\varepsilon_{IN.}$ ~ .0027 MM/MM.

(D) [$\bar{1}$11], $\Delta\varepsilon_{IN.}$ ~ .0027 MM/MM.

FIGURE 109. - CONCLUDED.
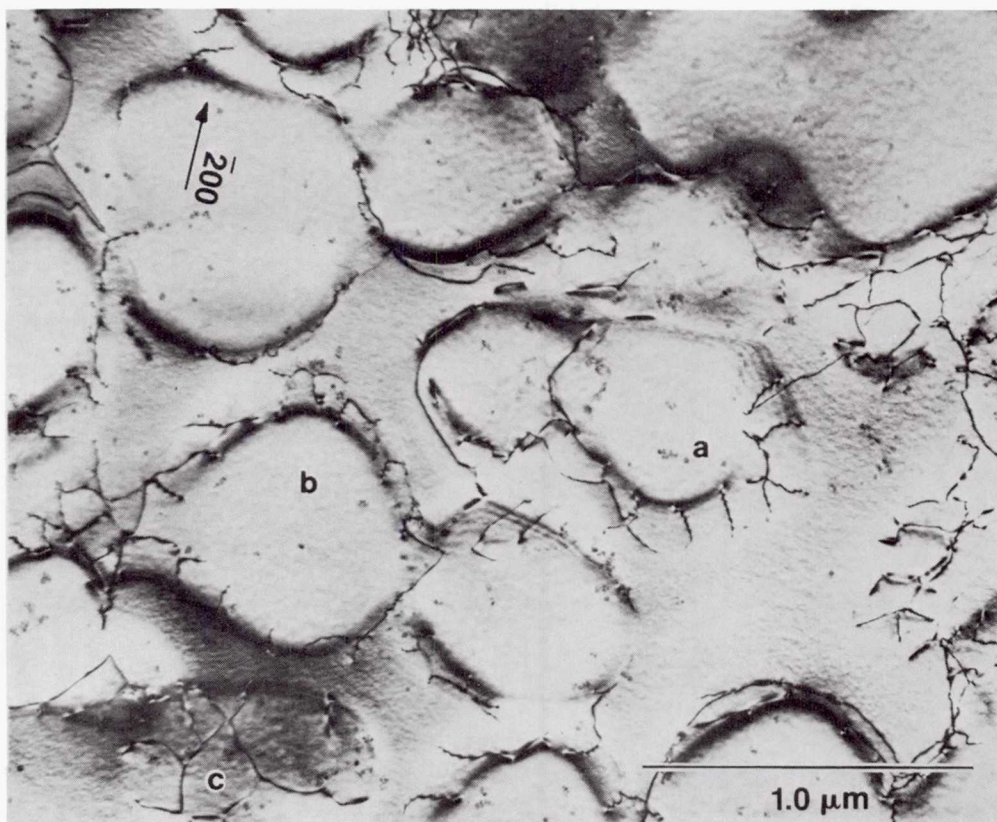
FIGURE 110(A). - THE DISLOCATION STRUCTURE OF A [001] LCF SPECIMEN, 1050 ^{O}C, $\Delta\epsilon_{IN.}$ = .0027 MM/MM ON CYCLE 1, [001] Z.A.
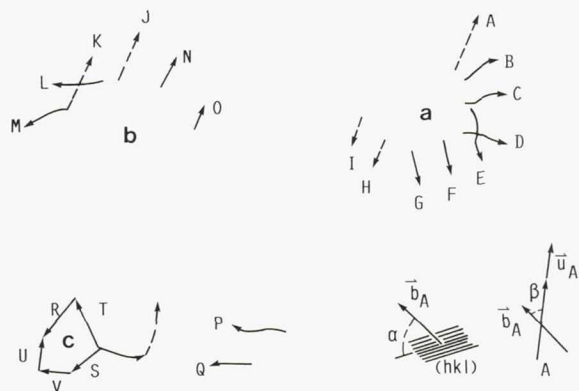
CD-87-29809

DISL.	BURGERS VECTOR $\bar{B}$	LINE DIR. $\bar{U}$	INTERF. PLANE (H K L)	$\bar{B}$-(HKL) ANGLE α	$\bar{B}$-$\bar{U}$ ANGLE β
A	1/2[011]	[$\bar{8}$ $\bar{1}$ $\bar{6}$]	($\bar{1}$ $\bar{1}$ 1)	0^0	60^0
B	1/2[$\bar{1}$10]	[$\bar{5}$ $\bar{2}$ 8]	($\bar{1}$ $\bar{1}$ 1)	0^0	77^0
C	1/2[$\bar{1}$10]	[0 $\bar{6}$ 8]	($\bar{1}$ $\bar{1}$ 1)	0^0	65^0
D	1/2[$\bar{1}$10]	[0 $\bar{6}$ $\bar{8}$]	(5 $\bar{7}$ 5)	59^0	65^0
E	1/2[110]	[6 $\bar{1}$ $\bar{8}$]	(5 $\bar{7}$ 5)	8^0	69^0
F	1/2[110]	[$\bar{1}$ $\bar{6}$ $\bar{8}$]	(5 $\bar{7}$ 5)	8^0	60^0
G	1/2[110]	[5 $\bar{2}$ $\bar{8}$]	(5 $\bar{7}$ 5)	8^0	77^0
H	1/2[0$\bar{1}$1]	[0 $\bar{1}$ $\overline{10}$]	(9 5 0)	20^0	51^0
I	1/2[0$\bar{1}$1]	[6 $\bar{4}$ $\bar{7}$]	(9 5 0)	20^0	78^0
J	1/2[011]	[$\bar{7}$ $\bar{2}$ 7]	(6 $\bar{6}$ 5)	4^0	70^0
K	1/2[011]	[$\bar{7}$ $\bar{3}$ 6]	(6 $\bar{6}$ 5)	4^0	77^0
L	1/2[$\bar{1}$01]	[2 7 6]	(6 $\bar{6}$ 5)	4^0	68^0
M	1/2[$\bar{1}$01]	[6 7 2]	(6 $\bar{6}$ 5)	4^0	73^0
N	1/2[$\bar{1}$10]	[5 $\bar{3}$ 8]	(6 6 5)	4^0	82^0
O	1/2[$\bar{1}$10]	[$\bar{5}$ $\bar{2}$ 8]	(6 6 5)	4^0	77^0
P	1/2[$\bar{1}$01]	[2 7 7]	(6 $\bar{7}$ 4)	8^0	70^0
Q	1/2[$\bar{1}$01]	[3 6 8]	(6 $\bar{7}$ 4)	8^0	70^0
R	1/2[$\bar{1}$01]	[9 5 $\bar{1}$]	(1 1 10)	39^0	47^0
S	1/2[$\bar{1}$01]	[8 6 $\bar{2}$]	(1 1 10)	39^0	46^0
T	1/2[101]	[$\bar{7}$ 7 3]	(1 1 10)	50^0	74^0
U	1/2[101]	[$\bar{8}$ 2 6]	(1 1 10)	50^0	14^0
V	1/2[$\bar{1}$10]	[2 10 $\bar{1}$]	(1 1 10)	0^0	56^0

FIGURE 110(B). - RESULTS OF THE ANALYSIS OF SELECTED DISLOCATIONS
   IN FIGURE 110(A).
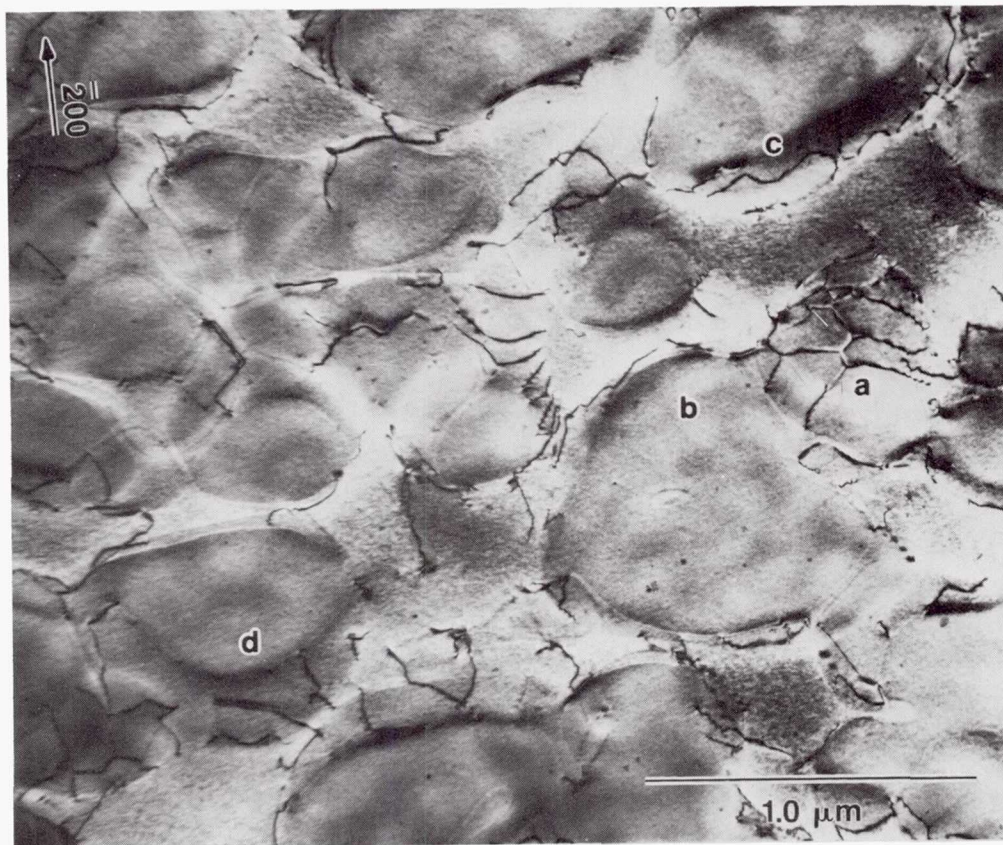
FIGURE 111(A). - THE DISLOCATION STRUCTURE OF A [$\bar{1}$11] LCF SPECIMEN, 1050 ^{O}C, $\Delta\varepsilon_{IN.}$ = .0027 MM/MM ON CYCLE 1, [012] Z.A.
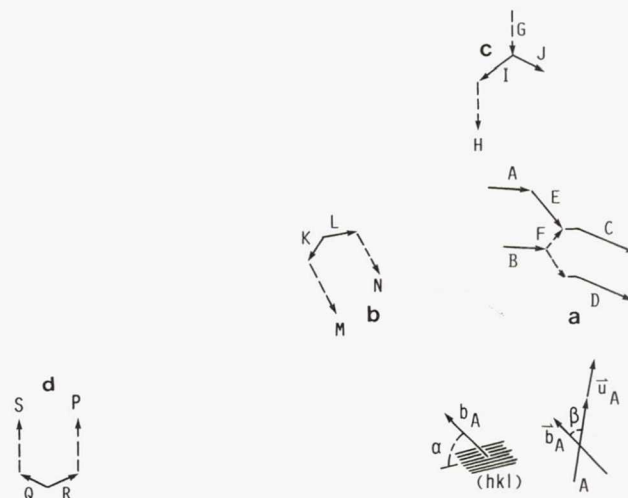
CD-87-29807

DISL.	BURGERS VECTOR $\bar{B}$	LINE DIR. $\bar{U}$	INTERF. PLANE (H K L)	$\bar{B}$-(HKL) ANGLE α	$\bar{B}$-$\bar{U}$ ANGLE β
A	1/2[101]	[2 $\bar{7}$ 6]	($\bar{1}$ 1 1)	0°	53°
B	1/2[101]	[1 $\bar{8}$ 6]	($\bar{1}$ 1 1)	0°	60°
C	1/2[101]	[1 $\bar{8}$ 6]	($\bar{1}$ 1 1)	0°	69°
D	1/2[101]	[$\bar{3}$ $\bar{8}$ 7]	($\bar{1}$ 1 1)	0°	75°
E	1/2[110]	[7 $\bar{2}$ 7]	($\bar{1}$ 1 1)	0°	70°
F	1/2[0$\bar{1}$1]	[$\bar{7}$ 7 0]	($\bar{1}$ 1 1)	0°	60°
G	1/2[011]	[10 0 $\bar{1}$]	(1 1 10)	50°	86°
H	1/2[011]	[10 $\bar{1}$ $\bar{2}$]	(1 1 10)	50°	78°
I	1/2[$\bar{1}$01]	[6 7 $\bar{3}$]	(1 1 10)	39°	49°
J	1/2[110]	[3 $\bar{1}$0 $\bar{2}$]	(1 1 10)	8°	62°
K	1/2[110]	[7 6 $\bar{2}$]	($\bar{1}$ 1 0)	0°	13°
L	1/2[$\bar{1}$01]	[$\bar{4}$ $\bar{6}$ 7]	($\bar{1}$ 1 0)	30°	39°
M	1/2[011]	[$\bar{8}$ 2 6]	($\bar{1}$ 1 0)	30°	56°
N	1/2[011]	[0 3 10]	($\bar{1}$ 1 0)	30°	28°
O	1/2[0$\bar{1}$1]	[$\bar{1}$0 2 1]	(1 5 9)	16°	86°
P	1/2[0$\bar{1}$1]	[$\bar{1}$0 2 1]	(1 5 9)	16°	86°
Q	1/2[$\bar{1}$01]	[$\bar{5}$ 8 $\bar{4}$]	(1 5 9)	33°	86°
R	1/2[$\bar{1}$10]	[$\bar{6}$ $\bar{7}$ 4]	(1 5 9)	16°	86°

FIGURE 111(B). - RESULTS OF THE ANALYSIS OF SELECTED DISLOCATIONS IN FIGURE 111(A).

179
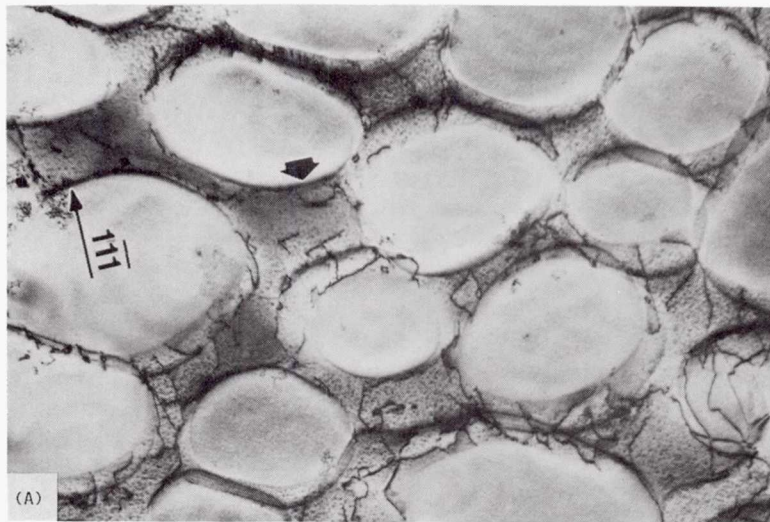
(A) [2$\bar{1}$3] Z.A., ($\bar{1}$11) INTERFACE INDICATED BY THE ARROW.
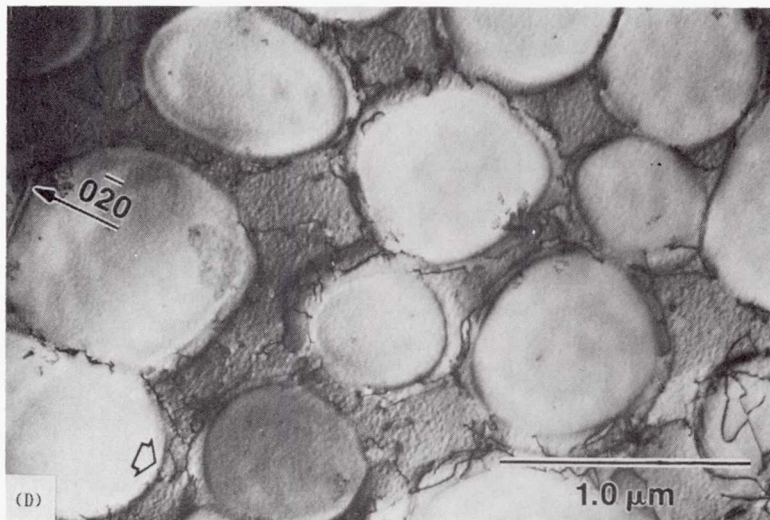
(B) [205] Z.A., (010) INTERFACE INDICATED.
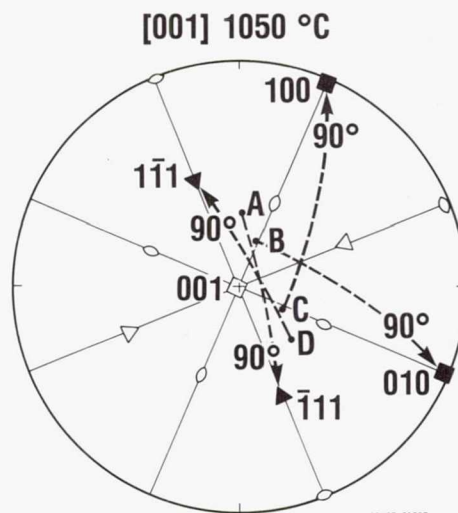
FIGURE 112. - MICROGRAPHS OF A TYPICAL TILTING EXPERIMENT OF AN [001] LCF SPECI-
MEN, 1050 °C, $\Delta\varepsilon_{IN.}$ = .0027 MM/MM ON CYCLE 1.
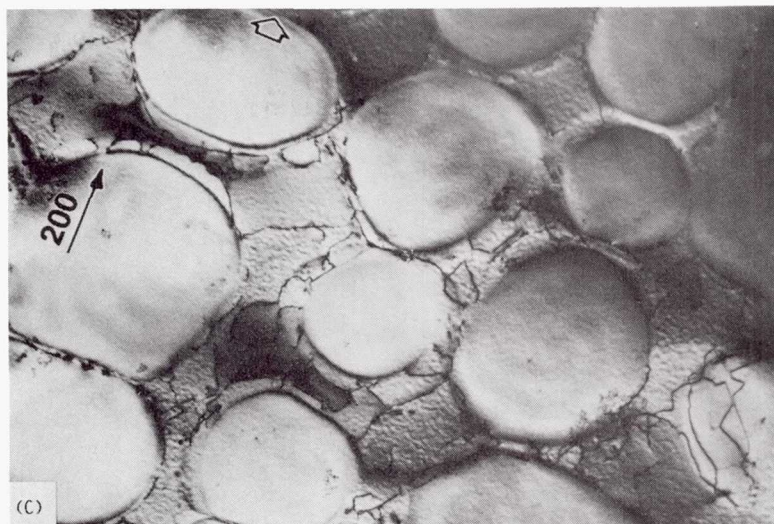
(C) [025] Z.A., (100) INTERFACE INDICATED.

(D) [Ī23] Z.A., (1Ī1) INTERFACE INDICATED.

[001] 1050 °C

CD-87-30297
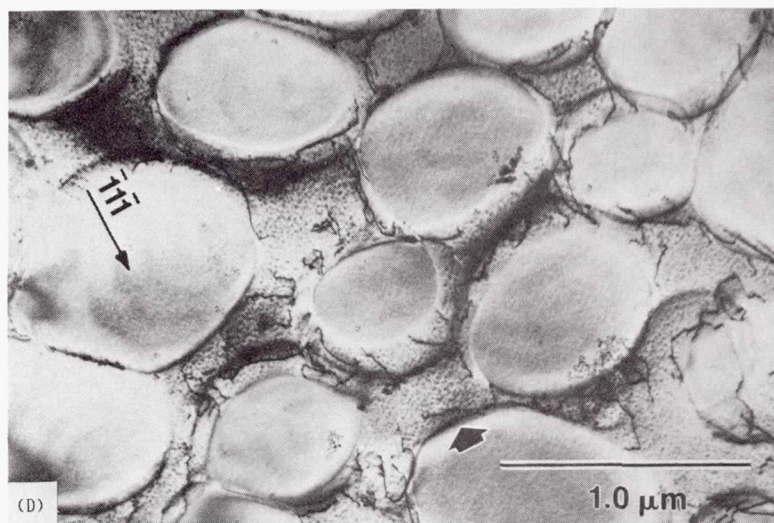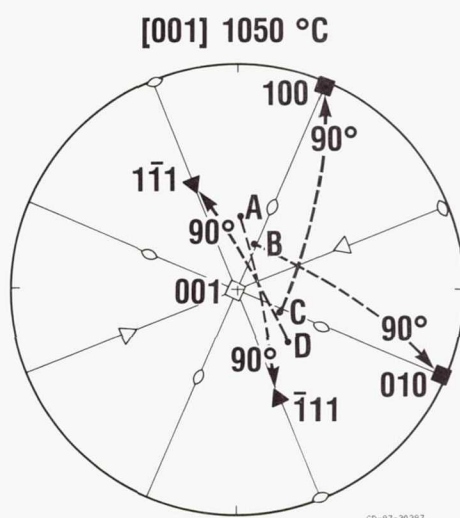
FIGURE 112. - CONCLUDED.
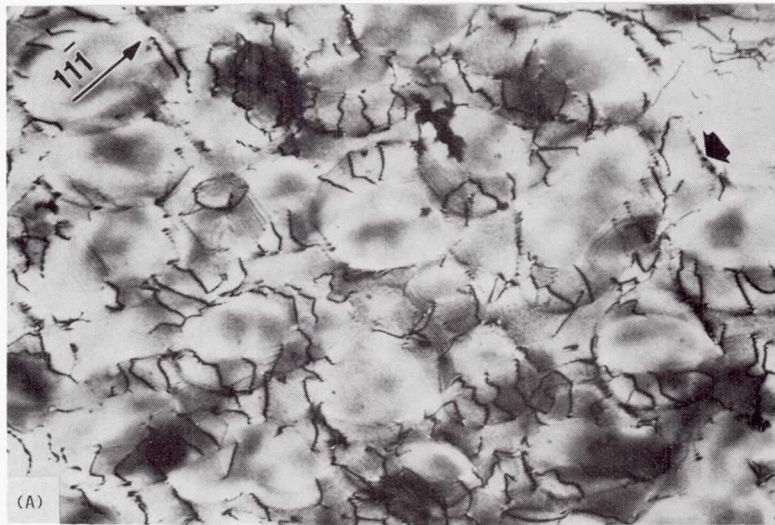
(A) [123] Z.A., ($\bar{1}\bar{1}1$) INTERFACE INDICATED BY THE ARROW.
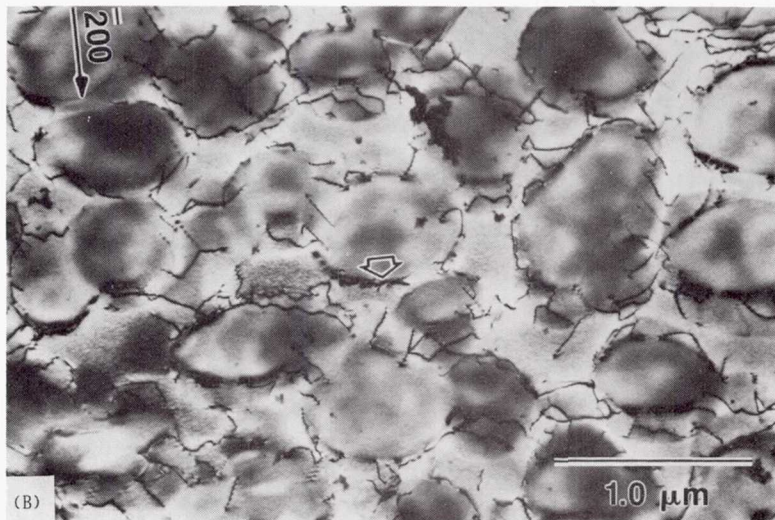
(B) [011] Z.A., ($\bar{1}$00) INTERFACE INDICATED.
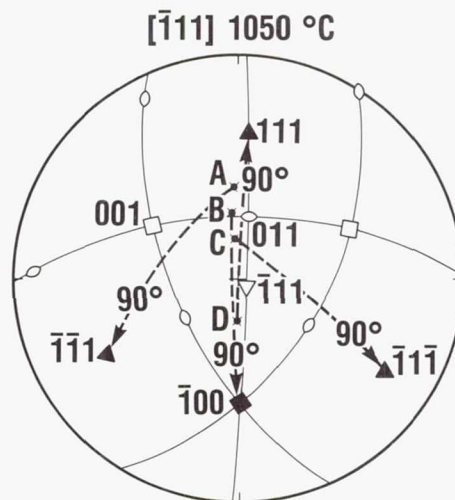
FIGURE 113. - MICROGRAPHS OF A TYPICAL TILTING EXPERIMENT OF A [$\bar{1}$11] LCF SPECIMEN, 1050 °C, $\Delta\varepsilon_{IN.}$ = .0027 MM/MM ON CYCLE 1.
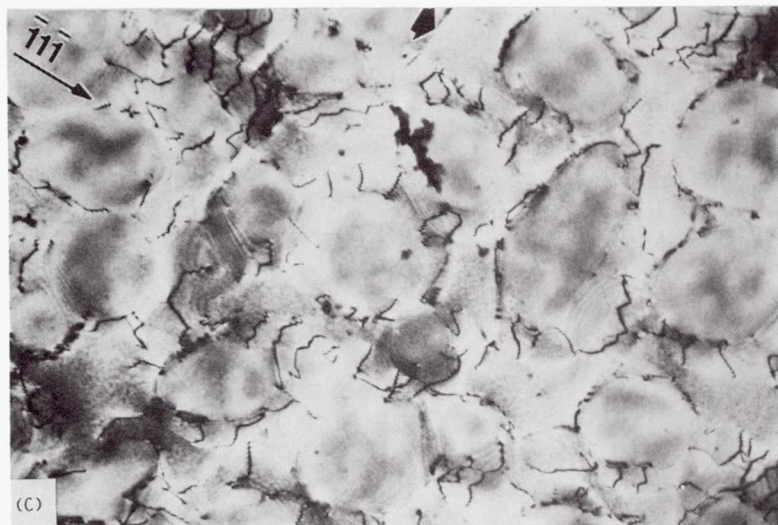
(C) [1̄23] Z.A., (1̄11̄) INTERFACE INDICATED.
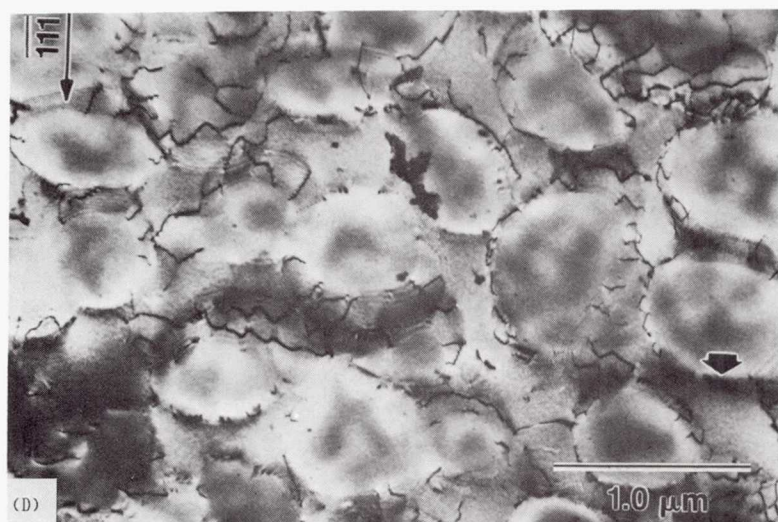
(D) [2̄11] Z.A., (1̄1̄1̄) INTERFACE INDICATED.

[1̄11] 1050 °C
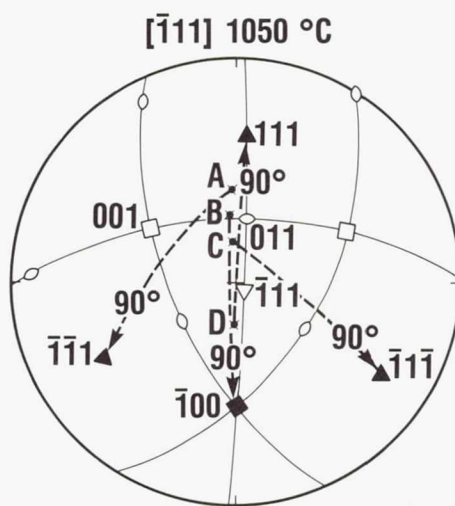
FIGURE 113. - CONCLUDED.
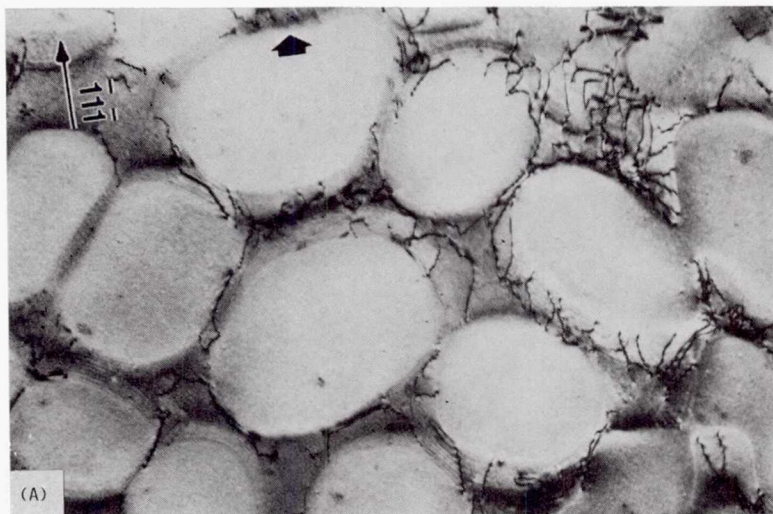
(A) [$\bar{1}$23] Z.A., ($\bar{1}$1$\bar{1}$) INTERFACE INDICATED BY THE ARROW.
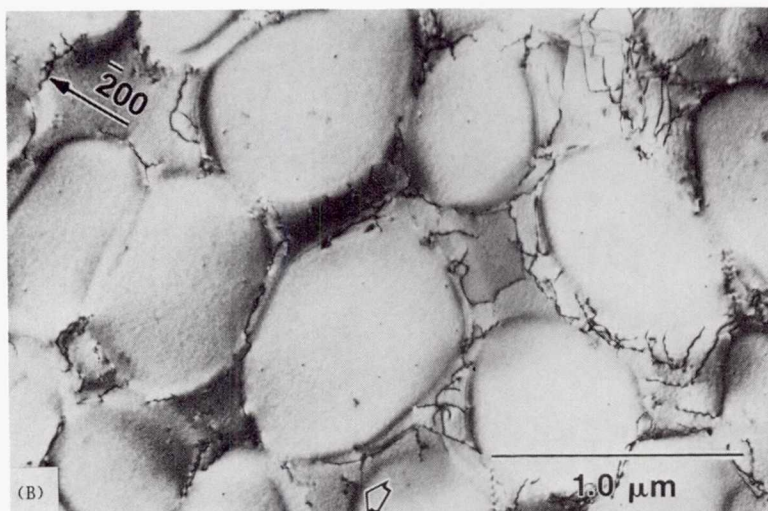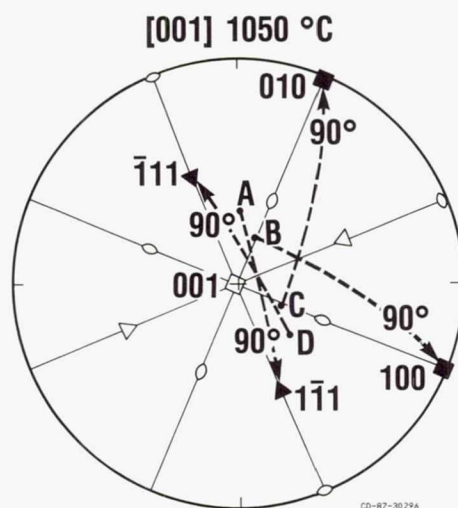
(B) [012] Z.A., ($\bar{1}$00) INTERFACE INDICATED.

FIGURE 114. - MICROGRAPHS OF A TYPICAL TILTING EXPERIMENT OF AN [001] LCF SPECI-
MEN, 1050 °C, $\Delta\varepsilon_{IN.}$ = .0010 MM/MM ON CYCLE 1.
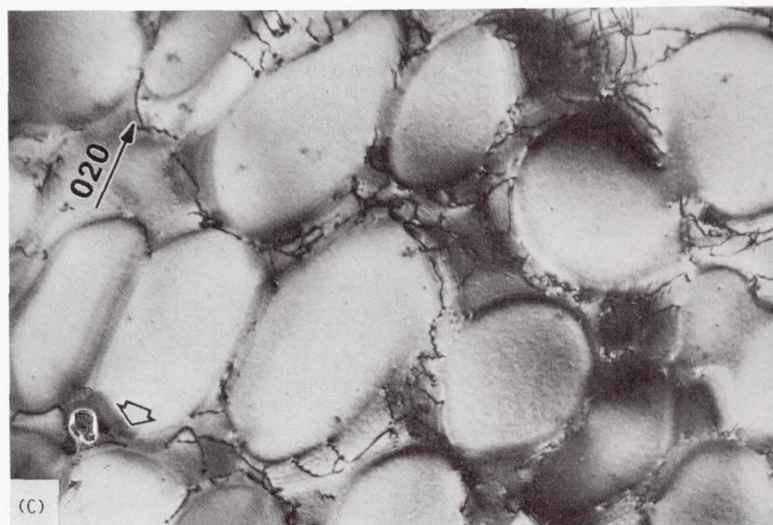
(C) [102] Z.A., (0$\bar{1}$0) INTERFACE INDICATED.

1.0 µm

(D) [2$\bar{1}$3] Z.A., (1$\bar{1}\bar{1}$) INTERFACE INDICATED.

[001] 1050 °C

CD-87-30296
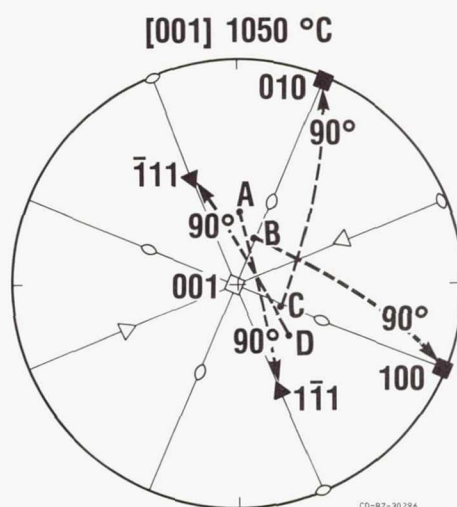
FIGURE 114. - CONCLUDED.

185
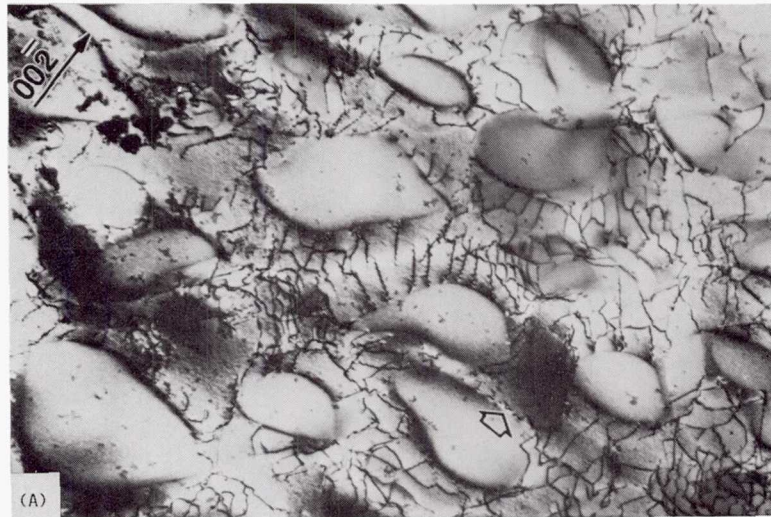
(A) [$\bar{1}$10] Z.A., (00$\bar{1}$) INTERFACE INDICATED BY THE ARROW.
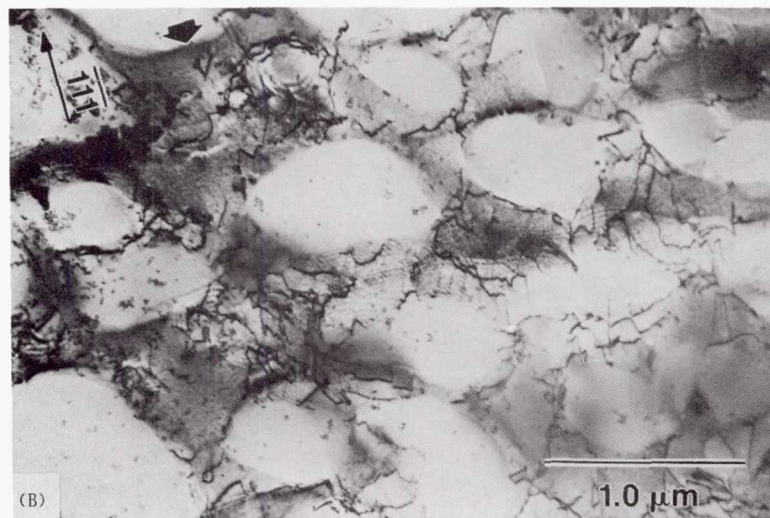
(B) [$\bar{1}$10] Z.A., (111) INTERFACE INDICATED.
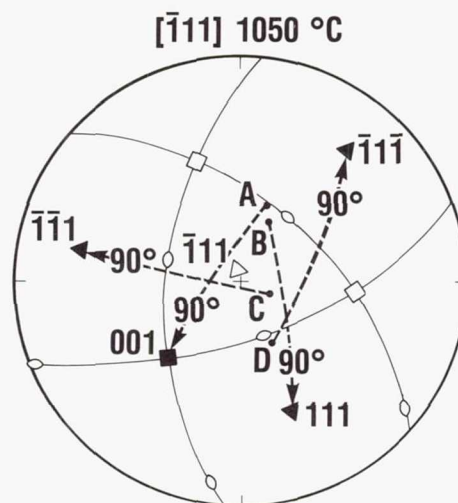
FIGURE 115. – MICROGRAPHS OF A TYPICAL TILTING EXPERIMENT OF A [111] LCF SPECI-
MEN, 1050 $^{\circ}$C, $\Delta\varepsilon_{IN.}$ = .0010 MM/MM ON CYCLE 1.
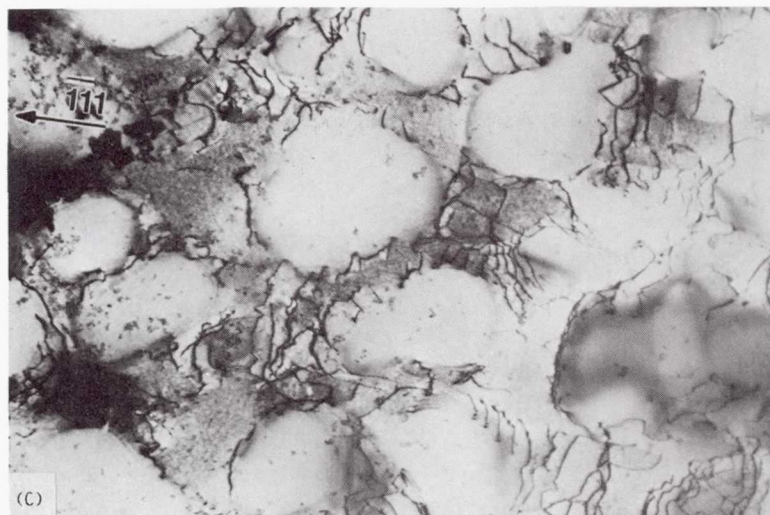
(C) [$\bar{1}$32] Z.A.
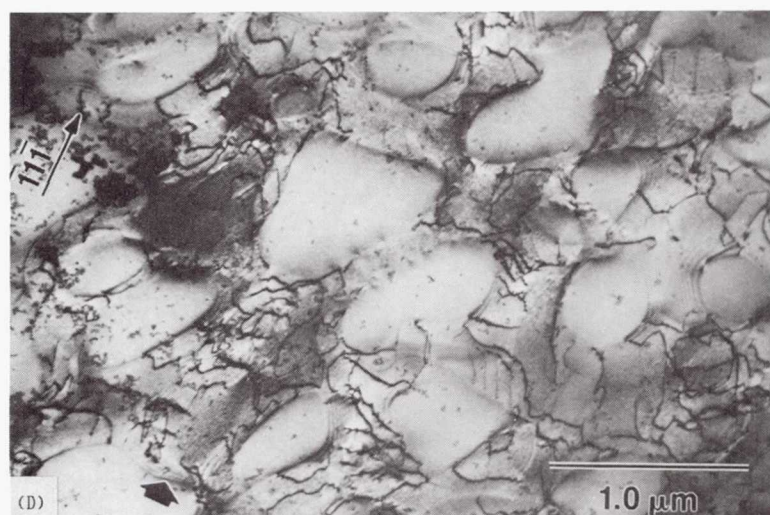
(D) [011] Z.A., ($\bar{1}$1$\bar{1}$) INTERFACE INDICATED.

[$\bar{1}$11] 1050 °C

CD-87-29818
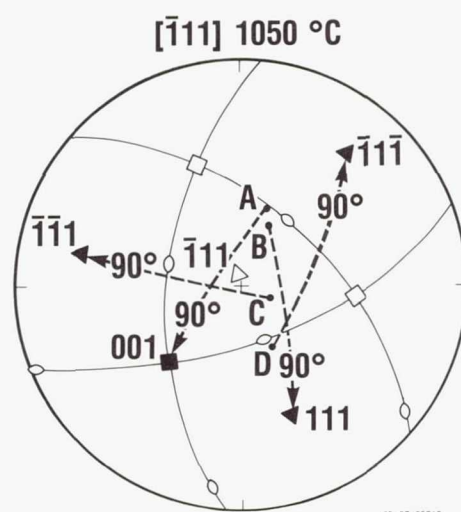
FIGURE 115. - CONCLUDED.

187
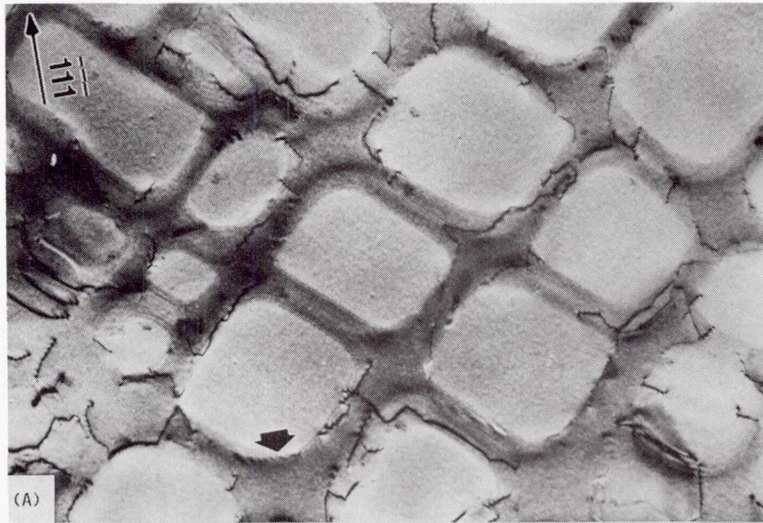
(A) [$\bar{2}\bar{1}3$] Z.A., (111) INTERFACE INDICATED BY THE ARROW.
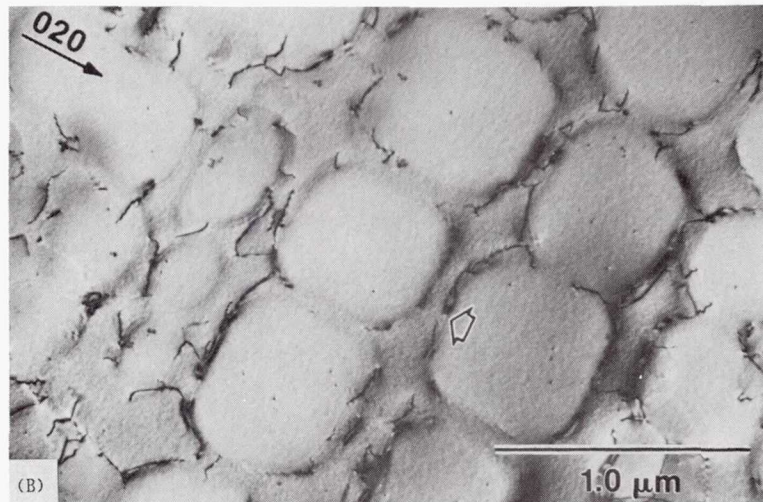
(B) [$\bar{1}02$] Z.A., (0$\bar{1}$0) INTERFACE INDICATED.
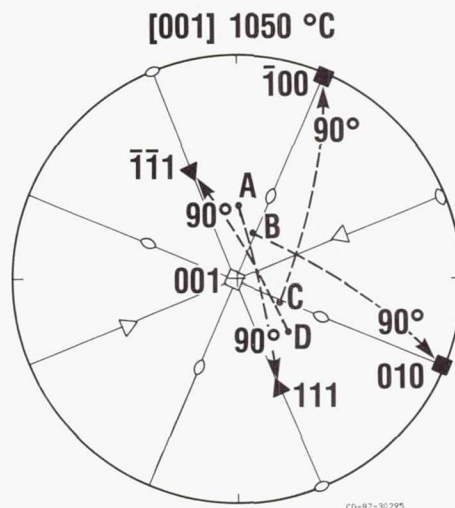
FIGURE 116. - MICROGRAPHS OF A TYPICAL TILTING EXPERIMENT OF AN [001] LCF SPECIMEN, 1050 °C, $\Delta\varepsilon_{IN.}$ = .0027 MM/MM ON CYCLE 1, INTERRUPTED AT 50 CYCLES.
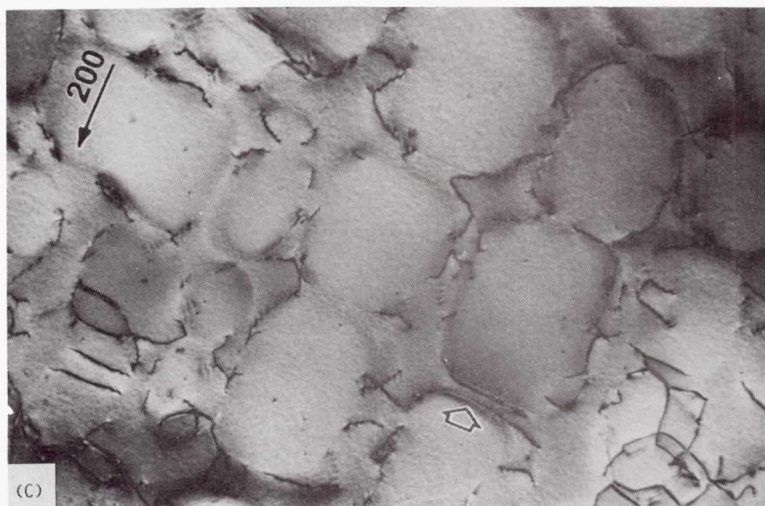
(C) [012] Z.A., (100) INTERFACE INDICATED.

1.0 μm
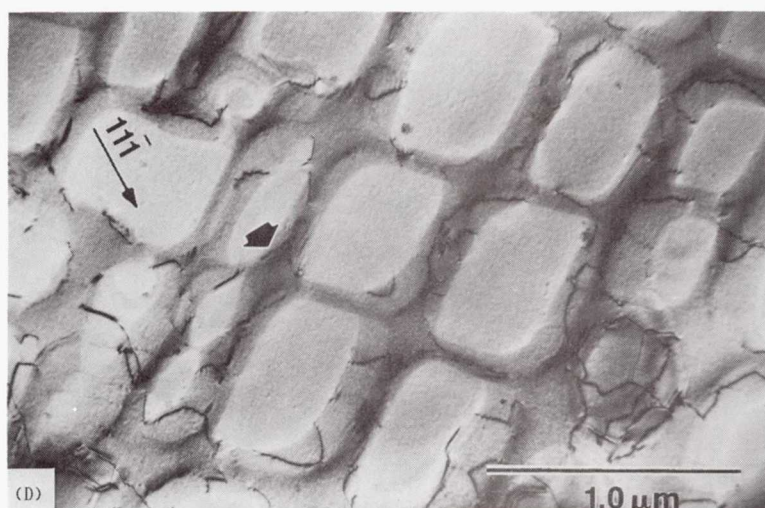
(D) [123] Z.A., (11 $\bar{1}$) INTERFACE INDICATED.

[001] 1050 °C

CO-87-30295
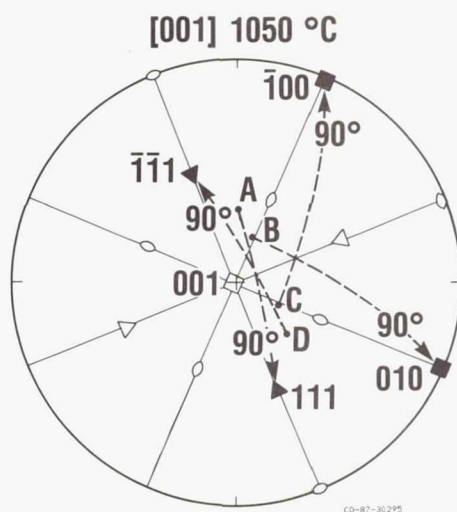
FIGURE 116. - CONCLUDED.

189

(A) [$\bar{2}$01] Z.A., (010) INTERFACE INDICATED BY THE ARROW.
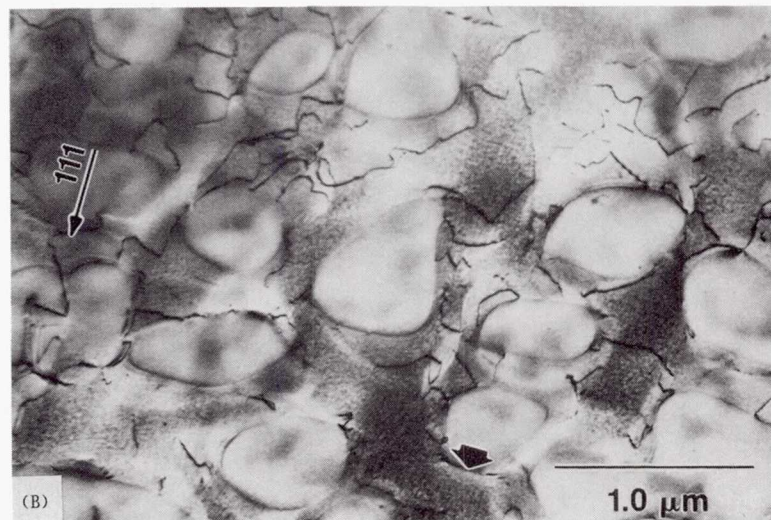
(B) [$\bar{1}$01] Z.A., (111) INTERFACE INDICATED.
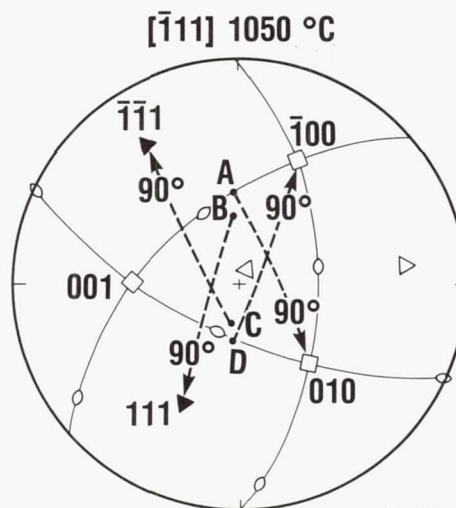
FIGURE 117. - MICROGRAPHS OF A TYPICAL TILTING EXPERIMENT OF A [$\bar{1}$11] LCF SPECIMEN, 1050 $^{\circ}$C, $\Delta\varepsilon_{IN.}$ = .0027 MM/MM ON CYCLE 1, INTERRUPTED AT 50 CYCLES.

(C) [011] Z.A., ($\bar{1}\bar{1}$1) INTERFACED INDICATED.

1.0 μm
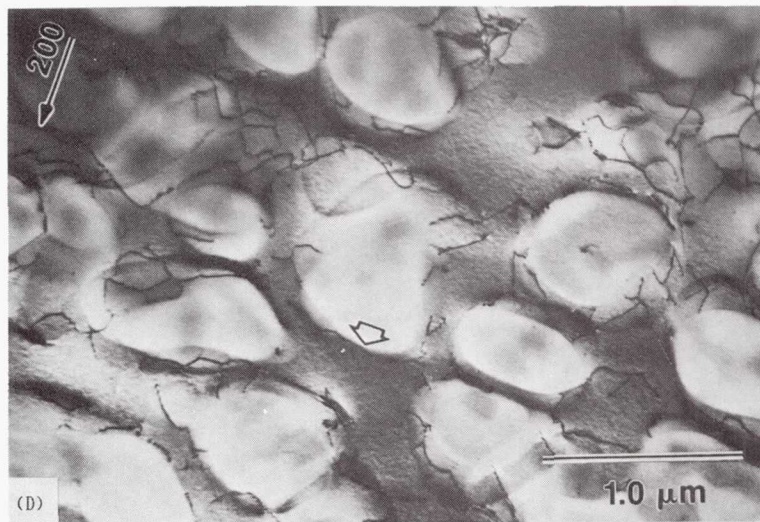
(D) [011] Z.A., (100) INTERFACE INDICATED.

[$\bar{1}$11] 1050 °C
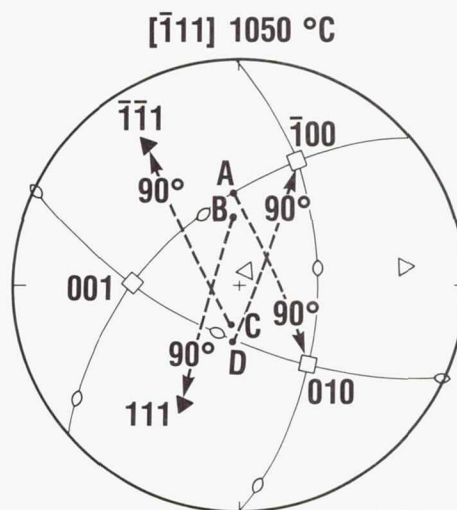
CD-87-29819

FIGURE 117. - CONCLUDED.

191
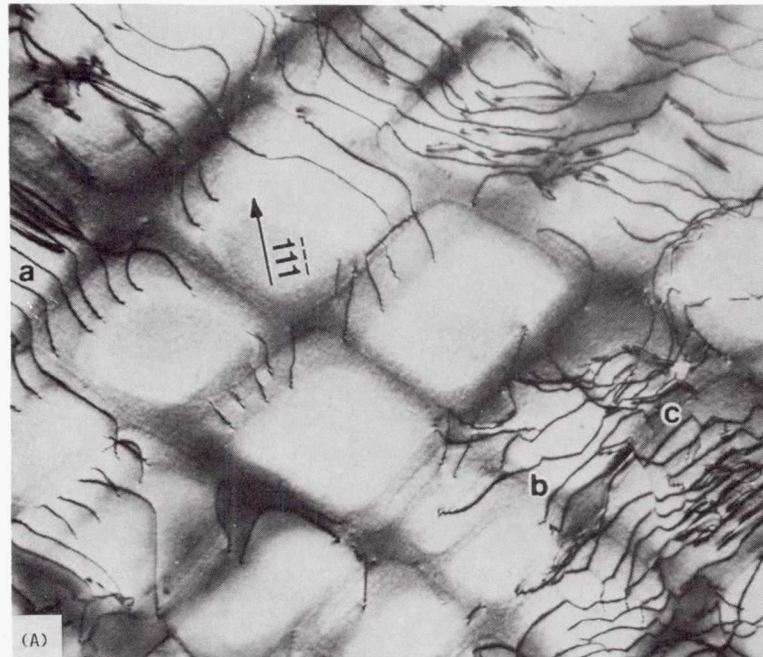
(A) [$\bar{2}$13] Z.A.
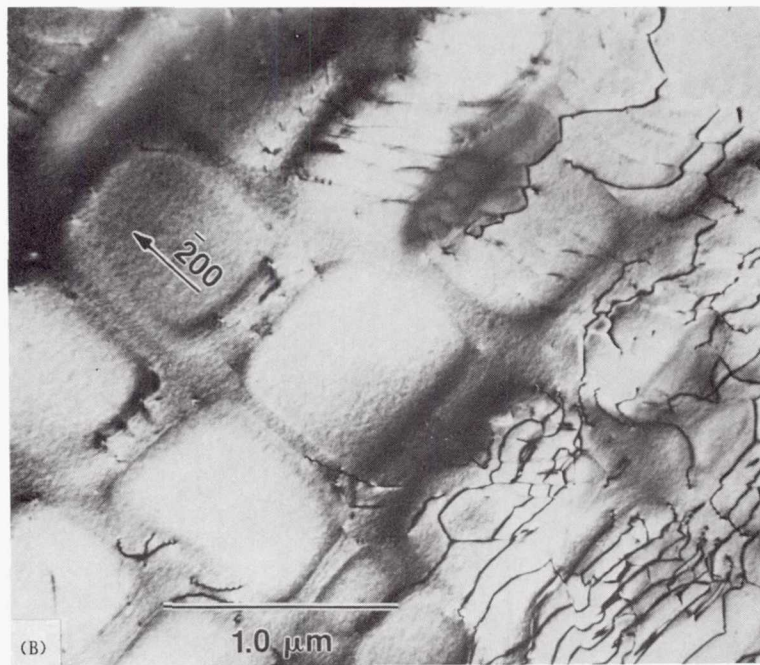
(B) [001] Z.A.

FIGURE 118. - MICROGRAPHS OF AN [001] LCF SPECIMEN, 1050 $^{\circ}$C, INTERRUPTED AT
$\varepsilon_{IN.}$ = .0015 MM/MM AT 1/2 CYCLE.

C-3

192
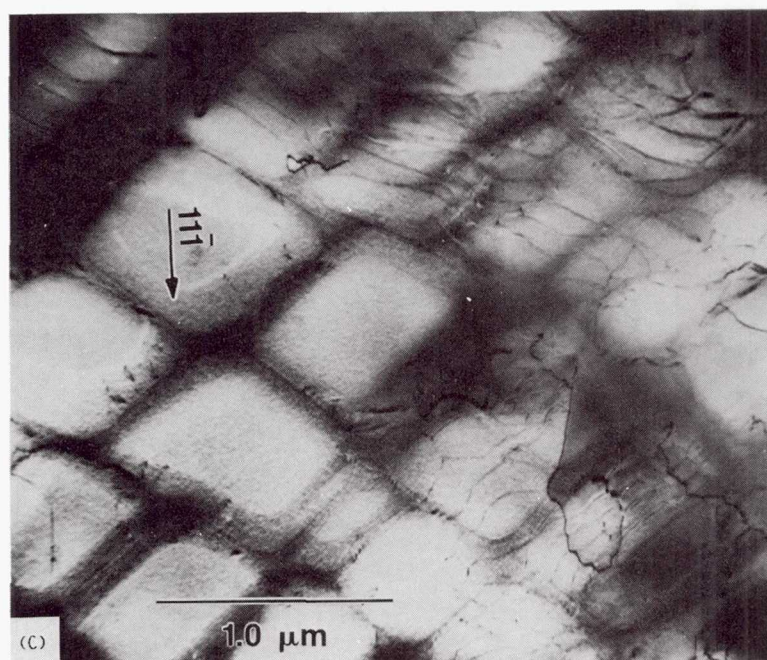
(C) [112] Z.A.

FIGURE 118. - CONCLUDED.
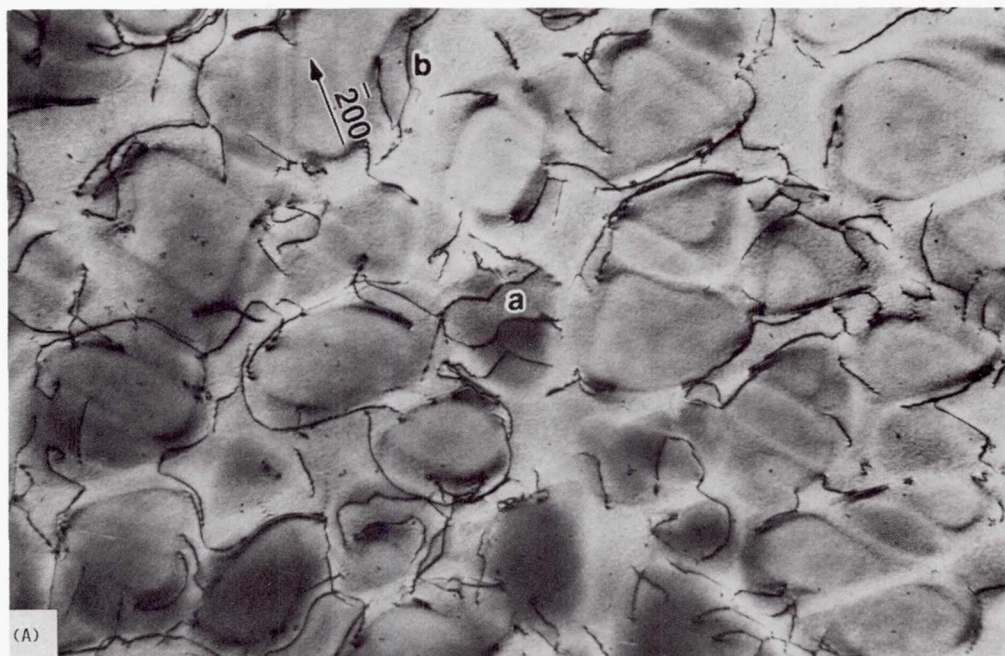
(A) [023] Z.A.
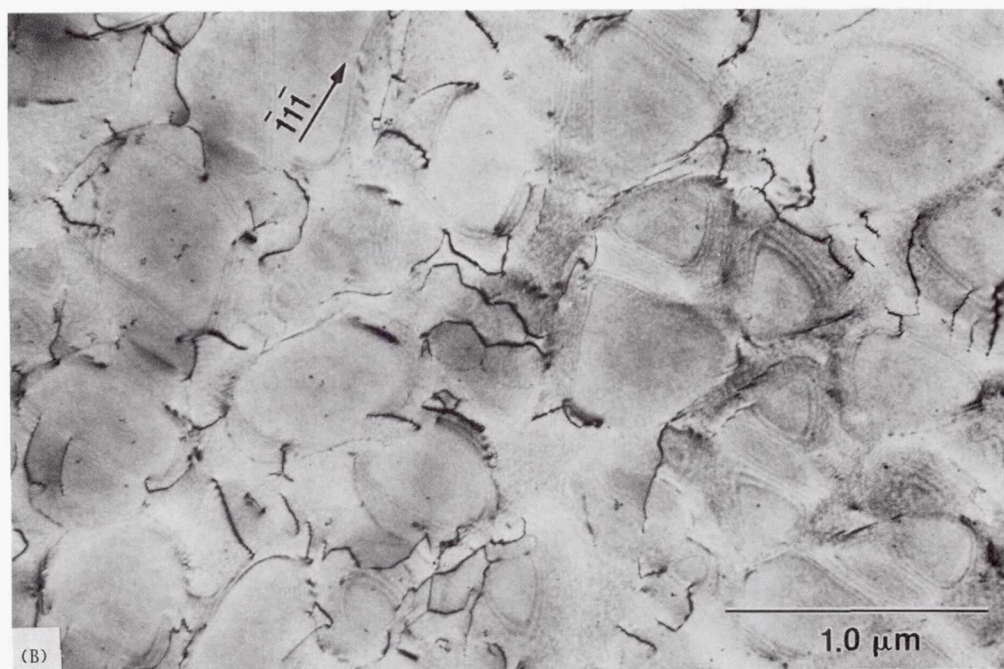
(B) [$\bar{1}23$] Z.A.

FIGURE 119. - MICROGRAPHS OF A [111] LCF SPECIMEN, 1050 °C, INTERRUPTED AT $\varepsilon_{IN.}$ = .0017 MM/MM AT 1/2 CYCLE.
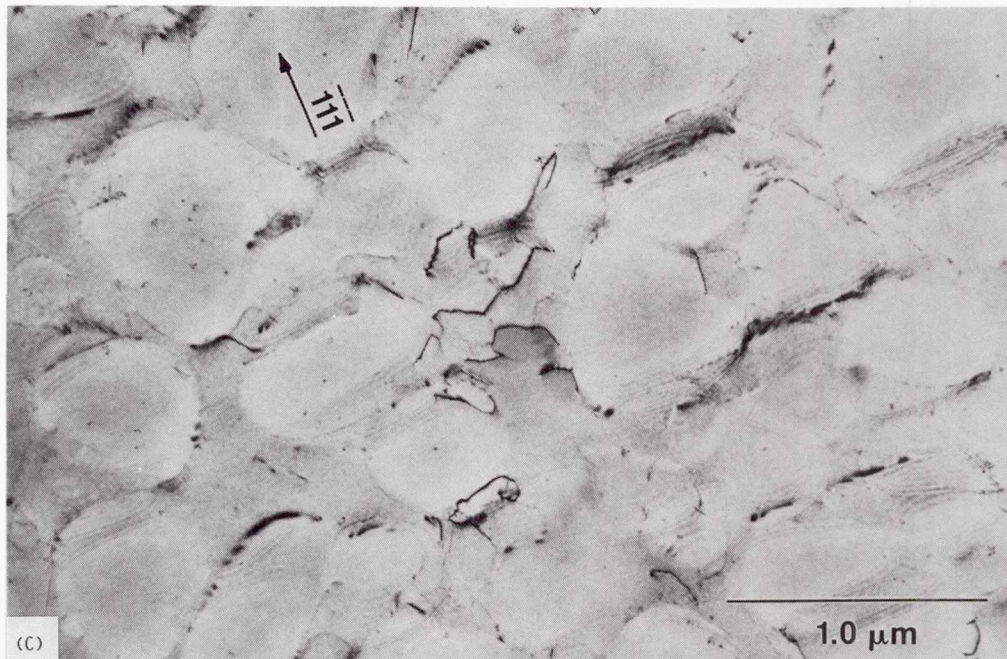
(C) [$\bar{2}$11] Z.A.

FIGURE 119. - CONCLUDED.
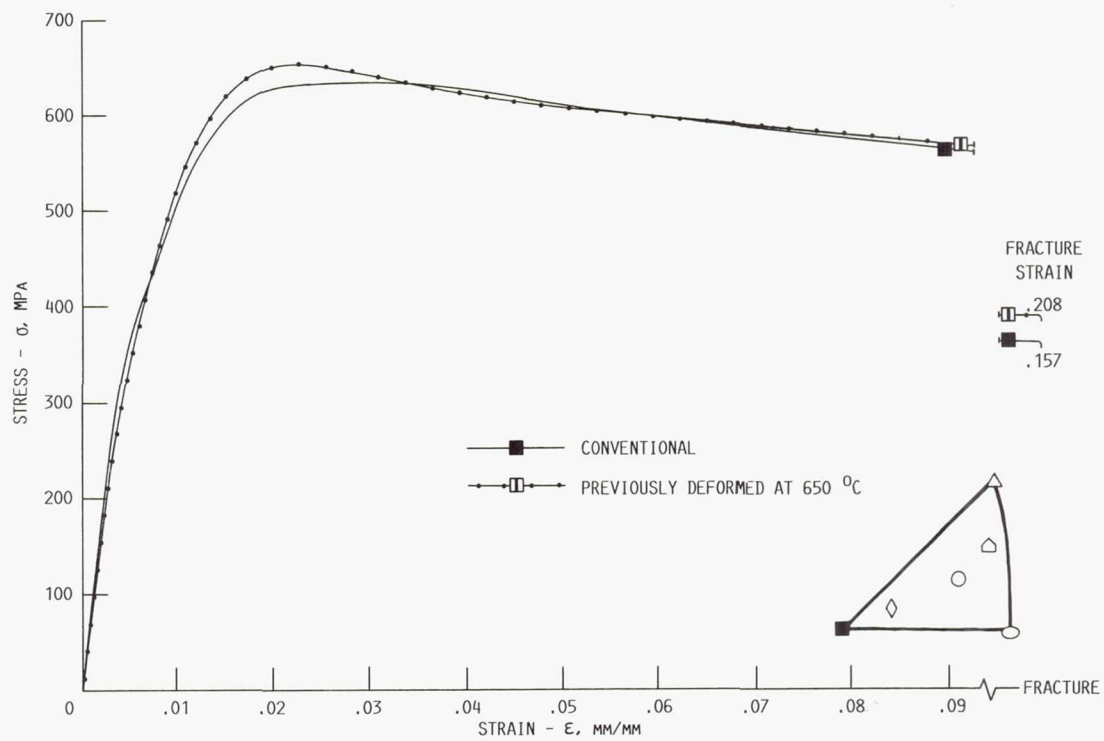
FIGURE 120. - THE AXIAL STRESS-STRAIN CURVES IN TENSILE TESTS AT 1050 °C OF [001] SPECIMENS WITH AND WITHOUT PRIOR LCF CYCLING AT 650 °C.

195

TENSILE SPECIMEN ROTATION
650 → 1050 °C
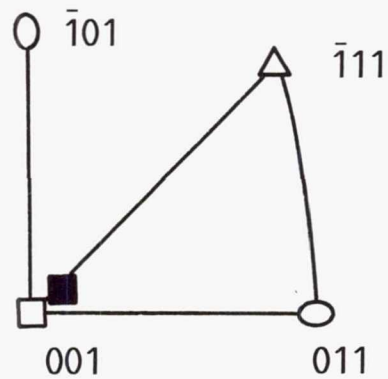
FIGURE 121. - THE CRY-
STALLOGRAPHIC ROTA-
TION OF THE SPECIMEN
AXIS IN A TENSILE
TEST AT 1050 °C
OF AN [001] SPECI-
MEN WITH PRIOR LCF
CYCLING AT 650 °C.
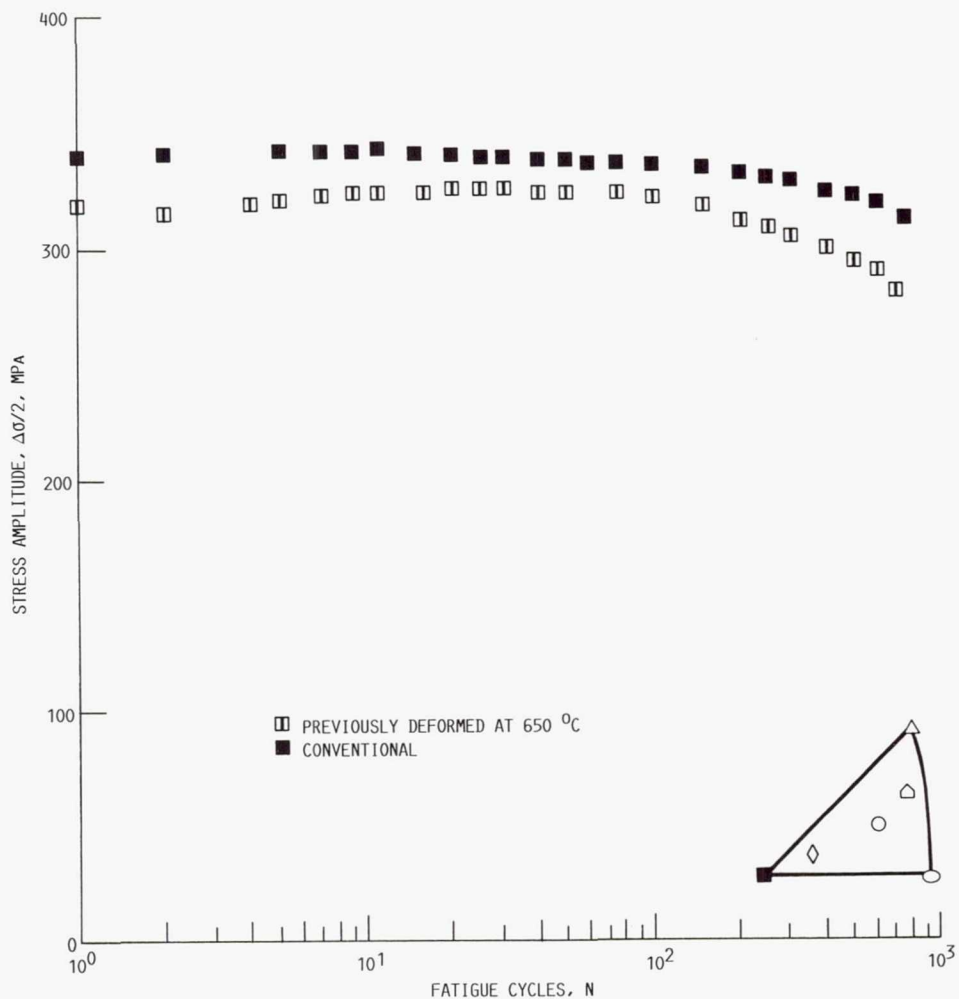
FIGURE 122. - THE LCF STRESS HARDENING RESPONSE OF [001] SPECIMENS AT 650 °C WITH AND WITH-
OUT PRIOR LCF CYCLING AT 650 °C.

196
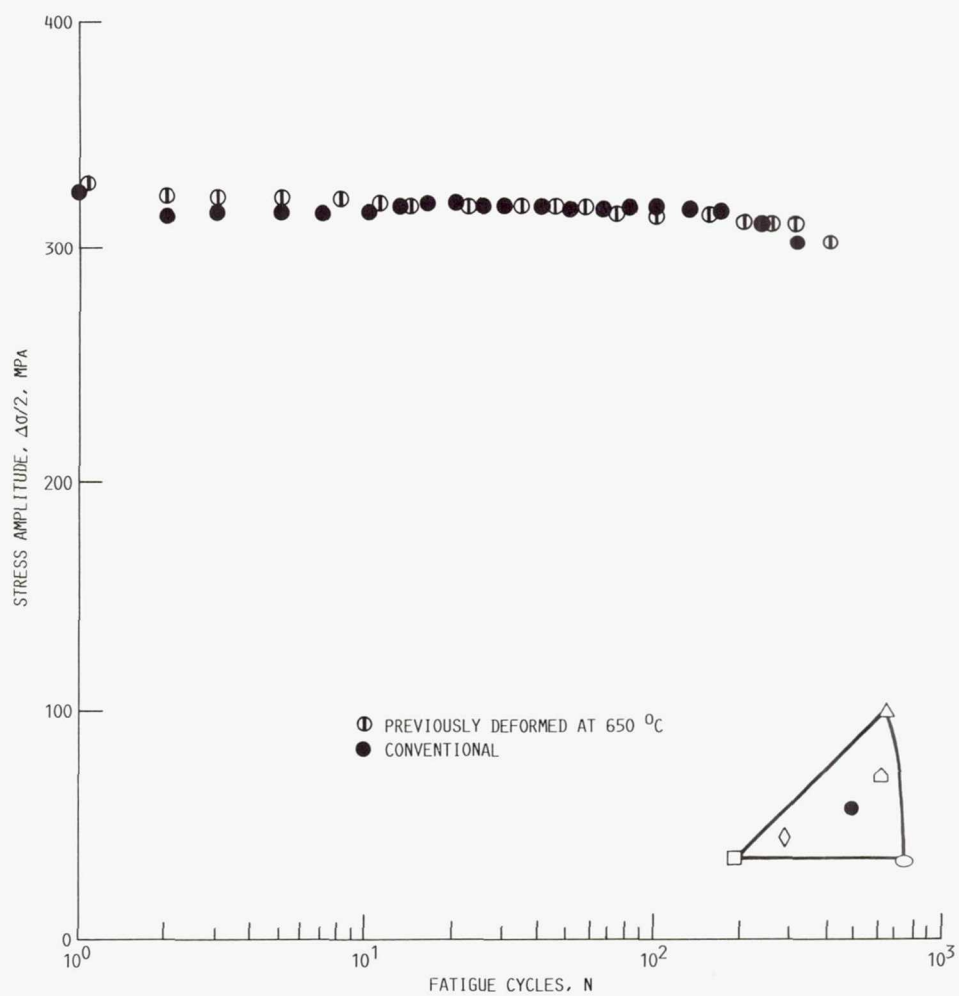
FIGURE 123. – THE LCF STRESS HARDENING RESPONSE OF [$\bar{3}$ 6 10] SPECIMENS AT 1050 ^{o}C WITH AND WITHOUT PRIOR LCF CYCLING AT 650 ^{o}C.

197
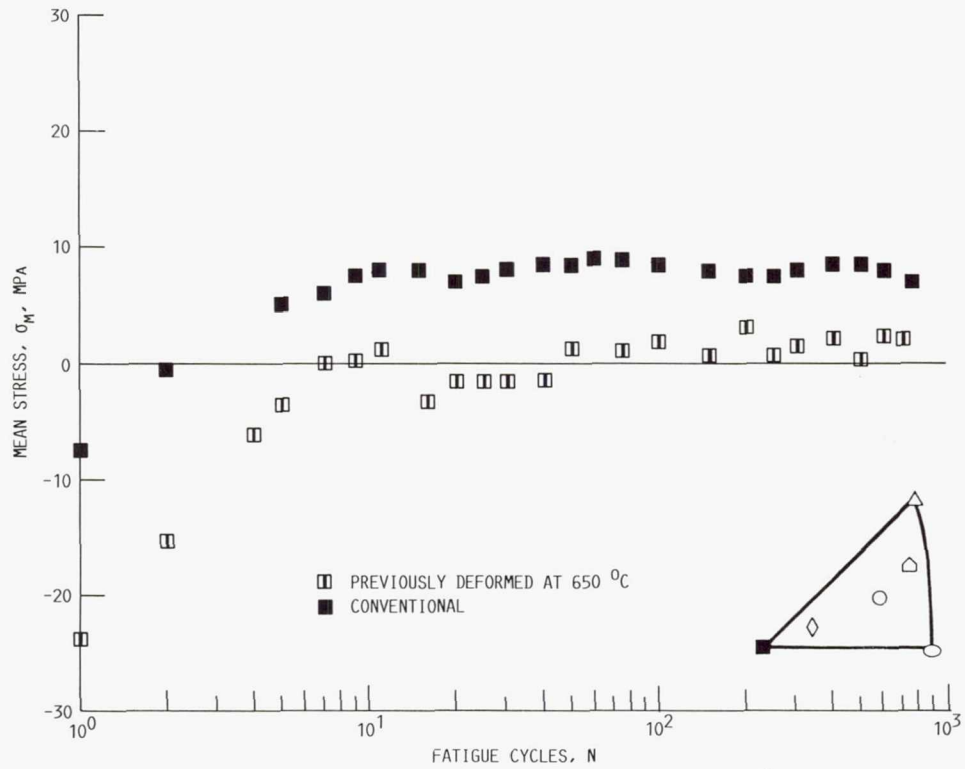
FIGURE 124. – THE LCF MEAN STRESS RESPONSE OF [001] SPECIMENS AT 1050 °C WITH AND WITHOUT PRIOR LCF CYCLING AT 650 °C.
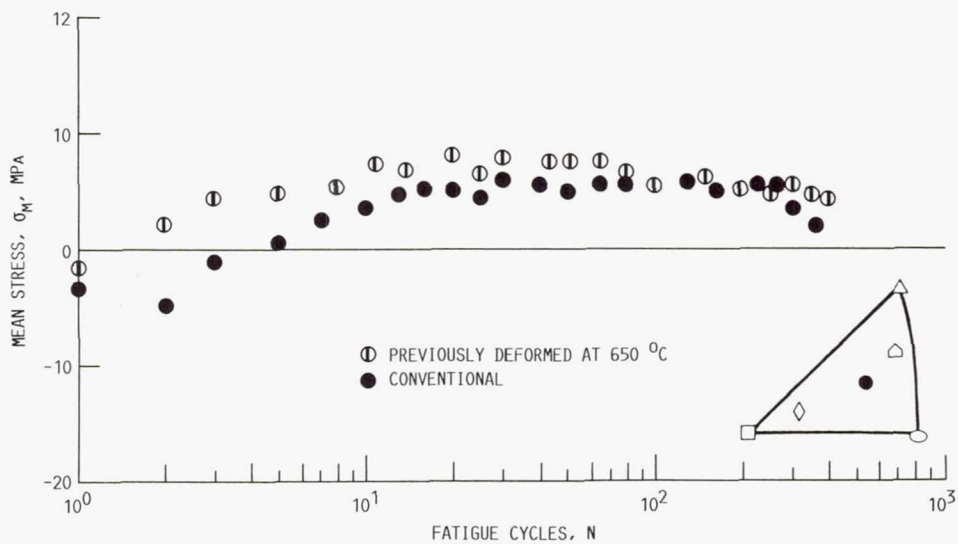
FIGURE 125. – THE LCF MEAN STRESS RESPONSE OF [$\bar{3}$ 6 10] SPECIMENS AT 1050 °C WITH AND WITH-OUT PRIOR LCF CYCLING AT 650 °C.
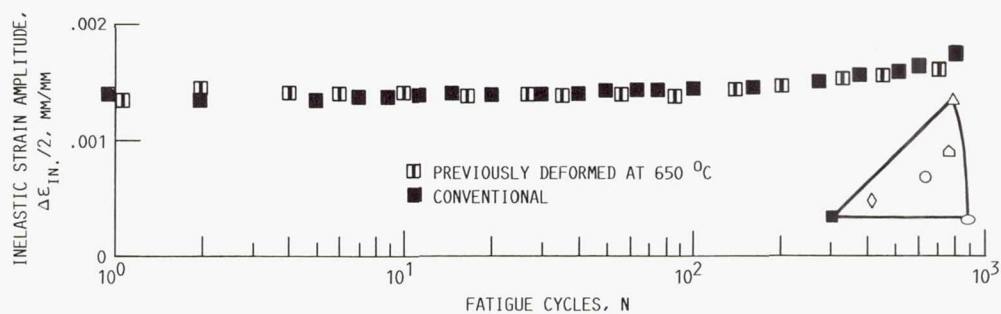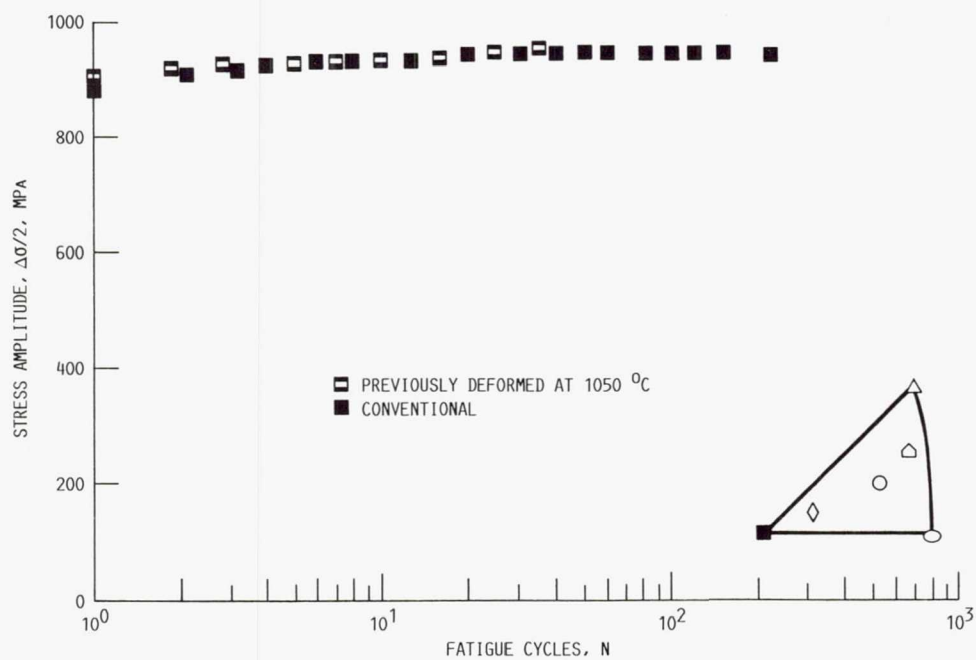
FIGURE 126. - THE LCF INELASTIC STRAIN RESPONSE OF [001] SPECIMENS AT 1050 °C WITH AND WITH-
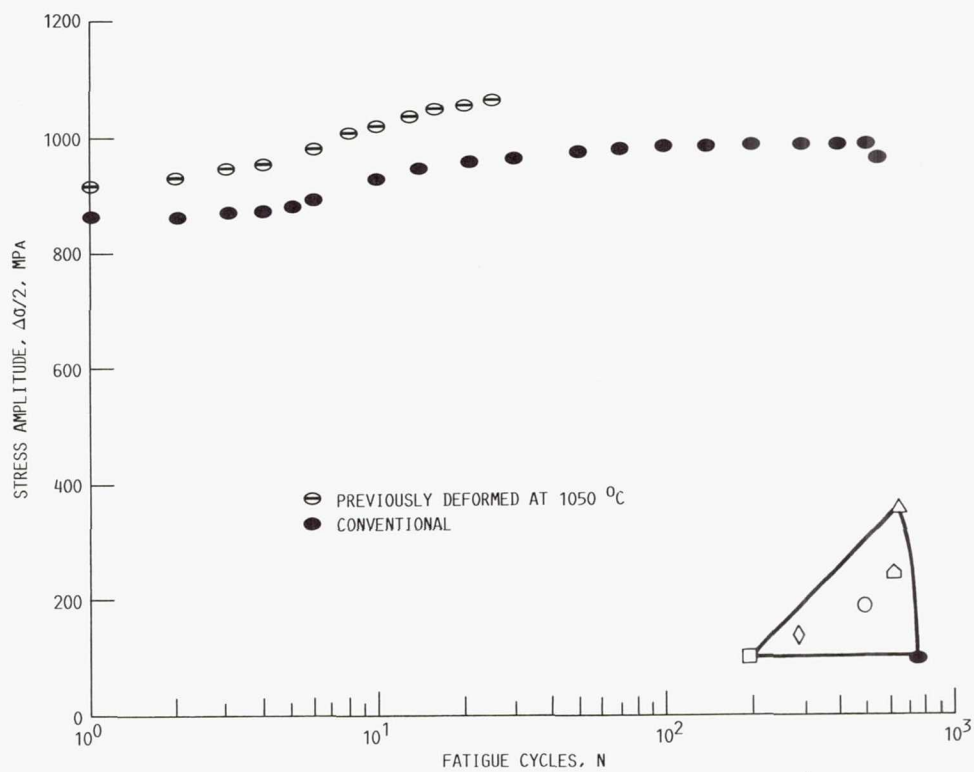OUT PRIOR LCF CYCLING AT 650 °C.
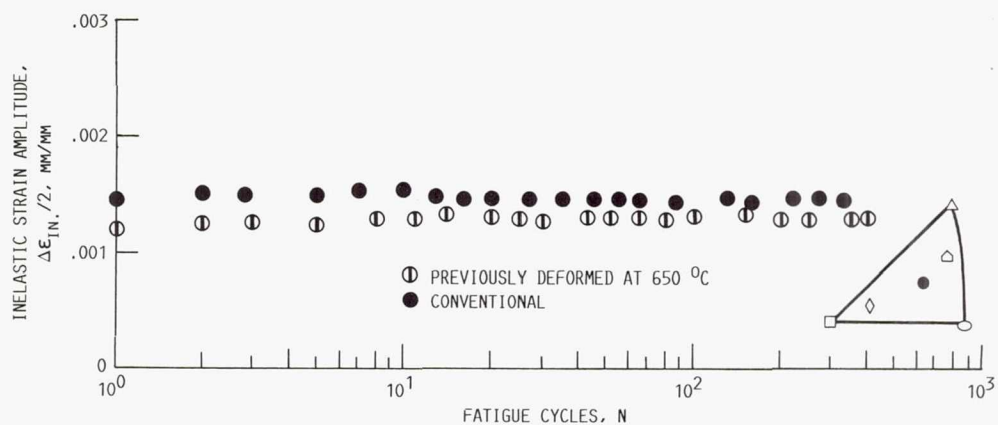
FIGURE 127. - THE LCF INELASTIC STRAIN RESPONSE OF [3̄ 6 10] SPECIMENS AT 1050 °C WITH AND WITH-
OUT PRIOR LCF CYCLING AT 650 °C.
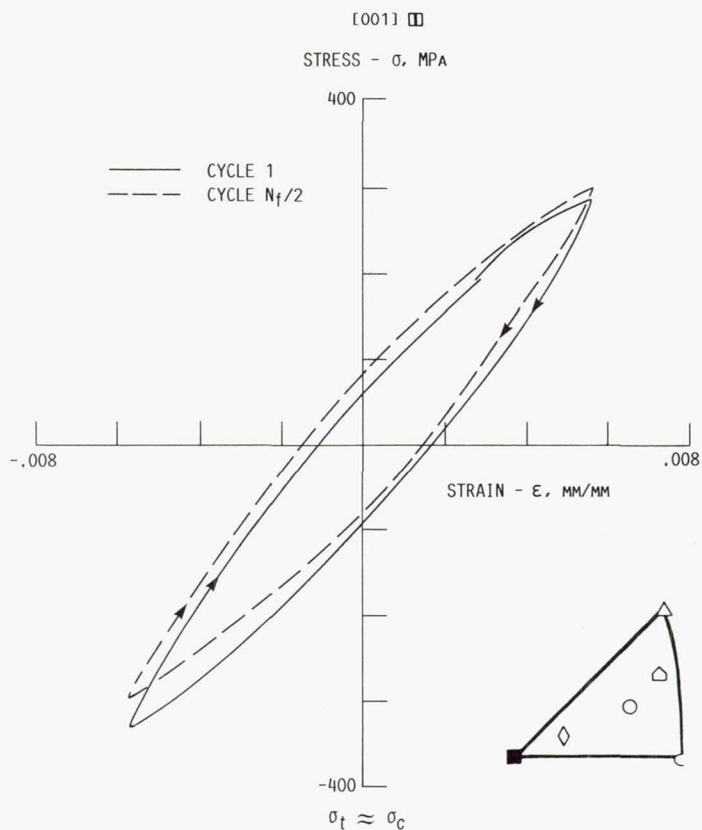
FIGURE 128. — TYPICAL LCF HYSTERESIS LOOPS OF THE [001] SPECIMEN AT 1050 $^{\circ}$C WITH PRIOR LCF CYCLING AT 650 $^{\circ}$C.
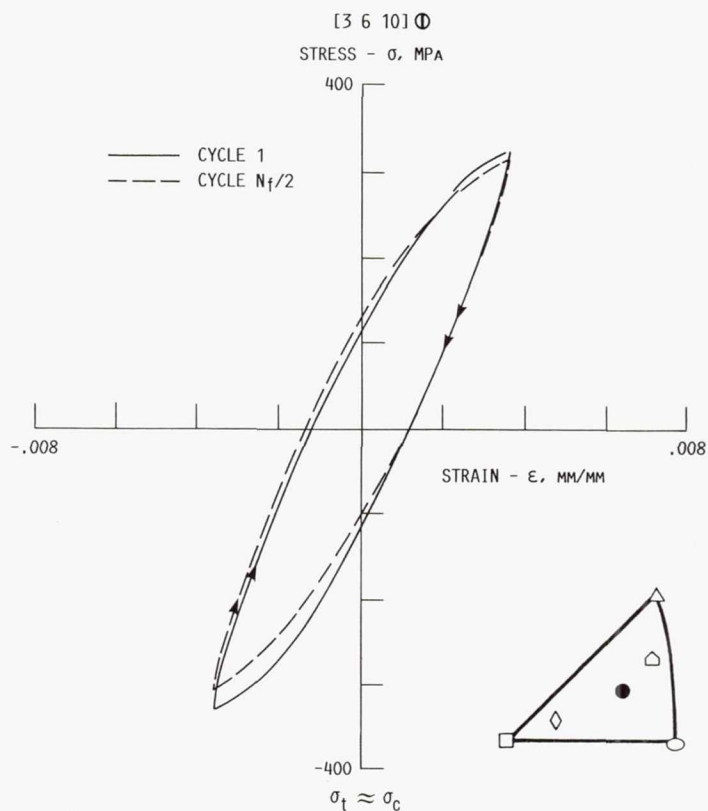
FIGURE 129. — TYPICAL LCF HYSTERESIS LOOPS OF THE [3 6 10] SPECIMEN AT 1050 $^{\circ}$C WITH PRIOR LCF CYCLING AT 650 $^{\circ}$C.

CD-87-29801
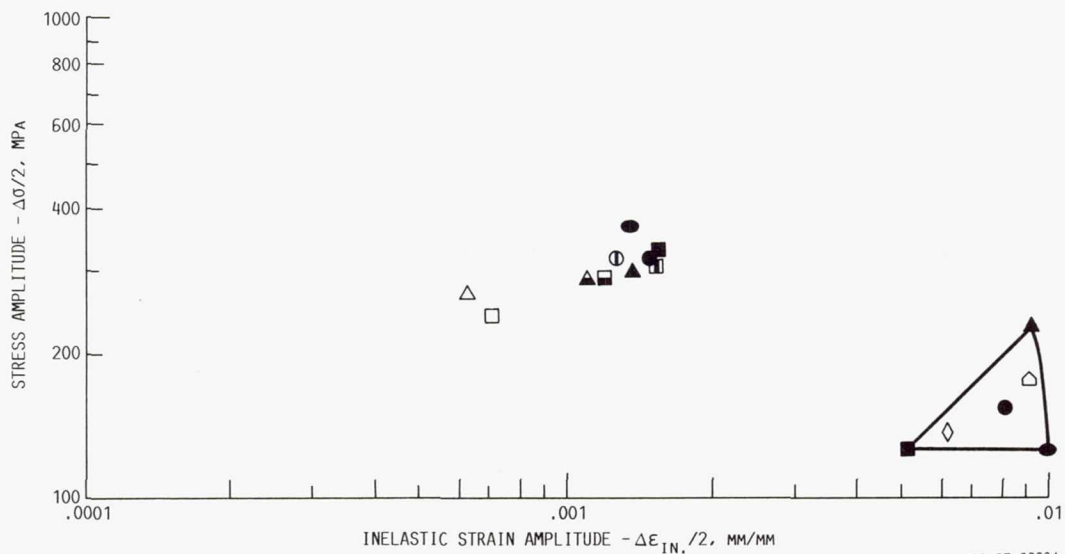
FIGURE 130. — THE CYCLIC STRESS-STRAIN RESPONSE AT HALF OF CYCLIC LIFE OF SPECIMENS WITH AND WITHOUT PRIOR LCF CYCLING AT 650 $^{\circ}$C.
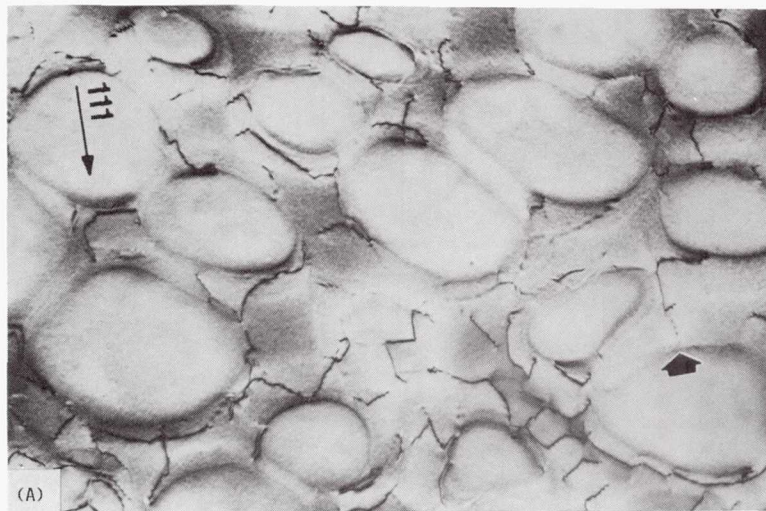
(A) [1̄2̄3] Z.A., (1̄1̄1̄) INTERFACE INDICATED BY THE ARROW.
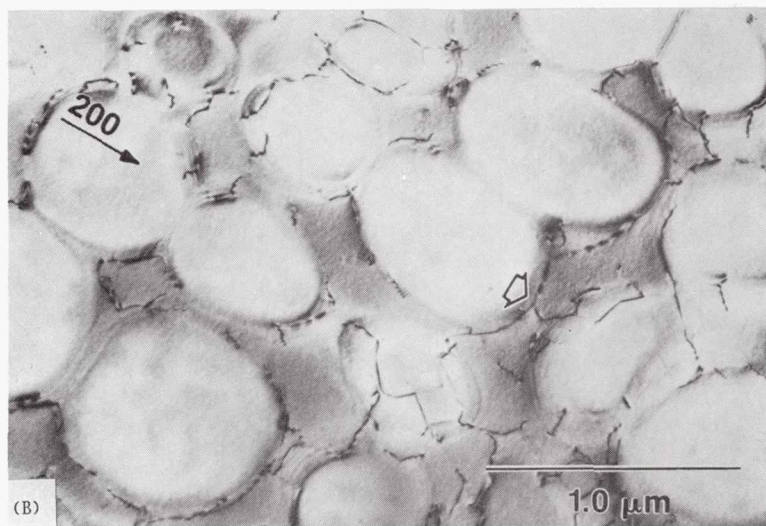
(B) [02̄5] Z.A., (100) INTERFACE INDICATED.

[001] 1050 °C

CD-87-30294
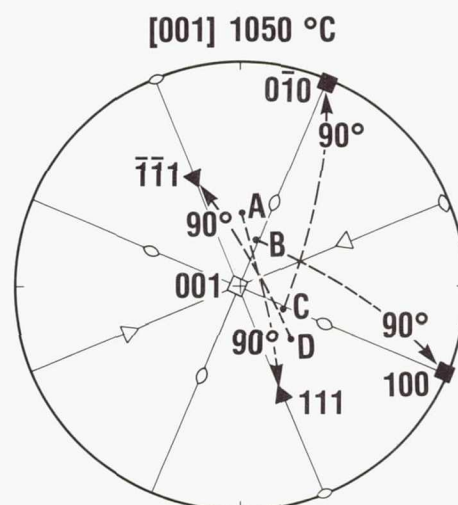
FIGURE 131. - MICROGRAPHS OF A TYPICAL TILTING EXPERIMENT OF AN [001] LCF
SPECIMEN, 1050 °C, $\Delta\varepsilon_{IN.}$ = .0027 MM/MM ON CYCLE 1, PREVIOUSLY GIVEN 20 LCF
CYCLES AT 650 °C.
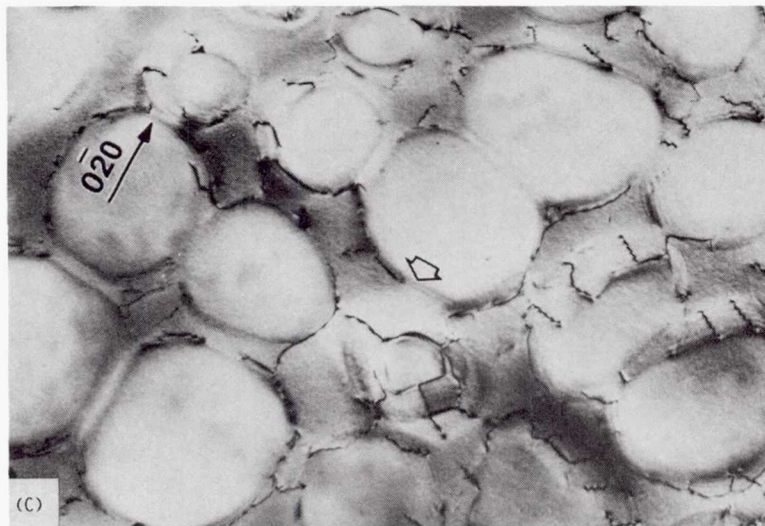
(C) [205] Z.A., (010) INTERFACE INDICATED.
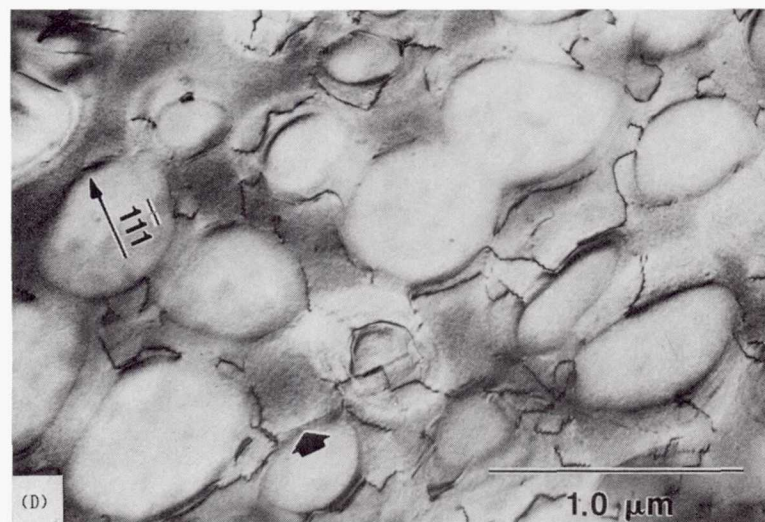
(D) [213] Z.A., ($\bar{1}\bar{1}1$) INTERFACE INDICATED.
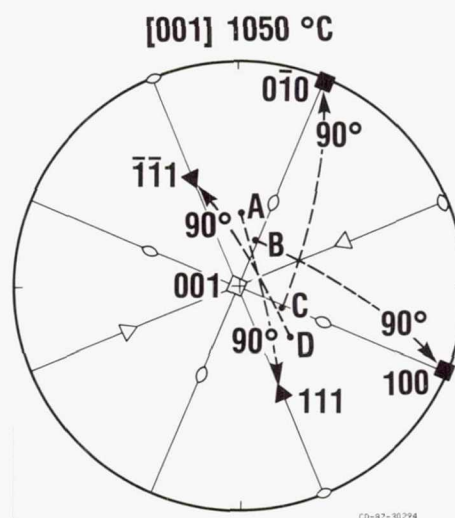
FIGURE 131. - CONCLUDED.
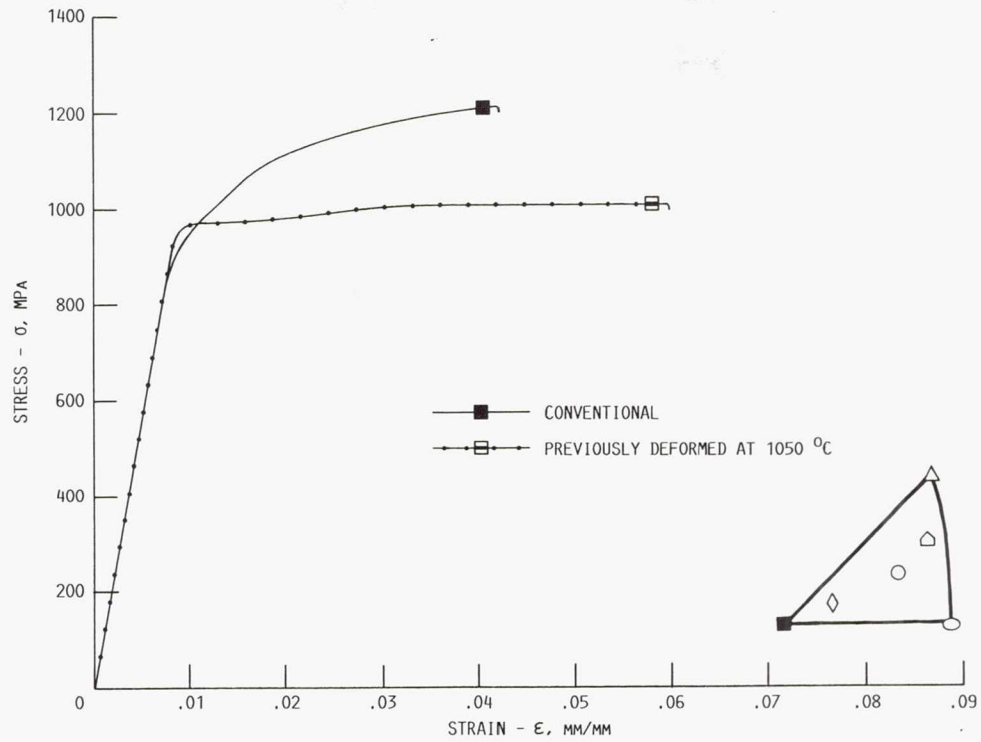
FIGURE 132. - THE AXIAL STRESS-STRAIN CURVES IN TENSILE TESTS AT 650 °C OF [001] SPECIMENS WITH AND WITHOUT PRIOR LCF CYCLING AT 1050 °C.
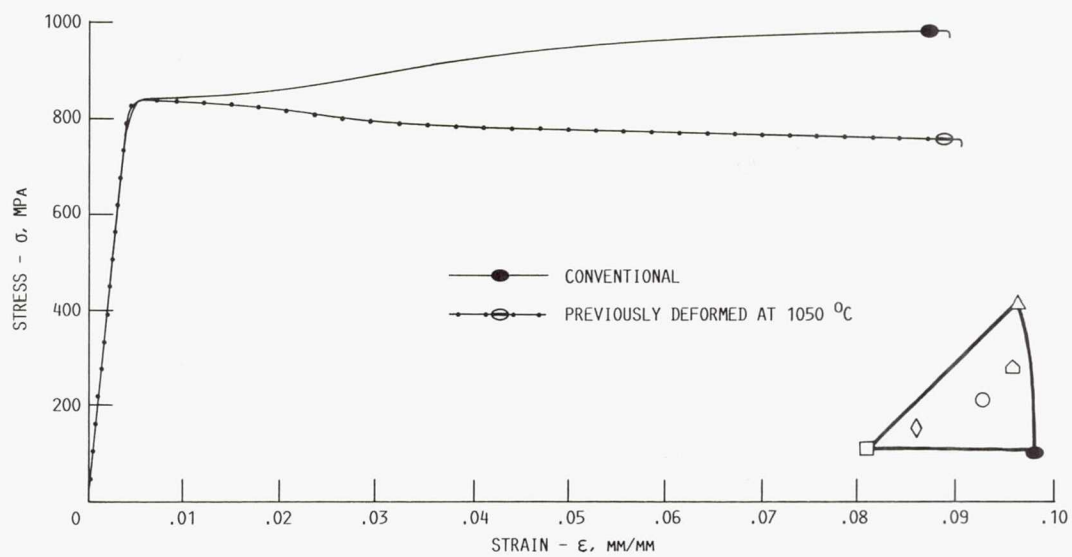
FIGURE 133. - THE AXIAL STRESS-STRAIN CURVES IN TENSILE TESTS AT 650 °C OF [011] SPECIMENS WITH AND WITHOUT PRIOR LCF CYCLING AT 1050 °C.

TENSILE SPECIMEN ROTATIONS
$1050 \rightarrow 650\ ^oC$
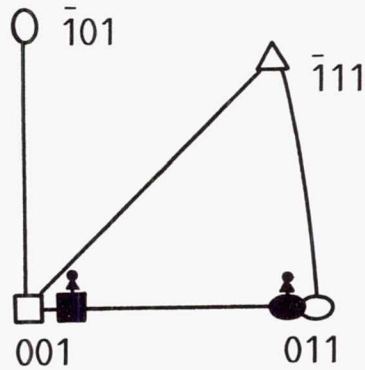
FIGURE 134. - THE CRYSTALLOGRA-PHIC ROTATION OF THE SPECIMEN AXES IN TENSILE TESTS AT 650 ^oC OF [001] AND [011] SPECIMENS WITH PRIOR LCF CYCLING AT 1050 ^oC.

1.0 mm
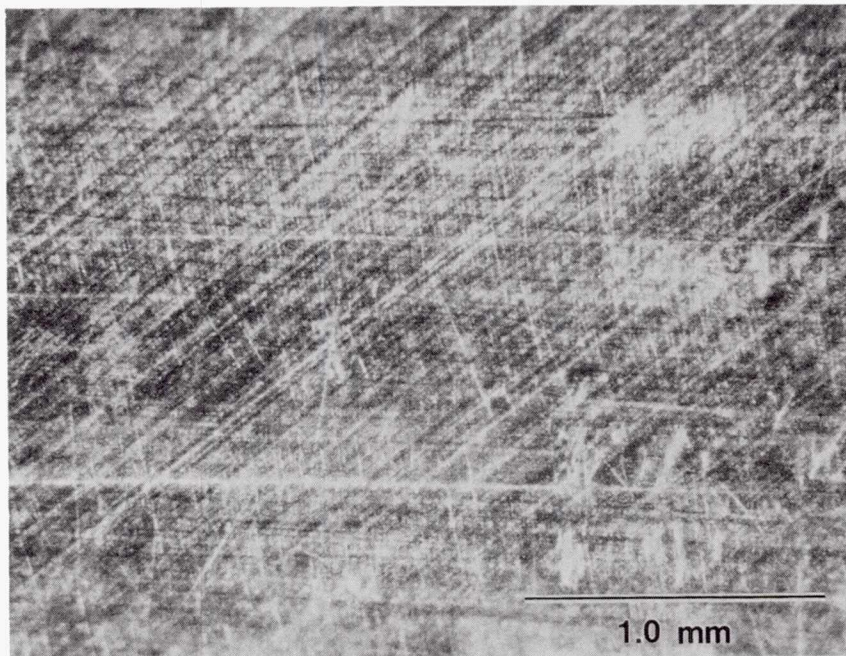
FIGURE 135. - SLIP OFFSETS OF AN [001] LCF SPECIMEN, 650 ^oC, $\Delta\varepsilon_{IN.}$ = .0016 MM/MM ON CYCLE 1, PREVIOUSLY GIVEN 50 LCF CYCLES AT 1050 ^oC.

FIGURE 136. - THE LCF STRESS HARDENING RESPONSE OF [001] SPECIMENS AT 650 °C WITH PRIOR LCF CYCLING AT 1050 °C.
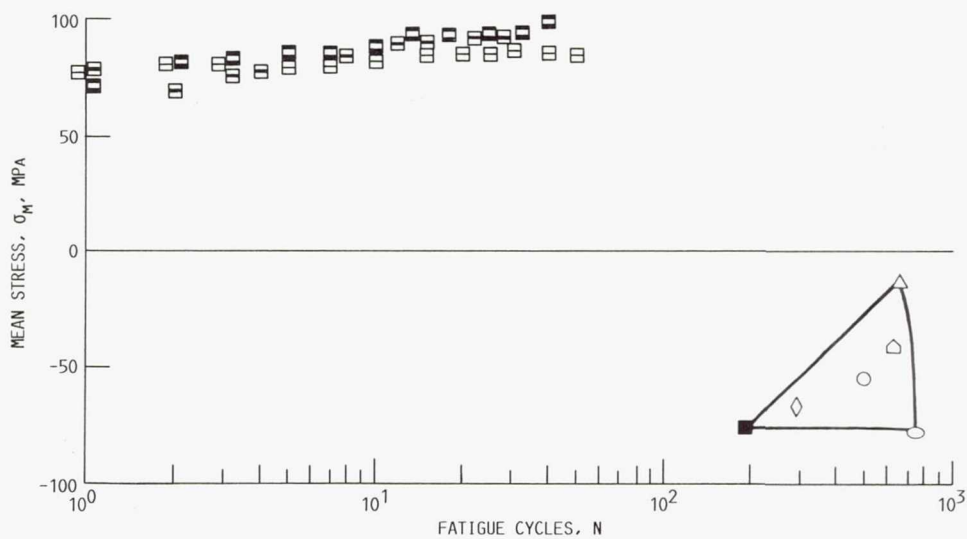
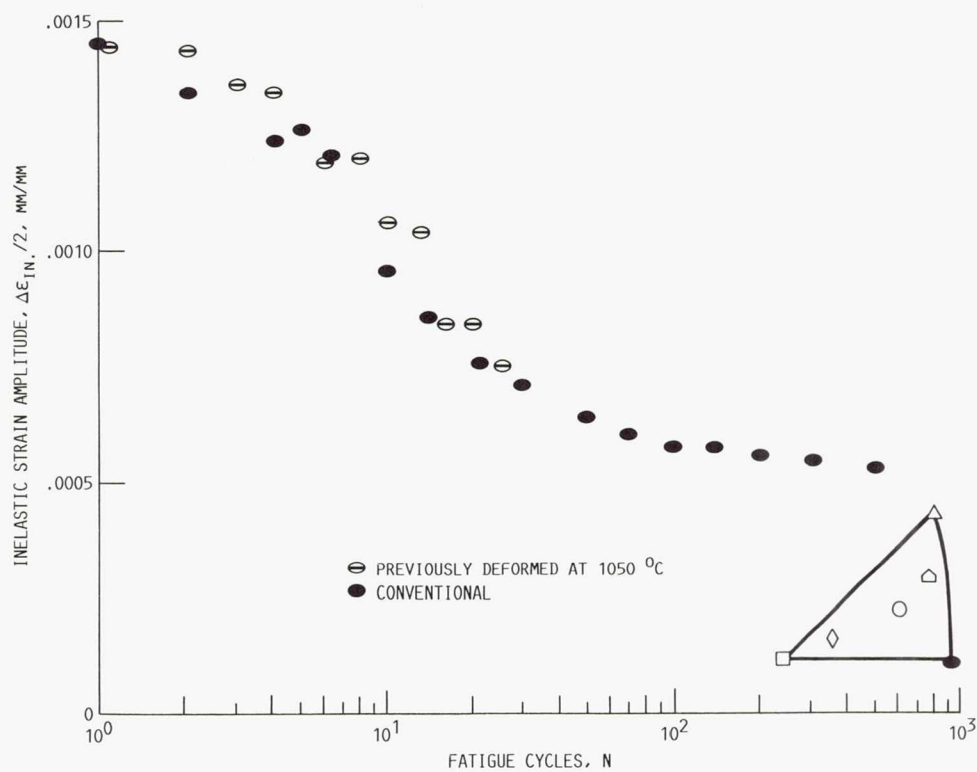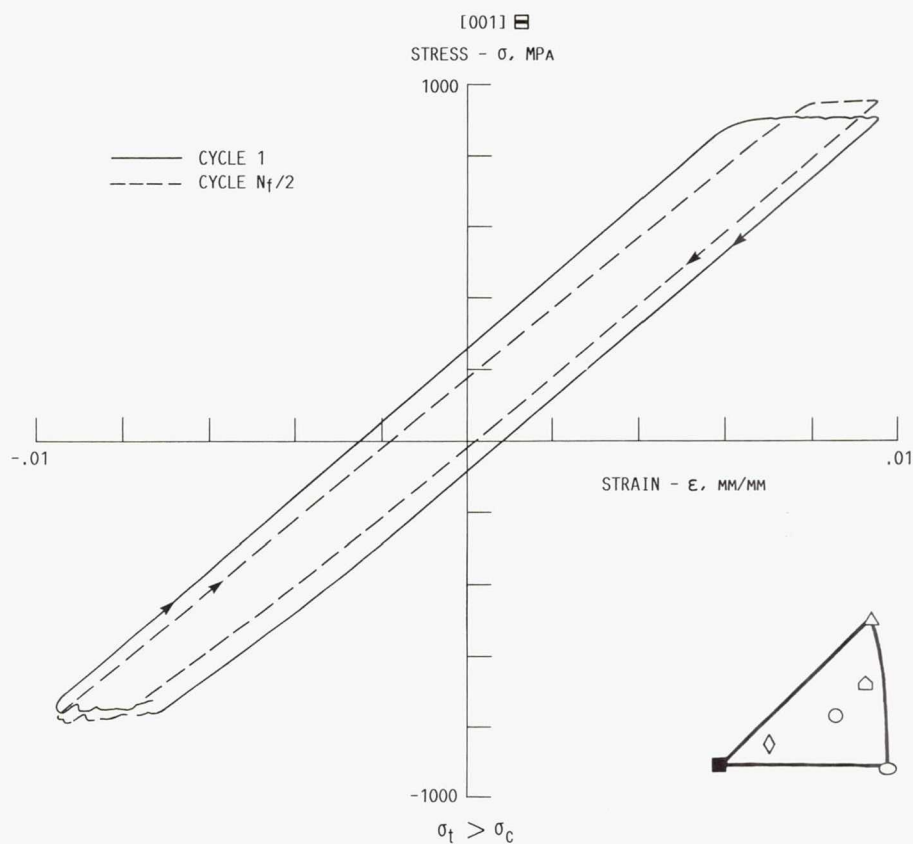FIGURE 137. - THE LCF MEAN STRESS RESPONSE OF [001] SPECIMENS AT 650 °C WITH PRIOR LCF CYCLING AT 1050 °C.
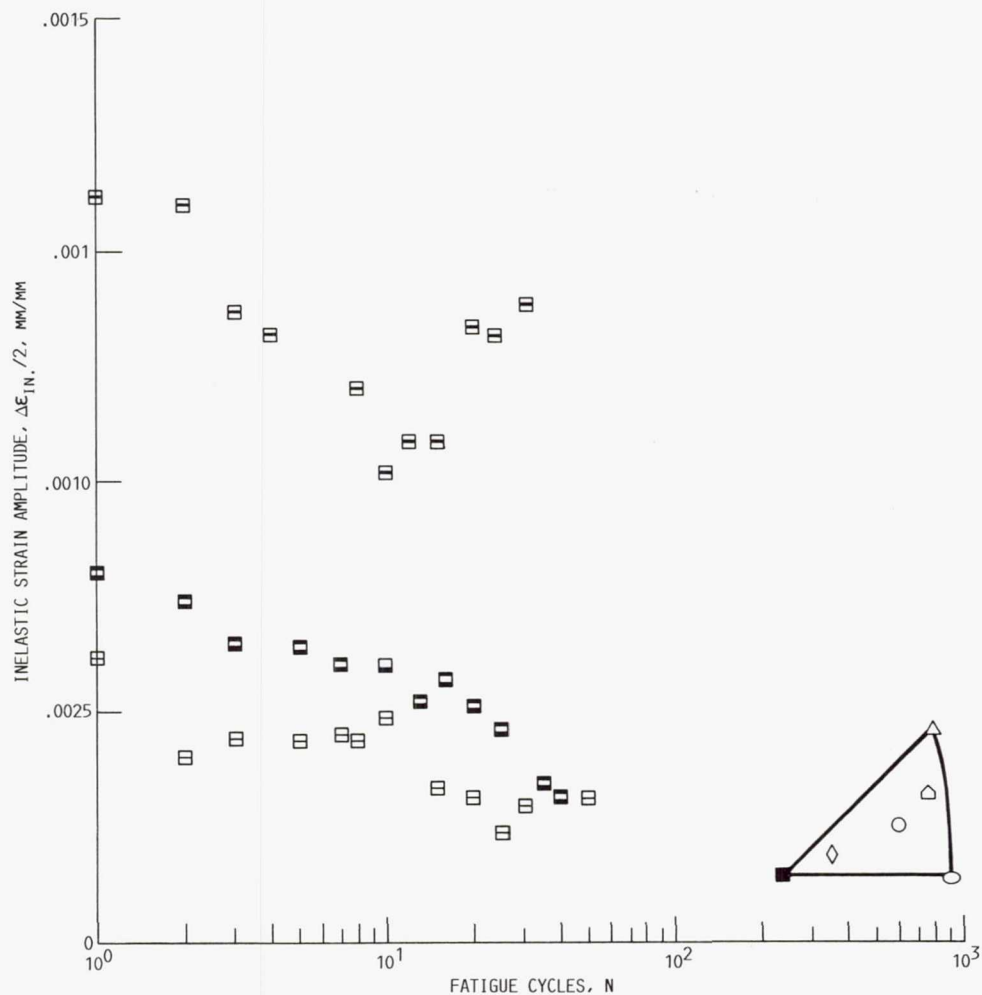
FIGURE 138. - THE INELASTIC STRAIN RESPONSE OF [001] SPECIMENS AT 650 ^{o}C WITH PRIOR LCF CYCLING AT 1050 ^{o}C.

FIGURE 139. - THE LCF STRESS HARDENING RESPONSE OF [001] SPECIMENS AT 650 ^{o}C WITH AND WITHOUT PRIOR LCF CYCLING AT 1050 ^{o}C.

FIGURE 140. – THE LCF STRESS HARDENING RESPONSE OF [011] SPECIMENS AT 650 °C WITH AND WITH-
OUT PRIOR LCF CYCLING AT 1050 °C.
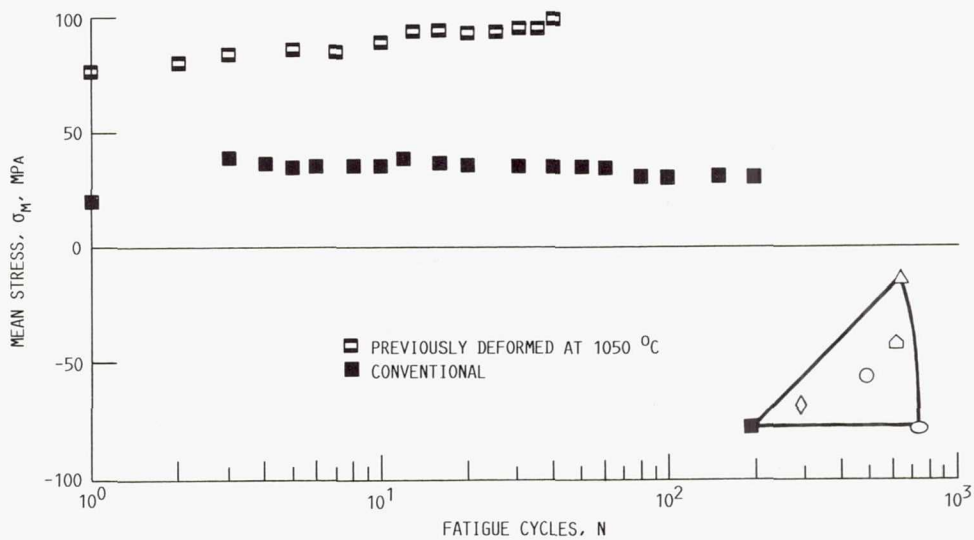
FIGURE 141. – THE LCF MEAN STRESS RESPONSE OF [001] SPECIMENS AT 650 °C WITH AND WITHOUT
PRIOR LCF CYCLING AT 1050 °C.
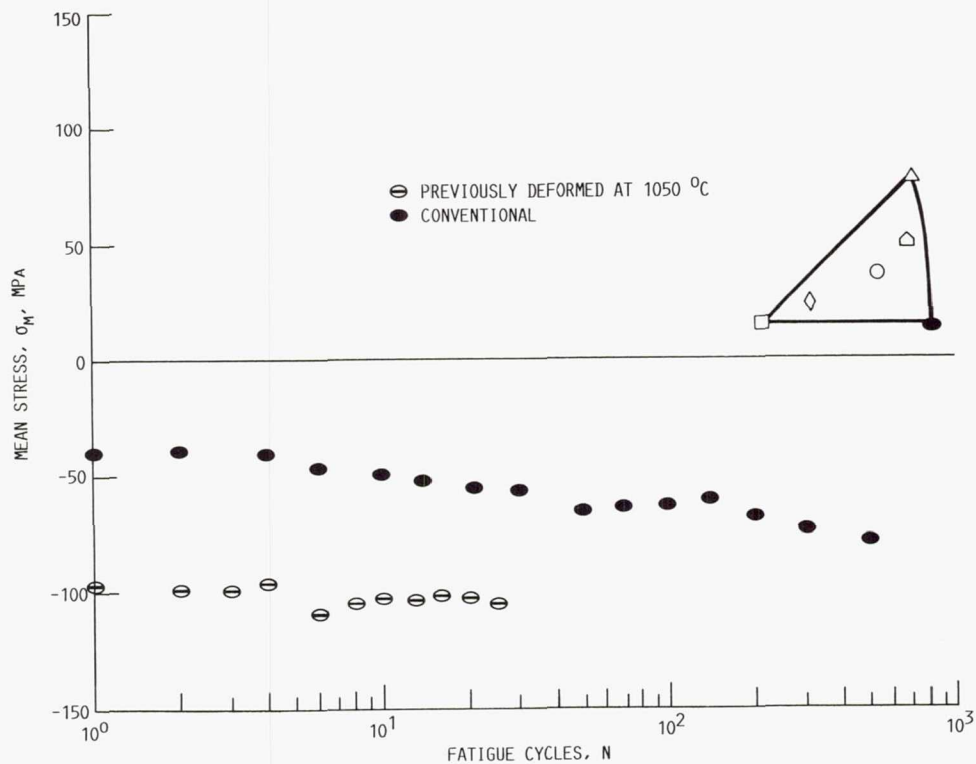
FIGURE 142. – THE LCF MEAN STRESS RESPONSE OF [011] SPECIMENS AT 650 °C WITH AND WITHOUT PRIOR LCF CYCLING AT 1050 °C.
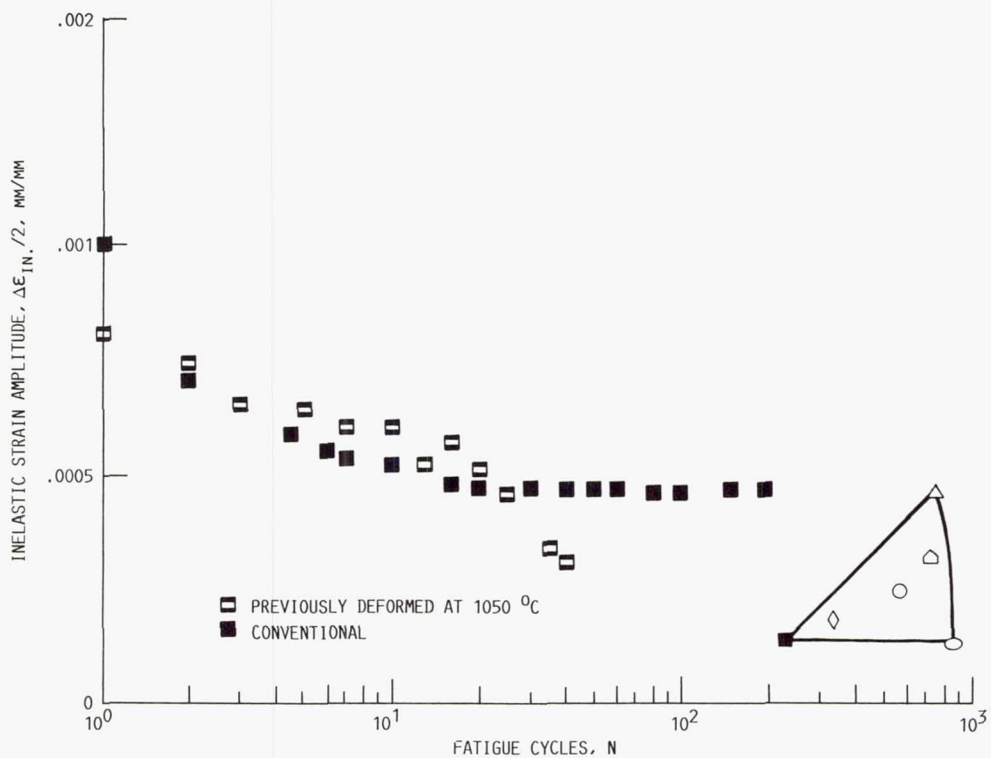
FIGURE 143. – THE LCF INELASTIC STRAIN RESPONSE OF [001] SPECIMENS AT 650 °C WITH AND WITHOUT PRIOR LCF CYCLING AT 1050 °C.

FIGURE 144. – THE LCF INELASTIC STRAIN RESPONSE OF [011] SPECIMENS AT 650 °C WITH AND WITHOUT PRIOR LCF CYCLING AT 1050 °C.

FIGURE 145. – TYPICAL LCF HYSTERESIS LOOPS OF THE [001] SPECIMENS AT 650 °C WITH PRIOR LCF CYCLING AT 1050 °C.
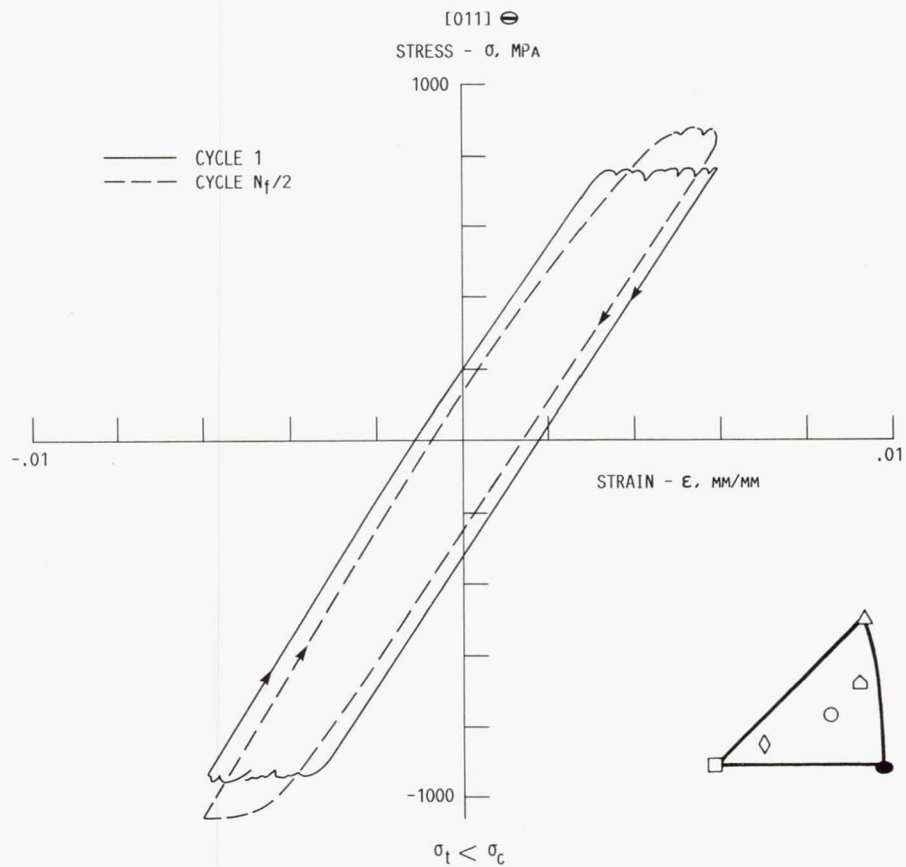
FIGURE 146. - TYPICAL LCF HYSTERESIS LOOPS OF THE [011] SPECIMENS AT 650 °C WITH PRIOR LCF CYCLING AT 1050 °C.
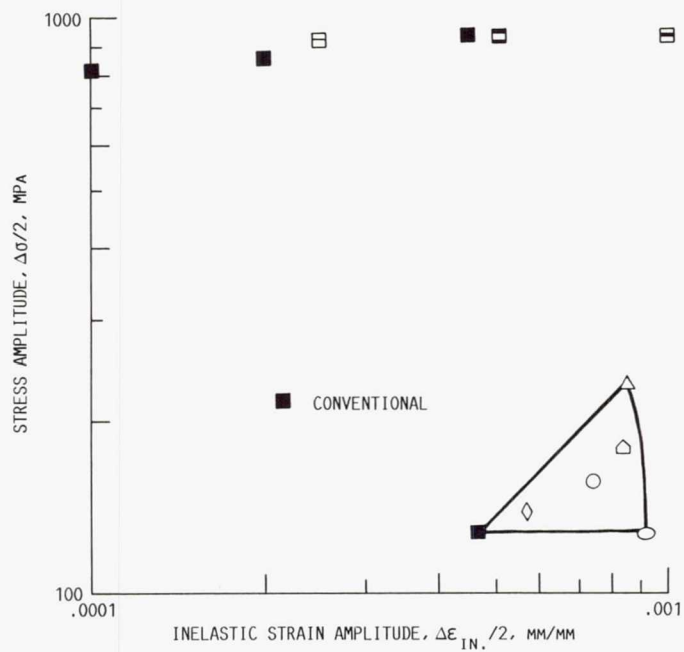
FIGURE 147. - THE CYCLIC STRESS-STRAIN RESPONSE AT HALF OF OF CYCLIC LIFE OF [001] SPECIMENS AT 650 °C WITH AND WITHOUT PRIOR LCF CYCLING AT 1050 °C.
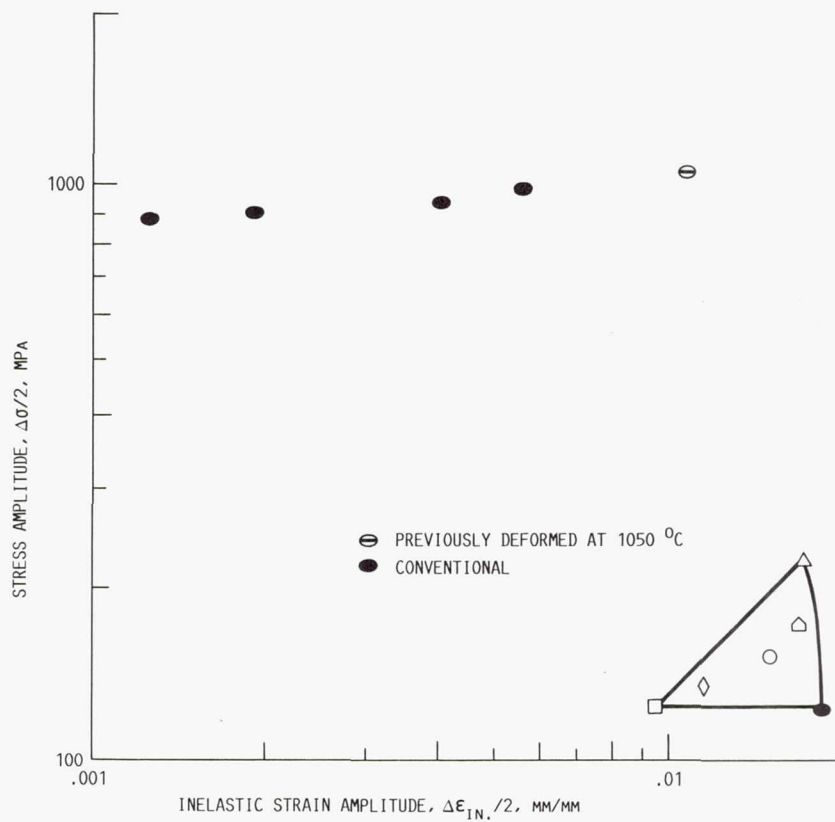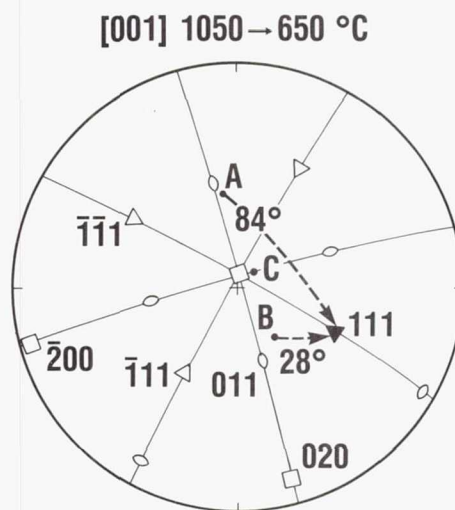
FIGURE 148. – THE CYCLIC STRESS-STRAIN RESPONSE AT HALF OF CYCLIC LIFE OF [011]
SPECIMENS AT 650 °C WITH AND WITHOUT PRIOR LCF CYCLING AT 1050 °C.
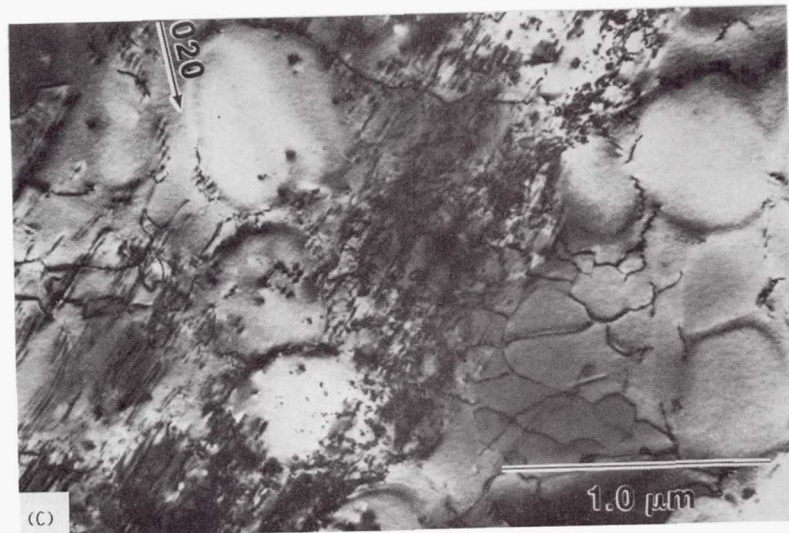
(A) [0$\bar{1}$1] Z.A.

(B) [123] Z.A.

[001] 1050 → 650 °C

CD-87-29812
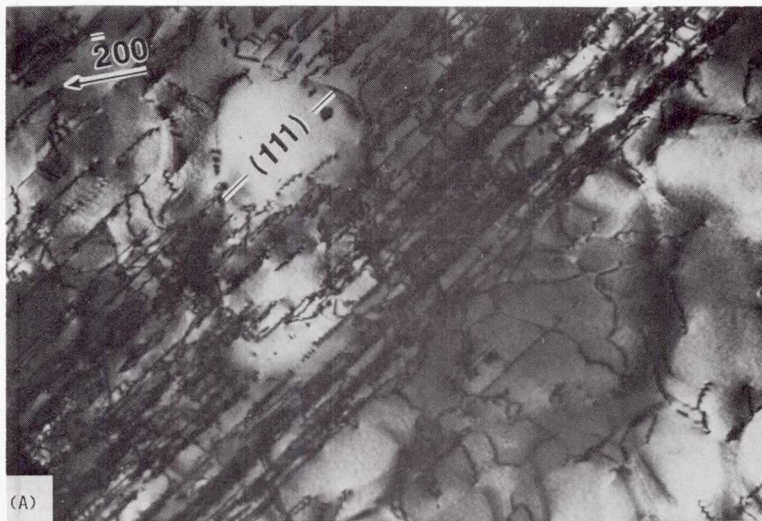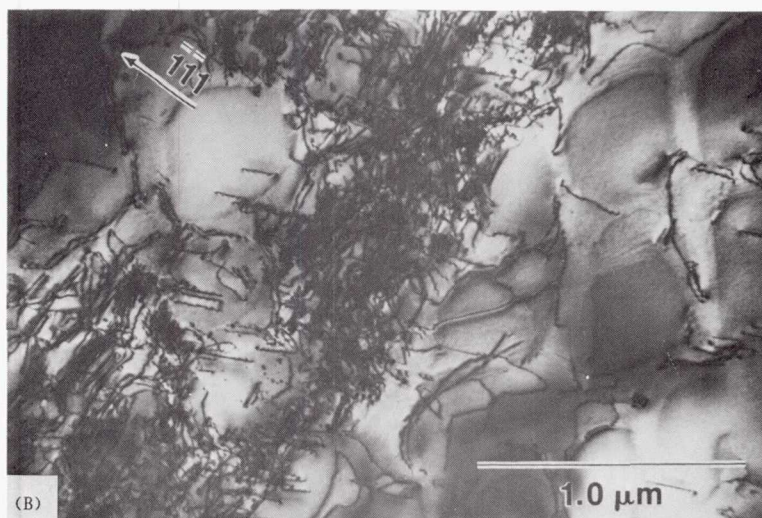
FIGURE 149. – MICROGRAPHS OF A TYPICAL TILTING EXPERIMENT OF AN [001] LCF SPECI-
MEN, 650 °C, $\Delta\varepsilon_{IN.}$ = .0016 MM/MM ON CYCLE 1, PREVIOUSLY GIVEN 50 LCF CYCLES AT
1050 °C.

212

(C) [001] Z.A.

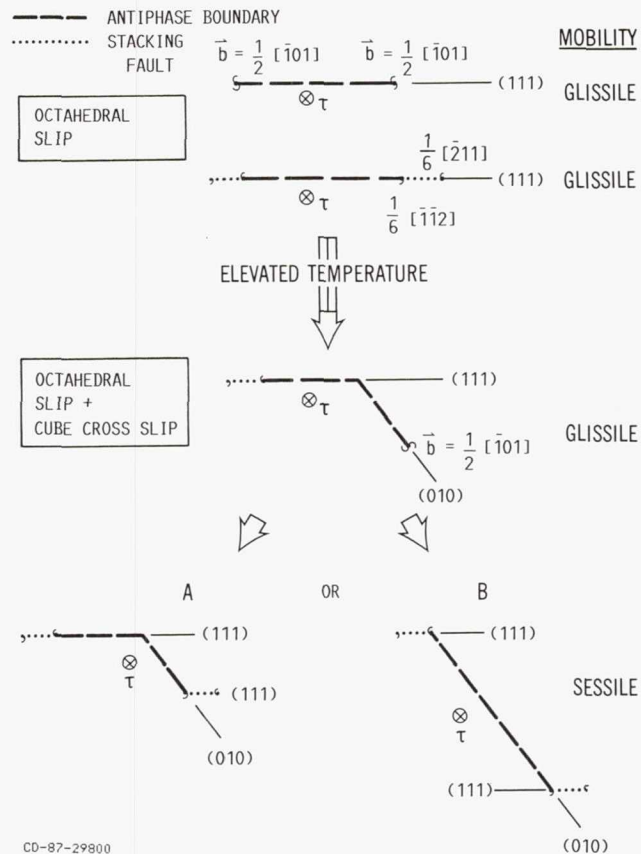## [001] 1050→650 °C
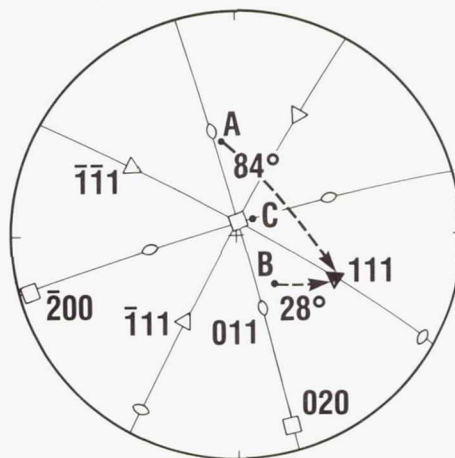
CD-87-29812

FIGURE 149. - CONCLUDED.

213

FIGURE 150. - SCHEMATIC ILLUSTRATIONS OF DISLOCATION PAIRS STORED
IN THE γ' PHASE DURING OCTAHEDRAL SLIP.

SCHEMATIC REPRESENTATION OF DISLOCATION PAIR IN γ' - PHASE WITH PORTION CROSS SLIPPED ONTO THE CUBE PLANE
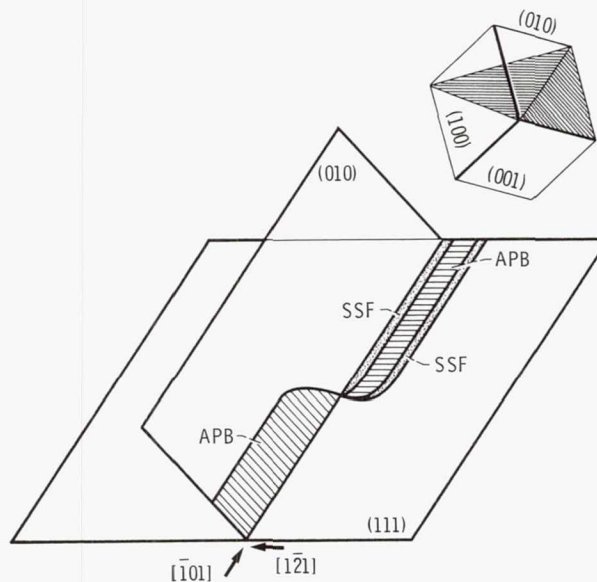

FIGURE 151. - SCHEMATIC ILLUSTRATION OF THE CROSS SLIP OF A DIS-
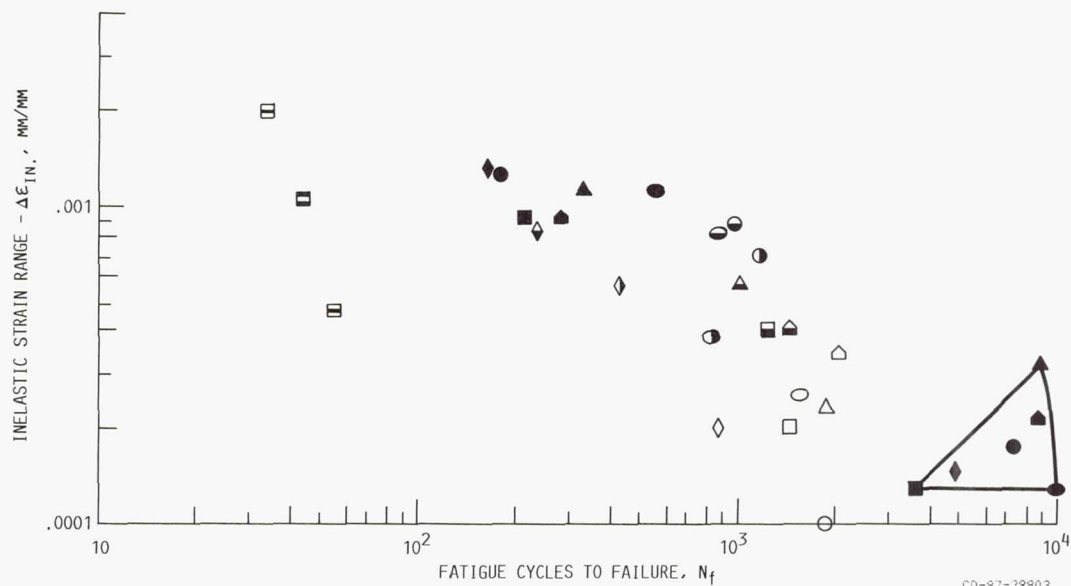LOCATION PAIR ONTO THE CUBE CROSS SLIP PLANE.

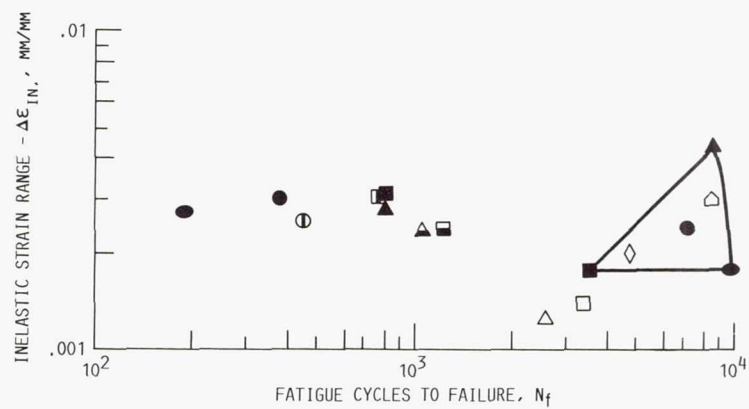FIGURE A1. – THE FATIGUE LIVES OF THE LCF TESTS AT 650 ^{O}C ON AN INELASTIC STRAIN RANGE BASIS.

CO-87-29803

CO-87-29802

FIGURE A2. – THE FATIGUE LIVES OF THE LCF TESTS AT 1050 ^{O}C ON AN
INELASTIC STRAIN RANGE BASIS.

NASA

National Aeronautics and
Space Administration

Report Documentation Page

1. Report No. NASA TM-100269	2. Government Accession No.	3. Recipient's Catalog No.

4. Title and Subtitle	
The Cyclic Stress-Strain Behavior of a Single Crystal Nickel-Base Superalloy	5. Report Date February 1988
	6. Performing Organization Code

7. Author(s)	8. Performing Organization Report No.
Timothy P. Gabb	E-3775
	10. Work Unit No. 505-63-01

9. Performing Organization Name and Address	
National Aeronautics and Space Administration Lewis Research Center Cleveland, Ohio 44135-3191	11. Contract or Grant No.
	13. Type of Report and Period Covered

12. Sponsoring Agency Name and Address	Technical Memorandum
National Aeronautics and Space Administration Washington, D.C. 20546-0001	14. Sponsoring Agency Code

16. Abstract

The utilization of single crystal nickel-base superalloys in load bearing structural applications requires the accurate prediction of monotonic and cyclic stress-strain response with proper consideration of variables such as temperature, strain rate, and temperature/deformation history. But the complexities involved in the deformation of these anisotropic alloys often precludes the application of classical continuum mechanics-based isotropic constitutive models. This behavior can often be more clearly understood and predicted through the relation of the mechanical response to the deformation mechanisms involved. The purpose of this study was to characterize the cyclic stress-strain response and corresponding deformation structures of the single crystal nickel-base superalloy PWA 1480 under a specific set of conditions. The isothermal low cycle fatigue response and deformation structures were characterized at a representative intermediate temperature, 650 °C, and high temperature, 1050 °C. Specimens oriented near the [001], [2 5 20], [3 6 10], [011], [2 3 4], and [111] crystallographic orientations were tested at 650 °C, where significant crystallographic orientation effects were expected. Specimens oriented near the [001] and [111] crystallographic orientations were tested at 1050°C, where more moderate orientation effects were expected. This enabled the characterization of the deformation structures at each of the two temperatures and their relationship to the observed cyclic stress-strain behavior. The initial yield strength of all specimens tested at 650 °C was controlled by the shearing of the γ' precipitates by dislocation pairs. Low cycle fatigue tests at 650 °C had cyclic hardening, which was associated with dislocation interactions in the γ matrix. The initial yield strength of specimens tested at 1050 °C was associated with dislocation bypassing of the γ' precipitates. Low cycle fatigue tests at 1050 °C had cyclic softening, associated with extensive dislocation recovery at the γ-γ' interfaces along with some γ' precipitate coarsening. Low cycle fatigue deformation at 650 °C was significantly affected by prior deformation at 1050 °C, but had little effect on subsequent low cycle fatigue deformation at 1050 °C. Low cycle fatigue deformation at 1050 °C was only slightly affected by prior deformation at 650 °C, and had major effects on subsequent low cycle fatigue deformation at 650 °C.

17. Key Words (Suggested by Author(s)) Low cycle fatigue Single crystals Nickle-base superalloys Deformation mechanisms		18. Distribution Statement Unclassified – Unlimited Subject Category 26	
19. Security Classif. (of this report) Unclassified	20. Security Classif. (of this page) Unclassified	21. No of pages 216	22. Price* A10